University of California
Santa Barbara

Phase-field dislocation dynamics modeling of multi-component alloys

A dissertation submitted in partial satisfaction
of the requirements for the degree

Doctor of Philosophy
in
Materials

by

Lauren T. W. Fey

Committee in charge:

Professor Irene Beyerlein, Chair
Professor Daniel Gianola
Professor Tresa Pollock
Abigail Hunter, Ph.D.

March 2023

The Dissertation of Lauren T. W. Fey is approved.

Professor Daniel Gianola

Professor Tresa Pollock

Abigail Hunter, Ph.D.

Professor Irene Beyerlein, Committee Chair

February 2023

Phase-field dislocation dynamics modeling of multi-component alloys

Lauren T. W. Fey

Acknowledgements

This work would not have been possible without all of the lovely people in my life. First, my advisor Prof. Irene Beyerlein has been a tremendous support throughout my entire Ph.D., and I have appreciated her guidance and positive attitude. I would also like to thank Abby Hunter for hosting me at Los Alamos and for her guidance and advice.

I am especially grateful for the fellow women in my cohort. I believe we were a book club at one point. Thank you all for the lunches, trivia nights, and camping trips.

I am very lucky to have such a supportive family. My parents' confidence in me gives me confidence in myself, and my siblings are truly fantastic and brighten my day every day with their messages. Even though we've been separated these last few years, remaining close with all of you has made me so happy.

I would also like to thank my grandpa, who taught me to love math, and my grandma, who taught me to love crafts. Both of these skills have been essential during my time in graduate school.

Above all, I am so grateful for my husband David for his love and support and of course, for Otis, who spreads joy everywhere he goes.

Curriculum Vitæ

Lauren T. W. Fey

Education

2023	Ph.D. in Materials (Expected), University of California, Santa Barbara.
2018	B.S. in Materials Science and Engineering, University of Illinois at Urbana-Champaign

Publications

Fey, L. T. W., Reynolds, C., Hunter, A., & Beyerlein, I. J. (2023). Phase-field modeling of dislocation-interstitial interactions, Journal of the Mechanics and Physics of Solids, Under Review.

Zheng, H., **Fey, L. T. W.**, Li, X. G., Hu, Y. J., Qi, L., Chen, C., Xu, S., Beyerlein, I. J., & Ong, S. P. (2022). Multi-scale Investigation of Chemical Short-Range Order and Dislocation Glide in the MoNbTi and TaNbTi Refractory Multi-Principal Element Alloys, npj Computational Materials, Under Review.

Fey, L. T. W., & Beyerlein, I. J. (2022). Random Generation of Lattice Structures with Short-Range Order. Integrating Materials and Manufacturing Innovation, 1-9.

Fey, L. T. W., Xu, S., Su, Y., Hunter, A., & Beyerlein, I. J. (2022). Transitions in the morphology and critical stresses of gliding dislocations in multiprincipal element alloys. Physical Review Materials, 6(1), 013605.

Fey, L. T. W., Hunter, A., & Beyerlein, I. J. (2022). Phase-field dislocation modeling of cross-slip. Journal of Materials Science, 1-15.

Fey, L. T. W., Tan, A. M. Z., Swinburne, T. D., Perez, D., & Trinkle, D. R. (2021). Accelerated molecular dynamics simulations of dislocation climb in nickel. Physical Review Materials, 5(8), 083603.

Smith, L. T. W., Su, Y., Xu, S., Hunter, A., & Beyerlein, I. J. (2020). The effect of local chemical ordering on Frank-Read source activation in a refractory multi-principal element alloy. International Journal of Plasticity, 134, 102850.

Xu, S., Su, Y., **Smith, L. T. W.**, & Beyerlein, I. J. (2020). Frank-Read source operation in six body-centered cubic refractory metals. Journal of the Mechanics and Physics of Solids, 141, 104017.

Xu, S., **Smith, L.**, Mianroodi, J. R., Hunter, A., Svendsen, B., & Beyerlein, I. J. (2019). A comparison of different continuum approaches in modeling mixed-type dislocations in Al. Modelling and Simulation in Materials Science and Engineering, 27(7), 074004.

Presentations

Fey, L. T. W., Zheng, H., Ong, S. P., Beyerlein, I. J. (2023) The Role of Short-Range Order in Multi-Principal Element Alloys. UCSB Winter Study Group on High Performance Materials, Santa Barbara, California.

Fey, L. T. W., Reynolds, C., Hunter, A., Beyerlein, I. J. (2022) Phase-field modeling of dislocation-interstitial interactions. Gordon Research Conference: Computational Materials Science and Engineering, Newry, Maine. (poster)

Fey, L. T. W., Xu, S., Su, Y., Hunter, A., Beyerlein, I. J. (2021) Modeling Dislocation Dynamics in Refractory Multi-principal Element Alloys. 2nd World Congress on High Entropy Alloys, Charlotte, North Carolina.

Smith, L. T. W., Hunter, A., Beyerlein, I. J. (2021) Phase-Field Dislocation Dynamics Modeling of Refractory Multi-Principal Element Alloys. TMS 2021, Virtual.

Smith, L., Xu, S., Su, Y., Hunter, A., Beyerlein, I. J. (2020) Phase Field Dislocation Dynamics Modeling of Refractory High Entropy Alloys. TMS 2020, San Diego, California. (poster)

Abstract

Phase-field dislocation dynamics modeling of multi-component alloys

by

Lauren T. W. Fey

Refractory metal alloys are candidates for the next generation of materials for extreme conditions, but challenges associated with their ductility, processability, and environmental resistance limit their application. Computational modeling and simulation can help understand the mechanisms underpinning these alloys' mechanical properties so they can be controlled in the future. In this dissertation, a mesoscale model, phase-field dislocation dynamics (PFDD), is extended to model the fundamental aspects of refractory alloys and used to simulate dislocation behavior in several refractory alloy systems.

First, the PFDD formulation is adjusted to simulate a newer class of materials, multi-principal element alloys (MPEAs). The behavior of Frank-Read sources is simulated in MoNbTi, revealing highly statistical behavior that is inherent to these random alloys. Simulations of long dislocations in the same material show start-stop dislocation glide, with the random nature of the MPEA providing both favorable kink-pair nucleation sites and local pinning points. A direct connection to atomistic short-range order is made, showing that the increase in strength with short-range order is caused by an increase in the local unstable stacking fault energy.

Then, a local concentration parameter is added to PFDD to simulate the effects of interstitial atoms such as oxygen and hydrogen. Both short-range and long-range interactions between interstitial atoms and dislocations are accounted for. Interstitial-dislocation interactions are simulated in two systems: Nb with O interstitials and W with H interstitials. The effect on dislocation core structures, critical glide stresses,

and mobility are simulated and discussed. This work provides both new insights into dislocation behavior in refractory materials and a new mesoscale framework for simulating other alloy systems of interest.

Contents

Chapter 1

Introduction

1.1 Motivation

There is increasing demand for materials that can withstand extreme temperatures and conditions. For example, the operating temperature of a jet engine is currently limited by the turbine blade material [1], so there is a strong motivation to develop new alloys that retain their strength at high temperatures. Fusion reactors are another example of materials under extreme environments, as plasma-facing materials must be able to withstand both high temperatures and high levels of radiation [2].

Due to their innately high melting temperatures, alloys composed of refractory elements are excellent candidates for high-temperature applications [1, 3]. These elements include Cr, Hf, Mo, Nb, Ta, Ti, V, W, and Zr, which form the so-called refractory block of the periodic table. In their pure forms, these elements form body-centered cubic (BCC) or hexagonal-close packed (HCP) lattices. Nb-based alloys are currently used in aerospace applications [4], while W is a leading candidate for plasma-facing materials in fusion reactors [2, 5]. There are still several obstacles that must be overcome before the use of these materials can become widespread. In particular, difficulties in processing

and the presence of interstitial atoms such as O and H can limit their applications [4].

A relatively new class of materials, multi-principal element alloys (MPEAs), have emerged and greatly expanded the potential composition space for refractory alloys. While conventional alloys are primarily composed of one element with small additions of other elements to tune the properties, MPEAs are composed of several elements with no one element composing the majority, forming a random solid solution [1]. First identified in the early 2000s, initial MPEAs had a face-centered cubic (FCC) structure [6]. The first refractory MPEAs were synthesized in 2010, forming a BCC solid solution [3]. Since then, research into refractory MPEAs has dramatically accelerated, and several promising refractory MPEA compositions have been identified experimentally, including the HfNbTaTiZr Senkov alloy [7]. Because of the nearly endless MPEA compositions that could be studied, computational modeling and simulation have become important filters for understanding MPEA behavior and identifying potential alloys with desirable properties.

There are still many open questions as to how these materials deform and what can be done to control their mechanical properties. As the motion of dislocations generally controls plastic deformation in metals, it is critical to understand the unique dislocation mechanisms and behaviors in these alloys. The presence of either interstitial atoms or the random nature of an MPEA can both significantly affect how dislocations behave and thus the macroscopic mechanical properties. Below, Sections 1.2 and 1.3 briefly summarize the current understanding of dislocation mechanisms in refractory alloys, including MPEAs and interstitial effects, in order to identify outstanding gaps in our knowledge.

1.2 Dislocations in multi-principal element alloys

While several refractory MPEA compositions with desirable mechanical properties have been identified experimentally, the dislocation mechanisms in MPEAs are not entirely understood. In conventional BCC materials, it is well-known that screw dislocations control the behavior due to their non-planar core structures [8, 9]. Screw dislocations must glide through thermally-activated kink-pair nucleation and migration, leading to significant temperature sensitivity in the mechanical response [8]. Some experimental observations of refractory MPEAs show numerous straight screw dislocations aligned in the $\langle 111 \rangle$ direction [10–12]. Combined with significant levels of dislocation debris and loops [11, 12], these observations suggest that dislocations in these refractory MPEAs are behaving in similar ways as in conventional BCC alloys. However, other experimental observations show dislocations with significant edge character, wavy morphologies, or slip on higher order glide planes, suggesting that there may be dislocation mechanisms that are unique to certain refractory MPEAs [13].

In more conventional alloys, solid solution strengthening models are used to understand the strength increase due to alloying. These models have been extended for MPEAs with some success [7, 14, 15]. According to classical solid solution theory, the dilute solute atoms create stress fields that interact with the stress fields of dislocations, thus increasing the dislocation glide stress. In an MPEA, the lattice is highly distorted due to the differing atomic radii of the constituents, creating a constantly changing landscape that the dislocation must traverse. In dilute binary alloys, this increase in yield strength due to solute atoms scales with $c^{1/2}$ where c is the concentration of solute [16]. For higher concentrations of solute, the strengthening scales with $c^{2/3}$ [17], but these laws break down in the extreme case of MPEAs. For example, the yield strength of $HfMo_xNbTaTiZr$ alloys increases linearly with increasing Mo content [18]. Traditional solid solution strengthen-

ing likely plays a role but does not tell the entire story of strengthening in MPEAs.

While solid solution strengthening generally concerns the long-range elastic interactions between the dislocation and solute atoms, the dislocation core structure itself is influenced by the atoms present at the core. In an MPEA, the random lattice causes the dislocation core structure to change along the dislocation line itself. Dislocation core structures cannot be observed experimentally, but atomic simulations can be used to gain insight. Density functional theory (DFT) calculations have been used to calculate the core structure of various refractory MPEAs, showing variations in the screw core structure of NbTiZr along the dislocation line, with the core spreading asymmetrically onto preferable planes [19]. In MoNbTaW, DFT calculations predicted a Gaussian distribution of dislocation core energies [20]. Molecular dynamics (MD) simulations also show variable core structures for both edge and screw dislocations [21]. Since the dislocation core energies vary from point to point in a random MPEA, dislocations may become trapped in low energy regions, further increasing the stress required for glide [22, 23].

In contrast to conventional BCC alloys, there is both experimental and computational evidence for that edge and mixed-character dislocations may play an important role alongside screw dislocations in controlling behavior. This effect was first observed in Nb-Mo and Nb-Rh binary alloys [24] but was again observed in refractory MPEAs such as TaTiNbHfZr and MoNbTi [13, 25]. In-situ measurements of dislocation velocities in Ti-Zr-Nb alloys show screw and edge dislocation velocities on the same order of magnitude, emphasizing that edge dislocations are not as mobile as often thought in these alloys [26]. Computational models for refractory MPEAs also predict mobilities of edge dislocations comparable to thse of screw dislocations. For example the predicted Peierls stress of an edge dislocation is only about half that of a screw dislocation at room temperature in NbTiZr or a Co-Fe-Ni-Ti alloy [19, 21]. Some models have even been proposed which suggest that edge dislocation glide is the limiting mechanism under certain conditions

[27, 28].

The dislocation mechanisms in MPEAs are further complicated by the presence of short-range order (SRO). While MPEAs do not contain long-range order by definition, SRO can appear through the preferential clustering of certain elements. SRO has been observed experimentally in both FCC MPEAs such as CoCrNi [29, 30] and VCoNi [31] as well as the BCC RMPEAs such as HfNbZr [32]. Further evidence of SRO in MPEAs have also been provided via density functional theory (DFT) and atomistic simulations [33–37]. Synthesis and processing levers, such as temperature, can be used to control the degree of SRO, which in turn can have a significant influence on the dominant dislocation mechanisms and mechanical properties. For instance, computational simulations have shown that a higher SRO in the NbMoTaW MPEA leads to increased barriers to dislocation motion, leading to higher strength [20, 22, 38, 39].

Fully understanding the dislocation mechanisms in MPEAs presents a significant challenge that will require a multitude of experimental and computational approaches. On the simulation front, atomistic approaches such as DFT and MD can reveal information on smaller length scale, such as the presence of SRO or the core structures of short, individual dislocations. To bridge the gap between atomistic information and macroscale properties, mesoscale models that can simulate longer dislocations and their interactions are necessary. Mesoscale models include phase-field and discrete dislocation dynamics models, which were first applied to MPEAs in 2019 [40–42]. These models show many of the same dislocation mechanisms that are seen experimentally and in atomistic simulations, such as wavy dislocation glide and statistical glide stresses, but the challenge lies in directly linking these mesoscale models with atomistic information.

1.3 Dislocation interactions with interstitial elements

In both refractory MPEAs and conventional refractory alloys, interstitial solute atoms, such as H, O, C, and N pose a significant challenge. These elements are readily dissolved into refractory alloys during processing, and even in small amounts (< 1 at%), interstitial atoms increase material strength at the expense of a drastic loss in ductility [43–45]. At low solute concentrations, the deleterious effects of these elements are caused by dislocation interactions with interstitials dissolved in the lattice [46, 47]. These interactions can generally be divided into short-range and long-range interactions. In the short-range, interstitial atoms alter the dislocation core structure and consequently the glide stress. In the long-range, interstitials and dislocations interact through their elastic stress fields.

The interaction between interstitial and dislocation stress fields causes interstitials to diffuse towards preferential sites in the lattice which lower their strain energy. A Cottrell atmosphere forms around dislocations as interstitial atoms preferentially segregate to tensile areas over compressive areas, locking the dislocation in place [48]. The interaction energy between an interstitial atom and an external stress field can be described analytically through linear elasticity. If the interstitial is in an elastic strain field ϵ^e_{ij}, the interaction energy is given by

$$\psi_{int} = -P_{ij}\epsilon^e_{ij} \tag{1.1}$$

where P_{ij} is the elastic dipole, a second rank tensor that fully characterizes the strain distribution around a point defect [49–51]. Another representation of the interstitial strain is the λ_{ij} tensor [51, 52]. These two tensors are related through the materials stiffness tensor c_{ijkl} [50] by

$$P_{ij} = V c_{ijkl}\lambda_{kl} \tag{1.2}$$

where V is the atomic volume for the host lattice. Through these equations, the Cottrell atmosphere around a dislocation can be predicted using the analytical solutions for dislocation stress fields.

In a BCC lattice, larger atoms, including O, will generally prefer the octahedral interstitial sites, while small atoms, including H, will prefer the tetrahedral sites. Unlike the interstitial sites in a close-packed lattice, the octahedral sites in a BCC lattice have a tetragonal symmetry, so there are three distinct orientations of the octahedral sites, each with the largest distortion aligned with a different <100>-type direction. This leads to a long-range effect that is specific to BCC lattices, known as the Snoek effect [53]. In a stress-free state, these orientations are energetically equal, but in a stress field, such as that created by a dislocation, interstitials will adopt the lowest energy orientation. Like the Cottrell atmosphere, this may pin the dislocation in place [54, 55].

When interstitials are very close to the dislocation core, the linear elastic approximation of dislocation-interstitial interactions breaks down. This is evident from examining the interaction energies, which measure the energy change of a solute due to a dislocation. Atomistic calculations of the interaction energy between a C interstitial and dislocations in Fe show that the calculated value diverges from the predicted value about 2 Å from the dislocation core [56]. At this distance, the interstitial begins to affect the dislocation core structure itself [57–59]. Notably, the BCC screw core structure changes from the so-called easy core to the hard core [57–61]. The reconstructed core has a modified Peierls barrier shape and magnitude, and can pin the dislocation and increase overall strength [57, 58, 62].

Kink-pair nucleation and migration, which is the dominant mechanism for screw dislocation glide in BCC materials [8], is also affected by interstitial atoms. Dislocations may be attracted to interstitials, making kink-pair nucleation towards an interstitial atom easier [45, 63, 64]. On the other hand, interstitials may pin kinks and thus inhibit kink

migration [63, 65]. Additionally, the formation of kinks on different glide planes can create immobile cross-kinks, pinning the dislocation [45, 64].

The combination of short- and long-range interactions leads to unique dislocation mechanisms that are not fully understood. For example, in some cases, H enhances dislocation glide [66–68]. Because H atoms are small and can diffuse through the lattice quickly, they move along with the gliding dislocation and reduce its effective stress field in a process known as hydrogen shielding. The lowered elastic stress fields reduce interactions with obstacles and other dislocations, thus increasing mobility [67]. However, there is still controversy over whether hydrogen shielding is the cause of hydrogen-enhanced plasticity, with some computational models not finding the effect [68–70]. Unlike H, larger interstitial atoms, like C and O, generally cannot diffuse fast enough to keep up with gliding dislocations. This can cause a serrated flow behavior in which dislocations repeatedly break free from and then are pinned by a trailing interstitial atmosphere, which is known as the Portevin-Le Chatelier effect [55, 71].

Due to the atomistic nature of interstitial-dislocation interactions, most modeling of interstitial effects is done with DFT or molecular statics/dynamics. DFT simulations are critical for determining the properties of isolated interstitial atoms [51] or, in some cases, dislocation core structures [57, 58, 60, 61], but the length scales are generally too short to simulate the interactions between interstitials and dislocations. MD simulations can access longer length scales, but the time scales are generally too short to capture significant interstitial diffusion [71]. Additionally, MD models require accurate interatomic potentials, which may not be available for all systems of interest.

Because simulating both interstitial diffusion and dislocation glide can be challenging with atomistic methods, there is great interest in developing mesoscale models to investigate the complex dynamics between dislocations and interstitials. Discrete dislocation dynamics (DDD) models have been developed to include interstitial atoms, primarily

self-interstitials in the context of radiation damage [72]. These models require the input of phenomenological rules that govern dislocation motion and hardening in the presence of obstacles. There is a need for atomistically-informed simulation tools that can address longer time and length scales in order to investigate the more complex and less understood dislocation mechanisms.

1.4 Phase-field dislocation dynamics

1.4.1 Background

In an effort to study time and length scale regimes beyond those accessible by atomistic simulations, many different mesoscale models for plasticity have been developed. At one extreme, continuum or crystal plasticity models simulate plasticity without tracking individual dislocations. Between continuum models and atomistic models lie mesoscale dislocation models, which resolve individual dislocations without resolving individual atoms. These models include discrete dislocation dynamics (DDD) and phase-field dislocation models. DDD is a force-based model in which dislocations evolve through a set of predefined rules and mobility laws [73]. Phase-field models, on the other hand, are energy-based and do not require the input of phenomenological rules.

Phase-field methods, as their name implies, were first developed to simulate the evolution of microstructural phases within a material. Phase-field models represent the current state of the system through order parameters, which indicate something about the phase at each point in space. The order parameters can represented conserved variables such as concentration [74] or non-conserved variables such as local ordering [75]. The total energy of the system is calculated from the order parameters and minimized to simulate evolution over time.

In a phase-field dislocation model, the order parameter represents the amount of local slip, and the dislocations are represented by boundaries between slipped and unslipped regions. Several models fit this definition, including the generalized Peierls-Nabarro (GPN) model, phase-field microelasticity, and phase-field dislocation dynamics (PFDD) [76–78]. In many cases, these formulations are numerically and physically equivalent [79, 80]. In this work, the term PFDD is used as the formulation originates from the work of Koslowski et al. [78].

1.4.2 Formulation

PFDD represents the dislocation structure through non-conserved order parameters $\phi^\alpha(\mathbf{r})$, which represent the amount of dislocation slip at a point $\mathbf{r} = (x, y, z)$ in space on slip system α with slip direction $\boldsymbol{s}^\alpha$ and slip plane normal $\boldsymbol{n}^\alpha$. When $\phi^\alpha(\mathbf{r}) = 0$ or 1, the point $\mathbf{r}$ is unslipped or slipped by a dislocation, respectively. The interface between regions with different integer values represents the dislocation core. The vector $\boldsymbol{\phi}$ represents all slip systems with components ϕ^α for $\alpha = 1$ to n_s where n_s is the number of slip systems.

The total energy density ψ is a function of slip on all available slip systems, and consists of the elastic energy, lattice (crystalline) energy, and external energy:

$$\psi(\boldsymbol{\phi}) = \psi_{\text{elas}}(\boldsymbol{\phi}) + \psi_{\text{latt}}(\boldsymbol{\phi}) - \psi_{\text{ext}}(\boldsymbol{\phi}) \tag{1.3}$$

The elastic energy is given by

$$\psi_{\text{elas}}(\boldsymbol{\phi}) = \frac{1}{2} c_{ijkl} \left(\epsilon_{ij}(\boldsymbol{\phi}) - \epsilon^p_{ij}(\boldsymbol{\phi})\right) \left(\epsilon_{kl}(\boldsymbol{\phi}) - \epsilon^p_{kl}(\boldsymbol{\phi})\right) \tag{1.4}$$

where c_{ijkl} is the elastic stiffness tensor, $\epsilon_{ij}(\boldsymbol{\phi})$ is the total strain, $\epsilon^p_{ij}(\boldsymbol{\phi})$ is the plastic

eigenstrain due to the dislocations. The plastic eigenstrain can be written as a function of the order parameters as

$$\epsilon_{ij}^{p}(\boldsymbol{\phi}) = \frac{1}{2}\sum_{\alpha=1}^{n_s} \frac{b^\alpha}{d^\alpha}\left(s_i^\alpha n_j^\alpha + s_j^\alpha n_i^\alpha\right)\phi^\alpha \tag{1.5}$$

where b^α is the Burgers vector magnitude and d^α is the slip plane interplanar spacing.

The total strain is related to the plastic strain in Fourier space as

$$\hat{\epsilon}_{kl} = [c_{iukv}q_u q_v]^{-1} q_j q_l c_{ijmn}\hat{\epsilon}_{mn}^{p} \tag{1.6}$$

where $\hat{}$ denotes the Fourier transform and $\boldsymbol{q}$ is the wavenumber vector. The quantity $[c_{iukv}q_u q_v]^{-1}$ is also known as the Green function G_{ki} [78, 81].

The lattice energy represents the energy barrier for dislocation glide and is therefore dependent on the crystallographic system. In one dimension, the lattice energy is usually given by the generalized stacking fault energy (GSFE) curve, while in two dimensions, it is given by the γ-surface [82]. In both cases, these functions represent the energy penalty associated with the breaking of atomic bonds within the slip plane.

The final term, the external energy, represents the work done by an externally applied stress state σ_{ij}^{app}:

$$\psi_{\text{ext}}(\boldsymbol{\phi}) = \sigma_{ij}^{\text{app}}\epsilon_{ij}^{p}(\boldsymbol{\phi}) \tag{1.7}$$

As slip is a non-conserved order parameter, the dislocation configuration evolves by minimizing the total energy via the time-dependent Ginzburg-Landau equation:

$$\frac{\partial \phi^\alpha}{\partial t} = -m_{disl}\frac{\partial \psi}{\partial \phi^\alpha} \tag{1.8}$$

where m_{disl} is a dislocation mobility coefficient.

1.4.3 Applications to BCC materials

To simulate dislocations within a BCC lattice with PFDD, a BCC-specific lattice energy must be used. Since dislocations in BCC do not form partials, only a one-dimensional GSFE curve must be calculated, which has been done with DFT for the {110}, {112}, and {123} slip planes for six refractory BCC elements (Figure 1.1) [83]. On the {110} plane, these curves are sinusoidal, and the peak value is known as the unstable stacking fault energy (USFE). Therefore, the lattice energy used in PFDD for BCC materials has the form

$$\psi_{\text{latt}}(\boldsymbol{\phi}) = \sum_{\alpha=1}^{n_s} \frac{\gamma_{usf}^{\alpha}}{d^{\alpha}} \sin^2(\pi\phi^{\alpha}) \tag{1.9}$$

where γ_{usf}^{α} is the USFE for the α slip system.

Dislocations in BCC lattices also exhibit a high degree of screw-edge anisotropy, with edge dislocations gliding much more easily than screw dislocations. To address this in PFDD, Peng et al. implemented a modification to the lattice energy to account for dislocation character [84]. The modified lattice energy has the form

$$\psi_{\text{latt}}(\boldsymbol{\phi}) = \sum_{\alpha=1}^{n_s} \beta(\theta) \frac{\gamma_{usf}^{\alpha}}{d^{\alpha}} \sin^2(\pi\phi^{\alpha}) \tag{1.10}$$

where $\beta(\theta)$ is known as the transition function and θ is the dislocation character angle ($\theta = 0$ corresponding to screw and $\theta = \pi/2$ corresponding to edge). The transition function can be fit to atomistic information about the relative mobilities of screw and edge dislocations. By fitting the transition function to molecular statics calculations of the Peierls stress of Ta [85], the correct morphology of expanding dislocations can be replicated in PFDD [84].

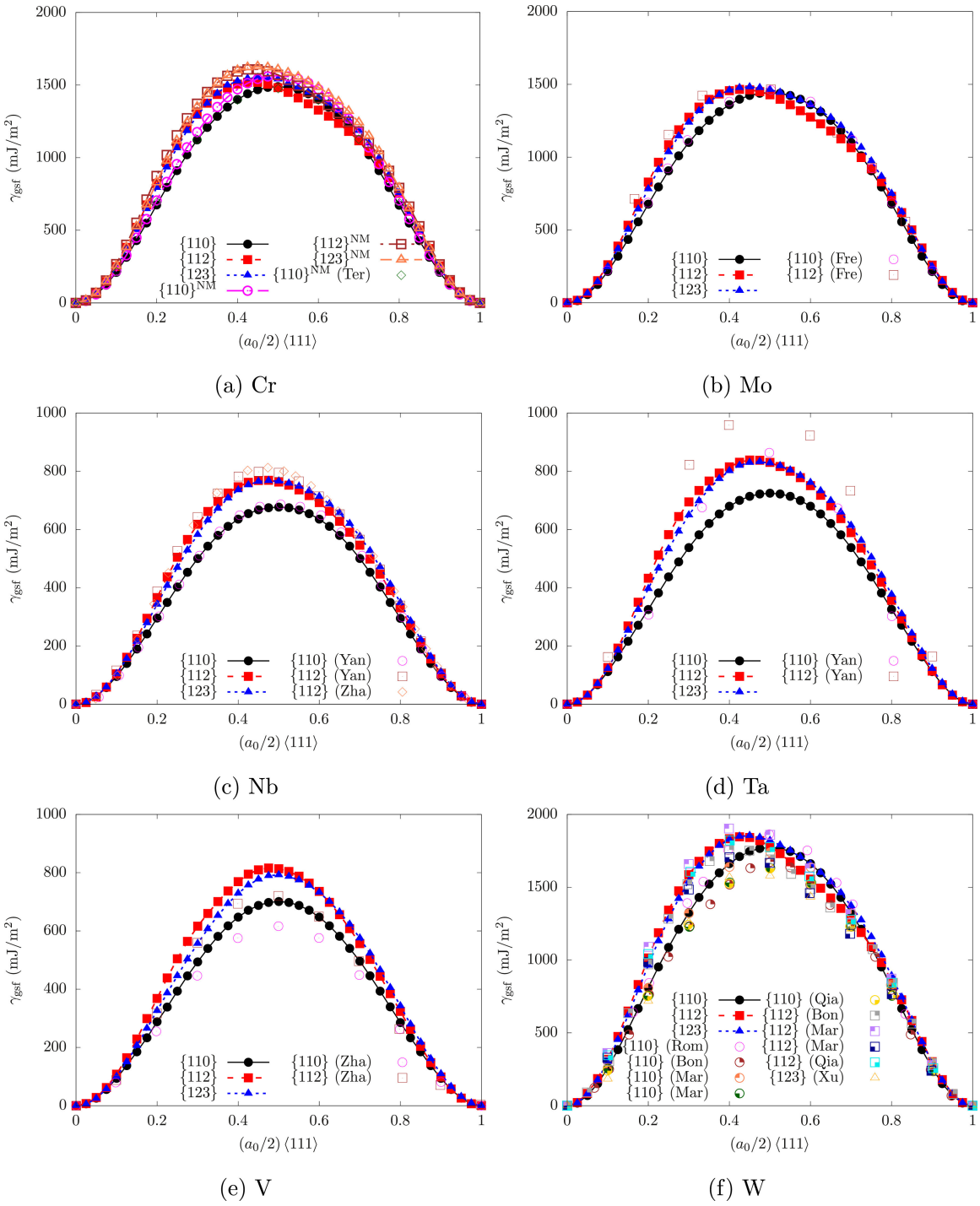

(a) Cr (b) Mo

(c) Nb (d) Ta

(e) V (f) W

Figure 1.1: The generalized stacking fault energy curves for six different pure refractory metals. The black, red, and blue lines show the curves as calculated with DFT in [83]. Other reference curves, also calculated with DFT, are taken from [86–96]. Figure adapted from [83].

1.5 This work

In this work, phase-field dislocation dynamics (PFDD) is used to investigate dislocations in refractory alloys, including MPEAs and pure refractory metals with interstitial atoms. Advancements are made to the PFDD formulation to account for the unique properties of these materials. This model is then used to simulate a variety of dislocation mechanisms and behaviors, including dislocation sources, glide of straight dislocations and loops, and cross slip.

In Chapter 2, extensions are made to PFDD to model refractory MPEAs for the first time. The operation of dislocations sources is simulated, revealing variability in the critical stress to operate the sources and size effects that are indicative of the underlying variable structure. The glide of long, straight dislocations is analyzed in Chapter 3, and the mechanisms for glide and distribution of glide stresses are discussed. Further modifications are made to PFDD in Chapter 4 to simulate cross slip in pure Nb, which also naturally incorporates the character-dependence of dislocations in BCC materials. The effect of SRO in refractory MPEAs is studied with PFDD in Chapter 5. A direct link is made between the atomistic arrangement of atoms in an MPEA and the mesoscale PFDD simulations through a novel method for creating random lattice with SRO. The mechanisms behind SRO-strengthening are investigated with PFDD and discussed.

In Chapter 6, PFDD is extended to include interstitials and their interactions with dislocations. Short- and long-range interactions are accounted for, as well as interstitial diffusion and the orientation-dependence of interstitial sites in BCC lattices. The PFDD results from this new formulation are validated through comparisons to analytical and atomistic models for the Nb-O model system. The extended model is used in Chapter 7 to investigate more complex dislocation mechanisms, and the effects of interstitials are compared for the W-H and Nb-O systems. Finally, future applications of these methods

and open questions are discussed in Chapter 8.

Chapter 2

Dislocation Source Operation [†]

2.1 Introduction

In this chapter, PFDD is employed to study the mechanisms and critical stresses associated with the activation of Frank-Read (FR) dislocation sources of both screw and edge character in a refractory MPEA. FR sources are a primary mechanism of dislocation generation, and the stresses to activate them are known to greatly affect yield strength and plastic flow in metals [98–101]. Because the behavior of dislocations in MPEAs will be statistical in nature due to the composition fluctuations, many iterations of each simulation are required to understand the average behavior. Therefore, a mesoscale modeling technique such as PFDD is necessary to reach the required lengths, times, and number of simulations. Atomistic methods, such as MD or DFT, are limited by computational power, and therefore cannot be used to study Frank-Read sources in a statistical manner. The model is applied to an equal-molar MoNbTi MPEA, which forms a single-phase BCC structure [102]. This MPEA exhibits an attractive combination

[†]This chapter adapted from Reference [97]: Smith, L. T. W., Su, Y., Xu, S., Hunter, A., & Beyerlein, I. J. (2020). The effect of local chemical ordering on Frank-Read source activation in a refractory multi-principal element alloy. International Journal of Plasticity, 134, 102850.

of plastic properties, with a 1100 MPa room temperature compressive yield stress and excellent thermally stability in yield stresses up to 1200°C. With atomic-scale data from MS and DFT calculations, a PFDD model is built for MoNbTi that considers both chemical composition fluctuations of varying ranges from less than 1 nm to over 10 nm and dislocation character-dependent glide resistance. The critical stress to nucleate dislocations from FR sources is statistical in nature and the variability in critical stress strongly depends on the range of the composition fluctuations. Analysis of the critical configurations for activation identifies a two-step process for FR source activation that involves athermal kink-pair formation at a location in the source length where the energy barrier is low. This leads to, on average, to lower critical stresses in the MPEA than in the reference material without composition fluctuations. Another important consequence is a much more severe size effect of FR source length on the critical stress than that derived from line tension alone. The length scale of underlying composition variations also affects the operation of a FR source and show that a distinct mechanism controls the behavior of FR sources in MPEAs as opposed to that in pure materials.

This chapter is structured as follows. The extensions to the PFDD formulation as it applies BCC MPEAs are described along with the necessary atomistic methods used to inform the PFDD simulations. Then, PFDD is used to simulate FR sources in two model materials. The first one is a reference, homogeneous approximation of MoNbTi, without composition fluctuations, but bearing the same bulk elastic moduli and lattice constants as the nominal random solid solution of this MPEA. The second one is the actual, heterogeneous MPEA MoNbTi, which includes variations in lattice energy due to changes in the local chemical composition. The distribution of critical stresses required to nucleate a dislocation loop from the FR sources is calculated, with and without line orientation-dependent resistance. The mechanisms for dislocation nucleation are analyzed and compared in the MPEA and the conventional reference material, with implications of these

mechanisms on the statistical dispersion and size effects on these stresses. Although this chapter focuses on one MPEA, the formulation, model, and trends described here can be generalized to consider other MPEA compositions and crystal structures.

2.2 Methods

2.2.1 PFDD formulation

The lattice energy density, ψ_{latt}, corresponds to the Peierls barrier that a dislocation must overcome in order to glide. The functional form of this term thereby varies based on the crystal structure of the material under consideration. Formulations have been previously proposed for FCC (including high entropy alloys) [40, 103, 104], BCC [83, 84], and hexagonal closed packed (HCP) [105] metals. To apply generally to these three crystal structures required ψ_{latt} to account for differences in crystallography and permit dissociation of perfect dislocations into extended dislocations, if energetically favorable. In the case of BCC metals and alloys, the dislocation cores remain compact [106–109], and can, therefore, be represented at the mesoscale as a perfect dislocation. The influence of the atomic structure of dislocation core on ψ_{latt} needs to be considered indirectly in PFDD and with information from atomic-scale calculations. Accordingly, Eq. (1.10) is modified such that ψ_{latt} is represented by

$$\psi_{lattice}(\phi) = A(x,y)\beta(\theta)\sin^2(\pi\phi) \tag{2.1}$$

where $A(x,y)$ corresponds to the energy barrier field in the (x,y)-plane and $\beta(\theta)$ is the transition function. In prior PFDD applications to pure metals [83], A was constant. MPEAs, however, exhibit atomic-scale fluctuations in chemical composition and configuration, rendering a spatially varying $A(x,y)$ within the slip plane. In a real MPEA, the

energy barrier will vary in all 3 dimensions. However, here only individual dislocations confined to a single slip plane are considered, so variation in the z-direction is neglected. As a dislocation glides within its slip plane, it will encounter different local environments which correspond to varying lattice energies. Here, the Peierls barrier coefficients and the orientation-dependent transition function are determined with atomistic calculations.

2.2.2 Informing PFDD with atomistic simulations

Atomistic simulations are used to inform the orientation-dependent resistance, $\beta(\theta)$, which incorporates the difference in mobility between edge, screw, and mixed-type dislocations in BCC metals [84]. In pure metals, dislocations lines are typically not straight and the character of a dislocation varies along the line due to line curvature. In MPEAs that show wavy dislocation line configurations, the dislocation line character will vary even more drastically along the dislocation line. This may become even more pronounced as the system evolves and the dislocation line moves, curves, and bows. Thus, an on-the-fly dislocation character identification scheme is used [84]. This procedure utilizes the gradient of the order parameter, $\vec{\nabla}\phi$, in 3D space to determine where the dislocation line is each time step, and its direction of maximum change. Using the slip plane normal, the vector tangent to the dislocation line, $\mathbf{t}$, at all points can be determined as:

$$\mathbf{t}(\mathbf{r},t) = \frac{\vec{\nabla}\phi(\mathbf{r},t) \times \mathbf{n}}{|\vec{\nabla}\phi(\mathbf{r},t) \times \mathbf{n}|} \tag{2.2}$$

where the tangent vector and gradient of the order parameter may change position over time, t, during evolution of the system. Once the tangent vector at all points along a dislocation curve, line or loop has been determined, the character angle, θ, can easily be identified by:

$$\theta = \arccos\left(\mathbf{t}(\mathbf{r}, t) \cdot \mathbf{s}\right) \tag{2.3}$$

where the tangent vector and slip direction are already normalized vectors.

Once the character angle of all dislocation lines within the system is known, some transition between the Peierls barrier for screw dislocations and the Peierls barrier for edge dislocation must be defined. Because screw dislocation motion dominates plastic flow in BCC metals, Peierls barriers of screw dislocations in pure BCC metals have been calculated previously with DFT [110–113]. However, such DFT calculations can be time consuming, and it is common for Peierls stress calculations to be performed using MS [85, 114], which require interatomic potentials. Furthermore, Peierls barrier calculations are less common for edge dislocations, which are well known to move more easily through the BCC crystal lattice. Even less common are Peierls stress calculations for dislocations of mixed character. As a rare case, [85] calculated the {111} plane Peierls stress in Ta for the full range of possible character angles. Such calculations proved ideal for informing the mathematical form of the orientation-dependent barrier function for PFDD simulations of anisotropic loop expansion and kink-pair motion in [84]. Yet, still to this day, such simulations can be time consuming to complete for many character angles and in different materials, especially MPEAs. Furthermore, they employ an interatomic potential, for which there can be many to choose from for one metal, and which can produce different results even for the same metal [115].

Recently, the local slip resistances (LSRs) for dislocations in MoNbTi were calculated using MS [13]. Because of the random nature of MPEAs, there is a distribution of LSRs for both screw and edge dislocations, with edge dislocations having lower slip resistances on average. This difference is incorporated into the PFDD model through the orientation-dependent barrier function $\beta(\theta)$ in Eq. (2.1). This function is defined as

$$\beta(\theta) = \left(1 - \frac{1}{R}\right)\cos^2\theta + \frac{1}{R}, \tag{2.4}$$

where R is the ratio between the average LSR for screw and the average LSR for edge dislocations in MoNbTi. The $\beta(\theta)$ function provides a smooth scaling for all dislocation character types, while preserving the ratio of Peierls barriers between edge and screw dislocations as determined by MS.

Based on MS calculations of several atomic instantiations of MoNbTi, it was found that, on average, the LSR for edge dislocations is about 22% of that of a screw dislocation [13]. Accordingly, $\beta(\theta)$ will be 1 for screw segments and 0.22 for edge segments with the magnitude of the lattice energy defined by $A(x, y)$, as shown previously in Eq. (2.1). In order to characterize the role of differences in screw-edge resistance, in some calculations, the orientation-dependent resistance is removed, in which case $\beta(\theta) = 1$ for all line orientations.

In addition to the transition function $\beta(\theta)$, the barrier height $A(x, y)$ must be specified in Eq. (2.1). Like prior PFDD simulations of BCC metals, this barrier is scaled by the USFE. Advantageously, GSFE curves can be calculated readily with DFT, removing any dependence on interatomic potentials. This attribute is particularly important for MPEAs, in which the local composition and configurations vary widely on an atomic scale.

Unlike in pure metals [116], in MPEAs, GSFEs in MPEAs are area-size dependent [117, 118], influenced by the particular composition and configuration of atoms in the plane being sheared. The MoNbTi GSFE curves were previously calculated with DFT [117] for {110}-type glide planes that sample a small area of the plane, representing a certain composition and configuration. These types were derived from random samplings of parallel {110}-type glide planes of small cross-sectional area taken from a nominally

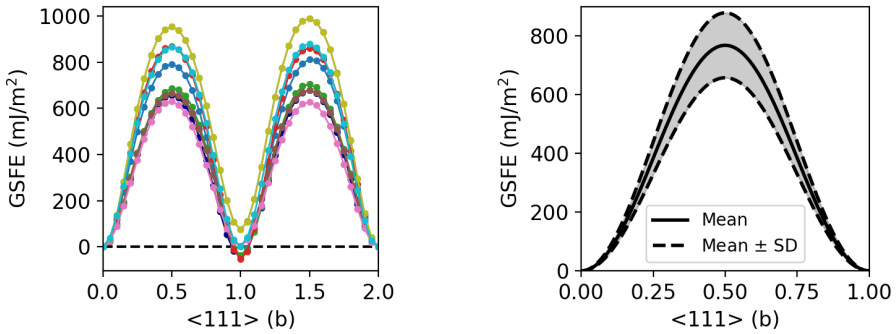

(a) DFT-calculated GSFE curves (b) GSFE curve used in PFDD

Figure 2.1: The left figure shows the 24 DFT-calculated GSFE curves in MoNbTi on the {110} glide plane family. There are 12 {110}-type glide planes each with two distinct GSFE curves. The mean USFE is 768 mJ/m^2. The right shows the idealized GSFE curve used in the PFDD simulations (Eq. (2.1)). The peak value of the GSFE curve varies depending on local composition, so a range of peak values is shown. Because the structure used to calculate the GSFE curves requires two 1b translations in the [111] direction to return to its original configuration, there are slight differences between the starting and ending energies for each GSFE curve. The barrier height is considered to be the average between the forward and reverse barrier.

equi-molar MoNbTi special quasirandom structures (SQS). The corresponding USFE values from this set of GSFE curves are broadly distributed. The mean USFE is 768 mJ/m^2 and the standard deviation is 111 mJ/m^2. For comparison, the USFE calculated from DFT for pure Nb is 677 mJ/m^2, and for pure Mo it is 1443 mJ/m^2 [83], showing that for some compositions within MoNbTi, the local USFE can be lower than that for Nb but none were higher than that for Mo. The range of USFE values for this MPEA is used to parameterize Eq. (2.1) to create an idealized, symmetric GSFE curve (Fig. 2.1b). To obtain a lattice energy density, ψ_{latt}, the USFE is divided by the interplanar spacing d_{110} to obtain the lattice energy coefficient $A(x, y)$.

The USFE distribution is incorporated into PFDD by randomly generating spatially correlated functions $A(x, y)$ for Eq. (2.1). The generation method is based on the approach developed by Hu et al. for creating correlated rough surfaces [119]. This formu-

lation can create many independent, random surfaces quickly by using the Fast Fourier Transform, and the only inputs required are the correlation length and mean and standard deviation of the USFE distribution.

To determine a spatial varying but correlated matrix, an autocorrelation function is defined as

$$ac(x,y) = \exp\left(-\frac{2.3(x^2+y^2)^{0.5}}{l}\right) \tag{2.5}$$

where l is the correlation length at which the autocorrelation drops to 10%. Neighboring points spaced within l are more likely to have the same USFE and when spaced beyond l they are more likely to be different.

The autocorrelation matrix is then used to define a filter matrix F as

$$F(x,y) = \mathcal{F}^{-1}\{\sqrt{\mathcal{F}\{ac(x,y)\}}\} \tag{2.6}$$

where $\mathcal{F}$ and $\mathcal{F}^{-1}$ denote the Fourier transform and its inverse, respectively. To generate a correlated matrix, an initial uncorrelated matrix, A_{uncorr}, of the desired dimension is created by drawing each value from a normal distribution with mean 0 and variance 1. This uncorrelated matrix and the filter matrix are convoluted to determine the correlated matrix:

$$A_{corr}(x,y) = F(x,y) * A_{uncorr} \tag{2.7}$$

Finally, the correlated matrix is scaled and shifted to give the correct mean and standard deviation for $A(x,y)$.

$$A(x,y) = \frac{s_{usf}}{d_{110}} A_{corr}(x,y) + \frac{\mu_{usf}}{d_{110}} \tag{2.8}$$

where μ_{usf} and s_{usf} are the mean and standard deviation of the USFE for the MPEA, calculated with DFT. While not directly apparent in Eq. (2.8), note that an important parameter associated with the calculation of $A(x, y)$ is the correlation length, l. Additional, independent surfaces are created by changing the initial matrix A_{uncorr}. As long as the initial matrices are chosen randomly and are independent of one another, the final correlated matrices will also be independent.

Eight different correlation lengths are studied: $1w_0$, $2w_0$, $3w_0$, $4w_0$, $5w_0$, $10w_0$, $15w_0$, $20w_0$, where w_0 is the core width of a screw dislocation in homogeneous MoNbTi. The width was determined by modeling a screw dislocation under zero stress. The dislocation core is considered to be where ϕ is between 0.1 and 0.9, giving a core width of approximately $2.15b$. This measured core width is highly dependent on the cutoff used to define the core. For example, using a cutoff of ϕ between 0.2 and 0.8 gives a width of $0.78b$, while a cutoff of ϕ between 0.05 and 0.095 gives a width of $5.36b$. $2.15b$ is chosen as the core width as this distance contains 80% of the Burgers vector associated with the dislocation, but caution should be exercised when interpreting this value as an absolute measurement of dislocation core width. As the extent of SRO is expected to be on the order of nanometers, the range of correlation lengths is chosen to span from about 0.5 nm to more than 10 nm. The exact value of the correlation length in a MoNbTi sample will depend on external factors such as temperature and processing conditions. Fig. 2.2 shows example $\{1\bar{1}0\}$ surfaces for six correlation lengths. For the sake of presentation, the regions are colored by their local value of $A(x, y)$. While the correlation length in each glide surface is fixed, the range of composition ordering are still distributed across the plane and transitions between regions of like composition are smooth.

In this model, the random variations within an MPEA are represented through fluctuations in USFE only, while elastic moduli and screw-edge mobility ratios are assumed independent of local composition. Position-dependent lattice energy has been used pre-

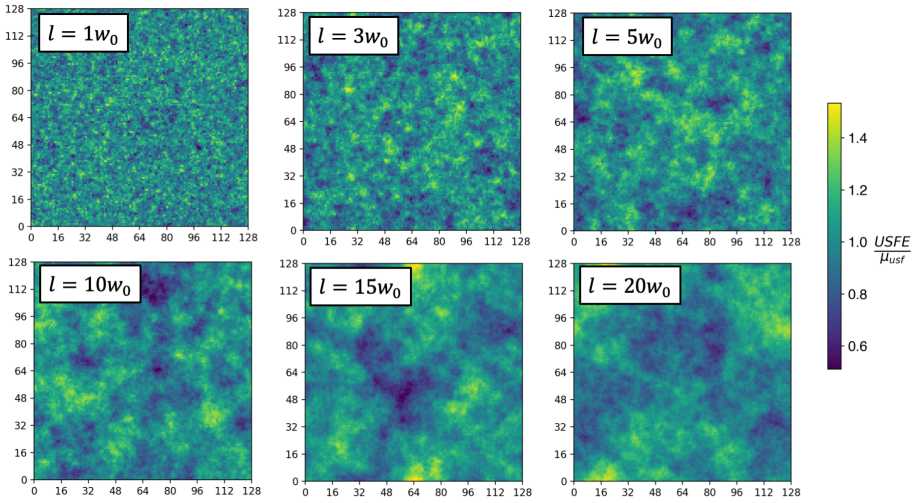

Figure 2.2: Example correlated surfaces with various correlation lengths, l.

viously in an FCC material using PFDD [40], as well as in a Peierls-Nabarro model [41]. Rao et al. showed that for nine different BCC MPEAs, the solute-dislocation interaction energy, which represents the change in dislocation energy caused by a solute atom, was strongly influenced by the change in USFE due to the solute [120]. While solute atoms also affect dislocation energies via other means, notably the solute size and modulus misfit, the change in USFE outweighs those contributions for screw dislocations in BCC MPEAs. Therefore, varying the lattice energy in PFDD in accordance with the underlying USFE will capture the heterogeneous nature of dislocation behavior in MoNbTi. Edge dislocations may interact differently from screw dislocations with the various ensembles of atom types, and here, these differences are accounted for through the transition function. The formulation permits, however, alternative character-dependencies, such as one that accounts explicitly for edge versus screw dislocation interactions with specific atomic neighborhoods.

Other properties such as elastic moduli or screw-edge mobility ratio may also vary within the MPEA, but these variations are expected to be second-order compared to

the variations in lattice energy. Recent calculations of an FCC MPEA revealed that the shear modulus varies within 4% of the mean for differing atomic configurations [104]. Therefore, significant variations in the elastic constants are not expected, and the elastic stiffness tensor is assumed constant throughout the simulation cell. Calculations of the screw-edge ratio in MoNbTi show variation from 2 - 80, with a mean screw-edge ratio of 4.65 [13]. However, in Section 2.4.2 it is shown that the effect of the screw-edge ratio is small compared to the effect of variations in lattice energy, so the screw-edge ratio is held constant throughout the alloy.

2.2.3 Simulation setup

In order to compare the behavior of an FR source in an MPEA with that in a pure metal, a reference case termed *homogeneous MoNbTi* is defined that uses the elastic constants and mean USFE (768 mJ/m^2) for MoNbTi, but with no spatial variations in the lattice energy (i.e., $A(x, y) = \mu_{usf}/d_{110}$), similar to a pure metal. The homogeneous MoNbTi also uses the same elastic moduli as the MPEA, and the same screw-edge ratio for the orientation-dependent energy barrier as defined in Eq. (2.4).

The MPEA is also compared with two of its pure metal constituents, Mo and Nb. The elastic constants and USFE are calculated in [83], and the screw-edge ratios are taken from the critical resolved shear stresses calculated with molecular dynamics for screw and edge dislocations [38]. This screw-edge mobility ratios are 30.66 and 18.11 for Nb and Mo, respectively.

Fig. 2.3 presents a schematic of the FR source simulation set-up used in this work. The simulation cell is rotated such that the $[1\bar{1}0]$ slip plane normal is parallel with the z-axis. A 128x128x128 computational grid is used with an interplanar spacing of $0.8165b$ (i.e., in the z-direction) and an in-plane grid spacing of $b = 2.79$Å. Calculation of the

elastic strain energy, Eq. (1.4), utilizes a Fast Fourier Transform, and accordingly, the model employs periodic boundary conditions. Elastic anisotropy is fully accounted for within the model [121]. Elastic constants for MoNbTi were calculated using DFT and a model SQS of a 3D random solid solution of MoNbTi. The same SQS used to calculate these constants is used to calculate the lattice energies [117]. The calculations provide cubic anisotropic constants C_{11}, C_{12}, and C_{44} equal to 252.13 GPa, 134.11 GPa, and 34.41 GPa, respectively, using the energy-strain method [122]. For convenience, critical stresses are reported in units of the equivalent isotropic shear modulus, which, for this cubic elastic material, is 41.29 GPa.

An FR source is built in a similar fashion to phase field model set-ups used previously [83]. An FR source is created in the system by creating a prismatic loop that spans between two slip planes as shown in Fig. 2.3. Two slip systems are considered. The first slip system is a $(1\bar{1}0)$ slip plane with a normal in the z-direction, while the second is a slip plane perpendicular to the first with a normal in the x-direction. Both use a [111] type Burgers vectors, with the direction of the Burgers vector depending on the orientation of the FR source. To create the prismatic loop, the order parameter corresponding to the second slip system is initialized with a value of 1 on three planes: two $(1\bar{1}0)$ glide planes located at the top and bottom of the prismatic loop (indicated in blue in Fig. 2.3), and the plane on which the prismatic loop itself is defined (indicated in green in Fig. 2.3), which is normal to the $(1\bar{1}0)$ plane. This configuration results in two pinned dislocation points with non-zero order parameter values on the two glide planes. The order parameters are set to zero outside of the prismatic loop. This prismatic loop is not permitted to evolve, according to Eq. (1.8), and hence, it remains stationary through-out the simulations. In addition, the dislocation segment at the bottom of the prismatic loop (i.e., at $z = 0$) is also restricted from evolving. Only the order parameters in the slip plane at $z = 64$ can evolve, so that the FR source can operate in this plane.

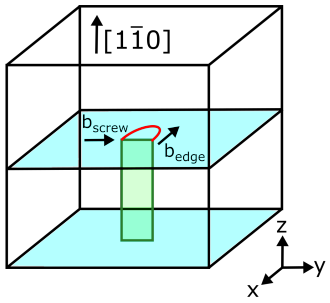

Figure 2.3: The simulation setup for a Frank-Read source. A prismatic loop is shown on green. Under an applied load, dislocation loops, shown in red, bow out from the edges of the loop on the two blue slip planes. The Frank-Read source is screw or edge-oriented depending on the orientation of the Burgers vector.

An FR source of length $20b$ is used in all simulations, unless stated otherwise. FR sources are studied for both edge- and screw-oriented sources with the Burgers vector oriented parallel to the FR-source for a screw-oriented source and normal for an edge-oriented, as shown in Fig. 2.3. To activate the source, a shear stress is applied in the direction of the Burgers vector of the initial FR source segment. The shear stress is increased in increments of 0.001μ. The quantity $m_{disl}\Delta t$, where Δt is the timestep, was set to 0.35 μ^{-1}. Note that all energy densities are normalized by the shear modulus μ and the timestep and mobility constant m_{disl} are unitless. Following each stress increment, the system is held at the current stress state for either 3000 timesteps or until the system converges, whichever comes first. System convergence is achieved when the norm of the order parameter changes by less than 10^{-5} between successive timesteps. The critical stress is surpassed when the FR source creates a full dislocation loop. The critical stress is then defined as the mean of the previous subcritical shear stress and the current supercritical shear stress.

To ensure that a 128x128x128 simulation grid is adequate for a $20b$ FR source and not strongly influenced by image effects, the critical stress for a $20b$ screw-oriented source

in the homogeneous MoNbTi reference material is calculated using simulation grids with side lengths 64, 128, and 256. The same grid resolution is used for all computational grids, which is b within the slip plane and $0.8165b$ in the direction normal to the slip plane (same resolution as mentioned above). The critical stress for all three sizes is 0.0885μ, indicating that the 128x128x128 grid size is adequate. As further confirmation, note that a similar conclusion was reached in recent PFDD work on FR source operation for six BCC refractory metals, varying widely in their lattice constants and elastic moduli [83].

2.3 Results

Loop expansion and the corresponding critical stresses for the FR sources are calculated for both the homogeneous MPEA, with uniform properties, and the heterogeneous MPEA, in which spatial variation in the lattice energy is considered. The critical stresses are calculated both without and with the orientation-dependent barrier function for screw-oriented sources and only with the orientation-dependence for the edge sources. To garner adequate statistics for analysis, for each l, 60 different correlated surfaces are created and FR source behavior on these surfaces is studied.

2.3.1 Homogeneous MoNbTi

To establish a basis for comparison, the homogeneous MoNbTi is studied first. Fig. 2.4 shows snapshots taken over time of a dislocation loop expanding from a screw-oriented FR source without and with the orientation-dependent barrier function (Figure 2.4(a) and (b), respectively), and an edge-oriented FR source with the orientation-dependent barrier function (Fig. 2.4(c)) in homogeneous MoNbTi. Loop expansion is shown at the respective critical stresses for each case. These critical stress values are reported for each

	Critical Stress (μ)	
	β=1	β=f(θ)
Screw	0.0885	0.0665
Edge	0.0705	0.0355

Table 2.1: The critical stress for Frank-Read source activation in homogeneous MoNbTi. The critical stress is lower for edge-oriented sources than screw-oriented sources. When $\beta = f(\theta)$, the orientation-dependent barrier function, is used character dependence of the lattice energy is accounted for.

case in Table 2.1. The loop expansion over time is visualized by drawing a contour line where $\phi = 0.5$, which corresponds to the center of the dislocation core. A darker red contour line corresponds to an earlier simulation time.

In all cases, an arc bows out from the FR source, eventually expanding and breaking away as a dislocation loop, which then propagates out of the simulation cell to annihilate with its periodic images. In a screw-oriented FR source without the orientation-dependent barrier function (Fig. 2.4a), the dislocation loop grows more or less isotropically because the edge and screw segments have similar energetic barriers for motion. However, the loop structure is not circular because the dislocation line will attempt to maximize screw-type segments due to their lower line energy with respect to edge-type segments. When the orientation-dependent barrier is included, as in Figs. 2.4b and 2.4c, the edge segments of the dislocation move much more quickly than the screw segments, leading to the formation of an oblong dislocation loop with long screw segments. The operation of FR sources seen in these three cases can be expected and thus, it serves as a good reference to identify any potential unexpected behavior that could emerge in the MPEA.

Table 2.1 shows that even without the orientation-dependent barrier, the required stress to bow out a dislocation loop is higher in the screw-oriented source than the edge-oriented source. This difference arises from the higher line energy associated with

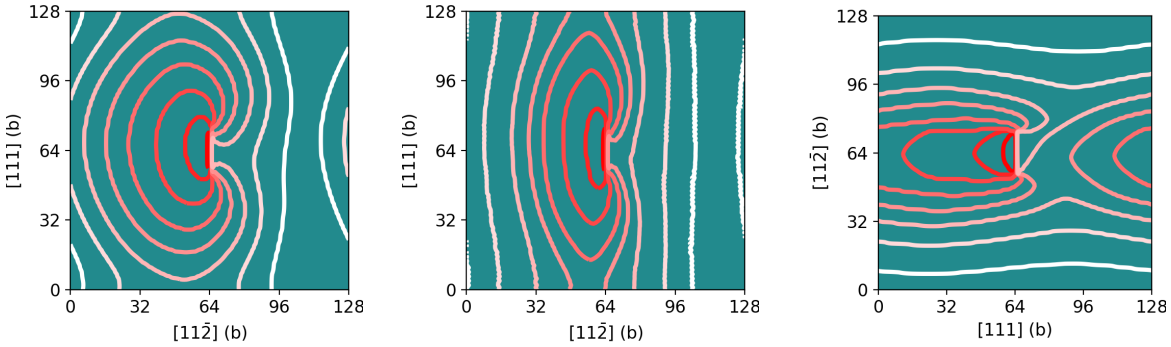

(a) Screw, $\beta = 1$ (b) Screw, $\beta = f(\theta)$ (c) Edge, $\beta = f(\theta)$

Figure 2.4: Snapshots of Frank-Read source loop expansion in homogeneous MoNbTi for three source setups at their respective critical stresses. Each curve shows the dislocation at a separate timestep of the same simulation, with progressively lighter pink curves showing later timesteps. The dislocation position is estimated by drawing a contour line where $\phi = 0.5$, which corresponds to the center of the dislocation core. When $\beta = f(\theta)$, the orientation-dependent barrier is used and the relative barrier for motion of edge, screw, and mixed-typed dislocations differs.

edge segments than screw segments, which makes it more difficult to create an initial bow-out that introduces edge-oriented segments than one that introduces screw-oriented ones. When the orientation dependence is included in the calculations, the critical stress drops by 25% and 50% in the screw- and edge-oriented cases, respectively. While the orientation-dependent barrier does not affect the lattice energy barrier for screw segments, any orientation of the FR source requires screw, edge, and mixed-type segments be created in order to generate a complete loop, so both orientations see a drop in critical stress.

2.3.2 Dislocation loop waviness

With the reference behavior established, the behavior of the same FR sources in the heterogeneous MoNbTi can be examined. As mentioned, these landscapes are characterized by l over which the barriers are similar (Fig. 2.2). A wide range of l are simulated

since the length scale over which the USFE and/or the Peierls barrier varies in actual MPEAs is unknown but finite and could be influenced by complex factors, such as thermodynamically driven SRO or proximity to grain boundaries [35, 123]. For each l considered, a total of 60 distinct realizations were studied for the screw- and edge-oriented cases with the orientation-dependent barrier, as well as the screw-oriented case without the orientation dependence.

Fig. 2.5 shows the progression of dislocation loop formation and expansion from a screw-oriented FR source without and with orientation-dependent barriers and an edge-oriented source with orientation-dependent barriers for an example lattice energy surface with $l = 5w_0$. The series of dislocation lines are shown on a glide plane with spatially varying and correlated lattice energy surface. As before, they are colored to represent the variation in the peak barrier due to local chemical clustering within the MPEA encountered by the dislocation loop as it expands.

Without considering orientation-dependent barriers (Fig. 2.5(a)), loop expansion looks qualitatively similar to that of the homogeneous MoNbTi reference case in Fig. 2.4(a), except the dislocation loop that is wavy and does not expand uniformly. As it extends and bows out under stress, the dislocation extends further through regions of low lattice energy (shown in purple), while it becomes temporarily pinned at areas of high lattice energy (shown in yellow). These high energy regions are soft obstacles, and the dislocation is able to pass through them with minimal bowing.

When the dislocation orientation dependence is taken into account (Fig. 2.5(b) and (c)), the growing dislocation loop from both the screw- and edge-oriented FR sources assume a much more oblong shape, as the edge segments extend much further than the screw segments owing to their lower barrier. The loops are less wavy and smoother than when the orientation-dependent barrier was not considered. In the case of the screw-oriented FR source, the dislocation grows outwards from the sides of the FR source, while

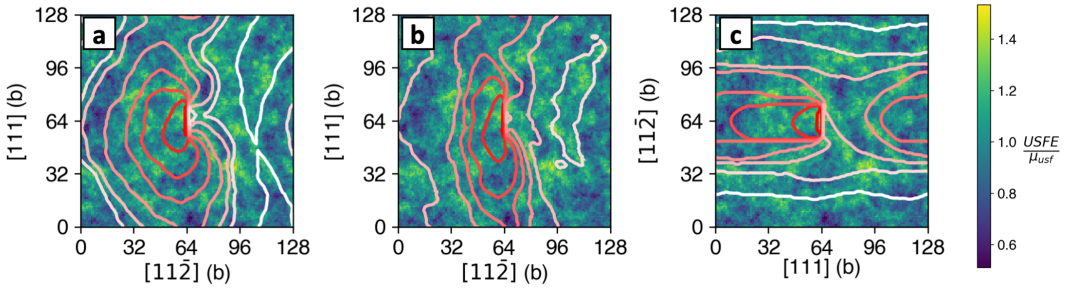

Figure 2.5: The expansion of Frank-Read sources under different conditions for the same lattice energy surface with $l = 5w_0$ under their respective critical stresses. (a) shows a screw-oriented source without the orientation-dependent resistance, while (b) shows the same source with the use of the orientation-dependent resistance. (c) shows an edge oriented source with the orientation-dependent resistance. The red curve is drawn at the contour where $\phi = 0.5$. Several snapshots throughout the loop expansion are superimposed with the lighter colored lines corresponding to later timesteps.

the screw portions bow out slowly. Eventually the edge segments annihilate one another, permitting the two long screw segments to continue gliding away from the FR source. These two screw segments are highly curved and wavy as they navigate the varying lattice energies in the MPEA. In the edge-oriented FR source case, the edge segment grows quickly away from the source, and the two initially straight screw segments begin to bow out, eventually meeting and annihilating, releasing the loop.

In Fig. 2.6, the effect of l on the operation of an FR source is examined. For this analysis, screw-oriented sources without the orientation-dependent barrier function are considered. Sample surfaces with l equal to $1w_0$ and $20w_0$ are presented. The loop on the $1w_0$ surface resembles the homogeneous case very closely (Fig. 2.4a), although the loop that is produced exhibits a minimal amplitude of waviness. On the other hand, the loop on the $20w_0$ surface expands unevenly, moving quickly through valleys of low lattice energy and expanding much more slowly over peaks of high energy. The behavior of FR sources in the MPEA with intermediate l scale falls between these two extremes.

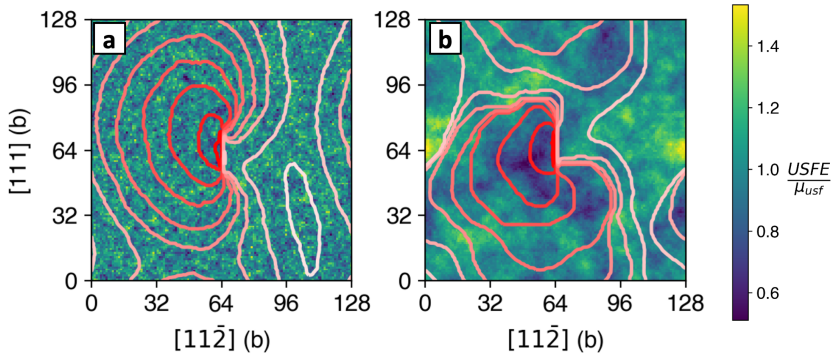

Figure 2.6: The expansion of a screw-oriented Frank-Read source using surfaces with different correlation lengths: $l = 1w_0$ and $l = 20w_0$ for (a) and (b), respectively. The red curve is drawn at the contour where $\phi = 0.5$. Several snapshots throughout the loop expansion are superimposed with the lighter colored lines corresponding to later timesteps.

In general, a longer range of composition ordering corresponds to greater deviations from the homogeneous case and an increase in the amplitude of the waviness in the dislocation loops that are produced.

2.3.3 Critical FR source activation stress

The critical stress to generate a dislocation loop from the FR source was calculated for each of the cases studied. This threshold stress is the stress required to expand the initially straight FR segment into a critical bow out configuration. The length scale over which the critical state is reached remains on the order of the FR source length itself, i.e., long before the loops shown in Figs. 2.5 and 2.6 are produced. Thus, the critical stress is established locally by the environment near the FR source. After it is reached, the loop propagates away from the source with no further increase in stress. The new loop is able to continue to glide unhindered out of the simulation cell and annihilate with the periodic image. This response is expected of a pure metal and seen in the case of the homogeneous material. Yet still, for the heterogeneous MPEA, the critical stress to activate the source

was also sufficient to propagate the shear loop away from the source, for all FR source orientations and all realizations of all l studied. Therefore, in spite of the broad range of barriers the dislocation encounters after being emitted from the source, none of them are so high that the stress required to nucleate the dislocation cannot overcome them. This response indicates that the nucleation stress is always higher than the propagation stress for the loop. Overcoming line tension stills plays a dominant role in source activation.

The distributions of critical stresses at each correlation length are shown in Fig. 2.7 for screw-oriented sources with and without the character-dependent barrier. For comparison, the critical stresses for sources in pure Mo, pure Nb, and homogeneous MoNbTi are also plotted. When the character-dependent barrier is included, nearly all realizations of FR sources in the MPEA exceed the critical stress for Nb,and many exceed the critical stress for homogeneous MoNbTi. For both scenarios shown, the distribution of critical stresses widens as the correlation length increases. Prior experimental studies on a various BCC MPEAs have reported room temperature yield strengths higher than any of the constituent yield strengths. The PFDD model predicts athermal dislocation nucleation stresses for MoNbTi above that of Nb but below that of Mo since the DFT-calculated USFE values lie in between those of Nb and Mo. Studies of propagation of long dislocations and dislocations arrays and considerations of thermal effects within the model may provide a different relationship between the MPEA and its constituents.

The calculations here show that the statistical dispersion in critical stresses among the different realizations is substantial, too great in some cases to be appropriately evaluated by standard Gaussian (or normal) statistical analyses. To determine the form of their statistical distribution, the 60 calculated critical stresses at each l are fit to a variety of probability distributions, using the appropriate axes scaling.

Fig. 2.8 shows lognormal probability plots for the critical stress distributions at $l =$ 1, 3, 5, and 20 w_0, wherein the axes are scaled such that a true lognormal distribution

would manifest as a straight line. The wrong distribution would exhibit deviations from linearity, particularly at the tails. Interestingly in all cases, the lognormal distribution consistently provides the best representation, with a higher R^2 value than either normal or Weibull distributions. Although not shown, all other cases studied here also exhibit lognormal character. This finding implies that conventional normal estimates of the mean and dispersion would not appropriately represent the expected values and dispersion in critical stress. Further, the fact that the distributions do not follow a Weibull distribution indicates that FR source activation is not a weakest-link phenomenon. In other words, activation is not based solely on the weakest energetic barrier on which the FR source lies but on a combination of factors.

To examine altogether the effects of l, FR source orientation, and orientation-dependent resistance, Fig. 2.9a plots the change in the lognormal mean critical stress (dots) and standard deviation (error bars) with increasing l. For comparison, the critical stress for the equivalent homogeneous case is shown by the dashed line, which is a deterministic value. For all l and FR source characters, the mean critical stress is less than the critical stress for the homogeneous case. Evidently, introducing spatial variation in energy barriers above and below the average barriers more often weakens rather than strengthens the source. Even more importantly, increasing the range of local chemical clustering by increasing the l does not appreciably alter the mean critical stress. The critical stress remains, on average, weaker than the homogeneous material for short and long l alike.

For the screw-oriented FR sources, the effect of the dislocation orientation-dependent resistance was examined. Similar to the homogeneous MoNbTi case (Table 2.1), including orientation-dependent barriers decreases the critical stress to activate the source. Significantly, the reduction in critical stress relative to that for the homogeneous material is, however, the same, whether or not orientation-dependent barriers are considered. Apparently, accounting for less glide resistance for the non-screw segments is not respon-

sible for weakening the MPEA relative to its homogeneous counterpart. Again, even with screw/non-screw orientation dependence, the introduction of spatially varying barriers lowers the average critical stress compared to the same material without such dispersion.

While the range of composition ordering l has little influence on the mean critical stress, it can greatly affect the variance in the critical stresses. The coefficient of variation (COV), defined as the ratio of the standard deviation to the mean, is calculated for each lognormal distribution of critical stresses (Fig. 2.9b). For all FR sources, statistical variation increases as l increases. Accounting for differences in glide resistance due to dislocation orientation reduces the variation in critical stress values, particularly for larger l (approximately $5w_0$ and greater), where the variation was the greatest. Compared to the screw-oriented sources, the edge-oriented FR sources show considerably less variation in critical stress. There is only a slight increase in variation in critical stress with l.

Of particular interest is the effect of local chemical ordering on the ratio of critical stress for the screw-oriented FR source to the edge-oriented FR source. Like the homogeneous material, for the MPEA, the critical stresses for the screw-oriented sources are higher than those for the edge-oriented sources. The screw-edge ratio for the critical stresses in the homogeneous material is 1.87, which is comparable to the mean screw-edge ratio in the MPEA of 1.76. However, the composition fluctuations lead to some considerable differences in their behavior. The screw FR sources exhibit far more variation in their strength than the edge. For the edge sources, the dispersion is smaller and less sensitive to l. Also, while both screw- and edge-oriented sources are weakened relative to the homogeneous MoNbTi, the screw sources experience a more substantial drops in critical stress. The edge sources have a critical stress 6% lower than the homogeneous case, whereas screw sources have critical stresses 12% lower. Another interesting aspect is that the screw sources are always stronger than the edge sources. Even for the larger correlation lengths, $l¿\ 5w_0$, for which the variance in critical stresses tends to be higher,

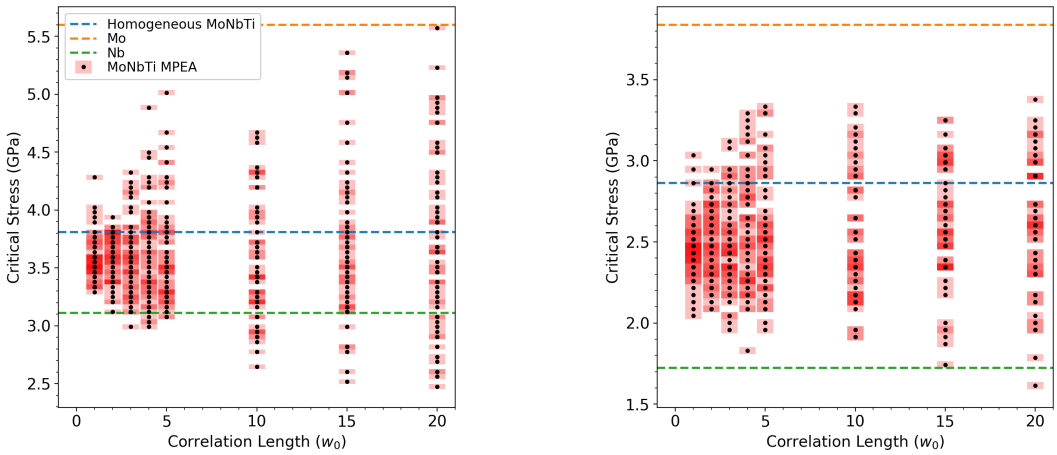

(a) Screw-Oriented Source, without Character-Dependent Barrier

(b) Screw-Oriented Source, with Character-Dependent Barrier

Figure 2.7: The critical FR activation stresses for screw-oriented sources both (a) without the character-dependent barrier and (b) with the character-dependent barrier. Each black dot is a separate PFDD simulation, and the pink box represents the upper and lower bounds of the calculated critical stress. Darker pink areas represent where several realizations have the same critical stress. The dashed lines show the pure reference cases of Mo, Nb, and homogeneous MoNbTi.

the screw-edge ratio in activation stresses still remains greater than one. For any individual realization, however, the screw-edge ratio can vary substantially. In some planes, it can be as small as 1.2, whereas in other planes, the ratio exceeds 2.5.

2.4 Discussion

In this work, PFDD simulations reveal significant effects of local chemical clustering on the operation of FR sources in an MPEA. The calculations show that on average the FR sources are easier to activate than the same source in a homogeneous material with nominal MPEA properties. The dispersion in the critical stresses exhibits a strong sensitivity to the range of composition ordering l. Specifically, the variance critical stress can be small when l is small but substantial when it is large, particularly when l is

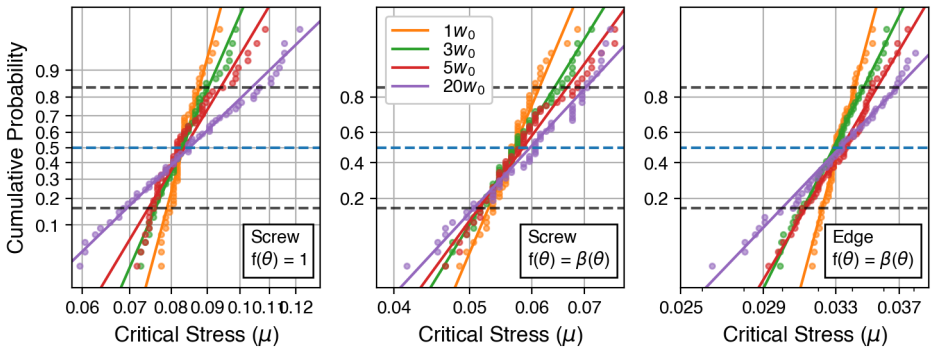

Figure 2.8: Lognormal probability plots of the critical stress for Frank-Read source activation. From left to right, the plots show a screw-oriented source without the orientation-dependent resistance, a screw-oriented source with the orientation-dependent resistance, and edge-oriented source with the orientation-dependent resistance. Four correlation lengths ranging from $2.15b$ to $43b$ are chosen to be representative. Where the best fit line crosses the dashed blue line corresponds to the mean critical stress, and the dashed black lines correspond to the mean critical stress plus or minus one standard deviation.

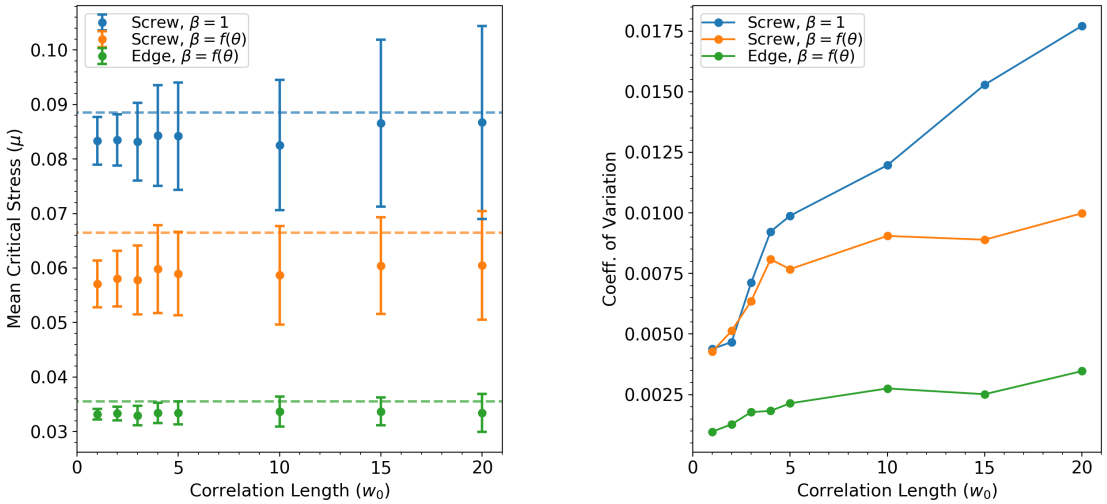

(a) Mean Critical Stress (b) Coefficient of Variation

Figure 2.9: (a) The critical stresses for Frank-Read activation at each l for three cases: screw without the orientation-dependent resistance, screw with the orientation-dependent resistance, and edge with the orientation-dependent resistance. In (a), the error bars represent the standard deviation of the critical stresses at each l. (b) The coefficient of variation (COV) for all three cases as a function of l.

4-5 times the dislocation core width. The edge-oriented FR sources also experience a reduction in strength, although less substantial than that of the screw sources. The edge sources also show smaller statistical variation in critical stress and lower sensitivity to the extent of clustering (i.e., l).

To understand the origin of these differences, the incipient stages of loop production were closely examined. The critical stress is associated with expansion of the initially straight dislocation segment to a certain critical configuration that must be reached in order for the loop to expand unstably. The marked differences in screw and edge source behavior suggests that different mechanisms leading to FR source activation may be involved. The FR sources in the homogeneous MoNbTi reference material operate in the classical manner with essentially no loop bowing observed at stresses below the critical stress, but once the critical stress is exceeded, the loop begins to bow out uniformly from FR source (Fig. 2.4).

In the heterogeneous MPEA, on the other hand, the mechanisms are different than the conventional process and depend on the line orientation of the source. When the stress is first applied to the edge-oriented sources, the line segment bows out as in the conventional case. While still at stresses below the critical stress, the edge segment glides forward, producing two long straight screw segments on either side, a consequence of its lower barrier compared to that of the screw. At the critical stress, in one of the low energy barrier regions along the screw portions, a kink-pair forms. This kink-pair expands outward initiating the formation the full dislocation loop (Fig. 2.10). The process of activation of the FR edge source, therefore, involves two steps: first, oblong bow-out forming long screw segments, and second, kink-pair formation on the screw segments. This basic edge-FR source process manifests in all slip plane realizations. The second step distinguishes the MPEA FR operation from that occurring in the homogeneous material.

For the screw-oriented sources in the MPEA, the dislocation loops also expands non-

uniformly under stress but by a different two-step mechanism than the edge-oriented FR sources. After the stress is applied, the dislocation will first bow out in the form of a kink-pair into a small region with low lattice energy (Figs. 2.11 and 2.12). Unlike conventional kink-pairs, this kink-pair is athermal and its width is related to the extent of the low energy barrier region along the source length. Next, the edge segments of the kink-pair moves sideways. For some cases, the edge segments can glide without any further increase in stress, and the critical stress corresponds to that needed for form the first kink-pair. In other cases, sub-critical kink-pairs form, below the critical stress. The critical stress corresponds to stress needed to enable the newly formed edge segments to glide through the higher energy regions. Both steps in activating the screw-oriented source are affected by the variable energetic barriers in the glide plane, making it distinct from the operation of the same source in the homogeneous material.

This mechanism explains the reduction in the critical stress needed to operate an FR source observed when the orientation-dependent barrier is incorporated. Analysis of source operation both with and without the orientation dependence finds that this two-step mechanism for activation of screw FR sources applies even when the orientation-dependent barrier is not considered in the calculations. In all situations, source activation relies on the side edge segments of the first kink-pair to overcome the local energetic barriers. However, when dislocation motion becomes dislocation character-dependent the critical stresses are reduced even further as it becomes easier for the newly created edge and mixed type dislocations segments to move. It is expected that the larger the difference between the barriers to move screw and edge, the lower the critical stresses to activate the FR sources.

These FR source activation mechanisms can also explain many of the observed trends in the critical stress for the MPEA. Due to the varying lattice energy surface, there is likely to be a lower-than-average lattice energy region along the length of the FR source,

allowing for the dislocation to bow out at a lower stress than the equivalent homogeneous material. Consequently, the FR sources on average are easier to activate in the MPEA with variable energetic barriers than the homogeneous crystal with an average barrier. Furthermore, because all of the lattice energy surfaces use the same mean and variance in the USFE, these low energy regions are equally likely to exist for all l, so the mean critical stress is not influenced by l. However, l affects the width of the peaks and valleys in lattice energy. An FR source in a material with a longer l will experience fewer variations in energy barriers along its length than one with a shorter l. Results show that the critical stress will be sensitive to the number of distinct energy barriers spanned by the FR source length. The fewer barriers encompassed by a source, the greater the variation will be among sources located in different locations of the glide plane and crystal. Particularly for l ¿ $8w_0$, the chances are higher that this $20b$ FR source will lie entirely in a region of uniform lattice energy. The influence of l on source activation for the screw-oriented sources is applicable with or without the orientation-dependent barrier. Thus, the growing dispersion in critical stress with l, i.e., extent of chemical ordering, is the same regardless of how much glide resistances differ based on dislocation orientation.

2.4.1 Frank-Read source size effects

The dependency of kink-pair formation on the extent of local chemical ordering suggests that many of the effects revealed here will become even more pronounced for longer FR sources. Calculations for the critical stresses for screw-oriented FR sources were repeated for source lengths that were two and three times longer ($L = 40b$ and $60b$) than the original $20b$ source. These simulations were performed for the screw-oriented FR source using the orientation-dependent barrier. It was determined that the current 128x128x128

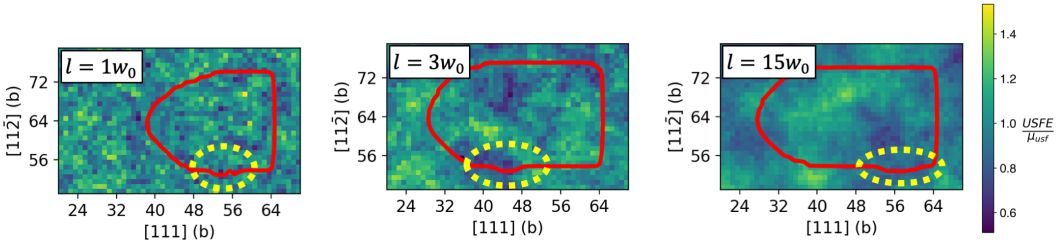

Figure 2.10: The early stages of loop growth in edge-oriented Frank-Read sources with the orientation-dependent resistance. Below the critical stress, a large bow-out with straight screw segments on the sides is present. At the critical stress, a small section of one of the screw segments expands into a low energy region (highlighted by the yellow dashed circle), leading to nucleation of a kink-pair and expansion of the full dislocation loop. Examples on three surfaces with different l are shown.

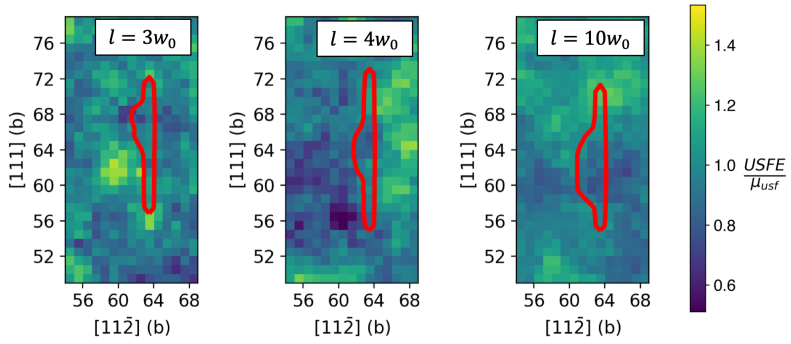

Figure 2.11: The early stages of loop growth in screw-oriented Frank-Read sources without the orientation-dependent resistance. A small section of the dislocation expands into a low energy region where a kink-pair is nucleated, thus expanding the loop. Examples on three surfaces with different l are shown.

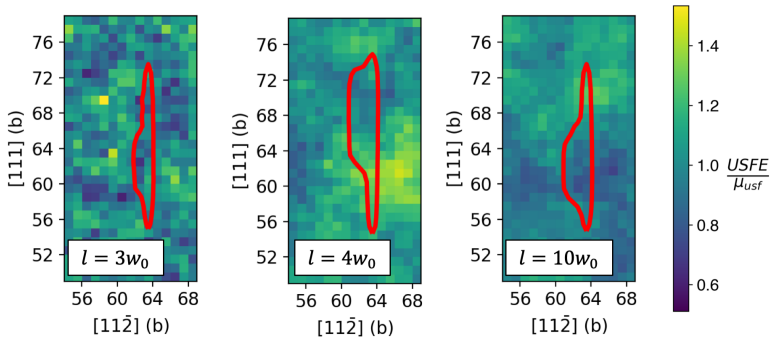

Figure 2.12: The early stages of loop growth in screw-oriented Frank-Read sources with the orientation-dependent resistance. A small section of the dislocation expands into a low energy region where a kink-pair is nucleated, thus expanding the loop. Examples on three surfaces with different l are shown.

cell size is sufficient for even these larger sources through a similar method as described in Section 2.2.3. The critical stresses were calculated for the same 60 energy surfaces at all eight previously studied ranges l. Statistical analysis of their distributions finds that like the $20b$ source, the critical stresses at each l follows a lognormal distribution.

Fig. 2.13a shows the mean and standard deviation in the critical stresses for each source size as a function of l. For comparison, the $20b$ results are also included, as well as the critical stresses for FR sources in the homogeneous material. Similar to the $20b$ source, the (lognormal) mean critical stresses for the larger sources do not differ appreciably with l, and the mean critical stress is always below the critical stress for the homogeneous case. As expected, the sources become easier to activate, as the source size lengthens. The important difference, however, is the greater size effect in critical stress for the MPEA compared to the critical stress for the homogeneous material. In fact, the critical stresses for the larger sources in the MPEA drop even further below the homogeneous case than those for the $20b$ source. The critical stresses for the $20b$ source are an average of 89% of the homogeneous critical stress, whereas the critical stresses are 85% and 77% of the homogeneous case for the $40b$ and $60b$ sources, respectively. Also

like the shorter $20b$ source, the variances in critical stresses increase as the l increases.

For the homogeneous case, the FR source size effect is a consequence of overcoming line tension to reach the critical configurations leading to an approximately proportional relationship with $\log(L)/L$ [124]. For the FR source in the MPEA, the mechanism for source activation is different and further, it gives rise to the more severe size effect than line tension alone. Fig. 2.14 shows the critical configurations for the $40b$ and $60b$ FR sources. Activation requires first forming a kink-pair followed by sideways glide of the newly created edge segments. This first kink forms where the lowest energy barrier exists. By increasing the length of the source, chances of encountering a low energy barrier to form the kink-pair increases.

To compare the source size scaling effects, the critical stress for the homogeneous material was calculated for L = $24b$, $30b$, $36b$, and $50b$ in addition to the previously calculated $20b$, $40b$, and $60b$ sources. These seven data points fit a power-law scaling very well with $R^2 = 0.986$ and give a scaling exponent of 0.11. Comparatively, the mean critical stresses for the $20b$, $40b$, and $60b$ sources in the MPEA fit a power-law scaling with a scaling exponent of 0.25. This emphasizes that the MPEA has a stronger FR source size dependence than the homogeneous reference case due to the increased presence of low energy barriers along the FR source length.

Unlike the conventional FR source operation, the FR source behavior in an MPEA with lattice energy fluctuations is controlled by low lattice energy regions along the source length. Longer source lengths sample more of the varying lattice energy surface, so there are more opportunities for a dislocation to bow-out into a weak area, thus making FR source activation easier. The difference in size effect between the MPEA and the homogeneous material results in an increasing gap between their critical stresses. The MPEA sources become much weaker than the homogeneous material sources. For the $20b$ sources with the largest correlation length ($20w_0$) and variance, 33% of the sources

in the distribution exceed the source strength of the homogeneous case. However, for the $60b$ sources for the same $l = 20w_0$ and for which the variance is the largest, just 12% of the sources exceed the homogeneous case. This trend implies that the longer FR sources in an MPEA are unlikely to exceed the strength of the homogeneous case due to the prevalence of low-strength areas.

The change in FR source activation mechanism with an MPEA also explains why the statistical variation in critical stresses decreases with FR length L. Fig. 2.13b shows the standard deviation normalized by the mean lattice energy (μ_{usf}/d_{110}) for the three source sizes studied. When the results are plotted against the ratio of FR source size to l, the data points for all three source sizes collapse into a single curve. The source size to correlation length ratio can be thought of as a proxy for the number of peaks and valleys the FR source sees along its length. A higher ratio causes less variation in the critical stresses because the FR source is sampling a larger number of fluctuations within the slip plane, while sources with a low ratio are only sampling a few peaks and valleys and are thus much more dependent on the specific placement of the FR source. The magnitude of the standard deviation appears to be captured by the number of peaks/valleys encountered by the source only, which suggests that the underlying variation in the lattice energy, which does not change with source size, is driving the variation of critical stresses. In fact, the standard deviation of the critical stresses follows a power-law relationship as the standard deviation scales with $(L/l)^{-0.30}$ as determined by the slope of the best-fit line in Fig. 2.13b.

2.4.2 Impact of the Character-Dependent Energy Barrier

To understand the effect of the character-dependent lattice energy barrier (Eq. (2.4)), several simulations were run with varying screw-edge ratios. The screw-edge ratio is cal-

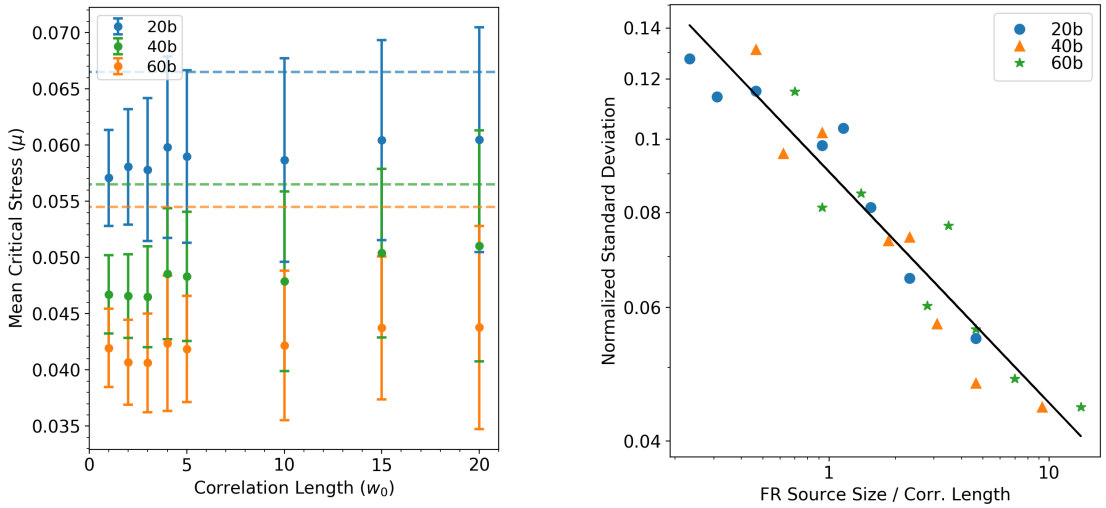

(a) Mean Critical Stress (b) Normalized Standard Deviation

Figure 2.13: (a) The critical stresses for Frank-Read source activation at each l for three different Frank-Read source sizes. All calculations use a screw-oriented source and include the orientation-dependent resistance. In (a), the error bars represent the standard deviation of the critical stresses at each l. (b) The standard deviation of the critical stresses plotted against the ratio of source size to correlation length. The standard deviation is normalized by the average lattice energy coefficient, μ_{usf}/d_{110}. The linear relationship in the log-log plot reveals a power law relationship with an exponent of -0.30.

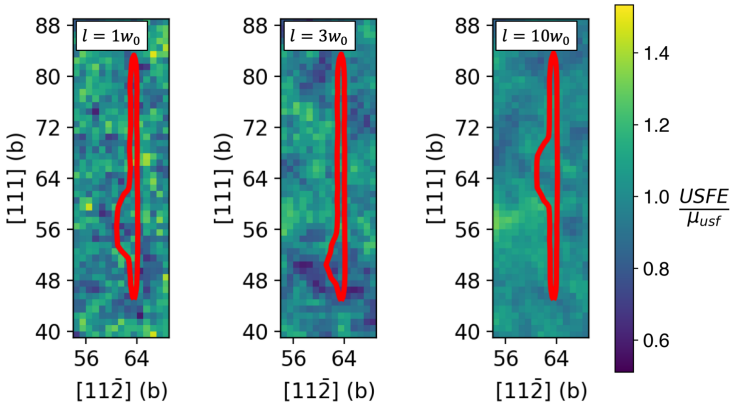

(a) 40b FR Source

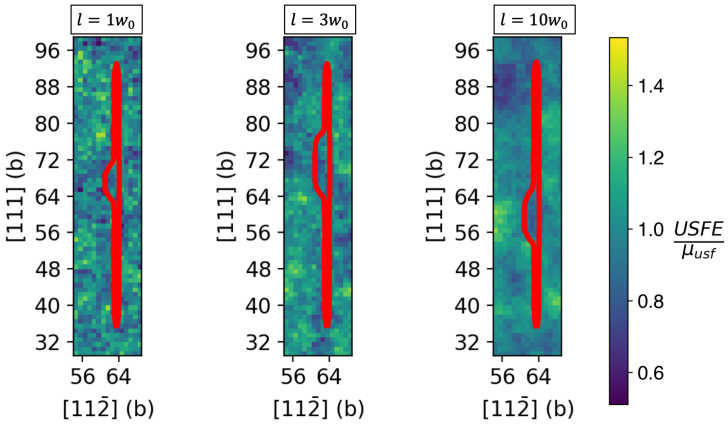

(b) 60b FR Source

Figure 2.14: The initial stages of Frank-Read source activation for the larger $40b$ and $60b$ FR source lengths.

culated using MS, which requires classical potentials for the MPEA of interest. Since these potentials may not exist for multi-component systems or may not accurately capture dislocation behavior, it is important to understand the sensitivity of the PFDD calculations to these input parameters. As an extreme case, 24 of the Frank-Read sources (3 of each correlation length) were rerun using a screw-edge ratio of 30. Screw-edge ratios in pure BCC metals may be on the order of 10s-100s, but it is expected that the ratios in BCC MPEAs are much lower. With this extreme difference between screw and edge lattice energies, the maximum decrease in critical stress for screw-oriented sources is 0.02 μ. The average decrease in critical stress is 0.0098 μ, which is a 16.8% decrease relative to the original calculations with a screw-edge ratio of 4.65. The edge-oriented sources show an even smaller dependence on the screw-edge ratio, with an average critical stress decrease of 0.001 μ, a 3% decrease. Therefore, the screw-edge ratio in PFDD has a higher order effect on the resulting critical stress compared to the underlying lattice energy fluctuations, which drive the statistical variation in critical stresses.

This work uses a simple, smooth interpolation between screw and edge energies for the character-dependent barrier (Eq. (2.4)), but other functional forms are possible. Peng et al. used a piecewise function with multiple local minimums for the character-dependent barrier of Nb and Ta, based on MS simulations of Ta [84]. Such calculations of a wide range of dislocation character types are computationally intensive and heavily dependent on the chosen potential, so this type of data is rare even for pure metals, and does not currently exist for multi-component systems. Nevertheless, to compare the effect of the functional form of the character-dependence, the critical stress for a Frank-Read source in Nb is calculated using the character-dependence calculated for Ta [85]. The Peierls stress has a local maximum at 71°, so dislocations of this character will be resistant to glide in addition to the pure screw dislocations. When the smoothly interpolated barrier is used (Eq. (2.4)), the critical stress drops from 0.0785 μ_{Nb} to 0.0435 μ_{Nb} for a screw-oriented

source. However, when the Ta character-dependence is used, the critical stress does not change from the no character-dependence case. This is attributed to the immobile 71° dislocations which inhibits kink-pair migration. For the edge-oriented source, the critical stress increases slightly from 0.0295 μ_{Nb} for the smoothly interpolated barrier to 0.0345 μ_{Nb} for the Ta barrier. This is expected as the barrier function $\beta(\theta)$ is 0.033 and 0.097 for edge dislocation with the smoothly interpolated barrier and Ta barrier, respectively. The form of the barrier function does indeed affect the critical stress by either allowing or suppressing kink-pair migration.

2.4.3 Implications on plastic behavior

In this work, glide was simulated on the $\{110\}\ \langle 111\rangle$ slip family, while in BCC crystals, slip on other families are possible. The present model can be used to study other slip modes and aid in identifying preferred systems [83]. Other modes will, however, have their own individual variations in energetic barriers and line orientation-dependencies, which would need to be taken into account. In principle, this methodology can also be used to study other refractory MPEAs, which will have their own distributions of local slip resistances and unique screw-edge differences [117]. Based on the present findings, it can be anticipated that MPEAs demonstrating greater fluctuations in composition or greater screw-edge mobility ratios would experience greater drops in the average FR critical stress drops relative to a homogeneous reference material. Moreover, since these results show that the statistical dispersion in the critical stresses scales with that of the underlying variation in lattice energy, it can be expected that MPEAs with less variation in lattice energies among the short-ranged ordered compositions, the less variation in activation stresses and vice versa. Here, SRO was not addresses directly, but generally, these findings imply that the range of chemical ordering, represented here by higher

values of l, affects the statistical variation in the critical stresses for activating sources and less so the mean value.

The statistical distribution of critical stresses for FR sources in the material can have macroscopic effects on its stress-strain behavior. Weaker FR sources will be activated quickly, which may lead to a high dislocation density and increased work hardening. Additionally, as the stress is increased, stronger FR sources will be activated, increasing the work hardening even further. Recent work on nanocrystalline metals, in which double-pinned sources in grain boundaries are the primary source for dislocations, find that with more variation in source strengths, the greater the strain hardening rate [125, 126].

While not explicitly considered here, as a dislocation slips through a crystal, the local compositions will change, which will alter the local USFE for subsequent dislocations [117, 123]. Hence, one can predict that after an FR source emits one dislocation loop at its critical stress, the underlying lattice energy surface will change, and a new critical stress for that FR source will be drawn from the lognormal distributions calculated here. This may lead to FR sources with low critical stresses being exhausted quickly, leaving behind a predominance of strong FR sources.

2.5 Conclusion

The PFDD formulation has been extended to study refractory MPEAs by including a spatially varying lattice energy coefficient and a dislocation character-dependence in the lattice energy. This new formulation was used to study the behavior of Frank-Read (FR) sources in MoNbTi. The shape of the expanding dislocation loop depends on the underlying correlation length, l, of the MPEA and the orientation of the FR source. The average critical stress to activate the FR source and create a full dislocation loop is not influenced by the underlying l, but the variance in the critical stress does increase with

clustering, represented by higher l. The critical stress for an FR source in the MPEA is on average lower than in the homogeneous MoNbTi due to a shift in mechanism for creating the initial dislocation bow-out. In the MPEA, the dislocation is able to create an athermal kink-pair into a lower energy region first and then expand outwards, allowing the dislocation loop to grow at a lower stress. This shift in mechanism leads to a significant size effect as the critical stress is dependent on the sampling of the underlying lattice energy surface, instead of merely the line tension of the dislocation bow-out. The statistical nature of FR sources in refractory MPEAs may play a role in their macroscopic mechanical properties by increasing dislocation densities and strain hardening.

Chapter 3

Glide on Higher Order Slip Planes [†]

3.1 Introduction

Atomic-scale simulation and experimental studies have shown that dislocations in MPEAs behave differently than in pure refractory metals or conventional, dilute refractory alloys [128, 129]. Due to the atomic-scale fluctuations in chemical composition in the glide planes of the dislocations, the critical stress is no longer deterministic and scale invariant, but depends on the length and location of the dislocation [97]. Atomic-scale simulations have shown that the local chemical changes result in a variable dislocation core structure along its line, causing the Peierls (lattice friction) stress for dislocation glide to concomitantly change along the dislocation line [19–22, 130, 131]. As an analogous measure to the Peierls stress for pure metals, the LSR of a short unit segment ($3b$–$4b$ in length) in a ternary MPEA MoNbTi were calculated with atomistic methods [132]. The LSRs varied substantially with a 60% coefficient of variation among dislocations in different locations in the material.

[†]This chapter adapted from Reference [127]: Fey, L. T. W., Xu, S., Su, Y., Hunter, A., & Beyerlein, I. J. (2022). Transitions in the morphology and critical stresses of gliding dislocations in multiprincipal element alloys. Physical Review Materials, 6(1), 013605.

Simulations of longer dislocations using atomistic or mesoscale dislocation dynamics methods have shown that mechanisms for dislocation glide are also unusual [97, 128]. In pure BCC metals, the edge-character dislocations move easily compared to the screw-character ones, where the screw-to-edge ratio in critical stress ranges from 10^2 to 10^3 [24, 85, 133]. Screw dislocations move by the formation and migration of kink-pairs, straightening after every kink-pair event and lying in wait for the next kink-pair event to occur [8, 134, 135]. Long ($> 100b$) straight screw dislocations are often seen in post-mortem microscopy of deformed BCC metals [135, 136]. In contrast, compared to dislocations in conventional metals, the dislocation motion seen in MD, mesoscale dislocation simulations, or in-situ or ex-situ microscopy studies for a wide range of MPEAs, has been described as wavy, tortuous, or jerky and for both edge and screw dislocations alike [13, 19, 21, 97, 123, 128, 137]. Dislocation waviness is generally understood to be a consequence of the variation in local lattice distortion, bond strengths, and dislocation core structure due to the atomic-scale variation in chemical composition. The statistically harder areas for the dislocation to shear serve as local pinning points and the dislocation bows between them, leading to the wavy appearance or pin/depinning jerky glide. Many MD simulation studies also have reported that the parts of a moving screw dislocation will locally cross slip onto other {110} planes, resulting in cross-kink pairs, which can also cause a wavy morphology and jerky motion [21, 131, 138, 139].

Another peculiarity emerging from MD simulations as a characteristic of dislocations in MPEAs is the markedly lower screw-to-edge ratio in critical stress. Values range from 2 to 10, easily an order of magnitude lower than that in pure metals [21, 25, 132]. Both the short segments used in the LSR calculations and the longer segments in the wavy glide calculations find screw-to-edge ratios in this range, indicating that the reduction cannot be attributed to dislocation lengths. As a final oddity worth mentioning, a recent study of the refractory MPEA MoNbTi found that dislocation slip occurred predominantly on

the higher-order {123} and {134} planes [13]. This is unexpected, as dislocation glide in pure BCC metals is typically attributed to the lower-order {110} and {112} planes [140, 141]. Apart from the LSR studies on MoNbTi [13, 132], most MD simulations of dislocations in BCC MPEAs studied glide on the {110} plane.

Because of the computational costs, many of these studies simulated a few dislocation samples moving over short distances. While a few instances can be sufficient for gleaning unusual mechanisms, the substantial variability in critical stress makes it challenging to understand relationship of unusual motion and the critical stress without statistically significant data and statistical analysis. Furthermore, due in part to the waviness, no standard method for defining the critical stress has been adopted. Some studies associate the critical stress with the threshold stress to initiate motion or to move a prescribed dislocation length over a prescribed distance. In the case of the LSR calculations, the short segments of the screw dislocations intentionally precluded study of kink-pair formation and migration.

In this chapter, PFDD is used to investigate the role of screw-to-edge ratio and lattice energy distribution on the morphological transitions and evolution of the critical stresses to move long screw dislocations in MoNbTi. The critical stresses to form dislocation loops from screw-oriented FR sources are also calculated for multiple glide planes. The calculations use generalized stacking fault energies of different areas in bulk random equimolar MoNbTi calculated from DFT to take into account the effects of chemical, distortional, and configurational fluctuations on local bonding and lattice energies. Because at the nanoscale on any given atomic glide plane, the elemental distribution cannot be truly uniformly random, some amount of random local clustering is presumed. For completeness, calculations treat a range of correlation lengths l, in which the extent of the local chemical clustering is short, less than 1 nm, to relatively long, 6 nm. Respecting the statistical nature of the underlying chemistry, hundreds of realizations are performed,

each over extended glide distances, hundreds of times the width of the dislocation core.

The simulations show that under mechanical straining, dislocation motion is described by successive intervals of wavy glide when the dislocation is gliding freely followed by full arrest when the dislocation nearly recovers its screw orientation. This glide mechanism leads to strengthening, in which the critical stress to re-activate motion increases with glide distance. Statistical assessment indicates that the amount of hardening directly scales with the dispersion in the underlying lattice energy distribution, in magnitude and correlation length. The analysis explains that motion initiates at the weakest region to form and migrate a kink-pair and stops when the entire region along the dislocation is too strong to initiate and migrate one. Unlike screw dislocation glide within its pure constituents, in the MPEA, temperature is not responsible for kink-pair formation and the critical resolved stress would not increase with glide. These findings are based on characteristics fundamental to MPEAs and explain why MPEAs behave differently than their pure constituents.

3.2 Methods

3.2.1 PFDD formulation and simulation parameters

The PFDD formulation used here is identical to that introduced for refractory MPEAs in Section 2.2.1. The lattice constant for MoNbTi is again $a_0 = 3.225$ Å and cubic elastic anisotropy with constants $C_{11} = 252.13$ GPa, $C_{12} = 134.11$ GPa, and $C_{44} = 32.41$ GPa is assumed [117]. The spatial distribution of $\psi_{\text{latt}}(\phi)(x, y)$ and the ratio R between screw to edge dislocations for a given type of slip plane are determined from atomistic simulations for four distinct slip planes.

For the USFE distributions in MoNbTi for the PFDD calculations to follow, the

values are taken from DFT and MS calculations reported for MoNbTi [117]. In brief, the calculations begin with a 3D special quasi-random structure of the MoNbTi. The γ-curves are calculated for a given plane with a cross-sectional area of 30 to $60b^2$, several times wider than the magnitude of the Burgers vector and longer than a complete lattice translation vector. The calculations were repeated for a sampling of 10–30 distinct areas in the volume for each plane type.

The USFE values are used to build correlated surfaces following the methodology in Section 2.2.2. An important physical length scale of the method is the correlation length l, which represents the extent of the local lattice energy in plane, or specifically, the distance two neighboring regions of distinct lattice energy are correlated more than 10%. As the lattice energy varies smoothly in the slip plane, any artificial modeling of phase boundaries is avoided. Since l is unknown but yet an unavoidable consequence of the atomic composition of MPEAs, calculations are repeated for l ranging from $1w_0$ to $20w_0$, where w_0 is the average core width of the dislocation in an average MoNbTi alloy on the $\{110\}$ plane, $2.15b$ [97]. The l range spans from one-tenth to twice the length of the FR source and approximately one-hundredth to one-fifth the length of the screw dislocation.

To build hundreds of realizations of correlated USFE slip planes for PFDD simulations, a Gaussian distribution is created from the USFE datasets provided by atomistic simulation. Fig. 3.1 presents the Gaussian distribution fits along with the discrete USFE distributions. The plane types exhibit USFE distributions distinct in mean and standard deviation, which are summarized in Table 3.1. For a pure metal, the USFE is often used to infer the preferred slip plane for dislocation glide [142, 143]. If the mean USFE is compared, the $\{110\}$ plane is the easiest and the $\{123\}$ plane the hardest, a ranking not unexpected for a pure metal. Yet, in MoNbTi, the coefficient of variations among these planes are not the same. Since the USFEs are widely distributed and dissimilar, the lower tails of these distributions follow a different ranking, suggesting that these

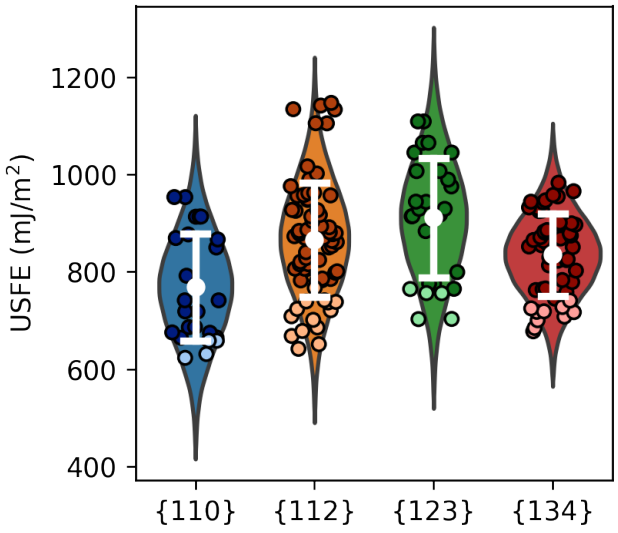

Figure 3.1: The USFE values calculated with DFT for each slip plane type and the normal distributions incorporated into the PFDD calculations. The mean and standard deviation for each plane are shown by the white point and error bars, respectively. The lighter colored points represent the bottom 20% of each distribution, where athermal kink-pairs are likely to be nucleated.

planes are more similar in their weaker regions than the mean value would suggest. The 20% lower quantile, for instance, which is shaded a lighter hue in Fig. 3.1, starts at 775 MPa, 760 MPa, 745 MPa, and 660 MPa, for the {112}, {123}, {134}, and {110} planes, respectively.

Finally an appropriate value for the screw-edge ratio R for each plane is also determined for MoNbTi. In prior work, using atomistic simulations, the LSR for a unit screw piece and edge piece less than 1 nm in length were calculated at different regions in a uniformly random volume of MoNbTi [13, 132]. The segment length modeled was intentionally made short so that the dislocation remains straight as it moves along the lattice vector in the plane, as in a classic Peierls stress calculation. Importantly, for the screw dislocation, this length is shorter than the width of a kink pair [144]. For PFDD calculations, R is taken as the ratio of the average screw to the average edge LSR, and the

plane-dependent R values are summarized in Table 3.1. All planes have a relatively low R, an emerging commonplace characteristic for MPEAs [15, 19, 21, 26, 129], compared to R for pure metals which is orders of magnitude higher [24, 133, 135, 145]. Among these four planes R still varies by one order of magnitude. The {112} plane represents a very low R plane, with only 1.4 and the {134} plane the highest with 11.8.

Together, the differences in USFE distribution and R among the four planes provides the opportunity to study their effect on dislocation dynamics in the same material. For each plane, 30 simulations of FR sources and 30 realizations of long dislocation propagation are performed per plane per l.

Table 3.1: The parameters used in the PFDD simulation for each plane type. The mean and standard deviation of the USFE are given in mJ/m^2. The screw-edge ratio (S.-E. Ratio is unitless. The grid spacings d_x, d_y, and d_z are given in units of the Burgers vector b. d_z is always the interplanar spacing in the slip plane normal direction, and d_y is the spacing in the Burgers vector direction.

	Mean USFE	S.D. USFE	C.O.V USFE	S.-E. Ratio	d_x	d_y	d_z
{110}	768	111	14.5%	4.65	1	1	0.8165
{112}	865	118	13.6%	1.40	0.8165	1	0.4714
{123}	911	125	13.7%	6.78	0.8135	1	0.3086
{134}	835	85	10.2%	11.8	0.8498	1	0.2265

3.2.2 Dislocation set up

The crystal is oriented such that the x and y axes lie in the slip plane and the z axis is aligned with the slip plane normal. The computational grid is orthogonal and the grid points coincide as closely as possible with the atomic positions [83]. Accordingly, the grid spacings in each direction depend on the slip plane being simulated. Previous work has shown that matching the grid points with the lattice points yields the best agreement with molecular statics (MS) calculations for dislocation cores [80]. Table 3.1 summarizes the grid spacings, where d_x and d_y are the spacings within the slip plane and d_z, the

interplanar spacing.

To study dislocation loop formation, an FR source is inserted onto the slip plane, using the method described in previous PFDD models [83, 97]. In all calculations, the length of the source is $20b$ and its Burgers vector is $(a_0/2)[111]$ and its plane lies in the center of the crystal. Both screw-oriented and edge-oriented sources are considered. 3D periodic boundary conditions and a computational grid size of $128 \times 128 \times 128$ are employed. This cell size has been shown previously to yield negligible effects of image dislocations present due to the periodic boundary conditions for sources of this length [83, 97]. A shear stress is applied in the slip plane and directed along the Burgers vector. Thus, the plane on which the FR source lies is the maximum resolved shear stress plane (MRSSP). The applied shear stress is raised in increments of 0.001μ (where μ is the isotropic Voigt averaged shear modulus and is equal to 43 GPa) until the source activates, after which it is held constant. At each stress increment, the solution procedure is run until convergence, which is defined as when the norm of the change in order parameters is less than 10^{-5} between successive time steps. For convergence, the quantity $m_{disl}\Delta t$, where Δt is the time step, is set to $0.05\mu^{-1}$.

To study long dislocation propagation, a screw-dislocation dipole with $(a_0/2)[111]$ Burgers vector is inserted onto the slip plane lying in the center of the crystal. The simulation cell dimensions are $256 \times 128 \times 128$, and periodic boundary conditions are employed in all three directions. The length in x is doubled to extend the distance the dislocations can glide. The dislocation is 128 b long within the periodic cell, and the dipole separation is 64 grid points in the x direction. A symmetrical USFE surface mirrored over the line $x = 128$ is used such that the two parallel dislocations experience identical USFE landscapes during glide. The applied shear stress is aligned with the plane of the dislocation and in the direction of its Burgers vector, making the plane of the dislocation the MRSSP. Application of the stress and solution procedure are the same

as described previously for loop formation.

3.3 Results

3.3.1 Dislocation Multiplication

First, the effect of USFE distribution and R on operation of a screw-oriented FR source is analyzed. The applied stress is raised just high enough to operate the dislocation source and then held constant. Fig. 3.2 shows the time sequence of the dislocation line from an activated source typical of each plane. The spatial variation in lattice energy across the plane for these chosen realizations is indicated by the color mapping of local USFE values. On the {110} plane, the most frequently studied plane in pure and MPEA refractory metals, the line morphology of the screw and non-screw parts are wavy. Particularly in the later sequences, the screw portions move slower than the edge portions and the ensuing loops are oblong. The morphology of the line in each time sequence from the source on the {112} plane have similar features, with the developing loops that are noticeably oblong. Similar wavy glide has been seen in MD simulations of other refractory MPEAs and has been a common observation for MPEAs [19, 21, 128, 129, 131]. In all the realizations, like those displayed in Fig. 3.2, each FR source eventually produces a full dislocation loop that glides unhindered out of the simulation cell. In none of the sequences shown does the dislocation loop fully arrest, although the waviness of some or all parts of the dislocation line may suggest otherwise.

The time sequence of the dislocation line for sources on the {123} and {134} planes show different morphologies. While the screw and non-screw portions are wavy, the lines are less tortuous than those on the {110} and {112} planes. Also, in contrast to the other two planes, the loops developing on the {123} and {134} planes have a lower aspect ratio,

signifying similar edge and screw mobilities. The smoother glide behavior and nearly equal mobilities are unexpected since these two higher order planes have the highest R. Transitions to smooth glide have been reported to occur at high applied driving stresses [128]. However, here, the applied stresses in the {123} and {134} examples are lower than those in the {110} and {112} examples. While the nearly face-centered cubic (FCC)-like behavior of FR sources on these planes is counter-intuitive, it is worth remarking that in experimental testing of this MPEA, dislocations are seen most often on these two planes in deformed material and less so on the {110} plane [13].

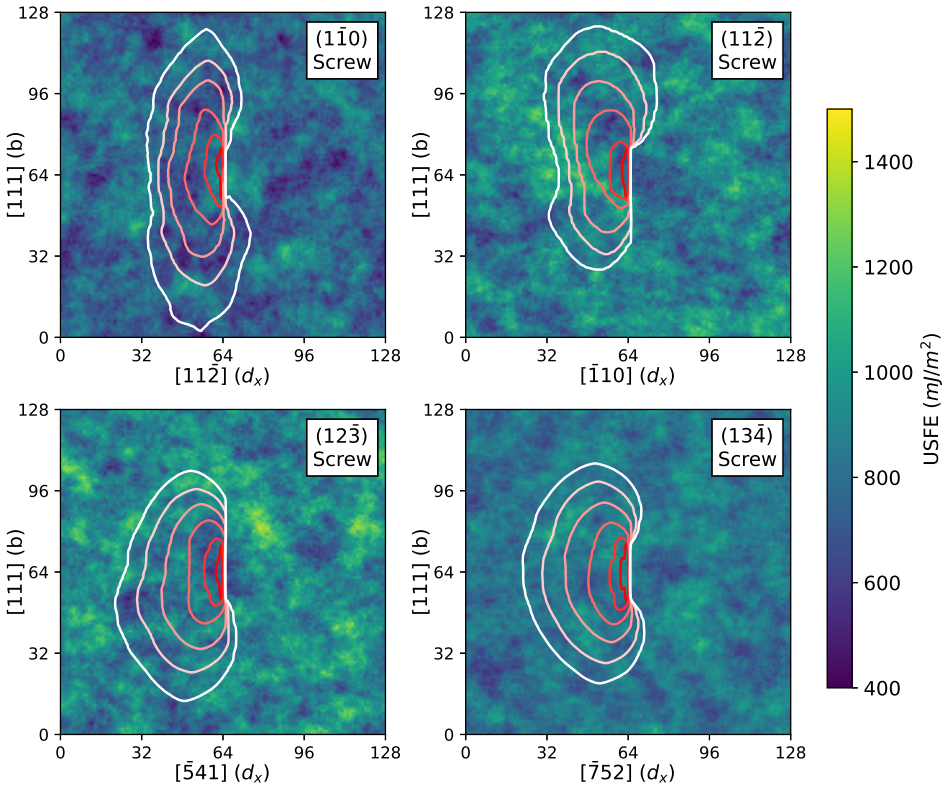

Figure 3.2: Representative examples of screw-oriented FR source operation on each of the four planes studied. All surfaces have correlation length l equal to $5w_0$. Dislocation lines are colored with respect to time. Lighter loops indicate a later time step than darker loops.

The critical stress, σ_{FR}, to activate each source was identfied. Fig. 3.3 shows values of

σ_{FR} for all 60 realizations for each of the eight l. The variation in σ_{FR} is clearly substantial, calling for a probability distribution that represents well each σ_{FR} distribution for a given l. The analysis proves the data fit a lognormal distribution in all cases. Comparing the lognormal mean, $\bar{\sigma}_{\mathrm{FR}}$, finds that, on average, the FR sources were hardest to activate on the {112} plane and easiest on the {134} plane. High critical stresses to move dislocations in MPEAs are thought to be related to the variation in lattice energy or the random occurrence of relatively larger local barriers [21, 128]. However, the mean and coefficient of variation (COV) in USFE for the {112} plane are not the highest nor for the {134} plane are they the lowest (see Table 3.1). Further, for no slip plane did l noticeably affect $\bar{\sigma}_{\mathrm{FR}}$.

To determine which properties govern σ_{FR}, the dislocation line morphology is examined at the moment σ_{FR} is reached and its relationship to the underlying USFE. In a pure metal, the dislocation line bows out between the two pinned ends, and the critical shear stress at which the line continues to glide unstably corresponds to a critical radius of curvature. In the MPEA, instead of bowing out uniformly, a kink-pair nucleates along the length of the source, and the edge-oriented portions of the kink-pair move along the dislocation line to advance the dislocation. Examples of these kink-pairs on screw-oriented FR sources are shown in the left column of Fig. 3.4. Activation of an FR source includes both kink-pair formation, with the screw protruding normal to the line, and kink-pair migration, with the two edge segments gliding apart. If the shear stress is removed before migration, the straight source is recovered. An activated kink-pair advances the screw portion of the dislocation line forward, into another region of the material, at which point another kink-pair activates. Through successive activation of kink-pairs, the dislocation line bows out. The edge portions having migrated to the pinned ends builds non-screw portions. While in time, the source bows out as in a pure metal (as seen in the early time sequences in Fig. 3.2), it is already in operation when it reaches this configuration

in an MPEA.

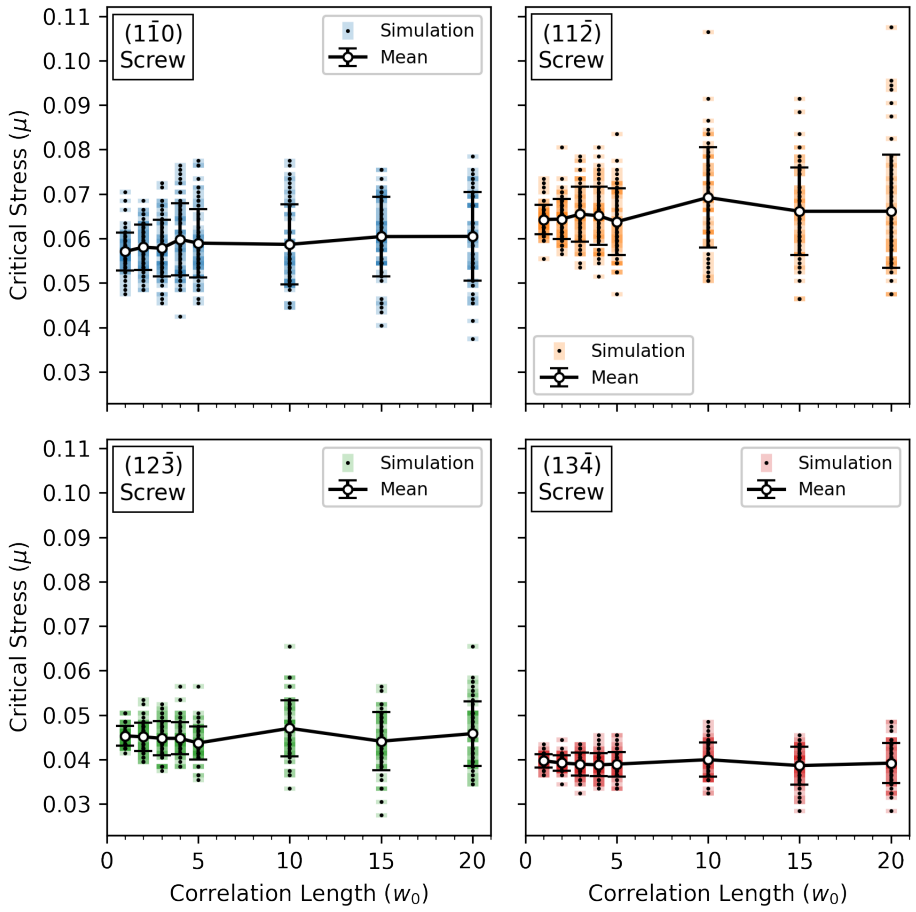

Figure 3.3: The critical stresses to activate a screw-oriented FR source on each plane. Each colored box is a separate simulation, and darker colors indicate where multiple simulations give the same critical stress value. The mean for each correlation length is also plotted with error bars corresponding to the standard deviation of the distribution.

It is, therefore, observed that the mechanism to activate unstable motion is a kink-pair. The kink-pair triggering event applies to all l and crystallographic planes. Identifying the size of a successful kink-pair is difficult, since by definition, the edge portions of the kink-pair immediately move apart, but it is clear that they are b in height and, when first formed, narrower than the length of the source, being approximately $1b$ to $3b$. More importantly, their size is found uncorrelated with l, in spite of the order-of-magnitude

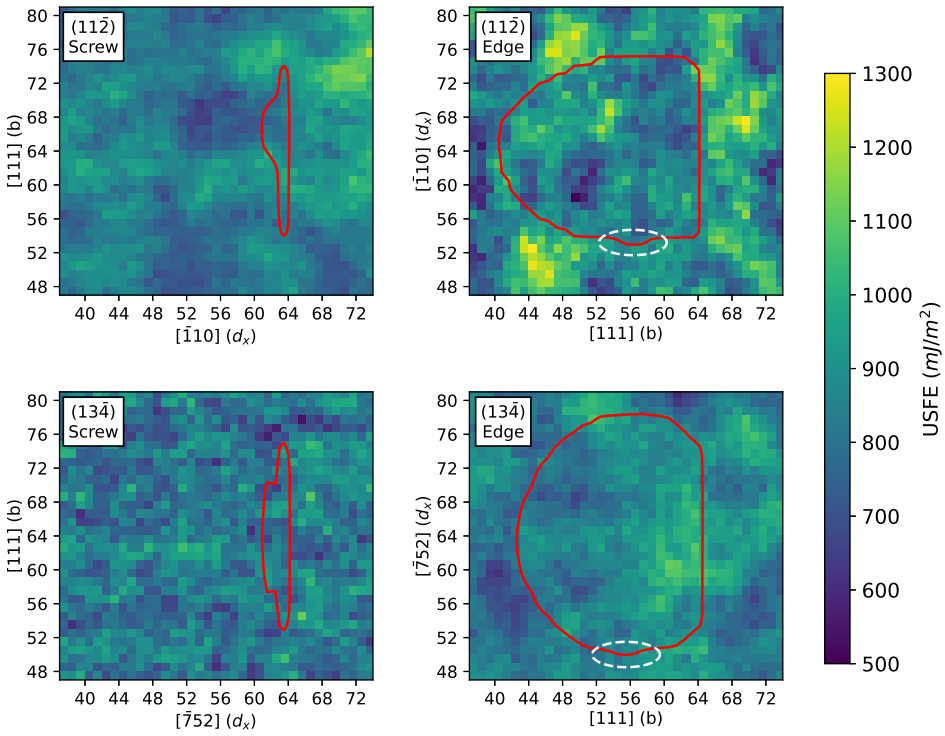

Figure 3.4: The critical stages of FR source activation for both a plane with a low screw-edge ratio, {112}-type, and a plane with a high screw-edge ratio, {134}-type. Both screw- and edge-oriented sources show kink-pair nucleation as the limiting step. Before these kink-pairs form, the dislocation will fall back to its original position if the stress is unloaded. The correlation lengths used in these examples range from $1w_0$ to $10w_0$.

wide range of l. Comparing the first successful kink-pair location with the underlying USFE for all cases finds that the former is strongly correlated with the weakest region along the initial source length. The weakest region means a low barrier to move both the screw and edge parts of the kink-pair. The lower tail of the USFE distribution, which applies to the screw parts, combined with the corresponding R, for the edge parts, and not the mean USFE, decide σ_{FR}. Accordingly, the {112} plane has statistically the hardest regions due to its low R, and the {134} the weakest regions due to its high R.

Next, the operation of edge-oriented FR sources of the same length are studied. The initially straight edge segments are not expected to move by kink-pair activation. Fig. 3.5 shows the time sequence of the dislocation lines as these sources operate under an applied

shear. A typical example is selected for each plane. On the {110} and {112} planes, the lines are wavy and the growing loops are elongated, indicating their two lateral screw portions are moving slower than the edges. On the {123} and {134} planes, a different scenario occurs. The developing loops adopt only slightly wavy lines and the loops expand nearly isotropically. The critical stress distributions σ_{FR} are obtained from the 60 realizations for a given l and slip plane. All data points are presented in Fig. 3.6. Like the screw-oriented sources, the lognormal mean of σ_{FR} for the edge-oriented sources are insensitive to l and indicate that sources are hardest to operate on the {112} plane and easiest on the {134} plane. These similarities suggest that the same mechanism activates edge and screw sources. However, with all else being equal, the edge sources are consistently weaker than the screw sources, and even the ratios of critical stress for screw to edge sources for all slip planes are similar, ranging from 1.5 to 1.7, and seemingly unaffected by R or the USFE distribution.

The line configuration corresponding to σ_{FR} is identified for the edge-oriented sources. Under subcritical stresses, the entire length of the source bows out between the two pinning points, forming two straight screw segments normal to the source. The source becomes critical when the loading state can activate a kink-pair along either of these two screw segments. Otherwise, the bowed-out dislocation recovers its original position when the stress is unloaded. Two examples are shown in the left column of Fig. 3.4. This is why σ_{FR} for edge-oriented sources follow the same relationship with the USFE as screw-oriented sources. Both are triggered by forming and migrating a kink-pair in the weakest USFE region along the straight screw portions of the dislocation. The edge cases are consistently about 60% weaker than the screw cases, since the edge-oriented source can sample more of the USFE surface by extending the screw dislocation lines.

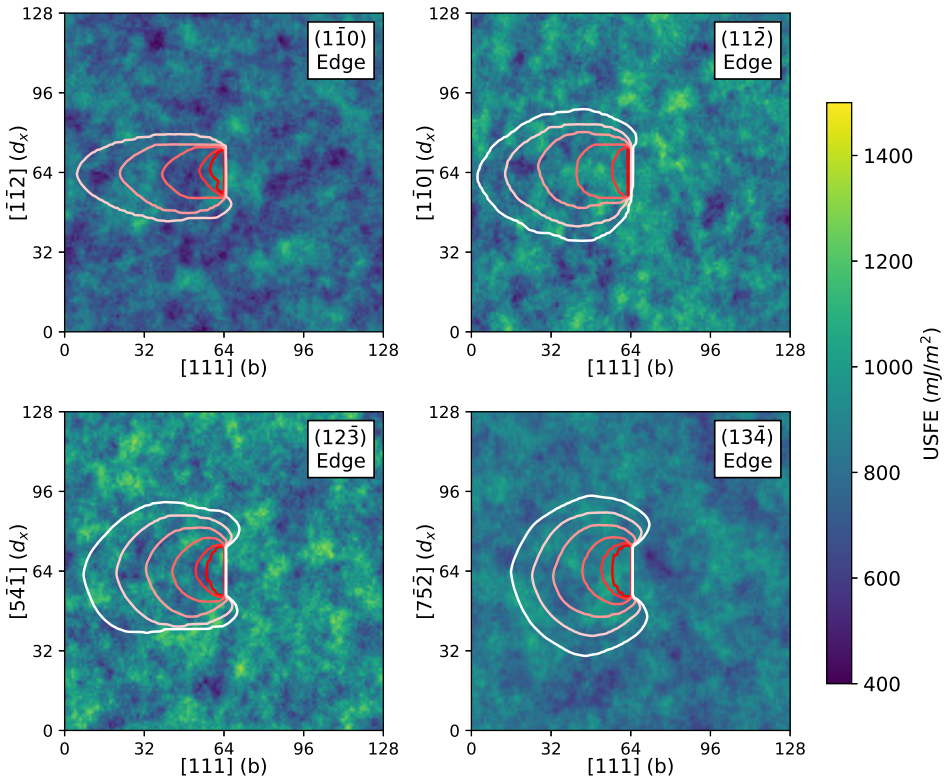

Figure 3.5: Representative examples of edge-oriented FR source operation on each of the four planes studied. All surfaces have correlation length l equal to $5w_0$. Dislocation lines are colored with respect to time. Lighter loops indicate a later time step than darker loops.

3.3.2 Dislocation Propagation

Next, dislocation propagation is studied by examining the role of the USFE and R on glide of a long screw dislocation, $>$ 40 nm in length, which is about 14 times greater than the FR source length. The dislocation is not pinned and can glide freely. Six different l ranging from $1w_0$ to $20w_0$ were studied with 30 distinct samplings from the USFE distributions for each. To determine the threshold stress to move the dislocation across the plane and outside of the simulation cell, the applied shear stress was slowly incremented until dislocation glide was observed. Fig. 3.7 shows several example stress-strain curves for each plane, all of which are unlike those expected in a pure metal. In a

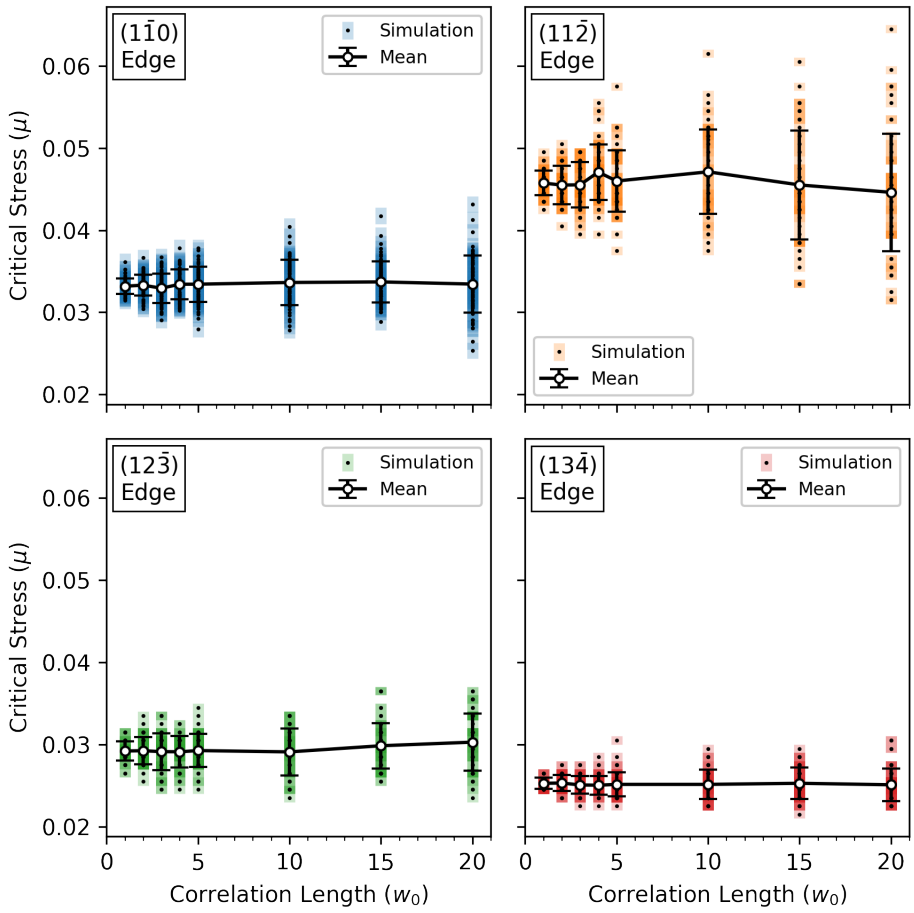

Figure 3.6: The critical stresses to activate an edge-oriented FR source on each plane. Each colored box is a separate simulation, and darker colors indicate where multiple simulations give the same critical stress value. The mean for each correlation length is also plotted with error bars corresponding to the standard deviation of the distribution.

pure metal, the critical stress to move a screw dislocation corresponds to that needed to form and migrate a kink-pair under a given temperature. It is deterministic and unvarying temporally or spatially, apart from the aid from thermal noise. For each glide plane in an MPEA, however, the responses among the different realizations are highly variable; no two are alike. They indicate stop/start motion, wherein the dislocations become pinned and stress increases are required to continue glide. Therefore, these dislocations experience strain hardening. Yet, unlike classic strain hardening, the amount of strain

between full stops varies, not necessarily increasing with each rise in stress. These curves terminate at the final stress needed for runaway glide out of the simulation cell. In most cases, the stress to initiate motion, σ_i, is not sufficient to sustain glide across the plane and is lower than the penultimate stress reached in the stress-strain curve, σ_f, which is designated as the stress required for the dislocation to escape the cell.

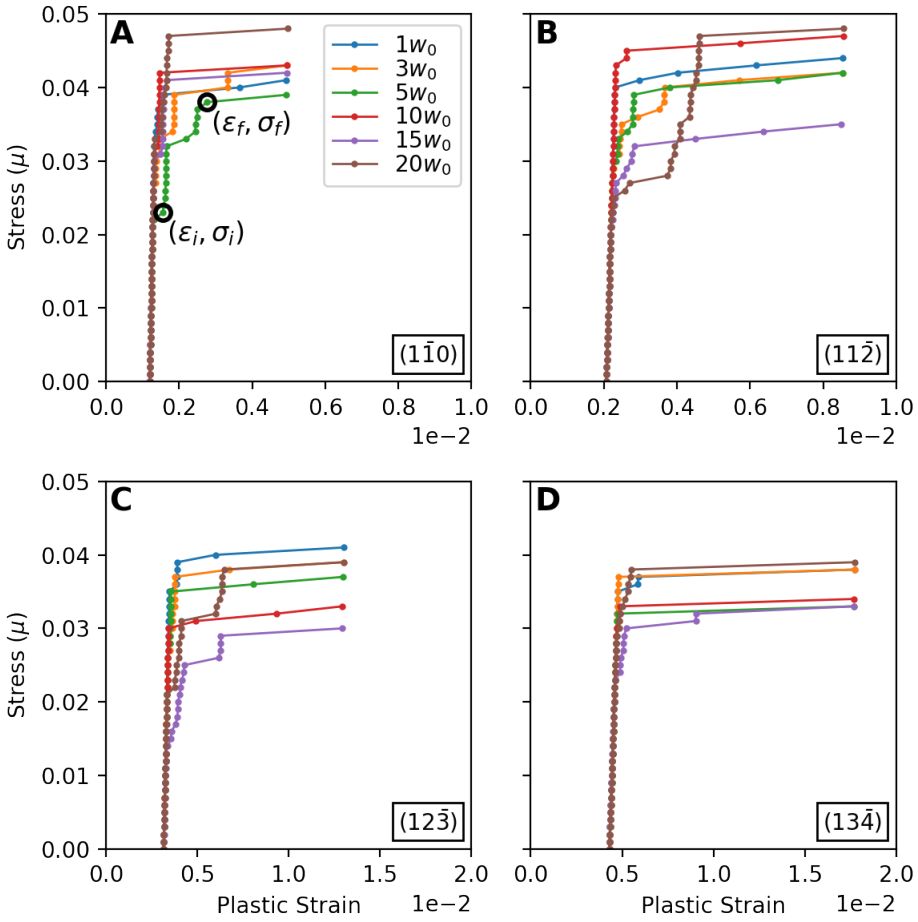

Figure 3.7: (A–D) Several stress-strain curves from screw dislocation propagation simulations on each slip plane type. The curves show a characteristic "staircase" as dislocations are pinned and unpinned several times before finally annihilating with periodic images. The definitions of σ_i and σ_f are illustrated in (A).

Due to the substantial variation, the critical stress results are analyzed from a statistical viewpoint. Fig. 3.8A compares the distributions for σ_i among the four planes.

As would be expected from the few examples in Fig. 3.7, substantial variation in σ_i is seen in all cases. An interesting observation is the persistent consistency in the mean and dispersion in the σ_i distributions in spite of differences in the USFE, l and R. These calculations suggest that average σ_i does not represent well the critical resolved shear stress to start the glide of a screw dislocation, is not sensitive to the spatial variation in lattice energies, and not a discriminating measure of preferred glide plane.

An analysis of σ_f presents markedly different observations. Fig. 3.8B shows the σ_f/σ_i distributions for the same cases. Motion of a screw dislocation on the {110} plane experiences not only the greatest increase in critical stress but also additional enhancements in resistance with l. However, glide on the {134} plane undoubtedly incurs the least strengthening and shows negligible dependence on l. The other two planes exhibit similar, non-negligible hardening propensity, like the {110} plane but to a lesser degree. This significant difference in σ_f/σ_i could explain the experimental observations of gliding dislocations on the {112}, {123}, and {134} planes, but not the {110} planes in this MPEA [13].

To understand the hardening behavior, the morphology of the dislocations is more closely examined under the applied shear stress. The dislocation line configuration changes in time and is wavy during most of the simulation. Fig. 3.9 shows a typical example for each slip plane throughout the full simulation time. In each case, the dislocation remains straight and in its original position under zero stress. When the stress is increased past a critical point, a kink-pair forms at some weak location and migrates some distance, advancing this part of the dislocation by b. Each advancement places that part of the screw dislocation into a new region, with a different random sampling of lattice energies, providing the opportunity to activate more kink-pairs. As the lattice energies vary over the long 40 nm length, when and where kink-pairs activate varies statistically. Under this glide mechanism, different kink-pair activation rates along the same

dislocation give it a wavy appearance. Waviness is a common observation among MD and other discrete dislocation dynamics simulations of dislocation lines tens of nanometers in length for a wide range of MPEAs [19, 21, 128, 129]. Here, the waviness originates from different parts of the same dislocation forming kink-pairs at different rates and it pertains to all four planes, for all l, and in all realizations, in spite of differences in the underlying USFE distributions, l and R. Only screw-character dislocations move in wavy glide via this mechanism. The waviness alone does not explain the differences in hardening seen in Fig. 3.7 and role of the USFE on σ_f.

To rationalize the USFE effects on strain hardening, dislocation line configurations are analyzed in relation to changes in stress. In all cases, the dislocation glides via a stop/start mechanism. It can be described as alternating intervals of non-stop glide under constant stress and full arrest requiring an increment in stress (Fig. 3.10). The dislocation takes on a wavy morphology as it glides continuously and then becomes nearly straight, close to its original screw orientation, when it completely stops. Continuous glide for the entire dislocation is sustained as long as any part of it can activate kink-pairs. The dislocation moves in free flight by statistical kink-pair activation, until it reaches a fully straight configuration when no kink-pair can be activated anywhere along its length. The additional applied stress needed to restart wavy glide from the fully arrested straight screw configuration is determined by the weakest region for forming and migrating a kink-pair anywhere along the dislocation line in its new location in the material.

During the intervals of wavy glide, the dislocation configuration is metastable. If the applied stress is removed during free glide, the stress-free equilibrium configuration is severely kinked, appearing to vary in character, not aligned with the original screw orientation. Examples of unloaded dislocation lines from all four planes are shown in Fig. 3.11. According to the PFDD simulations, the more rugged morphology of the

{110} and {112} planes compared to the other two planes becomes more pronounced in the stress-free state. Because R in the former planes are lower, kink-pair migration is more difficult, so arrested dislocation lines on these planes contain several edge-segments. With higher R values, kink-pair migration rates are higher, leaving the relaxed lines on the {123} and {134} planes smoother. These wavy dislocations are not unlike those observed experimentally in MoNbTi, where post-mortem investigation revealed wavy, predominantly non-screw, dislocation lines on {110}, {112}, and {123} planes [13].

As kink-pair activation controls the stop/restart behavior, the first kink-pair formed on each slip plane type is examined for two examples (Fig. 3.12). The kink-pairs on the top row correspond to the first kink-pair in the lower tail of the σ_i distribution, whereas the bottom row shows examples from the upper tail, i.e., the relatively stronger ones. In all cases, the critical kink-pair begins to form by extending a small "foot" $1b$ in height into a region with a relatively low USFE for formation and immediate migration. Thus, the mechanism to first start motion does not change, only the stress required to activate kink-pairs at the weak areas along the dislocation length. Drawing a parallel to brittle fracture, the stress σ_i to first move the dislocation is governed by the weakest link along the dislocation, wherein the link length is insensitive to l. The broad variation seen in σ_i in all cases would be characteristic of weakest-link behavior. The value of σ_i would consequently be mainly controlled by the lower tail of the USFE, which is similar for all USFE distributions here, explaining the similarity in the mean value of σ_i among the four slip modes.

Dislocations in all planes glide via this stop/restart mechanism in strain (or time). However, for the {110} plane, dislocations, on average, stop/restart more often in their excursion across the plane than the other planes. Many of the dislocations on the {134} plane are an exception, where in roughly half the cases, $\sigma_i = \sigma_f$. The heterogeneity in lattice energy across the plane increases with the variation in USFE and l. With

increased heterogeneity in lattice energy both in space and in magnitude, the dislocation is more likely to encounter a relatively harder location in material in which kink-pair activation is not possible along the entire length of the dislocation, causing it to fully arrest. Thus, for the most heterogeneous cases, the greatest hardening is seen where the glide resistance increases markedly with glide distance. This explains the increase in the ratio σ_f/σ_i with l for a given plane. To measure the strengthening provided by the heterogeneity, the hardening ratio, $(\sigma_f - \sigma_i)/\sigma_i$, is calculated, which is the ratio of the total rise in glide resistance to run the dislocation out of the cell (consistent signature of runaway) divided by the critical stress to first start its motion. Fig. 3.8C confirms the origin of hardening as posed; the strengthening increases with the dispersion (i.e., coefficient of variation) in the USFE.

3.4 Discussion

In studying the motion of long screw dislocations gliding over long distances, PFDD simulations show that their glide is controlled by the activation of kink-pair formation and migration. While kink-pair-controlled motion of screw dislocations occurs in pure BCC metals, the kink-pair nucleation frequencies depend on thermal fluctuations and scale with temperature and stress. Temperature introduces random thermal noise, and for a moving dislocation, represents statistical dispersion in driving force. Otherwise, under constant temperature and stress, the probability of forming and migrating kink-pair is the same along the length and invariant with location in the crystal. The dislocation moves by successive single kink-pair activation and straightening. While they are straight and arrested, they lie in waiting for a sufficient thermal perturbation to form and migrate the next kink-pair.

In the present work for an MPEA, the effects of temperature on the stresses to move

the dislocation and how the dislocation moves are not included. Specifically, the applied mechanical energy is not supplemented by thermal energy. The chemical composition randomness in the MPEA represents statistical dispersion in the energetic barriers for glide across the plane as opposed to random supply of thermal energy. Thus, the composition variations allow for kink-pairs to form randomly without the randomness from thermal noise. At a non-zero temperature, one would expect that kink-pairs will form more easily in the MPEA than in pure BCC metals because there are both thermal and compositional fluctuations present that can nucleate kink-pairs. Significant numbers of kinks forming on different slip planes can lead to immobile cross-kinks, which have been proposed to play an important role in BCC MPEAs [19, 139].

As in pure metals under temperature and stress, the arrested screw dislocation is nearly straight and the dislocation waits for sufficient additional energy, in the form of mechanical energy here, to form and migrate a kink-pair or multiple kink-pairs along its length. However, the statistical dispersion in lattice energy introduces periods of wavy travels between arrested states, which does not occur in pure metals. The waviness arises from variable kink-pair activation rates along the same line, leading to different nanoscale segments incurring different amounts of travel. The probability of kink-pair activation is not spatially invariant and depends on the level of heterogeneity in the lattice energy distribution. As another consequence, much of the glide plane slipped by a screw dislocation in an MPEA is accomplished by wavy glide, unlike in a pure metal. In fact, when the MPEA is unloaded, the dislocation collapses to wavy, non-screw state. This could explain prior microscopy studies of deformed refractory MPEAs that show highly kinked rather than straight dislocations [13].

In all cases of glide planes and correlation lengths, the glide initiates with successful formation and migration of a kink-pair in the weakest region along the length of the dislocation. This activation mechanism will impact the critical stress in several ways. First,

initial stresses depend on the lower tail of the lattice energy distribution, not its mean value. Second, the initial stress will be highly position-dependent and can be expected to vary substantially among different but otherwise like dislocations on the same glide plane. Third, since the dislocation cannot advance until the kink-pair migrates, the easier it is for the edge dislocations to move, i.e., the higher the value of R, the lower the initial critical stress. Last, the weakest link type phenomenon engenders a size effect, wherein longer is weaker. In actual materials, the lengths of screw dislocations can be much longer than those studied here ($128b$). The implication is that longer dislocations will experience even more variations along their lengths and even lower activation stresses. These outcomes result from the inherent compositional fluctuations characteristic of MPEAs and can be expected to apply to other MPEA systems as well.

Wavy or jerky dislocation glide is emerging as a common and persistent characteristic of dislocations in MPEAs. Several atomistic or mesoscale modeling simulations and some microscopy studies have reported wavy dislocations in glide or post-mortem [13, 19, 40, 97, 128]. Prior MD studies have associated tortuous morphology of dislocations of any character to randomly occurring pinning points and formation of cross kinks and/or interstitials and vacancies in some nanoscale segments [19, 21, 128, 131]. Similarly, mesoscale models of a generic dislocation have attributed wavy glide to dislocation bowing out between randomly occurring pinning points [40, 41]. Here in analyzing planar glide behavior of initially screw dislocations, wavy glide and jerky glide are classified as distinct behaviors. Wavy glide is a result of variable rates of kink-pair formation and migration along the length of the dislocation, where nanoscale segments with higher rates extend further. Wavy glide is not directly related to hardening, meaning the activation stress does not change, and any amount of atomic-scale variation in the underlying lattice energy will cause wavy glide. Jerky glide, on the other hand, is a result of the frequent transition between non-stop, free glide with non-zero kink-pair activation rates

and complete arrest with zero kink-pair activation rates. Jerky glide means hardening, in which the critical stress increases with strain. The greater the dispersion in lattice energy, the greater the hardening. This glide mechanism, involving wavy morphologies and jerky-induced hardening, is not applicable to initially edge-character dislocations.

Jerky glide and its associated hardening are studied over distances of just $96b$. The hardening seen in stress-strain curves among different dislocations on the same plane type vary substantially as well, such that no two pathways and stress-strain curves are alike. The greater the statistical variation in the USFE, in both content and length scale, the more pronounced the hardening. For the {110} plane, for which the greatest amount of hardening is observed among the four plane types, the critical stress increased, on average, 25–50% from its initial value. In contrast, the {134} plane showed the least. Experimental observations of dislocations in MoNbTi observe dislocations gliding on the {112}, {123}, and {134} planes, with notably fewer dislocations on the {110} planes [13]. In light of the current results, one could interpret this to mean that hardening, rather than the initial critical stress, selects the preferred glide plane. Nevertheless, it can anticipated that if the underlying USFE distribution has large dispersion with a long upper tail (high lattice energy with low probability), then hardening could continue with glide distances greater than the $100b$ simulated here.

Many MD simulations of dislocation glide in the {110} plane of MPEAs attribute the high critical resolved shear stress (CRSS) to the formation of cross-kinks along the same dislocation line [19, 21, 128, 131]. In the present simulations, the driving stress was intentionally applied so that the dislocation glide plane corresponded to the MRSSP of the dislocation; therefore, no driving stress component was applied to drive any part of the dislocation to cross slip onto another plane. Including thermal effects and/or other applied stress states would promote cross slip, however, the consequences would not necessarily be the same as in a pure metal. As mentioned, in simulating in-plane

glide, the motion involves wavy intervals, in which the original screw dislocation adopts a non-screw character, which would not present many opportunities for cross slip. The dislocation nearly recovers its straight screw orientation only when fully arrested under stress, which would then leave the possibility for forming kink-pairs on cross-slip planes.

3.5 Conclusions

In summary, PFDD was employed to study the role of screw-to-edge ratio and lattice energy distribution on the morphological transitions and evolution of the critical stresses to move long screw dislocations in the refractory MPEA MoNbTi. The atomic scale fluctuations in elements in MPEAs lead to dislocation-scale heterogeneity in the lattice energies associated with shearing the glide plane. Atomistic calculations find that the screw-to-edge ratios and the mean and dispersion in lattice energy distributions vary among the four plane types in the BCC MPEA MoNbTi, providing the opportunity to study their influence on dislocation dynamics in the same material. MPEA crystals were constructed with over 70 nm long glide planes with these lattice energy distributions and length scales over which the compositions associated with them are correlated. The variation in lattice energy, in both content and scale, leads to a strain hardening-like behavior, represented as an increase in the critical stress to activate glide with glide distance. When the variation is large, the dislocation moves in a stop/start motion, alternating between a wavy morphology in free flight and a nearly recovered straight screw orientation in full arrest. Substantial strain hardening behavior is associated with this glide behavior, where the critical stress increases, on average, 20–30% from the stress to first activate motion. In contrast, when the variation is small, the stress to initiate motion most often is the stress for runaway glide, indicating little to no hardening, and the dislocation motion is continually wavy. In all cases, the wavy glide is the result

of variable kink-pair formation and migration rates along the dislocation length, where portions with higher rates travel greater distances. The critical stress to move an isolated dislocation in pure metals would not exhibit the strain hardening seen here at the single dislocation scale. The strain hardening induced by atomic-scale composition fluctuations in MPEAs could play a part in explaining their superior strengths.

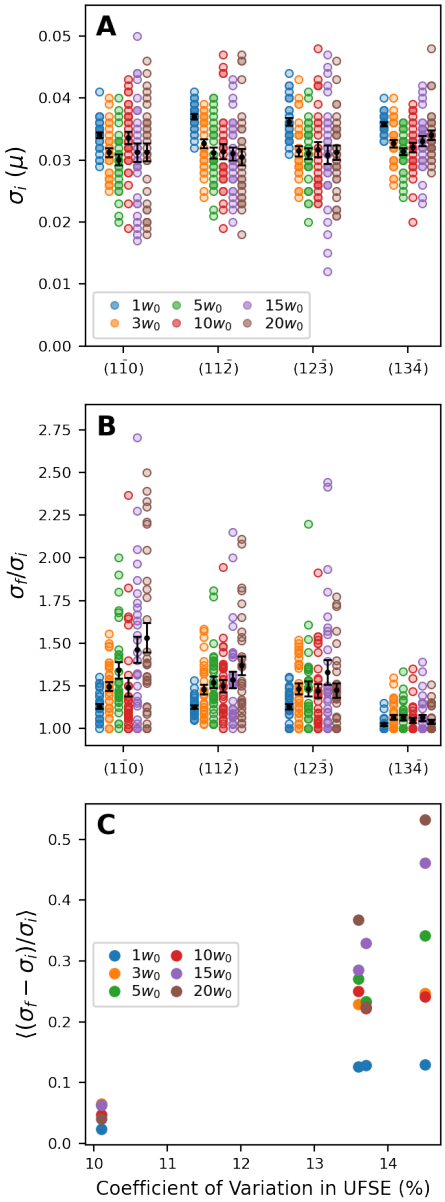

Figure 3.8: (A) The distribution of σ_i, the critical stress to initiate glide, grouped by plane type and correlation length. Darker symbols correspond to critical stresses shared by multiple iterations. The black dots show the mean stress for that correlation length and plane, with error bars equal to standard deviation across the 30 iterations. (B) The ratio σ_f/σ_i for each plane as a function of correlation length. This value corresponds to the amount of hardening that occurs during dislocation glide. (C) The quantity $(\sigma_f - \sigma_i)/\sigma_i$ for each correlation length plotted against the coefficient of variation of the underlying USFE surface. Higher variance in USFE leads to more hardening as the dislocation glides.

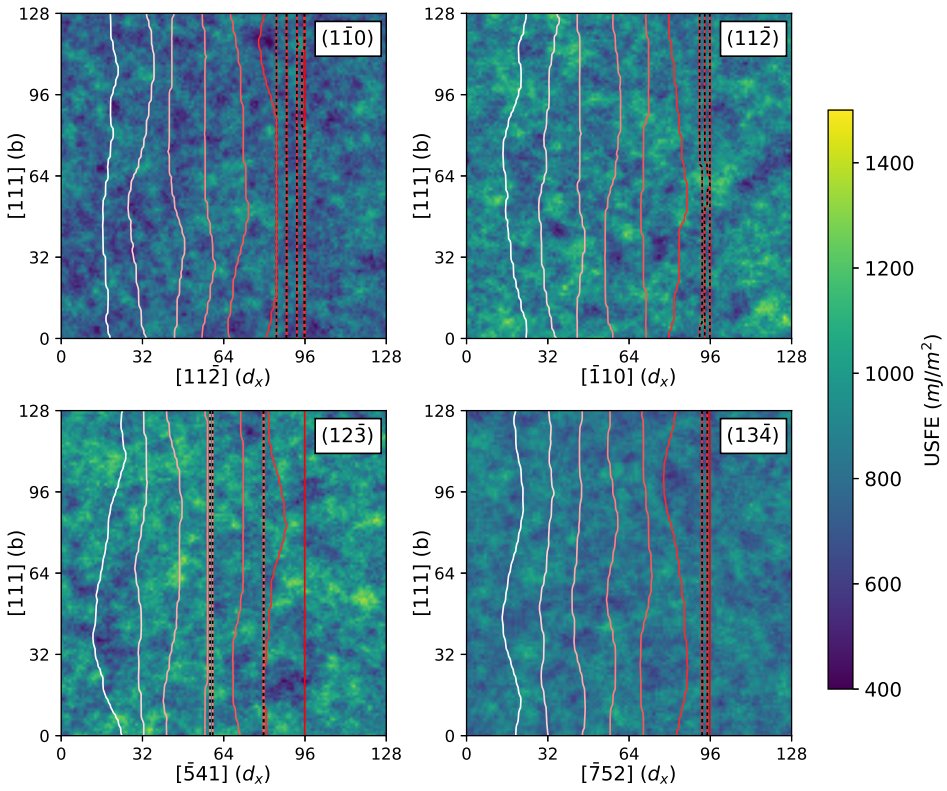

Figure 3.9: Representative examples of screw dislocation propagation on each of the four planes studied. The dashed lines indicate stable dislocations under stress, which require an increase in applied stress to advance. All four planes shown have a correlation length of $3w_0$, and dislocation lines are colored with respect to time, where lighter colors indicate a later time step.

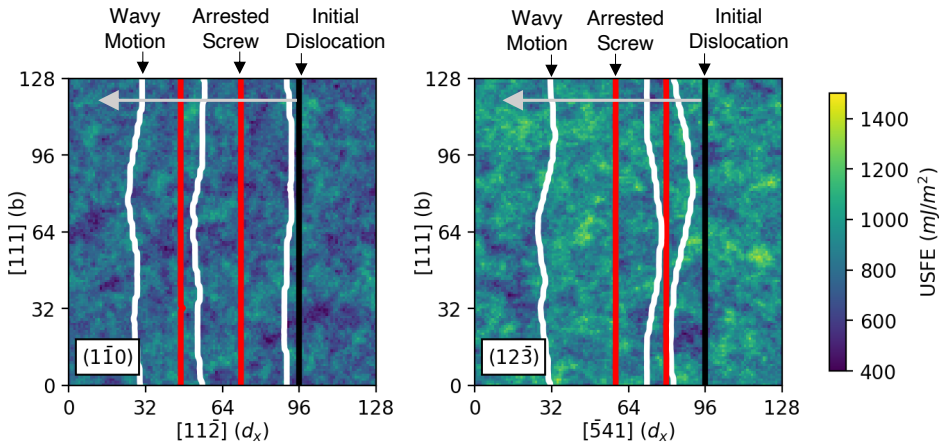

Figure 3.10: Representative examples of the progression of screw dislocation glide in MoNbTi. The initially straight screw dislocation (shown in black) appears wavy during glide (shown in white) but become arrested under stress and returns to a straight screw morphology (shown in red). These examples are from a {110}-type plane and {123}-type plane, but dislocation glide proceeds in a similar fashion for all planes studied. The correlation length l is $3w_0$ for both cases.

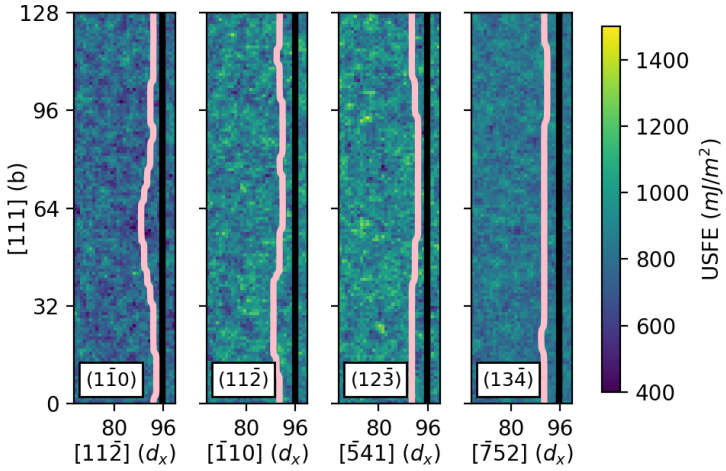

Figure 3.11: Examples of dislocations that were unloaded during glide in PFDD. The black line is the initial dislocation and the pink line is the unloaded dislocation. Just as the dislocations are wavy during glide, they remain wavy under zero stress if the stress is removed. The correlation length l is $1w_0$ for all four cases pictured.

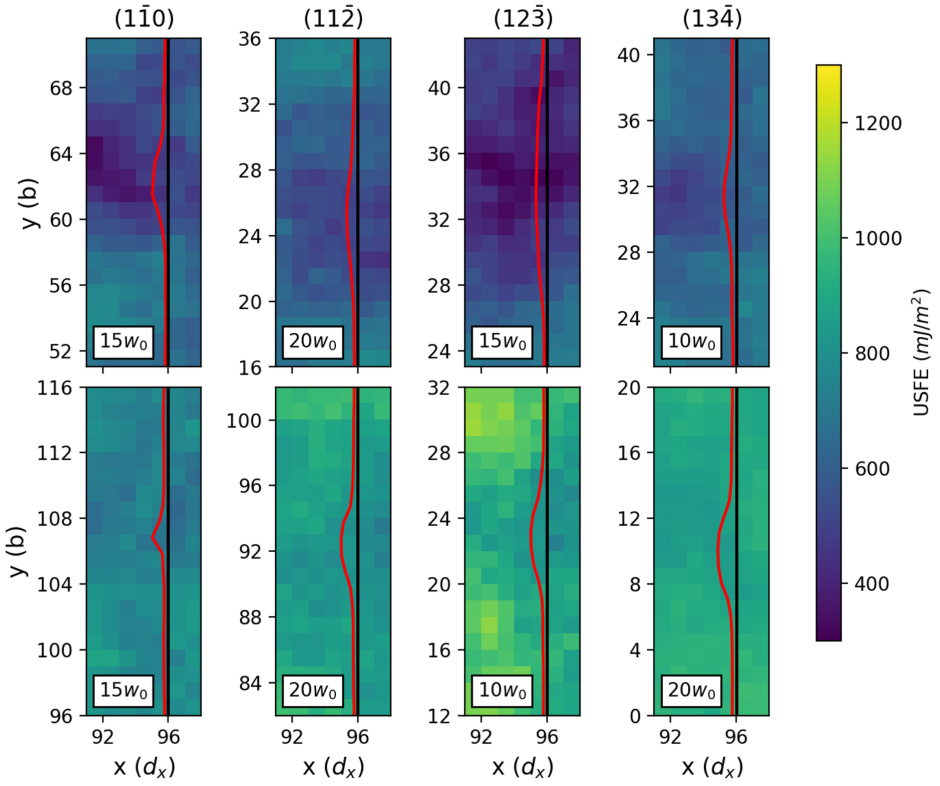

Figure 3.12: Examples of kink-pair nucleation on all four slip planes. The kink-pairs in the top row are nucleated on the weakest screw dislocation for their slip plane, while the bottom row shows kink-pairs on the strongest screw dislocation studied. The black line shows the initial placement of the dislocation at zero stress. Regardless of the slip plane, correlation length l, or critical stress, kink-pair nucleation controls the glide behavior of the dislocations.

Chapter 4

Cross Slip [†]

4.1 Motivation

Cross slip occurs when a dislocation changes its glide plane and is a crucial dislocation mechanism in refractory metals. Screw dislocations in BCC have a special, compact, non-planar core structure that enables them to cross slip easily [147]. The repeated cross slipping of screw dislocations in BCC materials is believed to cause wavy, non-crystallographic slip traces, and the ability to cross slip can affect the material's ductility and work hardening [135, 148–150]. At the same time, the BCC screw dislocation core also increases its resistance to move compared to edge character dislocations, making screw dislocation glide the rate-limiting deformation mechanism [135, 149]. Therefore, incorporating cross slip into computational dislocation models is critical for understanding refractory alloys, including refractory MPEAs.

The length scales accessed by dislocation simulation methods can range from the atomic scale, such as DFT or MD, to the mesoscale, including DDD and GPN models.

[†]This chapter adapted from Reference [146]: Fey, L. T. W., Hunter, A., & Beyerlein, I. J. (2022). Phase-field dislocation modeling of cross-slip. Journal of Materials Science, 1-15.

DFT has been used widely to calculate γ-surfaces, energetic landscapes associated with fault formation, and the core structures of dislocations in metals with compact and narrow structures [9, 147, 151, 152]. Many DFT studies of BCC metals have found that the cores of screw dislocations are non-planar and symmetric, equally spread on three planes, with six-fold symmetry sharing the same zone axis of the dislocation line and Burgers vector [9, 110, 147]. Studies of dislocation dynamics can be limited, due to short length and time scales, and to date, none have studied cross slip in BCC crystals [153, 154]. Compared to DFT, MD is able to reach slightly longer length and time scales in order to simulate the cross slip of screw dislocations [155–157]. These simulations can give valuable insight into the cross slip behavior of individual dislocations, including the formation of cross-kinks, pinning, and dislocation debris [45, 114, 138].

At longer length scales, DDD can simulate larger arrays of dislocations [73, 158–160]. Kinetic Monte Carlo has also been used to study dislocations in BCC metals, including the effects of cross slip [161, 162]. Both simulation methods are based on predetermined rules for dislocation interaction, mobility, and cross slip. The goal of these methods is usually to understand the collective behavior of large numbers of long dislocations over long periods of time, as opposed to atomistics, which is typically used to study short dislocations over short periods of time. The GPN model is another mesoscale computational technique that can represent discrete dislocations. Ngan first used GPN to calculate the non-planar screw core, the stress and strain fields it generates, and its self energy [163]. GPN models have been used to simulate cross slip in FCC crystals, but none have studied cross slip in BCC crystals [164].

In contrast to DDD, PFDD does not require pre-set rules to determine the when, where, and how dislocations move. Material parameters enter through the energetic terms in the functional and these can be supplied by atomistic simulation or experimental data. Early PFDD modeling studies usually considered just one slip system, simulating planar,

compact dislocation cores [78]. By including more slip systems in the formulation, PFDD was later used to model the dissociation of dislocations into partial dislocations in face-centered cubic (FCC) and hexagonal close-packed (HCP) metals [82, 105]. Multiple slip systems were also used to study the intersection of dislocations on different slip planes or the multiplication of dislocations from a Frank-Read source [83, 97, 165, 166]. However, cross slip, in which a full dislocation completely changes slip planes, has not been studied previously with PFDD. Prior PFDD models of BCC crystals have assumed a simplified planar dislocation core, requiring a correction term to account for screw-edge differences [84, 97].

In this chapter, PFDD is advanced to simulate the glide and cross slip of screw dislocations. The extended PFDD model captures the non-planar core structures of a screw dislocation and when under stress, the higher lattice friction and drag of screw dislocations relative to edge dislocations. The technique allows for simulations of kink-pair controlled glide and cross slip without the need for rules or properties based on local screw/edge character.

4.2 Methods

Here, the PFDD formulation is unchanged from Sections 1.4.2 and 1.4.3, although the computational details and choice of slip systems are modified. Dislocations with a $\frac{a}{2}[\bar{1}11]$ Burgers vector are simulated. This vector lies in many different potential slip planes, including three distinct {110}-type planes. In most prior PFDD simulations, an orthogonal, cubic grid has been used. In these cases, the system has been rotated so that the slip plane of interested is horizontal within the computational cell in order to minimize numerical error. However, when there are multiple active slip planes, inclined glide planes will be present and the density and spacing of grid points may not be equivalent on each

plane in an orthogonal grid. Thus, the inclined nature of the glide planes within the cubic computational grid may cause numerical differences in the PFDD model. PFDD was extended by Peng et al. extended to use non-orthogonal grids, including FCC and BCC grids [167]. To ensure the equivalence of all possible slip planes in the model, a BCC grid is used with primitive vectors $\boldsymbol{e}_1 = \frac{b}{\sqrt{3}}[11\bar{1}]$, $\boldsymbol{e}_2 = \frac{b}{\sqrt{3}}[\bar{1}11]$, and $\boldsymbol{e}_3 = \frac{b}{\sqrt{3}}[1\bar{1}1]$. The grid spacing in each direction is b, so grid points align with the atomic positions in a BCC lattice.

To compare the effects of using multiple slip systems, two different PFDD models are studied. First, in the *constrained* PFDD model, only one order parameter ϕ_1 is used. This is the traditional PFDD model for perfect planar dislocations. The slip direction $\mathbf{s}^1$ is $\frac{1}{\sqrt{3}}[\bar{1}11]$, and the slip plane normal is $\mathbf{n}^1 = \frac{1}{\sqrt{2}}[110]$. Second, in the *unconstrained* PFDD model, three active order parameters, ϕ_1, ϕ_2, and ϕ_3, are used to simulate three slip systems with slip directions $\mathbf{s}^1 = \mathbf{s}^2 = \mathbf{s}^3 = \frac{1}{\sqrt{3}}[\bar{1}11]$, respectively. The slip plane normals are $\mathbf{n}^1 = \frac{1}{\sqrt{2}}[110]$, $\mathbf{n}^2 = \frac{1}{\sqrt{2}}[01\bar{1}]$, and $\mathbf{n}^3 = \frac{1}{\sqrt{2}}[101]$.

As a model BCC material, Nb is simulated using the elastic constants and lattice parameter from experimental measurements made at room temperature [168], and the USFE used in Eq. (1.9) is calculated from DFT simulations for Nb calculated at 0K [83]. Elastic isotropy using the Voigt average is assumed resulting in an effective shear modulus $\mu = 39.64$ GPa and Young's modulus $E = 110.3$ GPa. The Burgers vector is 2.86 Å, and the USFE is 676.8 mJ/m^2. In the minimization, the quantity $m_{disl}\Delta t$ in Eq. (1.8) is set to 0.25 μ^{-1}. All simulations ran until convergence, which is defined as when the Euclidean norm of the change in order parameters is less than 0.0001. In the following calculations, the effect of temperature on dislocation core structures, critical stresses to glide or cross slip, and drag coefficients are not taken into account. The results here correspond to the athermal values.

The relaxed core structures of dislocations are examined in both the constrained and

unconstrained PFDD models. For the screw dislocation, the simulation cell contains a screw dislocation dipole on the (110) plane. The cell dimensions are 128, 32, and 128 grid points in the $\boldsymbol{e}_1$, $\boldsymbol{e}_2$, and $\boldsymbol{e}_3$ directions, respectively. Dislocation lines parallel to $[\bar{1}11]$ are placed on the (110) face of the simulation cell. Similarly for the edge dislocation on the (110) plane, an edge dipole is created in the simulation cell. Cell dimensions in this case are 128, 128, and 384 grid points in each primitive direction, and the dislocation lines are aligned in the $[1\bar{1}2]$ direction on the (110) face. Initially, only one order parameter, ϕ_1, is non-zero, and ϕ_2 and ϕ_3 are set to zero. In both the screw and edge case, the dislocation dipoles are separated by $64b$, and the dislocations are infinitely long due to periodic boundary conditions.

These dislocations are then studied under an applied stress to determine the critical stress to move them. A pure shear stress is applied in one of three orientations, such that the maximum resolved shear stress plane (MRSSP) corresponds to the (110) habit plane or one of the two cross slip planes, $(01\bar{1})$ and (101). In each case, starting from zero, the stress is increased in increments of 0.001μ. The stress at which the dislocation glides (the supercritical stress) and the previous stress value at which it does not (the subcritical stress) were determined.

Last, the expansion of a dislocation loop is simulated under a shear stress in order to study the screw/edge dependent glide. The initial dislocation loop is a perfect circle with radius $16b$, and 128 grid points were used in each primitive $\boldsymbol{e}_1$, $\boldsymbol{e}_2$, and $\boldsymbol{e}_3$ direction. The entire loop is placed on the (110) plane, which, again, is considered its habit plane.

4.3 Results

4.3.1 Dislocation Core Structures

Fig. 4.1 shows the calculated core structures of the edge and screw dislocations under zero stress from both constrained and unconstrained PFDD. In all cases, from the initial unrelaxed state, the cores of the edge and screw dislocations in their relaxed state have spread. In constrained PFDD, spreading is confined to the the (110) plane, so both edge and screw dislocation cores are planar. When unconstrained PFDD is used, however, the cores spread not only on the habit (110) plane but also onto the $(01\bar{1})$ and (101) planes, as shown by the non-zero order parameters ϕ_2 and ϕ_3 in Fig. 4.1.

For the screw dislocation, the ϕ_2 and ϕ_3 fields in the core indicate core spreading on the $(01\bar{1})$ and (101) planes, forming small fractional dislocations [142, 147]. These dislocations on the two cross slip planes are nearly symmetric to one another, as the order parameters ϕ_2 and ϕ_3 are similar when reflected across the (110) habit plane. The habit plane remains clear as the order parameter ϕ_1 transitions from 1 to 0 at the dislocation core, indicating that the dislocation spreads predominantly on the (110) plane.

For the edge dislocation, changes in ϕ_2 and ϕ_3 vary predominantly in the $y = 0$, plane, the (110) slip plane, and the magnitudes of these two order parameters are nearly identical. Again, the dislocation can lower its strain energy slightly by forming small, fractional dislocations. However, unlike the screw dislocation, the edge dislocation with line direction $[1\bar{1}2]$ only lies in the (110) slip plane, so its spread is limited even in unconstrained PFDD. The newly formed fractional dislocations represented by ϕ_2 and ϕ_3 lie only within the (110) plane and represent small amounts of slip in the Burgers vector direction but on planes other than the (110). The line direction of the screw dislocation, $[\bar{1}11]$, lies in all three potential slip planes. Therefore, in unconstrained PFDD, the core of screw dislocation is non-planar and exhibits mirror symmetry about the (110) habit

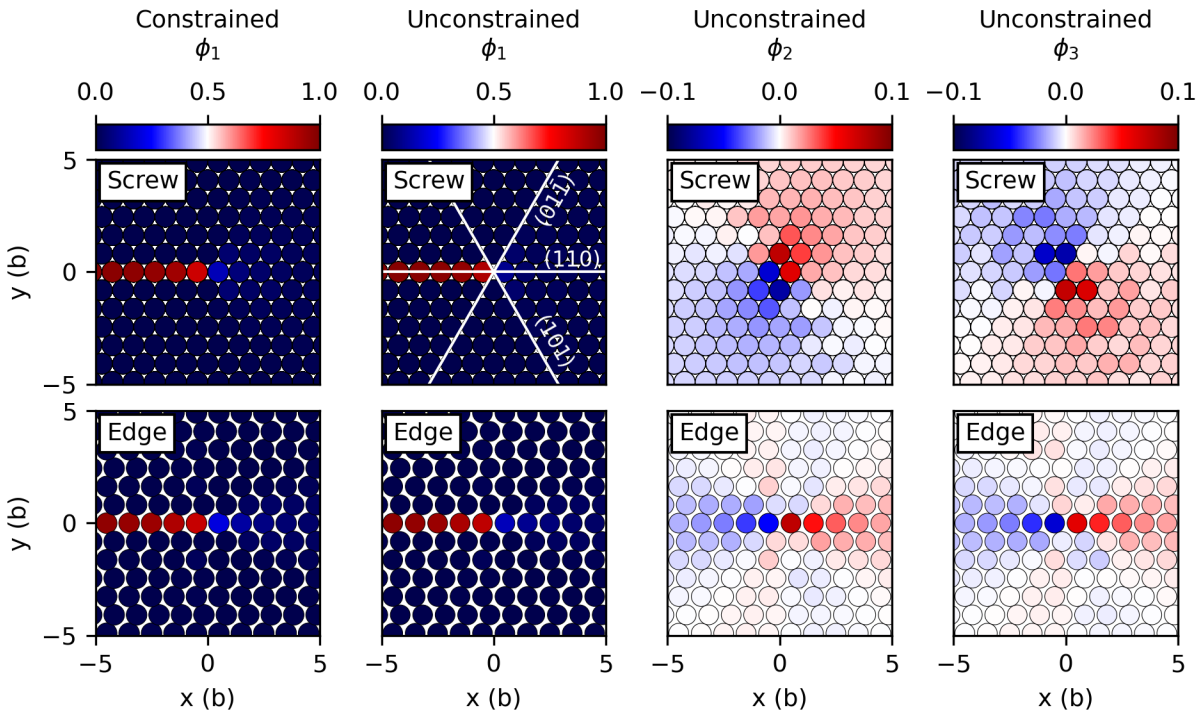

Figure 4.1: The order parameter fields of the dislocation core under zero stress in both the constrained (leftmost column) and unconstrained (three rightmost columns) PFDD models. The x-direction aligns with $[1\bar{1}2]$ and $[\bar{1}11]$ for the screw and edge cases, respectively. The y-direction is the slip plane normal [110] for both cases.

plane, while that of the edge dislocation is planar. Non-planar screw core structures are consistent with those calculated from atomistic calculations of dislocation cores [147].

The core structures for BCC dislocations, especially BCC screw dislocations, are distinct from core structures in close-packed crystals. Dislocations in both FCC and HCP crystals dissociate into partial dislocations, which can be observed experimentally [169], in atomistic simulations [170, 171], and in PFDD simulations [105, 172]. The partial dislocations form due to a local energy minimum in the generalized stacking fault energy surface [172]. As the GSFE surfaces for BCC crystals do not have a local minimum, the dislocation cores remain compact [173]. Unlike dissociated dislocations in close-packed crystals, the compact BCC screw dislocation line therefore lies in multiple slip planes,

allowing for the out-of-plane core spreading predicted from atomistic calculations and seen here in unconstrained PFDD simulations. This makes the use of unconstrained PFDD instead of constrained PFDD especially important for BCC materials.

The elastic strain fields produced by these dislocations are examined, beginning with the screw dislocation. Fig. 4.2 shows the out-of-plane σ_{xz} and σ_{yz} shear stress fields of a relaxed screw dislocation calculated by both PFDD formulations. For reference, these fields are compared with the those predicted from linear elastic isotropic dislocation theory, which does not take into account the configuration of the core. The stress fields calculated with PFDD qualitatively match the analytical solution. The stresses are most intense near the core and decay in magnitude when moving away from it and the regions of positive and negative stress are the same. The σ_{xz} stresses show Gibbs oscillations in the $[11\bar{1}]$ direction. These are Gibbs oscillations, which arise due to the difficulty of representing a discrete peak in Fourier space and have been observed in PFDD previously [167].

The magnitudes of the screw dislocation stress fields calculated with the unconstrained PFDD model are different from those of the analytical model and the constrained PFDD model. The non-planar core, spread on multiple planes, has weakened the stress field produced outside of the core. The Burgers vector is represented by a distribution of small fractional dislocations on the $(01\bar{1})$ and (101) planes. Compared to the constrained case with the planar core, the elastic σ_{xz} component has reduced by half and the σ_{yz} component by two-thirds, highlighting the significant effect of core spreading on the local stress fields. The Gibbs oscillations are present in both unconstrained and constrained PFDD, and their scaling with respect to the magnitude of the stresses is unchanged.

Fig. 4.3 compares the in-plane σ_{xx}, σ_{yy}, and σ_{xy} relevant for edge dislocations. As for the screw dislocations, the stress fields generated by the edge dislocation qualitatively

agree with those predicted by the linear elastic isotropic solution. The PFDD solution again displays Gibbs oscillations, especially in the σ_{xx} stresses. Like the screw case, the magnitude of the dislocation stress field is slightly reduced in the unconstrained case relative to the constrained case, but these differences are not as pronounced. The maximum σ_{xx} is only 1.10x higher in the constrained case, and σ_{yy} and σ_{xy} are 1.15x and 1.16x higher, respectively. Because the edge dislocation cannot spread onto multiple {110}-type slip planes, it is less affected by the choice of constrained or unconstrained PFDD.

In the analytical model of a compact dislocation line, the elastic line energy for a screw dislocation is lower than that for an edge dislocation. The line energy calculation involves integrating the elastic strain energy outside a small nanometer-sized radius around the dislocation. Since in PFDD, the model is built on linear elasticity, the entire dislocation is included in the calculation. The line energies of the relaxed dislocations in PFDD were calculated by integrating Eq. (1.4) within a cylinder of radius $28b$ around the dislocation core. The line energy per Burgers vector for the screw dislocation is $0.188\mu b^2$ and $0.0591\mu b^2$ for constrained and unconstrained PFDD, respectively. By allowing spread on multiple slip planes in unconstrained PFDD, the screw dislocation is able to lower its line energy by more than a factor of three. For the edge dislocation, the line energies are $0.291\mu b^2$ and $0.240\mu b^2$ for constrained and unconstrained PFDD, respectively. The small amount of spreading of ϕ_2 and ϕ_3 within the (110) plane in unconstrained slightly lowers the line energy, but not nearly as significantly as the screw dislocation case. Like the result from the analytical model, edge dislocations have a higher line energy than screw dislocations in both constrained and unconstrained PFDD.

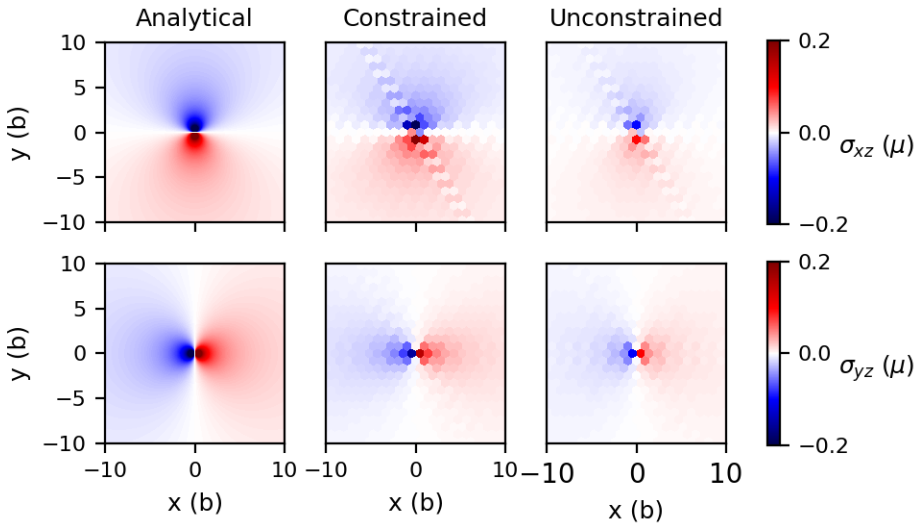

Figure 4.2: Stress fields generated by a screw dislocation as calculated from the constrained and unconstrained PFDD models compared to those from the linear elastic isotropic analytical solution. The x- and y-directions align with $[1\bar{1}2]$ and [110], respectively. The magnitude of the stresses near the core is reduced in the unconstrained PFDD due to core spreading.

4.3.2 Dislocation Glide and Cross Slip

The core structures of these dislocations will affect the stresses needed to move them and keep them in motion. The critical stresses to initiate glide of these dislocations were calculated using both the constrained and unconstrained PFDD. Table 4.1 presents the stress range within which the critical stress for dislocation glide lies. Ranges marked with † indicate dislocations that cross slip off the habit plane and glide on the plane corresponding to the MRSSP.

When the MRSSP is the habit plane, the applied stress is the Schmid stress. For both edge and screw dislocations and in both formulations, the dislocations glide in the (110) plane, provided the Schmid stress exceeds a critical value, given in Table 4.1. The core structures of these dislocations do not change during glide. For both constrained and unconstrained PFDD, the screw to edge ratio for glide stress is approximately 1.8.

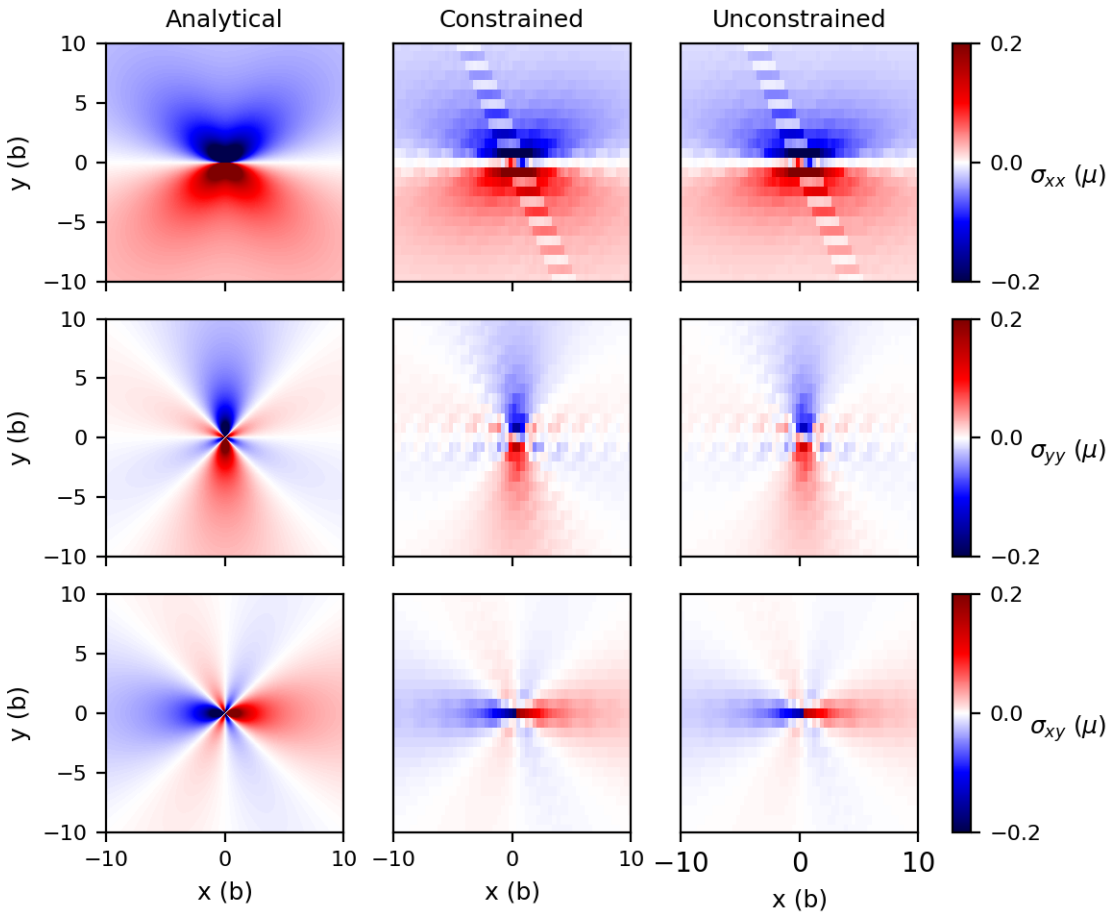

Figure 4.3: Stress fields generated by an edge dislocation as calculated from the constrained and unconstrained PFDD models compared to those from the linear elastic isotropic analytical solution. The x- and y-directions align with $[\bar{1}11]$ and $[110]$, respectively.

Table 4.1: Critical shear stresses required to initiate dislocation glide for different states of applied stress in units of μ, the effective elastic shear modulus. The maximum resolved shear stress plane (MRSSP) was either the (110) habit plane or one of the two cross slip planes, $(01\bar{1})$ and (101). The dislocations glide within the (110) habit plane except those marked with a †, which cross slip off the habit plane.

	Screw		Edge	
MRSSP	Constrained	Unconstrained	Constrained	Unconstrained
(110)	0.063-0.064	0.106-0.107	0.035-0.036	0.060-0.061
$(01\bar{1})$	0.126-0.127	0.131-0.132†	0.070-0.071	0.136-0.137
(101)	0.126-0.127	0.129-0.130†	0.070-0.071	0.129-0.130

The higher critical stress for screw compared to edge is commonly predicted from many PN models and molecular statics and results from the wider core for the edge than screw dislocations. The critical stress for screw and edge dislocation motion when the MRSSP is the (110) habit plane in unconstrained PFDD is, however, higher by 68% and 70% than those in constrained PFDD. The enhancement is due to the spreading of the dislocation cores onto multiple parallel or non-planar planes, outside of the habit plane in unconstrained PFDD (see Fig. 4.1). For both the screw and edge dislocations, non-zero values of ϕ_2 and ϕ_3 are present in the unconstrained case, which represent slip on the $(01\bar{1})$ or (101) planes and make dislocation glide more difficult on the (110) habit plane.

When the MRSSP corresponds to either the $(01\bar{1})$ or (101) plane, then the applied stress is considered a non-Schmid stress. In constrained PFDD, both the screw and edge dislocations glide on the (110) habit plane, even when the applied stress is non-Schmid. The non-Schmid stresses, however, need to be twice as high as the Schmid stress to initiate glide. The double enhancement is expected based on the orientation relationship between either cross slip plane and the habit plane.

In unconstrained PFDD, the response to a non-Schmid stress depends on the dislocation screw/edge character. The edge dislocation either remains sessile or glides in the (110) habit plane provided the applied stress is sufficiently high. The edge core, while

spread, is still planar, with non-zero values of ϕ_2 and ϕ_3 mostly lying within the (110) plane. It would be impossible for this core to cross slip onto the MRSSP. The screw dislocation, on the other hand, cross slips onto the MRSSP. The critical value of the non-Schmid stress for cross slip is more than twice the critical value of the Schmid stress for it glide within its habit plane. Cross slip is enabled as a consequence of the non-planar core structure of the screw dislocation (Fig. 4.1). Fig. 4.4 shows the order parameters after a dislocation cross slips from the (110) plane to the (101) plane. Values where the order parameter is one or more indicate slipped regions due to glide of a dislocation. Accordingly, cross slip is observed where the trail of grid points with $\phi_1 = 1$ stops, and a new trail of grid points with $\phi_3 = 1$ begins. At this intersection point, a right-handed $[\bar{1}11](110)$ screw dislocation oriented in the $[\bar{1}11]$ direction meets with a net zero pair of left-handed $[1\bar{1}\bar{1}](101)$ and right-handed $[\bar{1}11](101)$ screw dislocations. The first two dislocations annihilate and the remaining right-handed $[\bar{1}11](101)$ screw continues gliding on the (101) plane. As the screw dislocation glides away, the local plastic strain at the intersection is zero due to the opposite character of the two dislocations at that point. However, the lattice energy (Eq. (1.9)) is independent for each slip system, and therefore does not cancel, leaving a residual non-zero lattice energy at the intersection line. A different form of the lattice energy that combines slip from multiple planes, similar to that developed by Zheng et al. for FCC crystals [165], would be required for the lattice energies to cancel.

As expected in actuality, the PFDD model predicts the ability of screw dislocations to cross slip and edge dislocations to not cross slip. Importantly, the unconstrained PFDD formulation naturally accounts for this screw-edge difference through its calculation of the minimum energy core structure and not by rules or calculations of the dislocation character.

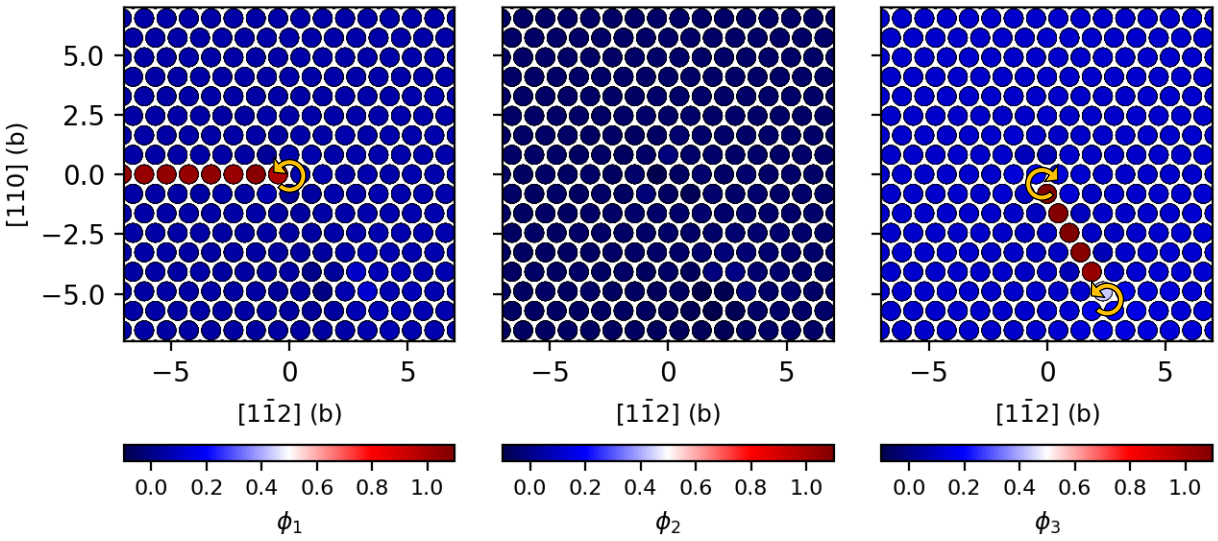

Figure 4.4: Cross slip of a screw dislocation from the (110) plane to the (101) plane. The arrows show the sense of the screw dislocations for each slip system.

4.3.3 Expansion of a Dislocation Loop

The foregoing study analyzes the effects of model formulation on the critical stresses to initiate glide of an originally stationary dislocation. Both formulations reveal a significant screw-edge character dependence in both the core structures and critical glide stresses. Next, the effects of the formulation on the glide resistance of an already moving dislocation are studied. Considering the known influence of dislocation character, the expansion of a dislocation loop, which bears all characters, is simulated using both formulations.

Fig. 4.5 shows the resulting loop shapes under an applied shear stress $\sigma = 0.12\mu$ at different time steps. In constrained PFDD, the dislocation loop expands into an oval shape as screw segments glide at a slightly slower rate than edge segments. The elongation of the screw portions over the non-screw portions can also be expected since the non-screw portions have higher line energy. As shown in the inset, the elongated

portion is curved and not pure screw. In unconstrained PFDD, the differences between the mobility of the edge and screw segments are much more pronounced. The non-planar screw cores are much more difficult to move than the planar edge cores, leading to a more oblong shaped loop than in the constrained case. Unlike in the constrained case, the screw segments are long and straight. While the edge and mixed character portions of the loop are able to glide continuously, with segments several Burgers long advancing together, the screw dislocation portion of the loop will only advance a 1-2 Burgers vector long segment at a time. This segment then grows outwards as the newly formed edge segments glide quickly along the length of the screw dislocation. This is indicative of a kink-pair nucleation and migration mechanism for screw dislocations in unconstrained PFDD. Experimental observations of dislocations in deformed BCC metals have often reported predominance of screw-type dislocations and when in motion, these segments are known to move via kink-pair nucleation and migration [8, 144, 174, 175]. Compared to constrained PFDD, unconstrained PFDD evidently offers a much better representation of the mechanisms of dislocation motion in BCC materials.

In Fig. 4.5, in unconstrained PFDD, the dislocations behave differently depending on their character. Non-screw dislocation motion is smooth, while screw dislocation motion is jerky in time. This staggered motion can be characterized by relatively long waiting times between kink-pair formation compared to the time required to form and migrate the kink-pair. When the applied stress increases from 0.12μ to 0.13-0.17μ, all portions of the loop move smoothly. The screw portions still move by the kink-pair mechanism but the waiting time between kink-pair formation becomes comparable to the time the kink-pair forms and migrates, leading to steady-like motion.

To compare glide rates for screw and edge segments, the loop calculations are compared at the higher applied stresses, 0.13-0.17μ, at which all portions of the loop move in a smooth manner. In each simulation, the velocity v of the screw and edge dislocation

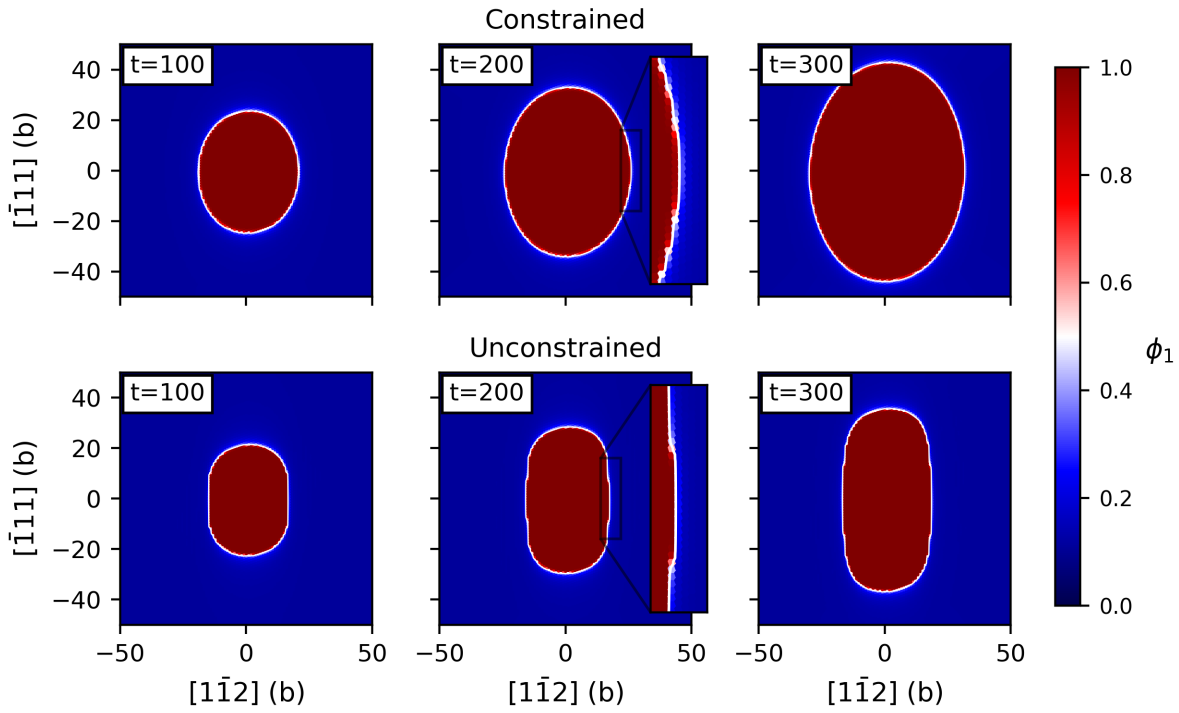

Figure 4.5: Expansion of a dislocation loop in both the constrained and unconstrained PFDD models. The dislocation line where $\phi_1 = 0.5$ is outlined in white. Both loops have a Burgers vector equal to $\frac{a}{2}[\bar{1}11]$. The unconstrained case exhibits more screw-edge anisotropy because of the slower glide of the screw dislocation resulting from its non-planar core. The insets show the differences in screw dislocation morphology in the two cases. The applied stress is 0.12μ.

portions is calculated as the change in radius of the loop in the $[1\bar{1}2]$ and $[\bar{1}11]$ directions per timestep, respectively. Given v, the corresponding numerical drag coefficient B can be calculated

$$B = \frac{\sigma b}{v} \tag{4.1}$$

where σ is the resolved shear stress in the slip plane. The parameter B has units of $1/m_{disl}$, where m_{disl} is the kinetic coefficient in Eq. (1.8). Below, it is verified that B is independent of the choice of m_{disl}, by repeating the calculations using $m_{disl}\Delta t = 0.2\ \mu^{-1}$ and $m_{disl}\Delta t = 0.3\ \mu^{-1}$ in the minimization. Fig. 4.6 compares B for the constrained and unconstrained PFDD. In both cases, the screw segments of the loop have a much higher B than the edge segments. It is worth noting that B correspond to athermal values. Temperature generally tends to increase drag, so the B found here could be considered practical lower bounds on drag resistance.

Fig. 4.6B studies the changes in the screw-to-edge B ratio with applied stress. In constrained PFDD, the ratio ranges narrowly from 1.82 to 2.09, increasing slightly with stress. These screw-to-edge drag ratios are comparable to 1.8, the screw-to-edge critical stress ratio to initiate motion of a straight dislocation. The screw/edge character dependence in static and dynamic resistance is maintained. Interestingly, in unconstrained PFDD, the drag ratio is much larger than the screw-to-edge critical stress ratio and is sensitive to the applied stress. The screw-to-edge drag ratio is 4.53 at 0.13μ, approximately two to two and a half times higher than the critical stress ratio and decreases to 3.36 at 0.17μ. The dislocation character dependence is accentuated when dislocations are dynamic and carrying plasticity, which is arguably just as, if not more, important than when they are static.

The screw-to-edge dislocation drag ratios reported in the literature vary widely from

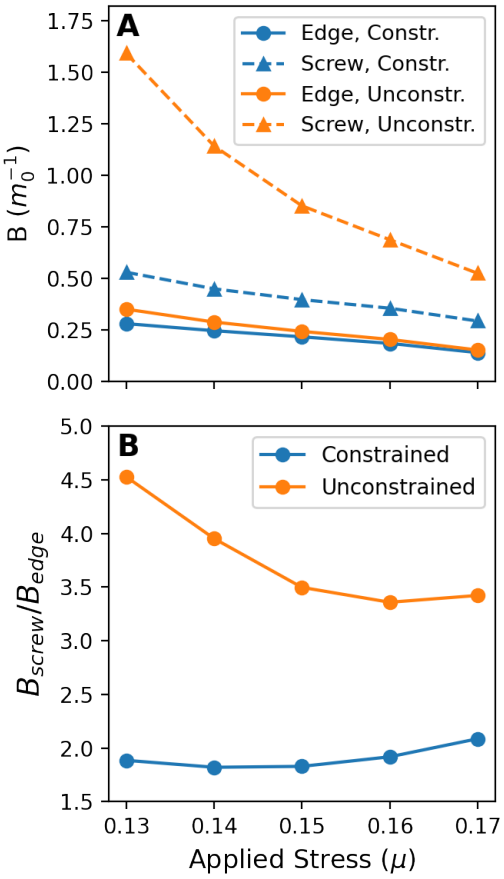

Figure 4.6: (A) The numerical drag coefficients calculated from the dislocation loop velocity simulations. (B) The ratio of the screw and edge numerical drag coefficients for both the constrained and unconstrained cases.

near unity to several orders of magnitude, depending on both applied stress and temperature [176–180]. Experimental measurements of Fe, K, and Nb at low temperatures give relatively small ratios between 1 and 2 [177, 178]. As temperature is increased to intermediate temperatures, this ratio tends to increase dramatically as edge dislocation glide becomes easier relative to screw [176, 180].

It is important to verify that the calculated B is independent of the chosen numerical value of m_{disl}. The calculated dislocation velocity, measured in Burgers vectors per timestep, depends on m_{disl} through the Ginzburg-Landau equation. This in turn affects

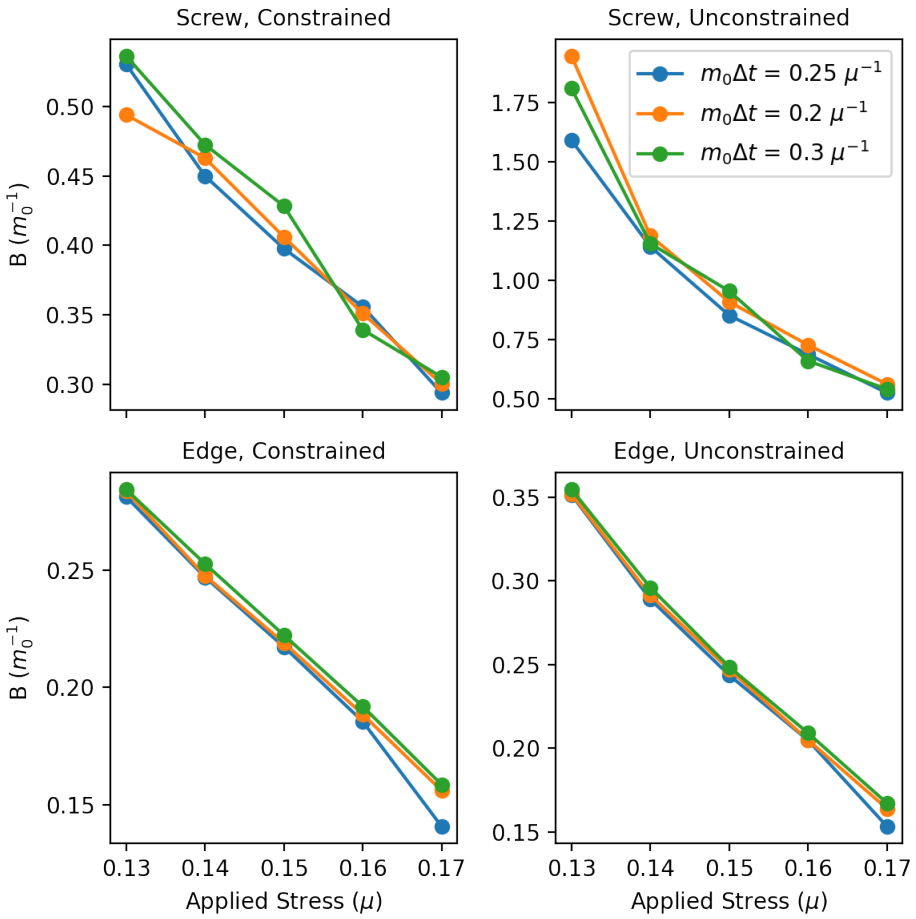

Figure 4.7: The drag coefficients for each dislocation type calculated with different values of $m_{disl}\Delta t$

the drag coefficient B (Eq. (4.1)). To ensure that the drag results presented here do not depend on the magnitude of m_{disl}, the same loop simulations in as in were repeated using $m_{disl}\Delta t$ equal to 0.2 μ^{-1}, 0.25 μ^{-1}, and 0.3 μ^{-1}. Fig. 4.7 shows the calculated numerical drag coefficients for both dislocation characters in both constrained and unconstrained PFDD. When normalized by $1/m_{disl}$, the results are consistent across each of the three values of $m_{disl}\Delta t$ tested. Small discrepancies, especially in the screw dislocation drag at lower applied stresses, are due to the jerky nature of screw glide at these stresses and therefore the inexact calculations of the glide velocity.

4.3.4 Cross Slip Around an Obstacle

In addition to the resistances to initiate and sustain motion, the ability of a dislocation to cross slip can affect macroscopic behavior. When a dislocation encounters an obstacle in its glide plane, cross slip allows the dislocation to bypass the obstacle and continue gliding. Earlier, it was demonstrated that a stationary screw dislocation can potentially cross slip provided that the applied MRSSP coincides with the cross slip planes and the amount of shear is sufficiently high, while an edge dislocation under the same driving force could not, regardless of the amount of shear. Here, unconstrained PFDD model is used to consider the propensity for a screw dislocation already in motion in its habit plane to cross slip when it encounters an obstacle in its habit plane. In this event, whether the screw dislocation cross slips should depend on the strength of the obstacle with all else being the same.

Fig. 4.8A shows the initial model set up. The simulation cell consists of a $[\bar{1}11](110)$ screw dislocation dipole with $32b$ spacing. The cell size is much larger, with dimensions 128, 4, and 256 grid points in each of the primitive cell directions $\boldsymbol{e}_i, i = 1, 2, 3$. In the path of the dislocation, a coherent crystallographic cylindrical precipitate with radius $8b$ is inserted, centered about the (110) plane. Its peak lattice energy, USFE, is greater than that of the surrounding Nb, making it much more resistance to slip transmission by the approaching dislocation. For a *weak* obstacle, the precipitate has a USFE 1.1 times that of Nb and for a *strong* obstacle, 1.25 times that of Nb.

A shear stress of 0.16 μ is applied to the $(12\bar{1})$ plane, which results in equivalent resolved shear stresses on the habit (110) plane and the $(01\bar{1})$ cross slip plane. Fig. 4.8A-F show the path taken by the screw dislocation for both the weak and strong obstacles, respectively. Initially, the dislocation glides on the habit plane in both cases. In the case of a strong obstacle, when the dislocation encounters the obstacle within the glide

plane, it cross slips onto the $(01\bar{1})$ plane, avoiding the obstacle. In the case of the weak obstacle, it does not cross slip but rather transmits through the precipitate, shearing it and continuing to glide on the (110) plane. As both of these simulations used the same stress conditions, the differences in dislocation behavior are due solely to the differing strengths of the obstacles.

A similar simulation is repeated for an edge dislocation. Fig. 4.8G-L present snapshots during the interaction between an edge dislocation and two obstacles with different strengths. Under the same stress conditions as above, the edge dislocation glides on the habit plane and shears through the precipitate when the obstacle USFE is 1.1x or 1.25x that of Nb, as in the screw simulations. When the strength of the obstacle is increased by making its USFE twice that of Nb, the dislocation is no longer able to shear the obstacle and becomes pinned at the boundary of the obstacle. Since the edge dislocation cannot cross slip, no further plastic strain can be accommodated.

4.4 Discussion

Prior PFDD simulations of BCC materials used a correction to the lattice energy term to account for differences between edge and screw dislocation glide [84, 97]. This correction scaled down the barrier for edge dislocations relative to screw dislocations in order to make their glide easier. Here, by using unconstrained PFDD, substantial differences in the drag between edge and screw dislocations are fundamentally accounted for through a more accurate representation of their core structures. These differences can cause screw-character dislocations to move by kink-pair formation and migration. In the standard formulation, kink-pairs would need to be inserted or promoted by introduction of a locally weak region. Last, note that the stresses associated with kink-pair formation and cross slip events reported here correspond to athermal values; both kink-pair forma-

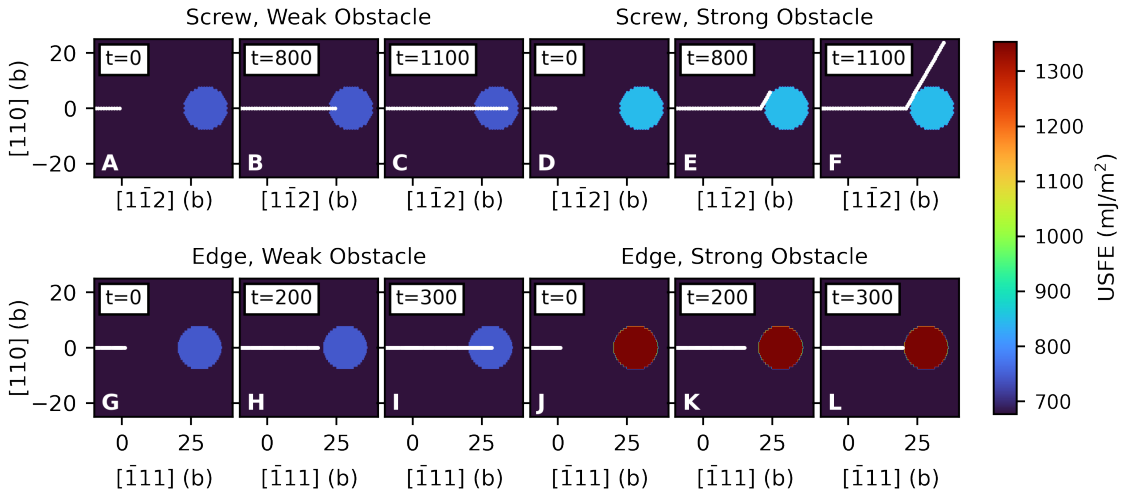

Figure 4.8: The interaction of dislocations in Nb with a cylindrical obstacle that has a higher local USFE than Nb. The underlying color corresponds to the local USFE, and the white line traces the path of the dislocation where the order parameters exceed 1. When the obstacle USFE is only 1.1x that of Nb, both the edge and the screw dislocation are able to shear the obstacle. When the obstacle has a USFE 1.25x that of Nb, the screw dislocation cross slips to avoid the obstacle. When the obstacle has a USFE 2x that of Nb, the edge dislocation becomes pinned and cannot cross slip.

tion and cross slip are known to be aided by thermal energy, so increases in temperature can help to overcome the barriers for kink-pair nucleation and cross slip.

This simple example of cross slip around a high-USFE obstacle shows how this model can be used to understand more complex dislocation dynamics. For example, cross slip of a portion of the dislocation line can create dislocation sources, increasing work hardening. Cross slip can also aid in dynamic recovery by allowing for dislocation annihilation. Future applications of unconstrained PFDD could include more complex dislocation motion and interactions, such as cross slip around other dislocations or an elastically misfitting obstacle.

4.5 Conclusion

PFDD was extended to model the character-dependent core structure and dislocation cross slip in a BCC material by employing a non-orthogonal BCC grid and making available multiple non-planar glide planes within the formulation. Compared to the original planar formulation, this model captures the low-energy, non-planar core structure of screw dislocations. The differences in core structure between edge and screw dislocations results in a higher degree of edge-screw glide anisotropy, leading to slower screw dislocation glide and more elongated dislocation loops. Using the new PFDD model, screw dislocations can move via kink-pair nucleation and when encountering a sufficiently strong obstacle can cross slip. Most importantly, these outcomes occur in these simulations without including any rules or correction terms. This model can be applied to more accurately study the glide and cross slip of dislocations in BCC crystals, including multi-component alloys.

Chapter 5

Short-range order [†]

5.1 Introduction

Chemical SRO, defined as the local preferential bonding of certain atom types, can exist in alloys that are otherwise disordered and have no long-range order [183]. SRO has been studied extensively in the context of binary alloys for decades [183–188]. There is renewed interest in SRO due to the emergence of MPEAs, which contain thermodynamically driven SRO [1, 29–31, 33–37, 39, 189–194].

SRO can play a role in the material properties of alloys. Fisher first proposed the idea of SRO strengthening in 1954, positing the presence of SRO would increase the dislocation glide stress due to the creation of a disordered interface as the dislocation disrupts the SRO [184]. Further studies have shown that dislocation behavior is influenced by SRO in both binary alloys [186] and MPEAs [20, 39, 123, 194–196]. With the possibility to

[†]This chapter adapted from Reference [181]: Fey, L. T. W., & Beyerlein, I. J. (2022). Random Generation of Lattice Structures with Short-Range Order. Integrating Materials and Manufacturing Innovation, 1-9. and Reference [182]: Zheng, H., Fey, L. T. W., Li, X. G., Hu, Y. J., Qi, L., Chen, C., Xu, S., Beyerlein, I. J., & Ong, S. P. (2022). Multi-scale Investigation of Chemical Short-Range Order and Dislocation Glide in the MoNbTi and TaNbTi Refractory Multi-Principal Element Alloys, npj Computational Materials, Under Review.

control SRO via processing comes the exciting potential to tune SRO and thus mechanical properties [30].

To model SRO, it must first be quantified, which is typically done via the Warren-Cowley (WC) parameters [183, 197], defined as

$$\alpha_{ij}^{k} = (p_{ij}^{k} - c_j)/(\delta_{ij} - c_j) \tag{5.1}$$

where α_{ij}^{k} is the WC parameter for the i-j pair type in the k-th nearest neighbor shell, p_{ij}^{k} is the probability that an atom is a j-type atom in the k-th nearest neighbor shell of an i-type atom, c_j is the overall concentration of type j, and δ_{ij} is the Kronecker delta. The WC parameter is zero for completely random alloys with no SRO. Positive WC parameters indicate preferred and non-preferred bonding pairs for like and unlike pairs, respectively, with the opposite being true for negative WC parameters. The WC parameters for chemical or magnetic SRO are generally temperature dependent, as SRO tends to increase with decreasing temperatures.

WC parameters are typically calculated with Monte Carlo (MC) methods, which involve randomly swapping atoms according to an energy criterion until equilibrium is reached. The energies can be calculated from atomistic methods, usually either DFT or MD. DFT is considered to be the more accurate of the two. However the system sizes used in most MC-DFT calculations of SRO are extremely limited, including about 100-200 atoms [30, 31, 37, 198, 199] with traditional methods or about 1000 atoms with cluster expansion methods [31, 35]. MC-MD simulations, on the other hand, require the creation of a classical potential, which leads to relatively less accurate calculations, but can use 1-3 million atoms [39, 123, 188, 200–203]. This system size approaches that required to study more complex material behaviors such as dislocation glide, but equilibrating the structures with MC-MD to introduce SRO is computationally intensive and can limit the

size and number of simulations [39, 201]. This limitation can be problematic in MPEAs where the properties are known to be highly probablistic and many iterations of the same simulation are desired [13, 132].

In this chapter, a new method is developed to generate large lattice structures with SRO. The method, Order Through Informed Swapping (OTIS), uses known WC parameters as input, and then starting from a completely random lattice, uses MC-like swapping to find a structure with the desired WC parameters. In this way, the computationally expensive MC-DFT or MC-MD calculations only need to be performed once using a smaller, tractable cell size. The WC parameters are then extracted and used to create unlimited lattices of any size that can be used as inputs to atomistic or mesoscale models. The flexibility of OTIS is demonstrated by creating lattices with SRO for two different BCC ternary MPEAS, one FCC ternary MPEA, and two BCC quinary MPEAs.

The lattices are then incorporated into a multiscale modelling approach to investigate the effects of SRO on dislocation behavior. A highly accurate atomistic potential is developed via machine learning for the Mo-Ta-Nb-Ti system [20, 204–207], and hybrid MC/MD are carried out for temperature-dependent SRO calculations to calculate the WC parameters, USFE values, and elastic constants for MoNbTi and TaNbTi. These two MPEAs are chosen since experimental observations find that their equimolar forms exhibit disparate mechanical properties, with the MoNbTi being substantially greater in tensile yield strength, peak strength and strain hardening than TaNbTi.

The values calculated from atomistics are input into PFDD simulations to predict stress-driven pathways taken by individual dislocations [208]. SRO strengthening manifests in both MPEAs, with the average USFEs and critical stresses to initiate and sustain propagation of dislocations increasing with SRO above those for the ideal random solid solution. SRO strengthening contribution scales linearly with degree of SRO. The calculations also reveal that gliding dislocations in subcritical conditions experience significant

hardening. This glide hardening is strongly correlated to the statistical dispersion in the local USFE, and since SRO tends to narrow the distribution in USFE, glide hardening decreases with degree SRO. In studying dislocation loop expansion across stress regimes, a transition between jerky and smooth dislocation glide is identified and related to stress sensitivity of kink-pair nucleation rates of the screw character portions. Finally, analysis reveals that initially screw- and edge-oriented dislocations will become wavy in glide yet move via different mechanisms—kink-pair formation and migration vs. pinning/depinning. Their individual glide mechanisms do not change with composition, amount of SRO, glide distance, or subcritical or overdriven loading conditions. These computations explain why MoNbTi is the stronger and has the greater strain hardening and forecasts that it is more amenable to SRO strengthening.

5.2 Generation of lattices with short-range order

5.2.1 Algorithm for creation of lattices with short-range order

Let n equal the number of component elements, c_i equal the concentration of type i, and α_{ij} equal the desired WC parameters in the first nearest neighbor shell. The simulation cell size is given in terms of the primitive vectors: $\boldsymbol{e}_1 = \frac{a}{2}[11\bar{1}]$, $\boldsymbol{e}_2 = \frac{a}{2}[\bar{1}11]$, and $\boldsymbol{e}_3 = \frac{a}{2}[1\bar{1}1]$ for a BCC lattice and $\boldsymbol{e}_1 = \frac{a}{2}[110]$, $\boldsymbol{e}_2 = \frac{a}{2}[011]$, and $\boldsymbol{e}_3 = \frac{a}{2}[101]$ for an FCC lattice. The cell dimensions are N_1, N_2, and N_3 in the directions $\boldsymbol{e}_1$, $\boldsymbol{e}_2$, and $\boldsymbol{e}_3$, respectively, for a total of $N = N_1 * N_2 * N_3$ lattice sites.

The OTIS algorithm is summarized in Figure 5.1. To begin, a lattice of the desired shape and size is created. The total number of nearest neighbor bonds will be $NZ/2$ where Z is the coordination number of the lattice. Given the probability p_{ij} of each bond type, which can be extracted from the WC parameters (Equation (5.1)), the desired number

of each bond type can be easily determined. The goal number of bonds is defined as an n x n matrix where each element is given by

$$g_{ij} = \frac{1}{2} N Z c_i p_{ij} \tag{5.2}$$

Each site is randomly assigned an initial element type, maintaining the desired overall concentration. The current bond numbers, which compose an n x n matrix denoted as c_{ij}, are calculated from this structure.

In each step of the OTIS algorithm, two unlike atoms are randomly selected, and, if the swap is favorable, swapped. Swapping is continued until $c_{ij} = g_{ij}$ for all pair types i-j. There are two major challenges with this method that need to be addressed. First, an acceptance criterion for swaps must be defined. Because the probabilities p_{ij} must sum to 1 for any atom type i and due to symmetry in g_{ij}, there are $n(n-1)/2$ constraints that must be met. There is only one value to optimize for a binary alloy, and this has been done previously for binary FCC lattices in the work of Gehlen and Cohen [209]. For MPEAs, the situation is more complicated. A swap that moves c_{ij} towards the goal g_{ij} for one pair type i-j may move other pair types further from the goal. For the entire structure, a distance d from the goal is defined as

$$d = \sum_{i,j} |c_{ij} - g_{ij}| \tag{5.3}$$

which gives the element-wise sum of the absolute difference of the current and goal matrices. During the swapping procedure, only swaps that lower d will be accepted. This means that all bond types are considered while swapping an i-type and a j-type atom, not just the i-j bond type.

The second challenge is how to choose atoms for swapping. As noted by Gehlen and Cohen, two atoms chosen completely at random are highly unlikely to be accepted for

a swap [209]. This causes a high rejection rate and an excessively long computation time to reach convergence. Instead, an informed, statistical swapping method is used by choosing from a subset of atoms that are more likely to give us an accepted swap. For each lattice site $\boldsymbol{x}$, define $\delta_{ij}^{\alpha}(\boldsymbol{x})$ as the change in c_{ij} if the atom at $\boldsymbol{x}$ is replaced by an atom of type α.

Now, let A-B be the atom pair to be swapped. First the A-type atom is selected. Instead of randomly choosing from all A-type atoms, an A-type atom is randomly selected from the subset of A-type atoms where $\sum_{i,j} |c_{ij} + \delta_{ij}^{B} - g_{ij}| < \sum_{i,j} |c_{ij} - g_{ij}|$. This means that the only A-atoms considered are those where d would be lower if a B-type atom were on that lattice site instead. If no A-type atoms that fit this criterion, the method reverts back to choosing from all A-type atoms. The chosen lattice site is denoted from either situation as x^A.

The next step is to choose the B-type atom, for which a similar procedure is used. Since x^A is known, it is included in the selection criterion. A B-type atom is randomly select from the subset of B-type atoms where $\sum_{i,j} |c_{ij} + \delta_{ij}^{B}(x^A) + \delta_{ij}^{A} - g_{ij}| < \sum_{i,j} |c_{ij} - g_{ij}|$. If there exists a site x^B that meets this criterion, the atoms at site x^A and x^B are swapped. If not, another unlike pair type is selected to swap and repeat the procedure. The pair types are rotated through sequentially (e.g. A-B, A-C, B-C, B-A, and so on) at each swapping step such that each pair type has an equal opportunity to be swapped.

After a pair of atoms is swapped, the current bond numbers c_{ij} are updated by adding $\delta_{ij}^{\alpha}(x^A)$ and $\delta_{ij}^{\alpha}(x^B)$ to c_{ij}. $\delta_{ij}^{\alpha}(\boldsymbol{x})$ must also be updated, but only for the two atoms that were swapped and their neighbors. With both, the maximum number of updates to δ_{ij}^{α} is $2(Z+1)$, a small fraction of the total size N.

The swapping process is repeated until c_{ij} is within some tolerance g_{ij} for pairs i-j. Here, a tolerance of $10^{-3}NZ/n$ is used. This gives final WC parameters within less than 1% of the desired WC parameters.

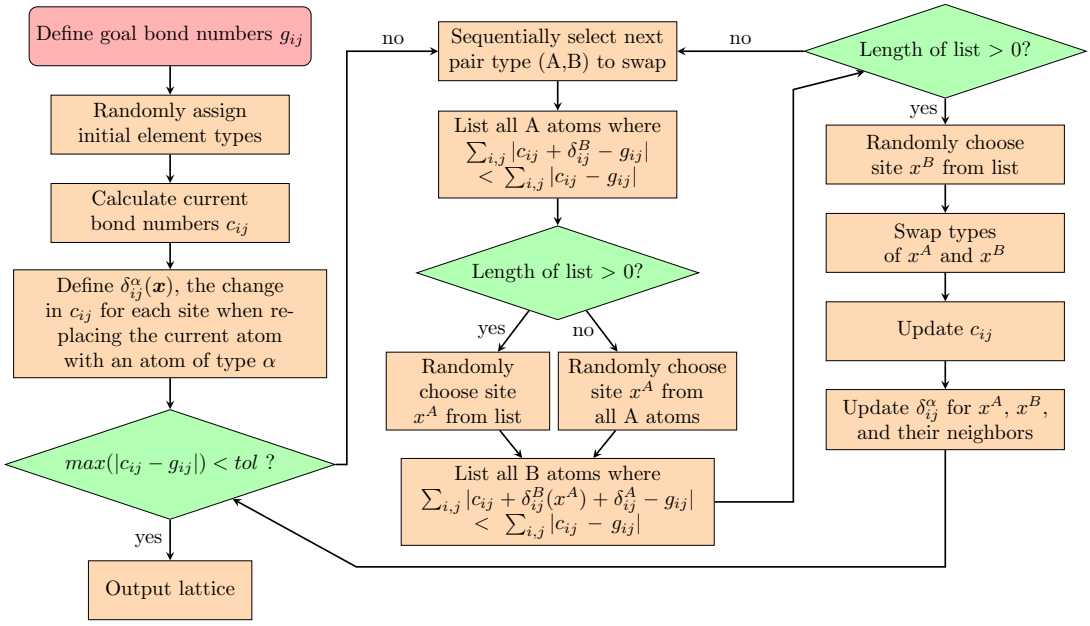

Figure 5.1: A flowchart showing the Order Through Informed Swapping (OTIS) algorithm

In the following section, OTIS is demonstrated by generating SRO lattices for several different MPEAs for which the WC parameters have been calculated previously, including MoNbTi, TaNbTi, CoCrNi, HfNbTaTiZr, and HfMoNbTaTi [39, 182, 210]. For each of these alloys, the WC parameters were calculated at multiple annealing temperatures with MC-MD using multi-component classical potentials, beginning with a random structure and performing MC until equilibrium is reached [123, 182]. The WC parameters at each temperature are listed in Tables 5.1 and 5.2. Considering the various alloy and temperature combinations sums to 16 unique sets of WC parameters. For each set, simulation cells are created with side lengths 16, 24, 32, 40, 48, 56, and 64, with 10 unique SRO lattices generated at each size. The software Ovito was used to visualize the lattices and confirm the correct numbers of each bond type [211].

MoNbTi						[182]
	Mo-Mo	Nb-Nb	Ti-Ti	Mo-Nb	Mo-Ti	Nb-Ti
300K	-0.338	-0.055	-0.121	-0.272	-0.405	0.162
1673K	-0.079	-0.012	-0.041	-0.049	-0.108	0.026

TaNbTi						[182]
	Ta-Ta	Nb-Nb	Ti-Ti	Ta-Nb	Ta-Ti	Nb-Ti
300K	0.109	-0.037	0.071	0.001	0.217	-0.076
1673K	0.025	-0.012	-0.010	0.023	0.026	-0.047

CoCrNi						[39]
	Co-Co	Cr-Cr	Ni-Ni	Co-Cr	Co-Ni	Cr-Ni
350K	-0.018	-0.108	0.470	-0.592	0.557	0.384
650K	-0.058	-0.123	0.363	-0.543	0.427	0.298
950K	-0.060	-0.116	0.163	-0.338	0.218	0.107
1350K	-0.068	-0.098	0.089	-0.256	0.119	0.059

Table 5.1: The Warren-Cowley parameters for calculated with Monte Carlo Molecular Dynamics for the ternary alloys.

HfNbTaTiZr								[210]
	Hf-Hf	Nb-Nb	Ta-Ta	Ti-Ti	Zr-Zr	Hf-Nb	Hf-Ta	
300K	-0.241	0.056	0.093	-0.199	-0.231	-0.250	-0.242	
600K	-0.082	0.013	0.087	0.075	-0.067	-0.138	-0.068	
900K	-0.052	0.007	0.059	0.047	-0.048	-0.088	-0.046	
	Hf-Ti	Hf-Zr	Nb-Ta	Nb-Ti	Nb-Zr	Ta-Ti	Ta-Zr	Ti-Zr
300K	-1.427	0.951	-0.151	0.964	-0.340	0.984	-0.221	-1.319
600K	-0.422	0.300	-0.127	0.471	-0.155	0.604	-0.059	-0.355
900K	-0.276	0.204	-0.086	0.306	-0.104	0.411	-0.039	-0.254

HfMoNbTaTi								[210]
	Hf-Hf	Mo-Mo	Nb-Nb	Ta-Ta	Ti-Ti	Hf-Mo	Hf-Nb	
300K	-0.171	-0.080	0.038	0.132	0.688	-0.606	-0.238	
600K	-0.124	-0.048	0.057	0.098	0.734	-0.627	-0.177	
900K	-0.108	-0.048	0.038	0.073	0.382	-0.441	-0.032	
	Hf-Ta	Hf-Ti	Mo-Nb	Mo-Ta	Mo-Ti	Nb-Ta	Nb-Ti	Ta-Ti
300K	-0.029	0.213	-0.275	-0.224	0.760	-0.167	0.832	0.942
600K	-0.067	0.384	-0.194	-0.206	0.827	-0.231	0.830	0.894
900K	0.028	0.014	-0.096	-0.131	0.470	-0.180	0.465	0.574

Table 5.2: The Warren-Cowley parameters for calculated with Monte Carlo Molecular Dynamics for the quinary alloys.

5.2.2 Random lattices

To compare the degree of SRO across multiple MPEAs and annealing temperatures, an SRO figure of merit Ω is introduced, defined as the quadratic mean of the WC parameters for unlike pair types:

$$\Omega = \sqrt{\frac{\sum_{i=1}^{n}\sum_{j=i+1}^{n}\alpha_{ij}^2}{n(n-1)/2}} \tag{5.4}$$

Only unlike pairs are included in this sum as this will include the $n(n-1)/2$ independent WC parameters, from which the WC parameters for the like pairs can be uniquely determined. By this definition, $\Omega = 0$ corresponds to no SRO, a completely random structure, and increases in Ω signify more extensive SRO.

To demonstrate the versatility of the OTIS method, three examples are presented with either BCC or FCC and either three (ternary) or five elements (quinary), all with relatively high values of Ω, which are expected to be the more difficult cases to create. Figure 5.2 shows the evolution of an equiatomic MoNbTi BCC lattice using the WC parameters from 300K ($\Omega = 0.469$) [182]. Starting from an initially random lattice, atoms are swapped using the OTIS algorithm until the desired SRO is achieved. The WC parameters from the final structure were recalculated by counting the number of each bond type with Ovito and confirmed to be within 1% of the prescribed WC parameters. This error can be decreased if desired by the lowering tolerance criteria. Figure 5.3 applies the OTIS algorithm to create an FCC equiatomic CoCrNi lattice structure using the WC parameters at 350K ($\Omega = 0.785$) [39]. For the same size, 32 x 32 x 32, the effect of increasing Ω from the BCC ternary to the FCC ternary is readily apparent by the clear regions of chemical segregation. Figure 5.4 shows an example lattice for the BCC quinary alloy HfNbTaTiZr using the WC parameters at 300K. Among the three examples, this one has the highest degree of SRO ($\Omega = 1.18$) [210]. Further, unlike the ternary alloys,

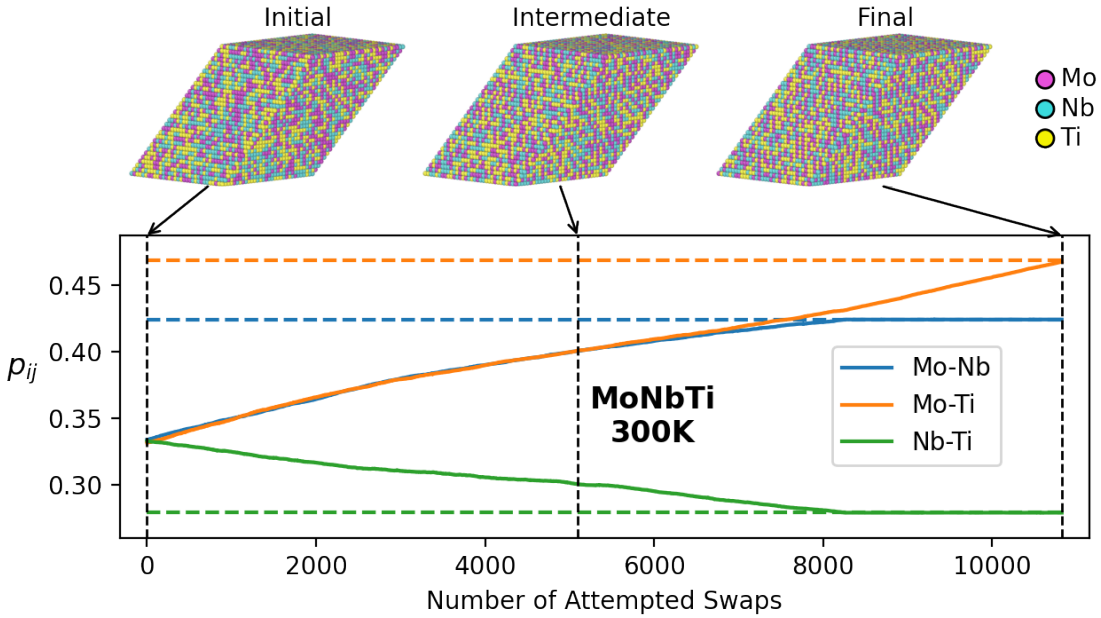

Figure 5.2: The creation of a 32 x 32 x 32 lattice for MoNbTi using the Warren-Cowley parameters at 300K. The solid lines show the current bond probabilies p_{ij} while the dashed lines show the goal probabilities.

which must meet three independent bond number constraints, a quinary alloy must meet 10. This case shows that because the OTIS algorithm takes into account all bond types when accepting or rejecting a move, it can still create a structure that meets the desired WC parameters despite the significant increase in bond number constraints.

Although all structures in Figures 5.2 to 5.4 have the same number of lattice sites (32768) and high degrees of SRO, the total number of attempted swaps required to reach the final goal varies widely, from about 11,000 to more than 47,000. To compare, the number of actual swaps are plotted in Figure 5.5A; that is, excluding the rejected swaps, to reach the desired WC parameter for all alloys, annealing temperatures (SRO degree), and a broad range of lattice sizes (number of lattice sites). The total number of swaps are averaged over the 10 SRO lattices generated for each alloy, size, and temperature. The

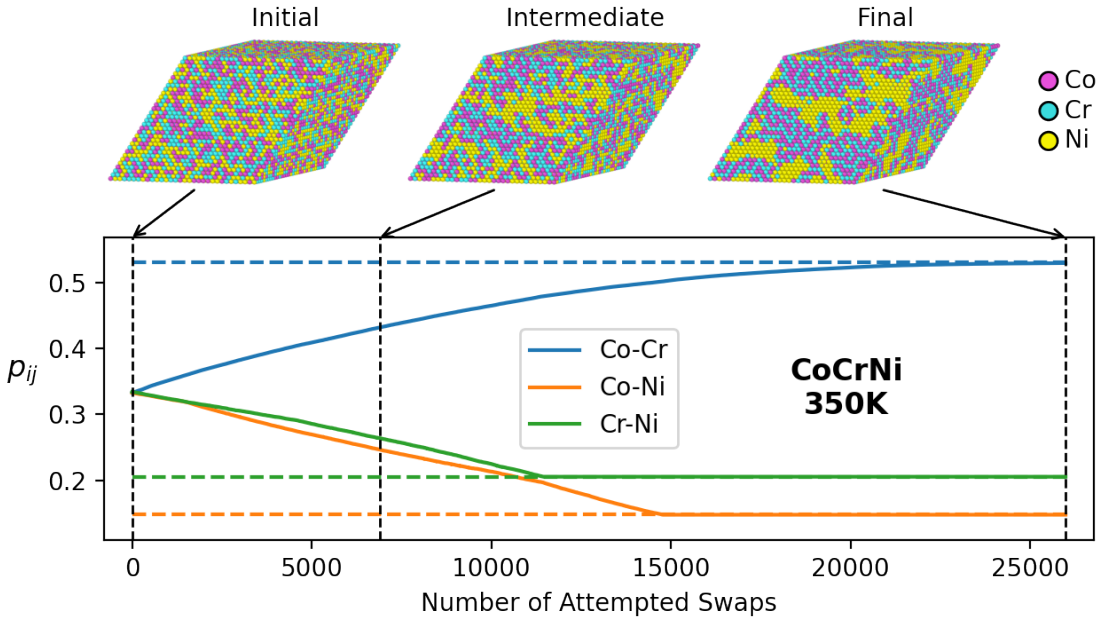

Figure 5.3: The creation of a 32 x 32 x 32 lattice for CoCrNi using the Warren-Cowley parameters at 350K. The solid lines show the current bond probabilies p_{ij} while the dashed lines show the goal probabilities.

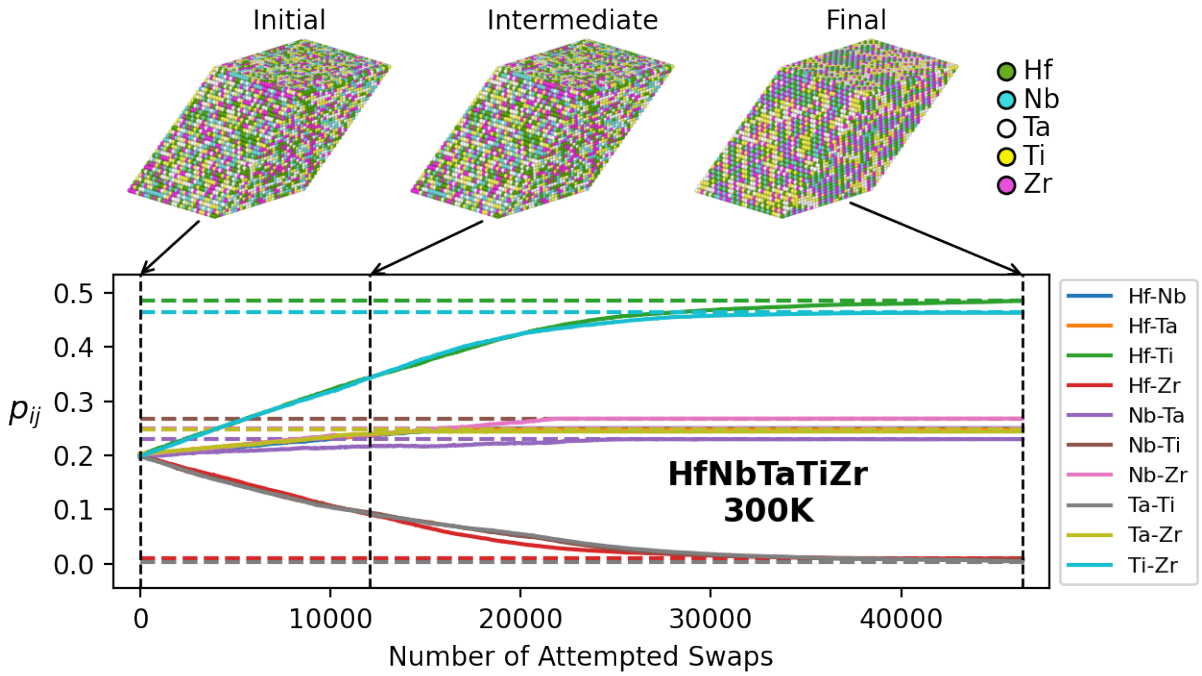

Figure 5.4: The creation of a 32 x 32 x 32 lattice for HfNbTaTiZr using the Warren-Cowley parameters at 300K. The solid lines show the current bond probabilies p_{ij} while the dashed lines show the goal probabilities.

number of swaps is linearly correlated with the total number of lattice sites, while the number of swaps per site depends on several intuitive factors. First, more extensive SRO, represented by higher values of Ω, increases the number of swaps required. Second, FCC lattices require more swaps than BCC lattices due to the higher coordination number and therefore higher number of bonds within the structure. Third, the quinary alloys tend to require more swaps than ternary alloys since there are more bond number constraints that must be met.

While OTIS uses informed swapping to identify bonds that are likely to be accepted, there are still instances when an iteration fails to find an acceptable pair and the swap is rejected. In all such cases, the initial acceptance rate, defined as the percentage of swaps accepted across all pair types, is 100% for the first few iterations of the algorithm. As individual pair types reach their goal bond numbers, it becomes more difficult to find an acceptable atom pair to swap, and the acceptance rate drops. This can be seen in Figures 5.3 and 5.4 when p_{ij} levels off as it approaches the goal numbers. The final acceptance rates range from 20% to 100%, and the acceptance rate does not appear to be sensitive to the system size, extent of SRO, or lattice type. In the cases tested here, the acceptance rate varies up to 46% when repeating the same OTIS simulation with a different random initial lattice.

The total simulation time, plotted in Figure 5.5B, is a function of the number of swaps required and the acceptance rate. On a personal computer, the average time to create a lattice with 262,144 atoms ranges from under two minutes for TaNbTi at 1673K to 11 hours for HfMoNbTaTi at 300K.

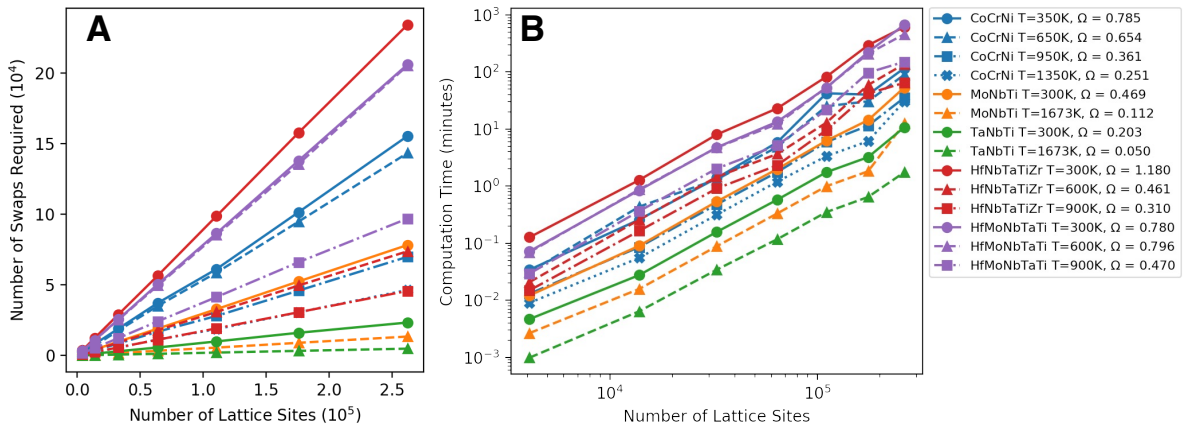

Figure 5.5: (A) The number of swaps required to reach the desired Warren-Cowley parameters for each alloy. (B) The average total simulation time on a personal computer for each alloy as a function of system size.

5.2.3 Scope and future applications

OTIS is a time-efficient method for generating large numbers of simulation cells with hundreds of thousands of atoms that can then be used in atomistic or mesoscale simulations. It can be used when direct MC-MD calculations would be prohibitively expensive or time-consuming for the simulation cell size, or when many distinct SRO lattices are desired. The example structures here all concern equiatomic MPEAs, but OTIS can be used for any system with SRO, including conventional binary alloys or non-equiatomic MPEAs. Although not currently a feature of the code, the method itself could used for other lattice types beyond BCC and FCC, including HCP. Additionally, while the focus of this work was chemical ordering, the method could be applied to other types of SRO such as magnetic SRO. The only requirement of the method is the input of known WC parameters. In cases where the WC parameters are calculated for multiple temperatures, one could interpolate the parameters to intermediate temperatures and use OTIS to create the SRO structure, thus completely bypassing the need for additional MC-MD or MC-DFT calculations to create atomic lattices for those annealing temperatures.

The OTIS code could also be advanced to consider WC parameters beyond the first nearest neighbor shell. While most studies only calculate and report the WC parameters from the first nearest neighbor shell, WC parameters can be calculated for the second nearest neighbor shell and beyond [209]. In these cases, the additional WC parameters would simply be added as new bond types, represented as additional rows and columns in the c_{ij}, g_{ij} and $\delta_{ij}^{\alpha}(\boldsymbol{x})$ matrices. In other words, A-B first nearest neighbor bonds would be considered separately from A-B second nearest neighbor bonds. The atom selection and acceptance criteria outlined here would account for all of these bond types when making swaps. Of course, this would increase the number of constraints that OTIS must meet to find a valid structure, but as shown here through the quinary MPEA calculations, OTIS can handle at least ten independent constraints.

5.3 Effect of short-range order on dislocations

5.3.1 Atomistic simulations

OTIS is combined with atomistic simulations and PFDD to study the effect SRO on dislocation behavior. Atomistic simulations here are enabled by the development of a highly accurate machine learning interatomic potential for the Mo-Ta-Nb-Ti system based on the moment tensor potential (MTP) formalism [204–207]. Fig. 5.6a provides an overview of the MTP fitting procedure, which is based on a well-established workflow developed previously [20, 38]. Full details of the potential fitting can be found elsewhere [182]. To investigate the effect of composition variations on SRO and dislocation glide, the training data were carefully selected to encompass all known unary, binary, ternary and quaternary phases in the Mo-Ta-Nb-Ti system. Fig. 5.6(b,c) show that extremely low test mean absolute errors (MAEs) were achieved for energies (4.1 meV·atom^{-1}) and forces

(0.067 eV·Å^{-1}), comparable to that achieved previously for the NbMoTaW RMPEA [20, 38]. The MTP also reproduces very well the DFT elastic constants for the constituent elemental systems. The shear moduli μ are 29.6 and 32.3 GPa for TaNbTi and MoNbTi, respectively, and the Young's moduli are 82.7 and 90.7 GPa, respectively.

To calculate the WC parameters, bulk BCC supercells with equimolar MoNbTi and TaNbTi as well as non-equimolar ternaries with elemental ratio of 3:4:4 and 3:1:1, i.e., $X_4Nb_3Ti_4$, $X_4Nb_4Ti_3$, $X_3Nb_4Ti_4$, X_3NbTi, $XNbTi_3$, XNb_3Ti, where X = Mo or Ta, were constructed. For each composition, three levels of SRO are achieved by studying the as-constructed random solid solution (RSS) and annealing at 300K and 1673K using MC/MD simulations with the MTP. The SRO for the final equilibrium structures is characterized using Warren-Cowley parameters. By definition, for a RSS, $\alpha_{ij} \approx 0$ and for greater degrees of SRO, the absolute value of α_{ij} increases. Fig. 5.7 shows the Warren-Cowley parameters for the annealed alloys. For all compositions, lower annealing temperatures lead to greater levels of SRO, consistent with previous studies.[35, 212]. For the same set of elements, greater degrees of SRO can be accomplished with off-equimolar stoichiometry, i.e., the 3:1:1 and 3:4:4 compositions, than equimolar. In materials annealed at 300 K, the SRO exhibited by MPEAs containing Mo ($Mo_xNb_yTi_z$) are much higher than those containing Ta ($Ta_xNb_yTi_z$). These two types of MPEAs would be expected to respond differently to the same processing condition or heat treatment, with MoNbTi being much more susceptible than TaNbTi.

Fig. 5.8 plots the calculated unstable stacking fault energy (USFE) on the {110} plane, shifting along with ⟨111⟩ directions for as-constructed RSS and samples equilibrated at two different annealing temperatures. In all cases, a higher concentration of Ti reduces the USFE. In the Mo-Nb-Ti system, greater concentrations of Mo increases the USFE, in agreement with a prior work using another interatomic potential [117]. On average, for the same composition, annealing at 300 K raises the USFE indicating

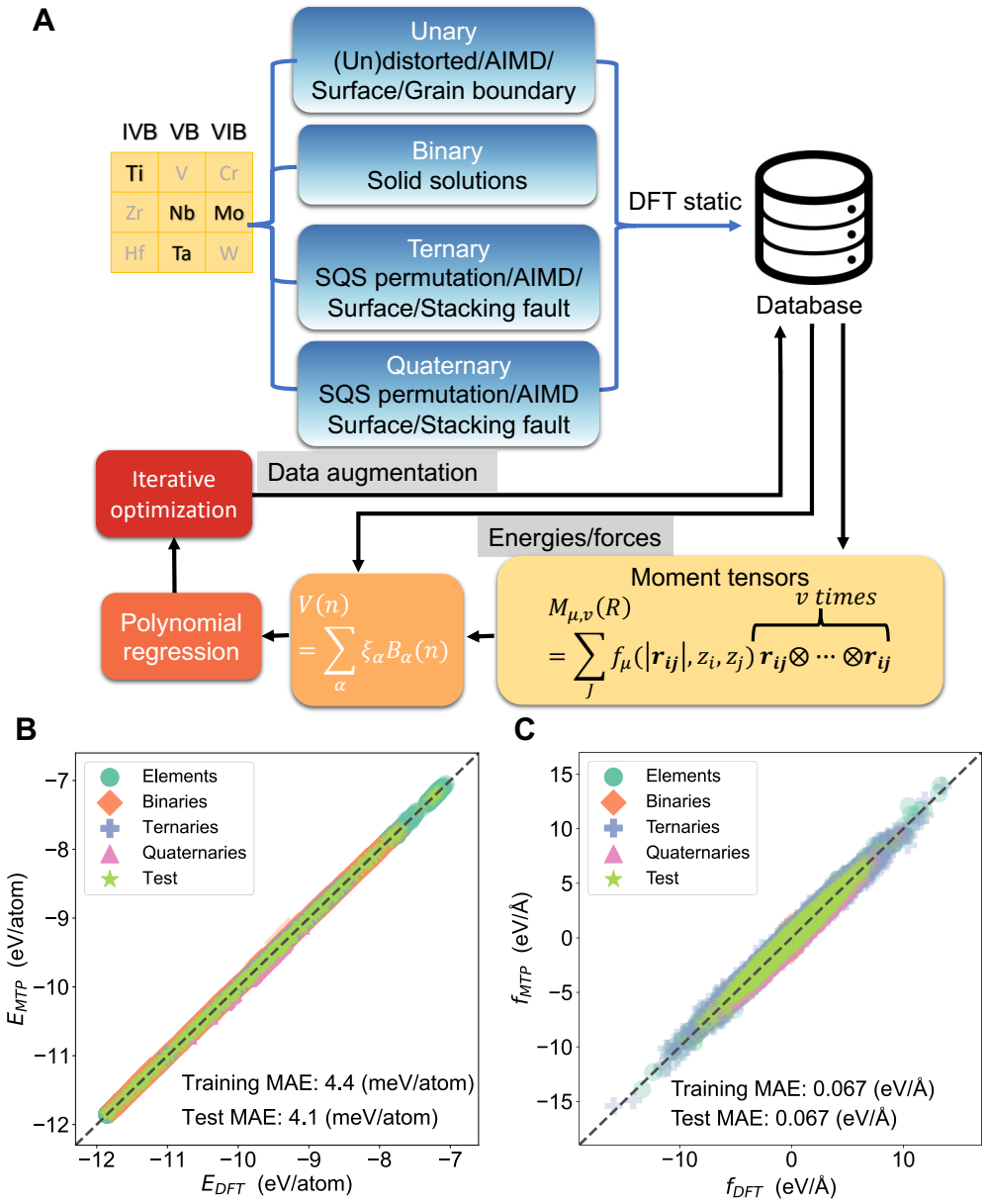

Figure 5.6: (a) Moment tensor potential development workflow. (b-c) Parity plots of the MTP predicted (b) energies and (c) forces against DFT values, broken down into elemental, binary, ternary and quaternary phases.

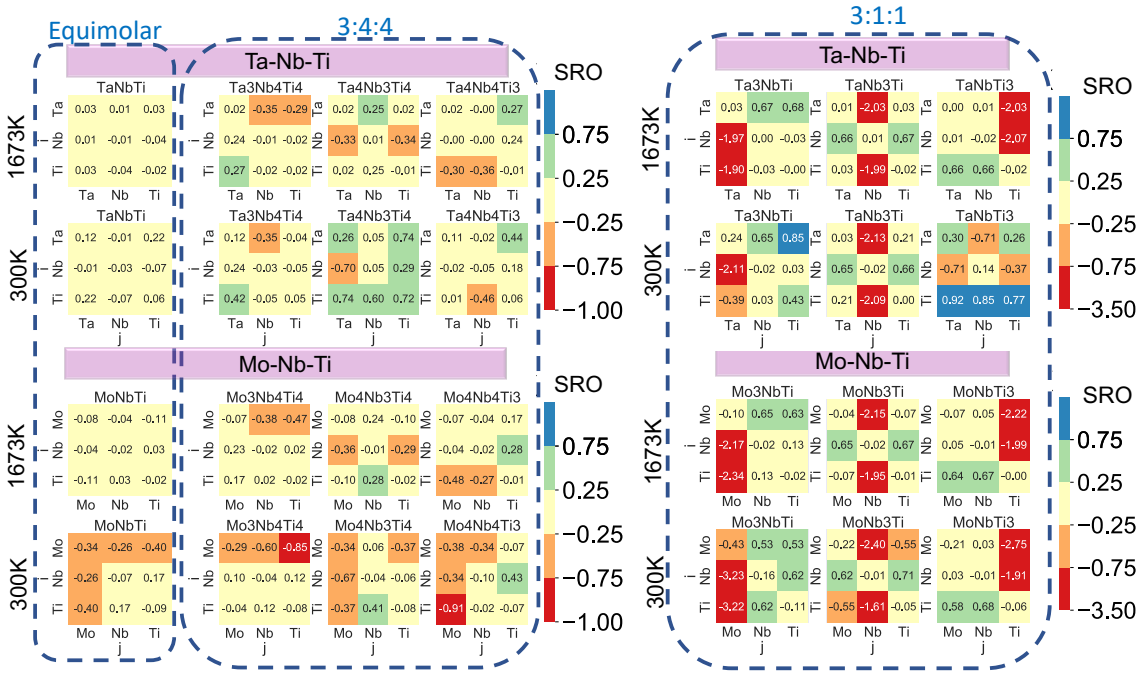

Figure 5.7: Heat maps of the equilibrium Warren-Cowley parameters α_{ij} for alloys annealed at 1673 K and 300 K. By definition, $\alpha_{ij} = \alpha_{ji}$ for equimolar systems, which is reflected in the heatmap with a diagonal symmetric color matrix. However, for the systems with non-equimolar composition, $\alpha_{ij} \neq \alpha_{ji}$. The color scale distinguishes between low SRO ($|\alpha_{ij}| < 0.25$), medium SRO ($0.25 \leq |\alpha_{ij}| < 0.75$) and high SRO ($|\alpha_{ij}| \geq 0.75$).

that SRO increases USFE. To correlate the USFE with its local composition, the local composition is determined based on the composition of the first nearest neighbor planes surrounding the cleaving plane. The correlations between the USFE of a plane and its local composition are consistent with those observed for average USFE of different bulk concentrations. Higher local fractions of Mo significantly increase the USFE, while higher fractions of Ta also increase the USFE but not as significantly as Mo. Higher fractions of Ti substantially decrease the USFE. The trend of USFE with local composition is consistent with the trends observed for the bulk composition as discussed above.

The SRO of different pairs from 300K also reflects the bonding preference in MPEAs. As shown in Fig. 2, for equimolar systems, the SRO of the Mo-Ti pair is negative (attractive interaction), while the Ta-Ti pair is positive (repulsive interaction). The SROs of Mo-Nb and Ta-Nb are both negative, but the value for the Mo-Nb pair (-0.26) is much more negative than that of the Ta-Nb pair (-0.01). Consequently, the MoNbTi corresponds to higher USFE compared to the TaNbTi. The driving forces for the differences in the SRO can be attributed to pairwise interactions, as explained from the perspective of binary formation energy, bond length, and electronegativity.

5.3.2 PFDD simulations

Using OTIS, BCC lattices were generated for MoNbTi and TaNbTi at annealing temperatures 300K and 1673K, as well as the RSS. Each lattice point was assigned a local composition based on the type of the atom and its neighbors. Atomistic simulations of the solute-dislocation interaction energy in BCC MPEAs showed that solute atoms beyond just the core of the dislocation significantly influence the dislocation energy [213]. In fact, the highest solute-dislocation interaction energy was found at the fifth nearest neighbor from the screw dislocation center. Therefore, the local composition of each grid

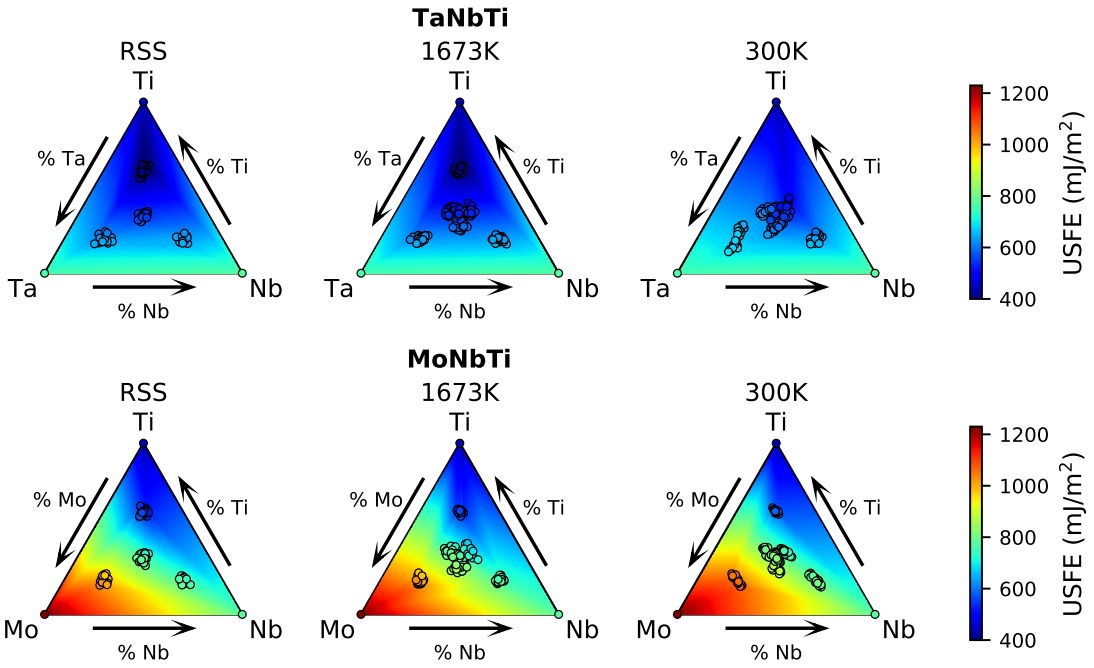

Figure 5.8: The USFE values calculated with the MTP as a function of the local composition around the fault plane in the two alloys at different levels of SRO. The values obtained from energy minimization using MTP are shown with dots. The values in the remainder of the triangles are interpolated from the calculated values and colored.

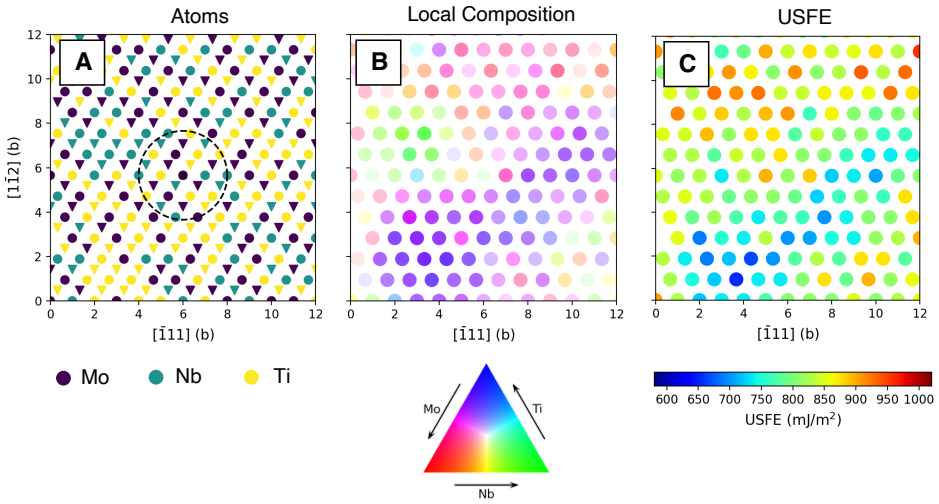

Figure 5.9: The conversion of an atomic lattice into local USFE values for use in PFDD.

point is determined using all the atoms within a cutoff radius of two Burgers vectors, which corresponds to and includes atoms up to the fifth nearest neighbor. Only atoms within the two adjacent (110) planes sheared by a dislocation are included for a total of 31 atoms. The composition of the grid point was associated to a local value of USFE, which were calculated above (Fig. 5.9).

In each PFDD simulation, three order parameters are used to represent three different slip systems, each with a Burgers vector $\frac{a}{2}[\bar{1}11]$. The slip planes are (110), $(01\bar{1})$, and (101), which makes cross slip possible and gives the distinct screw-edge differences seen in BCC materials [146]. A BCC primitive cell is used to define the lattice grid points with primitive vectors $\mathbf{p}_1 = \frac{b}{\sqrt{3}}[11\bar{1}]$, $\mathbf{p}_2 = \frac{b}{\sqrt{3}}[\bar{1}11]$, and $\mathbf{p}_3 = \frac{b}{\sqrt{3}}[1\bar{1}1]$. In each simulation, the first order parameter is set to 0 or 1 depending on the initial dislocation configuration to create a dislocation on the (110) plane. All other order parameters are initially zero. For the screw dislocation dipole simulations, a $128b \times 362b \times 136b$ simulation cell is used, and the dislocations are initially $362b$ long and separated by $32b$. For the edge dislocation dipole simulations, a $128b \times 128b \times 384b$ simulation cell is used, and the dislocations are also initially $362b$ long and separated by $32b$. In the dislocation loop simulations, a

$128b \times 128b \times 128b$ cell is used and the initial loop radius is $16b$.

PFDD is first used to study the role of SRO in the glide behavior of initially straight edge or screw dislocations. Due to the randomness in underlying fault energies, twenty independent realizations are performed for each alloy and each level of SRO. To study critical behavior, the applied shear stress is gradually increased in increments of 0.001μ until the dislocation glides and is held constant until it fully arrests.

Fig. 5.10 shows snapshots in time of edge dislocation glide. When the stress is initially applied and raised, the dislocation remains straight. Once the applied stress exceeds the first threshold, the edge dislocation becomes slightly wavy, as small portions of the dislocation line bow out into low USFE regions and are held back at the higher USFE regions. The stress must be increased further for the dislocation to glide, and small bowed out segments of the dislocation will glide independently through the lower USFE regions, dragging the neighboring (non-edge) segments through the higher USFE regions. The dislocation arrests several times during the simulation, each time requiring the stress to be raised to restart glide. The arrested dislocation morphologies are wavy, unlike the original pure edge orientation. The stop/start behavior leads to glide plane hardening, a continual increase in applied stress with increasing plastic strain, as seen in the stress-strain curve in Fig. 5.10. This is in contrast to PFDD simulations of pure metals, in which dislocations gliding have a single critical stress and remain straight during glide.

Screw dislocation glide proceeds in a different manner from edge dislocation glide. As the stress increases, the dislocation remains completely straight with pure screw character until a kink-pair only a few Burgers vectors wide is nucleated into a low USFE region. Kink-pairs form naturally when a screw dislocation segment advances by one Burgers vector in a location where the local applied stress exceeds the local resistance. Unlike the variable wavy bow out in the edge dislocation, these kink-pairs always have a height of just $1b$, and the kinks will usually, but not always, glide along the length of the screw

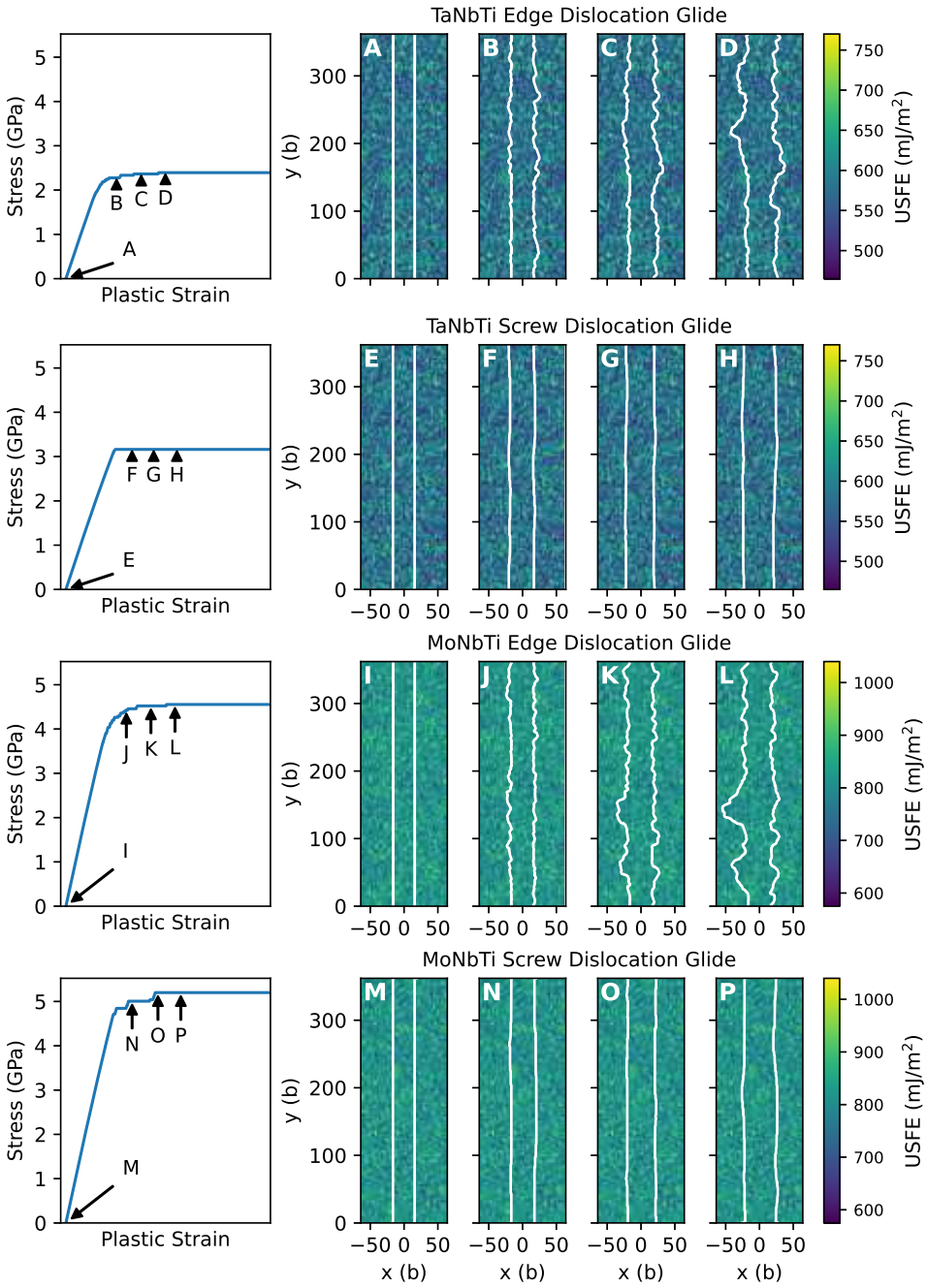

Figure 5.10: Representative examples of dislocation glide and their associated stress-strain curves. (A-D) and (E-H) show edge and screw glide, respectively, in a TaNbTi sample at 300K SRO. (I-L) and (M-P) show edge and screw glide, respectively, in a MoNbTi sample at 300K SRO.

dislocation to advance the full dislocation line forward. Like the edge dislocations, the screw dislocations may become arrested under stress, but unlike the edge dislocations, the arrested dislocation morphologies are nearly straight, apart from a few metastable kinks, recovering the original pure screw orientation. The start/stop mechanism of glide of the screw dislocation also leads to glide plane hardening, although at a lower level than edge dislocation glide plane hardening.

The different dislocation glide mechanisms can be related to differences in their core structures. The zero-stress, relaxed dislocation core structures, represented through the PFDD order parameters, are shown for MoNbTi in Fig. 5.11. Two MoNbTi core structures for both screw and edge dislocations are chosen: one in an "easy" region with a lower critical stress and one in a "hard" region with a higher critical stress. For comparison, core structures in a material with the pure Mo and pure Nb USFE are also shown. The elastic constants for all of these structures are the same, so any differences are attributable to USFE alone. The local dislocation core structure changes as the dislocation glides due to the changing local UFSE.

As is well-known for BCC materials and observed in prior PFDD simulations [146], screw dislocation cores spread onto the three equivalent 110-type slip planes while edge dislocation cores remain planar. The non-planar structure of screw dislocations is responsible for the increased glide stresses and the predominance of kink-pair nucleation glide mechanisms. The width w of the dislocation core in the (110) habit plane is estimated by measuring the distance between $\phi_1 = 0.05$ and $\phi_1 = 0.95$, using a linear interpolation between grid points as necessary. Higher local USFE values produce narrower dislocations. Dislocations in pure Mo have the narrowest cores, while Ti-rich regions of MoNbTi have the widest cores. Wider dislocation cores are associated with lower Peierls stresses [143], thus explaining the link between lower USFE and lower critical stresses.

Fig. 5.12A plots the stresses to initiate glide σ_i and the final stresses for runaway glide

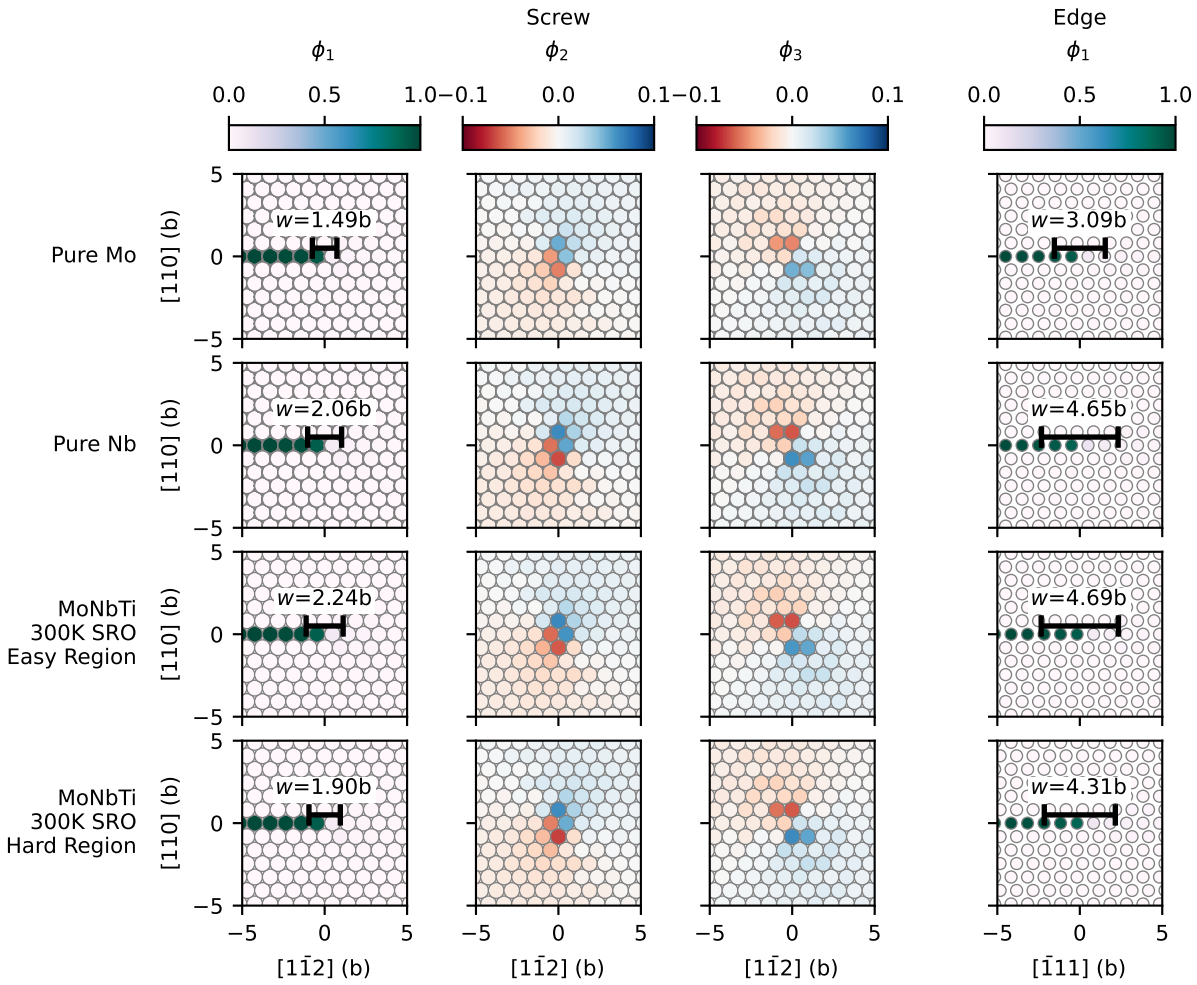

Figure 5.11: The order parameters at the relaxed dislocation cores under zero stress for MoNbTi. The first and second rows show dislocation in pure Mo and pure Nb, respectively, using the MoNbTi elastic constants. The third and fourth rows show dislocation segments with low and high critical stresses, respectively. The core width within the habit plane is annotated.

σ_f of edge and screw dislocations based on twenty independent initializations. Regardless of SRO, both σ_i and σ_f for the TaNbTi alloy are lower than those for the MoNbTi alloy. From Fig. 5.12B, mean glide resistance across the plane scales directly with the average USFE across the plane. Thus, changes in USFE caused by SRO have a direct influence on the stress to initiate and propagate dislocations, as seen in Fig. 5.12C. The higher the Ω, the higher the USFE is increased relative to the RSS case, which translates directly to increased glide resistance for both screw and edge dislocations.

The hardening in glide resistance is also related to the degree of dispersion of the USFE values in the glide plane as opposed to the mean. In Fig. 5.12D, the role of composition and its fluctuations is analyzed by adopting the fractional increase from σ_i to σ_f as a measure of glide-plane hardening. While screw dislocations do not experience significant hardening, the hardening of edge dislocations scales directly with the USFE COV for both alloys. The strikingly linear relationship even when considering both alloys implies that it transcends composition. Thus, apparent differences in the hardening seen in these alloys can be explained. Compared to TaNbTi, MoNbTi achieves, on average, greater hardening in the ideal random case and lower hardening in the highest Ω case.

Further, while hardening for both screw and edge dislocations increase as the USFE COV increases, the edge dislocations experience greater hardening than the screw dislocations for the same statistically sampled glide plane length (Fig. 5.12D). The edge dislocations glide by depinning of the segments at the relatively harder regions, segments which have reoriented to non-edge character due to bow out. Continued glide, therefore, relies on overcoming those local regions of higher resistance. Encountering a region ahead of the dislocation of even greater resistance than in the wake more likely occur when the dispersion in USFE is greater. The screw dislocation moves by producing short and narrow atomic advances of screw-oriented segments, i.e., kink-pairs, in the weaker regions and relying on the long advances of easier-to-move edge segments along the length of

the dislocation. Those local domains of higher resistance that are more likely encountered when the dispersion in USFE is higher, can be easily overcome by migrating edge dislocations. By virtue of their differing glide mechanisms, edge dislocations experience greater sensitivity to the dispersion in USFE and hence greater hardening than screw dislocations. Due to the narrow USFE distribution, screw dislocations in TaNbTi with 300K SRO experience essentially no hardening.

Fig. 5.12E examines the influence of Ω on hardening. It reveals that the role of SRO on hardening corresponds to the extent to which SRO affects the COV in USFE. As increased Ω tends to narrow the dispersion in USFE across the glide plane, it reduces glide-plane hardening. Since the TaNbTi alloy achieves lower Ω than MoNbTi for the same annealing treatment, hardening, like its strength, is weakly affected by SRO compared to MoNbTi.

Next, the effect of chemical fluctuations on screw/edge glide mobility is studied by examining loop expansion on the (110) slip plane at constant stress. For given applied stress, thirty dislocation loop expansion simulations are conducted representing different locations in a given alloy and SRO. For all cases, the anisotropy in screw/edge behavior reduces with increases applied stress. At low stresses, the difference in screw/edge behavior is large, causing the loop to expand into an oblong shape (Fig. 5.13A-D). The edge segments move continuously, constantly changing their wavy appearance. The screw dislocations advance very slowly, nucleating only a few kink-pairs at a time and recovering the nearly straight orientation with each advancement. As the applied stress increases, both screw and edge velocities increase and their ratio decreases towards unity. The loop expands more isotropically, almost FCC-like (Fig. 5.13E-H). Fig. 5.13H shows the loop at both low and high stress overlaid together. The two loops have similar widths ($103b$ and $101b$, respectively) but different heights ($38b$ and $51b$, respectively), demonstrating that higher stresses decrease the loop aspect ratio. The screw dislocation has clearly changed its mode of glide, as a result of a higher kink-pair nucleation rate. The screw portions

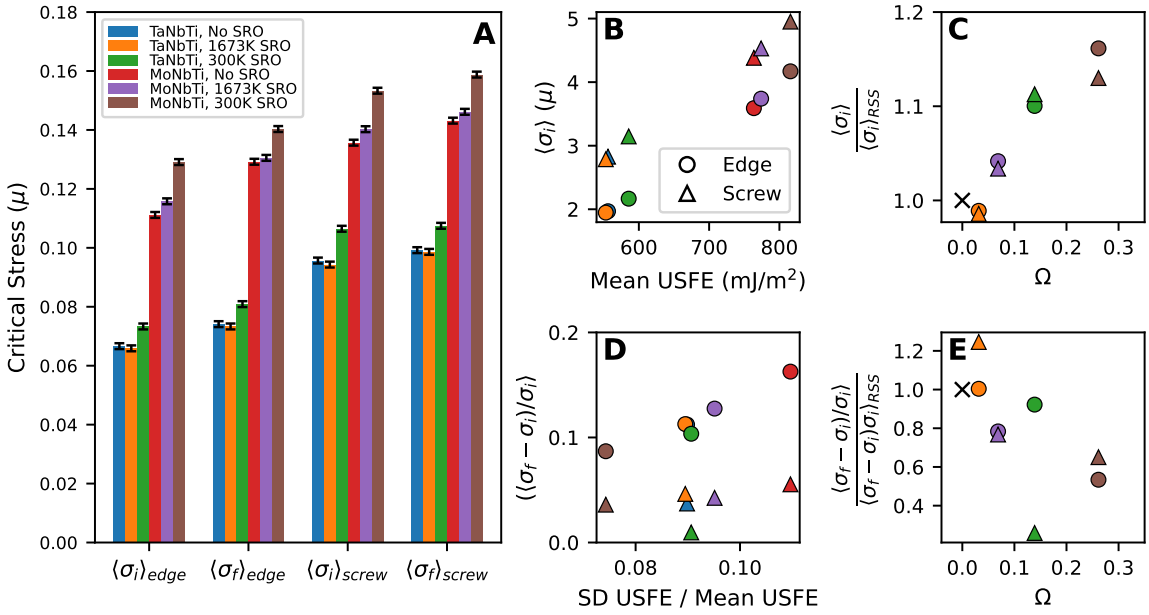

Figure 5.12: Critical stresses for dislocation glide. (A) The mean critical stress for dislocations in each of the alloys. The critical stresses for MoNbTi and TaNbTi are normalized by their respective shear moduli μ. The error bars show the resolution of the simulation, 0.001 μ. (B) The mean initial critical stress vs the mean USFE for each alloy. (C) The mean initial critical stress relative to the mean initial critical stress for RSS alloy vs the extent of SRO, represented by the SRO FOM. The black $\times$ represents the RSS case. (D) The hardening, represented by the difference in final and initial critical stresses, vs the coefficient of variation of USFE. (E) The hardening relative to the hardening for the RSS alloy vs the extent of SRO.

move continuously and adopt a wavy appearance, superficially much like the edge dislocations. Wavy screw glide, however, occurs as many kink-pairs nucleate simultaneously along the same dislocation. Newly advanced portions can nucleate further kink pairs, causing different portions of the dislocations to advance at different rates.

The two extremes of screw dislocation behavior are separated into "jerky" glide at low stresses and "smooth" glide at high stresses. To link the transition between jerky and smooth dislocation the rate of kink-pair nucleation, the waiting time between kink-pair nucleation events is calculated for all simulations. The waiting times from all thirty instantiations of loops are combined into a single distribution for a given alloy and applied stress, and the means are plotted in Fig. 5.14. Over 22,000 and 52,000 total waiting times were recorded for TaNbTi and MoNbTi, respectively, and each individual distribution contains at least 200 values. For both TaNbTi and MoNbTi, higher levels of SRO correspond to longer average waiting times and thus more jerky dislocation glide at all applied stresses. Normalizing the applied stresses by the average σ_i for screw glide, the three distinct SRO curves collapse into one. Thus, the critical stress to transition from jerky to smooth scales with Peierls strength or with static strength. SRO affects the transition stress in dynamic glide indirectly via its strengthening effect on static glide resistance.

5.4 Discussion

There are limited experimental measurements of the mechanical properties of TaNbTi and MoNbTi. The tensile yield stresses have been reported as 620 and 950 MPa for TaNbTi and MoNbTi, respectively [13, 214, 215], which are consistent with the dislocation dynamics predictions of higher glide stresses for MoNbTi. The ultimate tensile strengths are 683 and 1500 MPa, respectively, so MoNbTi exhibits significant strain

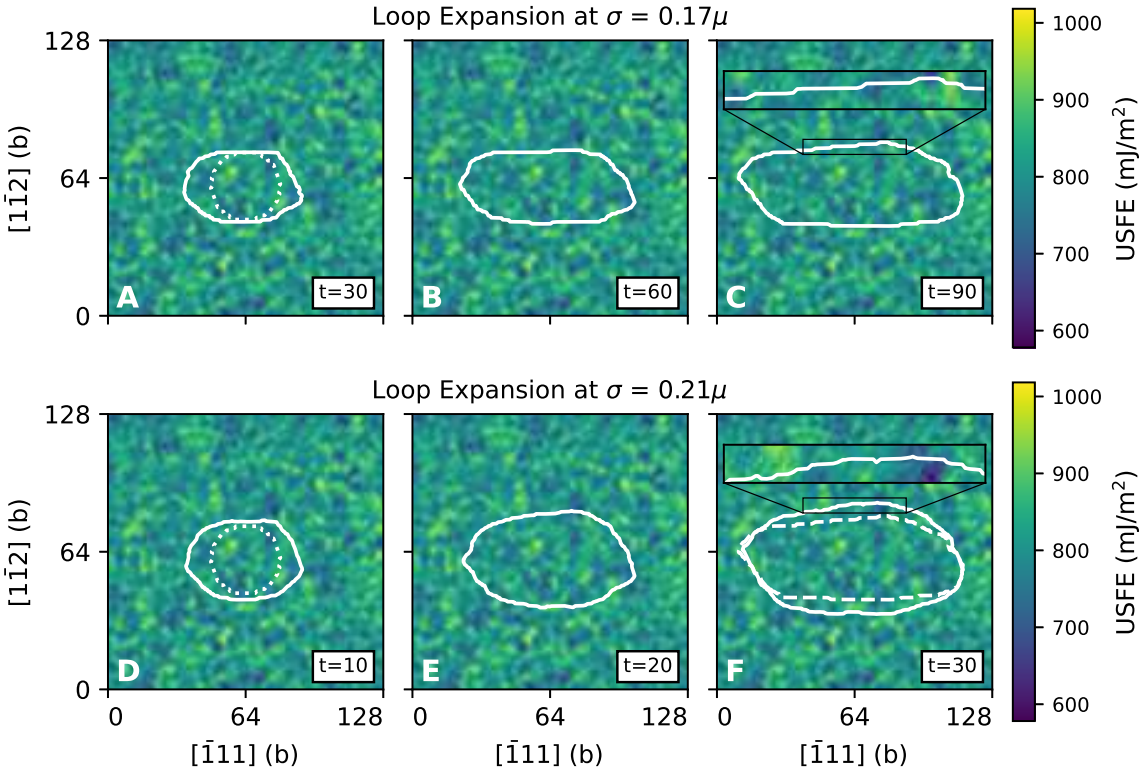

Figure 5.13: The same dislocation loop expanding in MoNbTi under different applied stresses. The initial loop shape is shown by the dotted lines in (A) and (D). When a lower stress is applied, the screw dislocation nucleates kink-pairs infrequently, causing jerky dislocation glide and remaining largely pure screw. At higher applied stresses, the screw dislocation nucleates many kink-pairs at once resulting in smoother glide and a wavy morphology. The final loop from (C) is reproduced by the dashed line in (F) to highlight the difference in aspect ratio between the two loops.

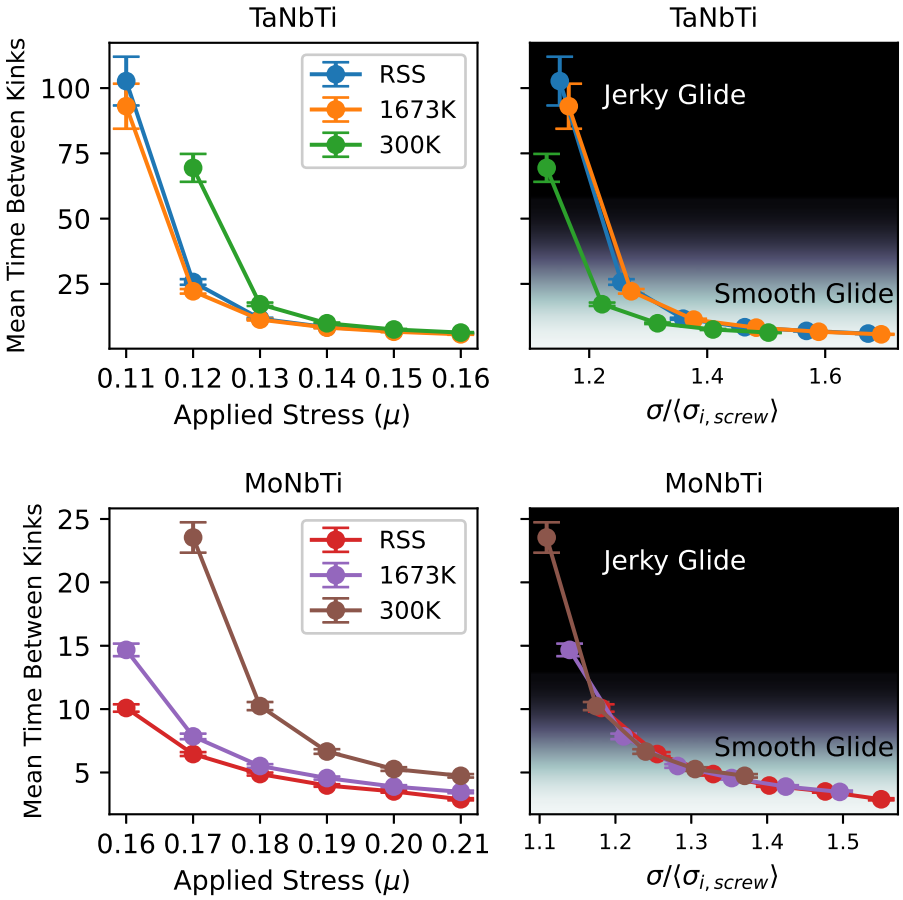

Figure 5.14: Average time between kink-pair nucleation events as a function of applied stress. The error bars show the standard error. The transition between jerky and smooth screw dislocation glide is determined by the applied stress relative to the dislocation critical stress.

hardening while TaNbTi does not. The PFDD simulations show higher hardening in MoNbTi than TaNbTi due to the increased coefficient of variation in USFE. The dislocation dynamics simulations also revealed that the amount of dislocation hardening is decreased by the presence of SRO, especially for MoNbTi. As edge dislocations undergo more hardening than screw dislocations, the PFDD simulations predict the differences in macro-scale strain hardening in these alloys are largely controlled by edge dislocation behavior.

From the Warren-Cowley parameter calculations, it is clear that MoNbTi has a higher propensity for SRO and will be more affected by processing conditions. There has been interest in tuning the SRO parameters through heat treatment, although experimentally this is difficult to achieve [30]. Findings indicate that MoNbTi is a better candidate for exploring SRO strengthening than TaNbTi since SRO promotes two relatively stronger Mo-Nb and Mo-Ti bonds. However, the relative increases in the average dislocation glide resistance due to SRO amount to less than 20% even in the most extreme cases, so large changes in the mechanical properties must be accompanied by changes in the chemical composition, not SRO alone.

Via MD simulations, a few studies have shown SRO-enhanced dislocation glide resistance [20, 30, 123] and one study on CoFeNiTi alloy reported a slight SRO softening [201]. Strengthening or softening was related to the formation of immobile dislocation segments via cross slip. Here, SRO strengthening in dislocation glide is demonstrated without cross slip. While the current dislocation model permits cross slip [146], it was not observed in the present calculations since the influence of thermal fluctuations is not taken into account. Including temperature would undoubtedly increase the chance for cross-slip or cross-kinking, adding another mechanism for SRO strengthening.

5.5 Conclusion

In this chapter, OTIS, a novel method to randomly generate atomic lattices with a given set of WC SRO parameters, was developed. The algorithm begins with a random structure and swaps atoms until the goal WC are reached. The method uses an informed selection criterion to choose the atoms for swapping, greatly increasing the efficiency and convergence of the algorithm. The code can be used to generate input structures for atomistic and mesoscale simulations without computationally intensive repeated MC simulations. These structures can the facilitate future studies of the effects of short-range order in multi-component alloys.

OTIS was combined with atomistic simulation methods and PFDD for a multi-scale investigation of dislocation mechanisms in MoNbTi and TaNbTi at different levels of SRO. Increased SRO is associated with higher mean USFE, thereby increasing the stress required for dislocation glide. The gliding dislocations experience significant hardening due to pinning and depinning caused by random compositional fluctuations, with higher SRO decreasing the degree of USFE dispersion and hence, amount of hardening. Finally, PFDD simulations of expanding dislocation loops show that the morphology is affected by the applied stress, with higher SRO requiring higher applied stresses to achieve smooth screw dislocation glide.

Chapter 6

Interstitial Solute Atoms in PFDD [†]

6.1 Introduction

Interstitial solutes, such as O, C, and H, greatly affect the mechanical properties of body-centered cubic (BCC) metals. Even in small amounts (< 1 at%), interstitial atoms increase material strength at the expense of a drastic loss in ductility [43–45]. At concentrations below the interstitial solubility limit, these changes are generally attributed to the interaction of dislocations and interstitial atoms [46, 47].

Dislocations may interact with interstitials through several different mechanisms, which can generally be broken into short-range and long-range interactions. In the short-range, interstitials change the dislocation core structure, notably the screw core structure from the so-called easy core to the hard core [57–61]. The reconstructed core has a modified Peierls barrier shape and magnitude, and can pin the dislocation and increase overall strength [57, 58, 62]. Kink-pair nucleation and migration, which is the dominant mechanism for screw dislocation glide in BCC materials [8], is also affected by

[†]This chapter adapted from Reference [216]: Fey, L. T. W., Reynolds, C., Hunter, A., & Beyerlein, I. J. (2023). Phase-field modeling of dislocation-interstitial interactions, Journal of the Mechanics and Physics of Solids, Under Review.

interstitial atoms. Dislocations may be attracted to interstitials, making kink-pair nucleation towards an interstitial atom easier [45, 63, 64]. On the other hand, interstitials may pin kinks and thus inhibit kink migration [63, 65]. Additionally, the formation of kinks on different glide planes can create immobile cross-kinks, pinning the dislocation [45, 64].

In the long-range, dislocations and interstitials interact through their elastic stress fields [56, 217]. A Cottrell atmosphere forms around dislocations as interstitial atoms preferentially segregate to tensile areas over compressive areas, locking the dislocation in place [48]. A related phenomenon, the Snoek effect, is specific to BCC materials [53]. In a BCC lattice, larger interstitials such as O and C occupy the octahedral interstitial sites, creating a tetragonal distortion. There are three possible orientations of the octahedral sites, each with the largest distortion aligned with a different <100>-type direction. In a stress-free state, these orientations are energetically equal, but in a stress field, such as that created by a dislocation, interstitials will adopt the lowest energy orientation [53]. Like the Cottrell atmosphere, this may pin the dislocation in place [54, 55].

Simulating both interstitial diffusion and dislocation glide can be challenging. The time and length scales associated with atomistic simulations are generally too short to capture significant interstitial diffusion [71]. Therefore, there is great interest in developing mesoscale models to investigate the complex dynamics between dislocations and interstitials. Discrete dislocation dynamics (DDD) models have been developed to include interstitial atoms, primarily self-interstitials in the context of radiation damage [72]. These models require the input of phenomenological rules that govern dislocation motion and hardening in the presence of obstacles.

Phase-field models have also been used to study dislocations and solute atoms [218]. Recently, Zheng et. al developed a phase-field model to study H interstitials in FCC materials [70, 219]. By adding a concentration phase-field variable, they simulated both

the short- and long-range interactions of H with dislocations in Ni. The model assumes interstitial diffusion is essentially instantaneous, and the interstitials always remains in equilibrium with gliding dislocations. However, some important mechanisms, such as the Portevin-Le Chatelier effect, in which dislocations are repeatedly pinned by trailing solute atoms, depend on the interplay between dislocation and interstitial velocities [55, 71].

Here, the PFDD framework is extended to include interstitial solute atoms in a BCC lattice. Unlike other mesoscale models, an interstitial mobility is included that governs the timescale over which interstitials diffuse. Due to the symmetry of the BCC lattice, there are multiple possible orientations of interstitial sites. Multiple phase-field variables are employed and coupled to track the concentration of interstitials in each site type. Short-range interactions are accounted for by a concentration-dependent stacking fault energy, and long-range interactions are accounted for by modifications to the elastic energy. Full elastic anisotropy is employed, which atomistic simulations have shown is necessary to accurately capture dislocation-interstitial interaction energies [56].

The new PFDD formulation is described in Section 6.2. As the interstitial formulation relies on the gradients in the dislocation stress field, a modified Green's function is employed to minimize Gibbs oscillations. The new PFDD-interstitial method is applied to Nb-O as a model system. The concentration-dependent stacking fault energy and elastic dipole are obtained from *ab initio* calculations and input into the model. First the effects of interstitial O on the structure of screw and edge cores in Nb is studied. Then, the Cottrell and Snoek atmospheres are formed around screw and edge dislocation cores through interstitial diffusion, and the critical stresses is calculated for dislocations to break free from these interstitial atmospheres. As cross-kinking is an important strengthening mechanism [45], the ability of screw dislocations to cross slip and the associate critical stresses are studied. The implications of these results and future applications of the method are

discussed.

6.2 Methods

6.2.1 Phase-field formulation

To simulate interstitial atoms within the PFDD framework, a conserved phase field variables $c^\beta(\mathbf{r})$ is added, which represents the local concentration of interstitials of type β at point $\mathbf{r}$. The type β can be used to represent different interstitial elements or interstitial site types e.g., octahedral and tetrahedral. Here, β is used to represent the three distinct orientations of octahedral sites within a BCC lattice. The maximum concentration of a site type β is c^β_{max}. The vector $\boldsymbol{c}$ contains all local concentrations with components c^β for $\beta = 1$ to n_{int} where n_{int} is the number of interstitial site types. Let c^{tot} represent the total concentration at a point, $\sum_{\beta=1}^{n_{int}} c^\beta$.

The total energy density ψ is now a function of both slip and interstitial concentration, and consists of the elastic energy, lattice (crystalline) energy, and external energy:

$$\psi(\boldsymbol{\phi}, \boldsymbol{c}) = \psi_{\text{elas}}(\boldsymbol{\phi}, \boldsymbol{c}) + \psi_{\text{latt}}(\boldsymbol{\phi}, \boldsymbol{c}) - \psi_{\text{ext}}(\boldsymbol{\phi}, \boldsymbol{c}) \tag{6.1}$$

The elastic energy is given by

$$\psi_{\text{elas}}(\boldsymbol{\phi}, \boldsymbol{c}) = \frac{1}{2} c_{ijkl} \left(\epsilon_{ij}(\boldsymbol{\phi}, \boldsymbol{c}) - \epsilon^p_{ij}(\boldsymbol{\phi}) - \epsilon^{int}_{ij}(\boldsymbol{c})\right) \left(\epsilon_{kl}(\boldsymbol{\phi}, \boldsymbol{c}) - \epsilon^p_{kl}(\boldsymbol{\phi}) - \epsilon^{int}_{kl}(\boldsymbol{c})\right) \tag{6.2}$$

where c_{ijkl} is the elastic stiffness tensor, $\epsilon_{ij}(\boldsymbol{\phi}, \boldsymbol{c})$ is the total strain, $\epsilon^p_{ij}(\boldsymbol{\phi})$ is the plastic eigenstrain due to the dislocations, and $\epsilon^{int}_{ij}(\boldsymbol{c})$ is the interstitial eigenstrain. By including the interstitial eigenstrain in the elastic energy, long-range interactions between the

dislocation and the interstitial are accounted for. The eigenstrain for the interstitials is given by

$$\epsilon_{ij}^{int}(\boldsymbol{c}) = \sum_{\beta=1}^{n_{int}} \lambda_{ij}^{int,\beta} c^{\beta} \tag{6.3}$$

where $\lambda_{ij}^{int,\beta}$ is a tensor describing the strain introduced by an interstitial atom [51, 52]. The λ^{int}-tensor is related to another commonly measured parameter, the elastic dipole P_{ij}^{int}, through the materials stiffness tensor c_{ijkl} via Equation (1.2) [50]. The elastic dipole can be calculated readily through atomistic simulations [56, 220] and converted to a λ^{int}-tensor for PFDD simulations.

For a BCC lattice, the lattice energy has the form

$$\psi_{\text{latt}}(\boldsymbol{\phi}, \boldsymbol{c}) = \sum_{\alpha=1}^{n_s} \frac{\gamma_{usf}^{\alpha}(\boldsymbol{c})}{d^{\alpha}} \sin^2(\pi\phi^{\alpha}) \tag{6.4}$$

where γ_{usf}^{α} is the unstable stacking fault energy (USFE). To account for the short-range effects of interstitials at the dislocation core, γ_{usf}^{α} is now a function of interstitial concentration.

The external energy now includes the dependence on interstitial eigenstrain:

$$\psi_{\text{ext}}(\boldsymbol{\phi}, \boldsymbol{c}) = \sigma_{ij}^{\text{app}} \left(\epsilon_{ij}^{p}(\boldsymbol{\phi}) + \epsilon_{ij}^{int}(\boldsymbol{c})\right) \tag{6.5}$$

As in prior PFDD models, the dislocation order parameter evolves via the Ginzburg-Landau equation (Eq. (1.8)), which requires the partial derivative of each energy term with respect to ϕ^{α}. The partial derivative of the elastic energy is most easily written in Fourier space. First, the elastic energy term can be rewritten in Fourier space as

$$\hat{\psi}_{\text{elas}} = \frac{1}{2}\hat{A}_{mnuv}(\hat{\epsilon}_{mn}^{p} + \hat{\epsilon}_{mn}^{int})(\hat{\epsilon}_{uv}^{p*} + \hat{\epsilon}_{uv}^{int*}) \tag{6.6}$$

where $\hat{A}_{mnuv} = c_{mnuv} - c_{kluv}c_{ijmn}\hat{G}_{ki}\xi_j\xi_l$, G_{ki} is the Green's tensor, $\boldsymbol{\xi}$ is the wavenumber vector, and a superposed $\hat{}$ denotes the Fourier transform [78]. For simplicity, replace the tensor $\frac{1}{2}\sum_{\alpha=1}^{n_s}\frac{b^\alpha}{d^\alpha}\left(s_i^\alpha n_j^\alpha + s_j^\alpha n_i^\alpha\right)$ in Eq. (1.5) with $\lambda_{ij}^{disl,\alpha}$.The derivative is then given by

$$\widehat{\frac{\partial\psi_{\text{elas}}}{\partial\phi^\alpha}} = \hat{A}_{mnuv}\lambda_{mn}^{disl,\alpha}(\hat{\epsilon}_{uv}^{p*} + \hat{\epsilon}_{uv}^{int*}) \tag{6.7}$$

which is the form used in the PFDD code.

The remaining derivatives of the lattice and external energy contributions are given by

$$\frac{\partial\psi_{\text{latt}}}{\partial\phi^\alpha} = \frac{\gamma_{usf}^\alpha(\boldsymbol{c})}{d^\alpha}\sin(2\pi\phi^\alpha) \tag{6.8}$$

$$\frac{\partial\psi_{\text{ext}}}{\partial\phi^\alpha} = \sigma_{ij}^{\text{app}}\lambda_{ij}^{disl,\alpha} \tag{6.9}$$

Unlike slip, the total concentration c^{tot} is conserved, but interstitials are able to diffuse between the different site types β to lower their chemical potential. Therefore, interstitial diffusion will occur in two steps. First, the interstitials will be equilibrated at a point $\boldsymbol{r}$ between the different site types β. Second, the total concentration c^{tot} will diffuse in space. The chemical potential at 0K is given by

$$\mu^\beta = \frac{\partial\psi}{\partial c^\beta} = \frac{\partial\psi_{elas}}{\partial c^\beta} + \frac{\partial\psi_{latt}}{\partial c^\beta} - \frac{\partial\psi_{ext}}{\partial c^\beta} \tag{6.10}$$

Calculating the chemical potential requires the partial derivative of each energy term with respect to concentration. An analogous equation to Eq. (6.7) can be written for $\frac{\partial\psi_{\text{elas}}}{\partial c^\beta}$, but it is more informative to calculate the derivative in real space. The total elastic energy can be written as

$$\psi_{\text{elas}}(\boldsymbol{\phi}, \boldsymbol{c}) = \frac{1}{2} c_{ijkl} (\epsilon_{ij}^{elas,disl}(\boldsymbol{\phi}) + \epsilon_{ij}^{elas,int}(\boldsymbol{c}))(\epsilon_{kl}^{elas,disl}(\boldsymbol{\phi}) + \epsilon_{kl}^{elas,int}(\boldsymbol{c})) \tag{6.11}$$

where $\epsilon_{ij}^{elas,disl}$ and $\epsilon_{ij}^{elas,int}$ are the elastic strains due to the dislocation only and interstitials only, respectively. Rearranging gives

$$\begin{aligned}\psi_{\text{elas}}(\boldsymbol{\phi}, \boldsymbol{c}) = \frac{1}{2} c_{ijkl} \epsilon_{ij}^{elas,disl}(\boldsymbol{\phi}) \epsilon_{kl}^{elas,disl}(\boldsymbol{\phi}) + \frac{1}{2} c_{ijkl} \epsilon_{ij}^{elas,disl}(\boldsymbol{\phi}) \epsilon_{kl}^{int,disl}(\boldsymbol{c}) \\ + \frac{1}{2} c_{ijkl} \epsilon_{ij}^{int,disl}(\boldsymbol{c}) \epsilon_{kl}^{elas,disl}(\boldsymbol{\phi}) + \frac{1}{2} c_{ijkl} \epsilon_{ij}^{int,disl}(\boldsymbol{c}) \epsilon_{kl}^{int,disl}(\boldsymbol{c})\end{aligned} \tag{6.12}$$

$$\psi_{\text{elas}}(\boldsymbol{\phi}, \boldsymbol{c}) = \frac{1}{2} \sigma_{ij}^{disl}(\boldsymbol{\phi}) \epsilon_{ij}^{elas,disl}(\boldsymbol{\phi}) + \frac{1}{2} \sigma_{ij}^{int}(\boldsymbol{c}) \epsilon_{ij}^{elas,int}(\boldsymbol{c}) + \sigma_{ij}^{disl}(\boldsymbol{\phi}) \epsilon_{ij}^{elas,int}(\boldsymbol{c}) \tag{6.13}$$

The first term does not depend on $\boldsymbol{c}$ and can be neglected in the chemical potential. The derivative of the second term is μ_0, which represents the formation energy for the interstitial and is equivalent for the three different octahedral orientations [221]. The final term can be rewritten as $\sigma_{ij}^{disl}(\boldsymbol{\phi}) \epsilon_{ij}^{elas,int}(\boldsymbol{c}) = -\sigma_{ij}^{disl}(\boldsymbol{\phi}) \epsilon_{ij}^{int}(\boldsymbol{c})$ [81]. Therefore, the elastic contribution to the chemical potential is

$$\frac{\partial \psi_{\text{elas}}}{\partial c^\beta} = \mu_0 - \sigma_{ij}^{disl} \lambda_{ij}^{int,\beta} \tag{6.14}$$

This equation is independent of c^β and allows the interstitial concentrations to be redistributed efficiently over the various site orientations. The remaining contributions to the chemical potential are given by

$$\frac{\partial \psi_{\text{elas}}}{\partial c^{\beta}} = \mu_0^{\beta} - \sigma_{ij}^{disl} \lambda_{ij}^{int,\beta} \tag{6.15}$$

$$\frac{\partial \psi_{\text{latt}}}{\partial c^{\beta}} = \sum_{\alpha=1}^{n_s} \frac{\partial \gamma_{usf}^{\alpha}}{\partial c^{\beta}} \frac{1}{d^{\alpha}} \sin^2(\pi \phi^{\alpha}) \tag{6.16}$$

$$\frac{\partial \psi_{\text{ext}}}{\partial c^{\beta}} = \sigma_{ij}^{\text{app}} \lambda_{ij}^{int,\beta} \tag{6.17}$$

where μ_0^{β} is a reference chemical potential and σ_{ij}^{disl} is the stress field created by the dislocation only, neglecting the interstitials. Importantly, if γ_{usf} has a linear dependence on concentration, each term is independent of c^{β}.

At 0K, the interstitials will fill the site types with lower chemical potentials first. At a point $\boldsymbol{r}$, the chemical potential for each site type is calculated, and the site types are sorted from lowest to highest chemical potential. The total concentration c^{tot} is assigned to site types, beginning with the lowest μ^{β} site type until that site type is filled ($c^{\beta} = c_{max}^{\beta}$) and continuing until the total concentration has been distributed. The overall chemical potential μ for point $\boldsymbol{r}$ is then determined as the unfilled site with lowest μ^{β} i.e., where additional interstitial concentration would flow.

Now that the μ for each site has been determined, the interstitial flux $\boldsymbol{J}$ is simply given by Fick's first law:

$$\boldsymbol{J} = -m_{int} \nabla \mu \tag{6.18}$$

where m_{int} is the interstitial mobility, which is equal to

$$m_{int} = D c^{tot} / k_B T \tag{6.19}$$

where D is the diffusivity coefficient, k_B is the Boltzmann constant and T is temperature.

The change in total concentration at a site is given by

$$\frac{\partial c^{tot}}{\partial t} = -\nabla \cdot \boldsymbol{J} = \nabla \cdot (m_{int} \nabla \mu) \tag{6.20}$$

6.2.2 Unstable stacking fault energies

The lattice energy in Eq. (6.4) requires the USFE as a function of interstitial concentration. Fan et al. is followed calculated the effect of substitional solute atoms on the stacking fault energy of Mg, and their method is followed here [222]. An interstitial site i, depending on its orientation and distance from the stacking fault (SF), will have an interaction energy with the SF given by

$$E^i_{int-SF} = \left(E^{int,i}_{SF} - E^{int,i}_{bulk}\right) - \left(E_{SF} - E_{bulk}\right) \tag{6.21}$$

where E^i_{int-SF} is the interstitial-SF interaction energy, $E^{int,i}_{SF}$ is the total energy of a simulation cell with an interstitial and an SF, $E^{int,i}_{bulk}$ is the total energy of the cell with an interstitial in the bulk, and E_{SF} and E_{bulk} are the total energies of an interstitial-free cell with and without a SF, respectively.

The USFE for a given local concentration is then

$$\gamma_{usf}(\boldsymbol{c}) = \gamma_{usf}(0) + \sum_{i=1}^{n} \frac{c^i E^i_{int-SF}}{A} \tag{6.22}$$

where $\gamma_{usf}(0)$ is the interstitial-free USFE, n is the total number of sites considered, A is the area per atom of the fault plane, and c^i is the concentration of site i.

6.2.3 Atomistic calculations

Elastic dipole calculation

The elastic dipole calculation method is outlined by Clouet et al [51]. The elastic dipole is a model of a point defect in a crystal which can fully describe its long range elastic field and interactions with external stresses. The dipole P_{ij} is a second-rank tensor and is calculated as the first moment of the point-force distribution:

$$P_{ij} = \sum_{q=1}^{N} F_i^q a_j^q \tag{6.23}$$

where the force distribution consists of N forces $\boldsymbol{F}_i^q$ acting at position $\boldsymbol{a}^q$. In mechanical equilibrium, the interaction energy of the point defect can be characterized as

$$E^{int} = -P_{ij}\epsilon_{ij}^{ext}(\vec{0}) \tag{6.24}$$

where $\epsilon_{ij}^{ext}(\vec{0})$ is the external strain tensor at the point defect. The total energy of a simulation cell with a point-defect can be written as follows

$$E(\epsilon) = E_0 + E^{PD} + \frac{V}{2}c_{ijkl}\epsilon_{ij}\epsilon_{kl} - P_{ij}\epsilon_{ij} \tag{6.25}$$

The first two terms are the total energy of the pristine crystal and the point defect. The third term is an expression of the strain energy due to any distortions to the pristine crystal. The final term accounts for the interaction energy from the elastic dipole.

After taking a derivative of the total energy with respect to strain and normalizing by the simulation cell volume V,

$$\langle\sigma_{ij}(\epsilon)\rangle = c_{ijkl}\epsilon_{kl} - \frac{1}{V}P_{ij} \tag{6.26}$$

If a calculation is conducted in constant strain conditions by fixing the cell volume and shape, then ϵ_{ij} is fixed to zero and the equation further simplifies to

$$P_{ij} = -V\langle\sigma_{ij}\rangle \tag{6.27}$$

Thus, the elastic dipole P_{ij} can be directly calculated from the residual stresses determined through first principles calculations. To this end, DFT calculations are performed on a 128 Nb atom cell using the VASP [223–226] software package. These calculations employed the projector augmented wave (PAW)[227, 228] method and generalized gradient approximation (GGA) with the Perdew, Burke, and Ernzerhof (PBE)[229] functional, selecting a 575 eV planewave energy cutoff and a Γ-centered 4x4x4 k-point grid. The calculations were also spin polarized calculations, in which all structures are initialized in ferromagnetic states. In all cases, they relaxed to nonmagnetic states.

With this approach, the pristine Nb structure is relaxed to a force convergence of 0.02 eV/A, allowing the cell volume, shape and atomic position to fully relax. An oxygen atom is then inserted into an interstitial octahedral site. The structure was then relaxed again, but with a fixed cell volume and shape, to an energy convergence of 1e-5 eV. Structural relaxations were then carried out with a Gaussian smearing of partial occupied states with a width of 0.1 eV, while final static calculations were performed with the tetrahedron method with Blöch corrections to improve accuracy. The stress states of the static calculations with and without the interstitial oxygen were compared to determine the residual stresses and calculate P_{ij} with Eq. (6.27).

Unstable stacking fault energy calculation

The interstitial-SF interaction energies are calculated with DFT using VASP [230]. The projected augmented wave method is used with a plane-wave basis with cutoff energy

of 600 eV, and the Methfessel–Paxton smearing method is used with a smearing width of 0.2 eV. The conjugate gradient scheme is used to relax the ionic positions until the energy change is less than 10^{-4} eV. A simulation cell is created with size and orientation $\boldsymbol{x} = a[\bar{1}1\bar{2}]$, $\boldsymbol{y} = 6a[110]$, and $\boldsymbol{z} = \frac{a}{2}[\bar{1}11]$ where the equilibrium lattice parameter a for Nb equals 3.324Å [83] (Figure 6.1). This cell contains 36 atoms and 12 (110) layers, where the stacking fault plane area A is 23.4 Å^2. A vacuum layer of 12 Å is added to the $\boldsymbol{y}$-dimension to create a series of non-interacting slabs. The k-point mesh is 15 x 1 x 15. The energy of this structure after relaxation is E_{bulk}. To obtain E_{SF}, the rightmost six (110) layers are shifted by $\frac{a}{4}[\bar{1}11]$. The two outermost (110) layers on either side of the simulation cell are frozen, and all other atoms are allowed to relax in the $\boldsymbol{y}$ direction only.

Excluding sites within the frozen layer, this structure contains 14 unique octahedral sites. The [100]- and [010]-oriented sites exist between (110) planes and the [001]-oriented sites are within the (110) planes. For each calculation of $E^{int,i}_{bulk}$, an oxygen atom is placed at one of these sites, and all atoms except for the frozen layers are allowed to relax. The rightmost six (110) layers of the relaxed structure are shifted by $\frac{a}{4}[\bar{1}11]$, and atoms are relaxed again in the $\boldsymbol{y}$ direction only to calculate $E^{int,i}_{SF}$. For the two sites within the SF itself, the nearest neighbor atoms to the interstitial are also allowed to relax to account for the change in neighbors due to the SF. The resulting structures are visualized with Ovito [211].

Within PFDD, the concentration c^i is assumed to be equal to the concentration c^β for that site type. For the three octahedral orientations, Eq. (6.22) can be written as

$$\gamma_{usf}(\boldsymbol{c}) = \gamma_{usf}(0) + \frac{c^{[100]}}{A}\sum_{i=1}^{n^{[100]}} E^i_{int-SF} + \frac{c^{[010]}}{A}\sum_{i=1}^{n^{[010]}} E^i_{int-SF} + \frac{c^{[001]}}{A}\sum_{i=1}^{n^{[001]}} E^i_{int-SF} \quad (6.28)$$

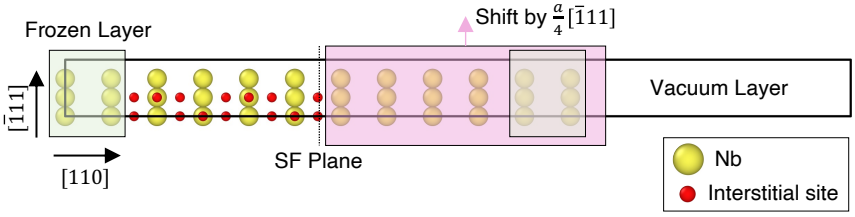

Figure 6.1: The simulation cell used to calculate the stacking fault-interstitial interaction energies. The interaction energies are calculated for 14 distinct octahedral interstitial sites indicated by red dots. The pink region is shifted by $\frac{a}{4}[110]$ to create a stacking fault.

where the first sum is over the [100] site types, the second over the [010] site types, and the third over [001] site types.

6.2.4 Phase-field simulation setup

In all PFDD simulations, a non-orthogonal BCC simulation cell with primitive vectors $\boldsymbol{e}_1 = [11\bar{1}]$, $\boldsymbol{e}_2 = [\bar{1}11]$, and $\boldsymbol{e}_3 = [1\bar{1}1]$ is used with grid spacing equal to one Burgers vector [167]. Periodic boundary conditions are used in all three dimensions. To allow for cross slip of screw dislocations, three slip systems are used, ϕ^1, ϕ^2, and ϕ^3. All three have slip direction $\mathbf{s}^1 = \mathbf{s}^2 = \mathbf{s}^3 = \frac{1}{\sqrt{3}}[\bar{1}11]$. The slip plane normal vectors are $\mathbf{n}^1 = \frac{1}{\sqrt{2}}[110]$, $\mathbf{n}^2 = \frac{1}{\sqrt{2}}[01\bar{1}]$, and $\mathbf{n}^3 = \frac{1}{\sqrt{2}}[101]$.

To create a screw dislocation, the order parameter ϕ^1 is set to one between two dislocations parallel to $[\bar{1}11]$ on the (110) plane. All other order parameters are set to zero. The simulation grid is $128b$ x $8b$ x $128b$, creating infinitely long screw dislocations separated by $64b$. To create an edge dislocation, the order parameter ϕ^1 is set to one between two dislocations parallel to $[1\bar{1}2]$ on the (110) plane, with all other order parameters equal to zero. The simulation grid is $128b$ x $128b$ x $384b$, creating two infinitely long edge dislocations separated by $64b$.

The applied stress to the simulation cell is always a pure shear stress with the maxi-

mum resolved shear stress plane (MRSSP) corresponding to the (110) habit plane or one of the two cross slip planes, $(01\bar{1})$ and (101). To find the critical stress to glide on one of these planes, the stress is increased from 0 in increments of $0.001G$ where G is the shear modulus until dislocation glide is observed.

Experimental values are used for the elastic stiffness tensor of Nb, setting $C_{11} = 245$ GPa, $C_{12} = 132$ GPa, and $C_{44} = 28.4$ GPa in Equations (1.2) and (1.4) [168]. Full elastic anisotropy is employed. The Voigt-averaged shear modulus $G = 39.64$ GPa is only used to normalized the energy densities and stresses. The lattice parameter a is set to the experimental value of 3.301Å [168]. The interplanar distance d^{α} in Equation (1.5) is set to 0.8165.

In the Ginzburg-Landau minimization (Eq. (1.8)), the quantity $m_{disl}\Delta t$ is set to $0.25G^{-1}$. The quantity $m_{int}\Delta t/c^{tot}$ is also set to $0.25G^{-1}$ (Eq. (6.19)). By defining the mobility constants as the product of mobility and the simulation time step, there is no physical time scale in the current simulations. In what follows, evolution is compared among different situations for a fixed number of time steps. The dislocation configuration is considered converged if the Euclidean norm of the change in order parameters between successive timesteps is less than 10^{-4}.

6.2.5 Minimizing Gibbs oscillations

Due to the discrete Fourier transform used in calculating the elastic strains, the stress fields calculated by PFDD exhibit Gibbs oscillations in the periodic directions. While the presence of these oscillations was known previously [167], they were generally ignored since their presence is primarily in the out-of-slip plane direction and therefore not seen by the gliding dislocations. However, when considering the case of interstitial diffusion, the presence of artificial local minima and maxima in stress causes significant problems.

Interstitial atoms will pool into wells of low chemical potential that are not true local minima and are simply artifacts of the Fourier solver. Reducing Gibbs oscillations is, therefore, necessary to reliably simulate interstitial diffusion.

Gibbs oscillations appear due to the difficulty of representing a discontinuous function in Fourier space, and researchers in many fields have developed various methods to minimize their presence [231]. Here, two separate methods are employed to minimize the Gibbs oscillations in PFDD. First, a modified Green's function is employed, which was first introduced by Willot [232]. In PFDD, the total strain is given in Fourier space by

$$\hat{\epsilon}_{kl} = [c_{iukv} q_u q_v]^{-1} q_j q_l c_{ijmn} \hat{\epsilon}^0_{mn} \tag{6.29}$$

where $\hat{}$ denotes the Fourier transform, ϵ^0_{mn} is the total eigenstrain (Eqs. (1.5) and (6.3)), and $\boldsymbol{q}$ is the wavenumber vector. The quantity $[c_{iukv} q_u q_v]^{-1}$ is the Green's function G_{ki} [78], so this original form is denoted G^0 to represent the original Green's function. This expression is derived using continuous differentation of the strains. Willot replaces the continuous derivatives with finite difference approximations [233]. The finite differences are calculated using a centered, rotated grid in which the strains are evaluated at the centers of the voxels and the displacements are evaluated at the corners [232]. In this formulation, the total strain is given by

$$\hat{\epsilon}_{kl} = [c_{iukv} k_u(\boldsymbol{q}) k_v(\boldsymbol{q})]^{-1} k_j(\boldsymbol{q}) k_l(\boldsymbol{q}) c_{ijmn} \hat{\epsilon}^0_{mn} \tag{6.30}$$

where

$$k_j(\boldsymbol{q}) = \frac{i}{4} \tan\left(\frac{\boldsymbol{q} \cdot \boldsymbol{e}^l}{4}\right) \left(1 + e^{i\boldsymbol{q}\cdot\boldsymbol{e}^1}\right) \left(1 + e^{i\boldsymbol{q}\cdot\boldsymbol{e}^2}\right) \left(1 + e^{i\boldsymbol{q}\cdot\boldsymbol{e}^3}\right) \xi^l_j \tag{6.31}$$

where $\boldsymbol{e}^j$ and $\boldsymbol{\xi}^j$ are the primitive vectors in real and Fourier space, respectively, and the

form is generalized from [232] to account for non-orthogonal grids. This formulation is denoted G^R for the rotated Green's function.

Figure 6.2(A) and (B) compare the stress field of a screw dislocation with G_0 and G^R as calculated with PFDD. The Gibbs oscillations, most prominent in the $[11\bar{1}]$ direction, are significantly reduced by using the modified Green's function. Smaller oscillations still appear in the $[\bar{1}11]$ direction, so a second modification, a Gaussian blur, is added to the strain calculation [234]. An approximate 3x3x3 Gaussian filter matrix F is defined as

$$F = \begin{array}{ccc} \frac{1}{64} & \frac{1}{32} & \frac{1}{64} \\ \frac{1}{32} & \frac{1}{16} & \frac{1}{32} \\ \frac{1}{64} & \frac{1}{32} & \frac{1}{64} \end{array} \quad \begin{array}{ccc} \frac{1}{32} & \frac{1}{16} & \frac{1}{32} \\ \frac{1}{16} & \frac{1}{8} & \frac{1}{16} \\ \frac{1}{32} & \frac{1}{16} & \frac{1}{32} \end{array} \quad \begin{array}{ccc} \frac{1}{64} & \frac{1}{32} & \frac{1}{64} \\ \frac{1}{32} & \frac{1}{16} & \frac{1}{32} \\ \frac{1}{64} & \frac{1}{32} & \frac{1}{64} \end{array} \tag{6.32}$$

The blurred strain is the convolution of the calculated strain and F. This effectively reassigns the strain at each point to be a weighted average of its strain and its neighbors' strains. Since the Gibbs oscillations are between nearest neighbor points, this drastically reduces any oscillations, as shown in Figure 6.2(C) and (D).

To completely eliminate the most prominent Gibbs oscillations in the calculated stress, it is sufficient to use either only G^R or only the Gaussian blur (Figure 6.2(E)). However, the interstitial diffusion depends not just on the local value of stress, but on its second derivative through the chemical potential. The chemical potential μ due to the dislocation stress field is predicted using Equation (6.15), and its Laplacian is plotted in Figure 6.2(F) along the $[11\bar{1}]$ direction. For clarity, only the blurred values are shown, as the unblurred values show much more extreme oscillations. While $\nabla^2\mu$ exhibits oscillations when using G^0 and the Gaussian blur, it is monotonically increasing when using G^R and the Gaussian blur. Even though the oscillations from using G^0 are small

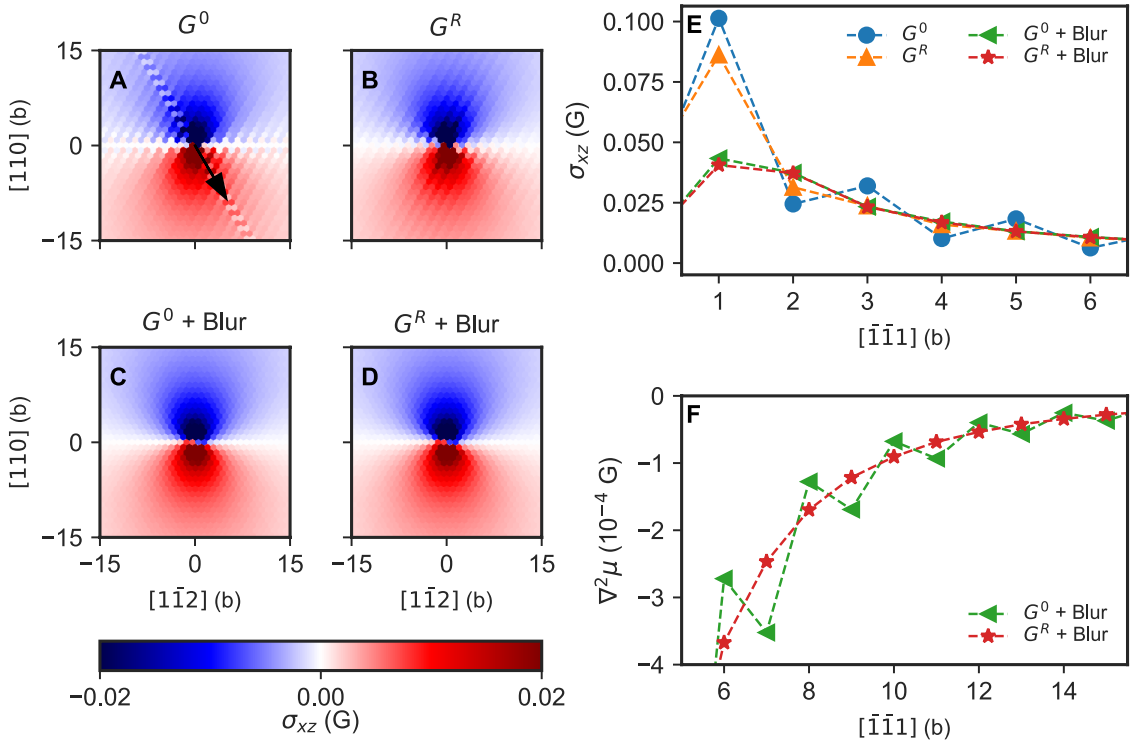

Figure 6.2: (A)-(D) The xz component of stress around a screw dislocation as calculated with PFDD. (A) shows the field for the original PFDD formulation. (B),(C), and (D) show the field using a rotated, centered Green's function, a Gaussian blur, and both, respectively. (E) The xz component of stress plotted in the [$\bar{1}\bar{1}$1] direction, indicated by the black arrow in (A). (F) The Laplacian of the chemical potential in the [$\bar{1}\bar{1}$1] direction

in magnitude, they compound over time as the concentration at a grid point evolves at a different rate than its neighbors, leading to larger magnitude oscillations in the local interstitial concentration. For this reason, both G^R and the Gaussian blur are used in all subsequent simulations. In addition to the stress and strain calculations, which affect interstitial diffusion, this will also affect the elastic energy calculation, which uses the Green's function.

6.3 Results

6.3.1 Nb-O interstitial parameters

The elastic dipole tensor for oxygen in Nb is calculated to be

$$P = \begin{pmatrix} 11.4 & 0 & 0 \\ 0 & 4.45 & 0 \\ 0 & 0 & 4.45 \end{pmatrix} eV \tag{6.33}$$

for a [100]-oriented interstitial site. The [010]- and [001]-oriented sites have P_{11} swapped with P_{22} or P_{33}, respectively. Only one experimental measurement of this tensor was found in the literature [235, 236]. These Snoek effect measurements reported P_{11} = 11.8eV and $P_{22} = P_{33}$ = 4.89eV, giving good agreement with the above DFT result. Converted to the λ^{int}-tensor through the experimental elastic constants, λ_{11}^{int} = 0.485 and $\lambda_{22}^{int} = \lambda_{33}^{int}$ = -0.0645.

The DFT-calculated interstitial-SF interaction energies are shown in Figure 6.3. The [100]- and [010]-oriented sites, which lie between (110) slip planes, have essentially identical, positive interaction energies which decay towards zero as the distance from the SF plane increases. The interstitial sites within the SF itself become distorted upon shearing, and have a slightly lower interaction energy than those $1d_{110}$ from the SF plane. The important difference is that the [001]-oriented sites, which lie within (110) planes, have interaction energies that are dependent on whether shearing changes the number of neighboring Nb atoms. When the interstitial is directly adjacent to the SF plane, the interaction energy is negative. At this site, there is one Nb neighbor in the [110]-direction which lies across the SF plane. After shearing by $\frac{a}{4}[\bar{1}11]$, the interstitial now straddles two Nb neighbors across the the SF plane, giving it seven neighbors instead of

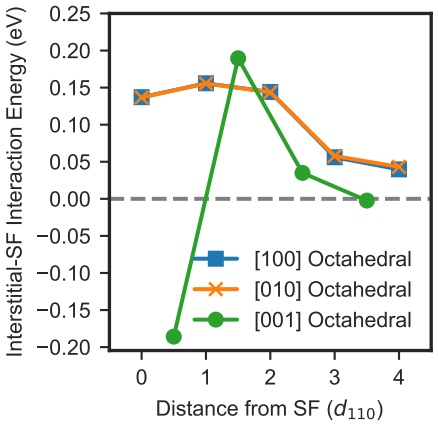

Figure 6.3: The interstitial-stacking fault interaction energies for each interstitial site as a function of distance from the stacking fault plane.

six, and thus an increased site volume. At all other sites, the interstitial neighbors are unchanged upon shearing, and interaction energies are positive and decay towards zero as the distance from the SF increases.

Inserting these interaction energies into Equation (6.28) yields

$$\gamma_{usf}(\boldsymbol{c}) = 677 + 1100c^{[100]} + 1100c^{[010]} + 74c^{[001]}[\mathrm{mJ/m^2}] \tag{6.34}$$

for the (110) plane. The interstitial site types are rotated accordingly for the $(01\bar{1})$ and (101) planes.

The simulation cell size used here only includes interstitial sites up to $4d_{110}$ from the SF. The magnitude of the interaction energy at $4d_{110}$ is 26% of its peak magnitude for the [100]- and [010]-oriented sites. While it is very likely that interstitial sites further from the SF will have also have non-zero interaction energies, they are expected to continue to decay from this value towards zero. In contrast, the interaction energies for the [001]-oriented sites decay much more quickly, and reach nearly zero at the fourth site from the SF.

6.3.2 Relaxed dislocation cores in static interstitial field

First, let us consider the situation in which the interstitials are immobile to understand their effect on the dislocation core structures. The core structures, represented by the three active order parameters, are shown in Figure 6.4 for dislocations relaxed in interstitials fields with constant concentration c^{tot} between 0 and 0.05. Interstitial diffusion is disallowed by setting $m_{int} = 0$. The total concentration is equally divided among the three available site orientations. As observed in previous works, both screw and edge dislocations show slight spreading within the (110) plane, while only screw dislocations spread onto the $(01\bar{1})$ and (101) cross slip planes. Visually, the shape of the core and type of spreading (i.e. planar or non-planar) is not significantly influenced by the interstitial concentration. However, the width of the dislocations within the (110) plane slightly narrows with increasing concentration. The dislocation core width is defined as the distance within the (110) slip plane from where $\phi^1 = 0.05$ and $\phi^1 = 0.95$, using a linear interpolation between grid points as necessary.

The simulations are repeated using only the long-range dislocation-interstitial interactions (by setting γ_{usf} to a constant 677 mJ/m^2) or the short-range interactions (by setting $\lambda_{ij}^{int} = 0$). For a homogeneous interstitial field, only the short-range interactions affect the dislocation results since the interstitial strain is constant throughout the cell. Therefore, the narrowing of the dislocation core width is caused solely by the increase in γ_{usf} with increasing oxygen concentration.

6.3.3 Interstitial distribution around dislocations

In actuality, the interstitials may not be uniformly distributed throughout the cell, but may instead segregate around defects based on the local chemical potential. The diffusion of oxygen interstitials is simulated around previously relaxed and frozen screw

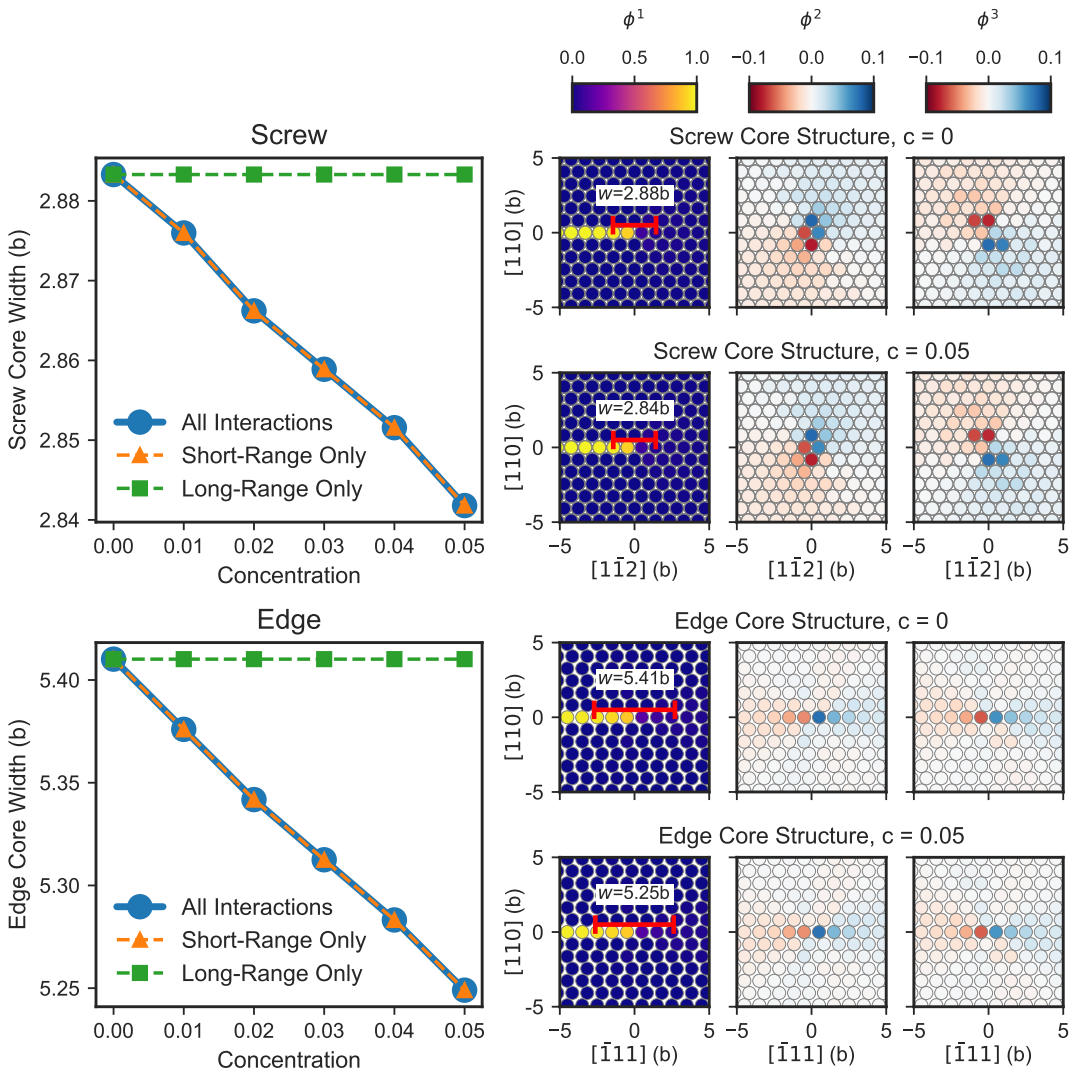

Figure 6.4: (Left) The equilibrium dislocation core widths for screw and edge dislocations as a function of oxygen concentration. (Right) The dislocation core structures for screw and edge dislocations represented by the PFDD order order parameters.

and edge dislocation cores using initial concentrations c_0 ranging from 0.01 to 0.05. Figure 6.5(A)-(D) and Figure 6.6(A)-(D) show the evolution of total concentration around a screw and edge dislocation core, respectively. The simulations show that, when normalized by c_0, the evolution of the interstitial concentration is independent of the initial concentration. Since the chemical potentials are independent of the local concentrations $\boldsymbol{c}$, the concentration only comes into play through the interstitial mobility m_{int}, which scales with the local c^{tot} (Eq. (6.19)). In all cases, the shape of the interstitial concentration field is immediately apparent once diffusion begins and only intensifies over time. The change in interstitial concentration decreases at each time step but does not reach zero. At 0K, the equilibrium state will have the interstitials completely filling the lowest energy sites and all other sites empty [237], which does not occur within the simulation time period.

The evolution of local interstitial concentration is primarily due to the long-range elastic interactions between the interstitial and dislocation stress fields. Figure 6.5(E)-(G) show the long-range portion of the chemical potential (Equation (6.15)) around a screw dislocation for the three different octahedral site orientations, as calculated from the PFDD stress fields. The chemical potential for each site is identical with a 60° rotation. Unlike a hydrostatic interstitial strain, such as those in FCC crystals, the tetragonal symmetry of the BCC octahedral site allows the interstitial to interact with the shear stress field surrounding a screw dislocation. Taking the minimum of these three chemical potentials gives an overall energy landscape with three-fold symmetry (Figure 6.5(H)), where each of the three lobes prefers a different site orientation, matching prior computational predictions [238]. Local maximums in the overall chemical potential are formed where the individual chemical potential surfaces intersect. This causes a local depletion of interstitials at these cusps, which can be seen by the purple lines in Figure 6.5(D). When c^{tot} is decomposed into the three site orientations (Figure 6.7(A)-

(C)), each site is preferred in the lobe where its chemical potential is lowest, as expected. [238]

Because the edge dislocation has hydrostatic stress components in addition to shear components, its interaction with the interstitials is substantially different that of the screw dislocation. The long-range chemical potentials of the [100]- and [010]-oriented sites are identical but mirrored across the $(\bar{1}11)$ plane, while the form of the chemical potential for the [001]-oriented sites is unique. For all sites, the chemical potential is lowered when the interstitial is below the slip plane, where the hydrostatic stress is tensile. The combined chemical potential (Figure 6.6(H)) is not radially symmetric like the screw dislocation and shows a clear preference for sites in the tensile region. This is seen in the local depletion of interstitials above the slip plane in Figure 6.6(D). Unlike the screw dislocation, each site orientation is preferred in three distinct, non-continguous regions around the edge dislocation, forming a total of nine interfaces between regions of different preferred site orientations (Figure 6.7(D)-(F)).

These interstitial atmospheres can be compared and contrasted with those calculated analytically. Considering long-range, elastic interactions only, the distribution of interstitials in a dislocation stress field is given by [237]

$$\chi(\boldsymbol{r}) = \left(1 + \frac{1-\chi_0}{\chi_0} + exp\left(-\frac{E_{int}(\boldsymbol{r})}{k_B T}\right)\right)^{-1} \tag{6.35}$$

where χ is the interstitial fraction, equal to $c_{tot}/3$, χ_0 is the average interstitial fraction, and E_{int} is the interstitial-dislocation interaction energy. The interaction energy is calculated using the anisotropic PFDD stress fields (Eq. (1.1)), and the predicted equilibrium interstitial concentrations at $T = 300$K are shown in Fig. 6.8 along with the PFDD simulation results. Like the PFDD results, the analytical screw dislocation atmosphere shows three distinct lobes, and the analytical edge dislocation atmosphere

shows depletion above the slip plane and increased interstitial concentration below the slip plane.

However, there are several key differences between the analytical predictions and those simulated with PFDD. First, the analytical prediction shows the final, equilibrium distribution while the PFDD simulations capture intermediate steps during the interstitial diffusion. Second, the analytical solution includes temperature, while the PFDD simulations are performed at 0K. This causes the interstitials in PFDD to flow towards local minimums in chemical potential only with no temperature or entropic effects. The locally depleted regions on the boundaries between different interstitial orientations are created by this 0K behavior and are therefore not present in the analytical solution. The equilibrium 0K atmosphere, as noted by Cai et al. would show the lowest chemical potential regions completely filled with interstitials ($\chi = 1$) and all other regions completely depleted of interstitials ($\chi = 0$) [237]. By simulating interstitial diffusion, PFDD has the advantage of capturing intermediate and meta-stable interstitial concentration fields. Finally, analytical calculations typically assume elastic isotropy, while PFDD accounts for full elastic anisotropy.

6.3.4 Dislocation glide

After relaxing the interstitial concentration for 2000 timesteps, the concentration fields are frozen and a shear stress applied to the (110) slip plane, starting from zero and incrementing by $0.001G$. The stress required to initiate dislocation glide is recorded and shown in Figure 6.9 as a function of average oxygen concentration c_0. The breakaway stress σ_b, defined as the stress required to glide completely across the simulation cell, is indicated by the closed symbols. Below σ_b, the dislocations are able to glide a short distance before becoming pinned again. An initial critical stress σ_i is defined as the stress

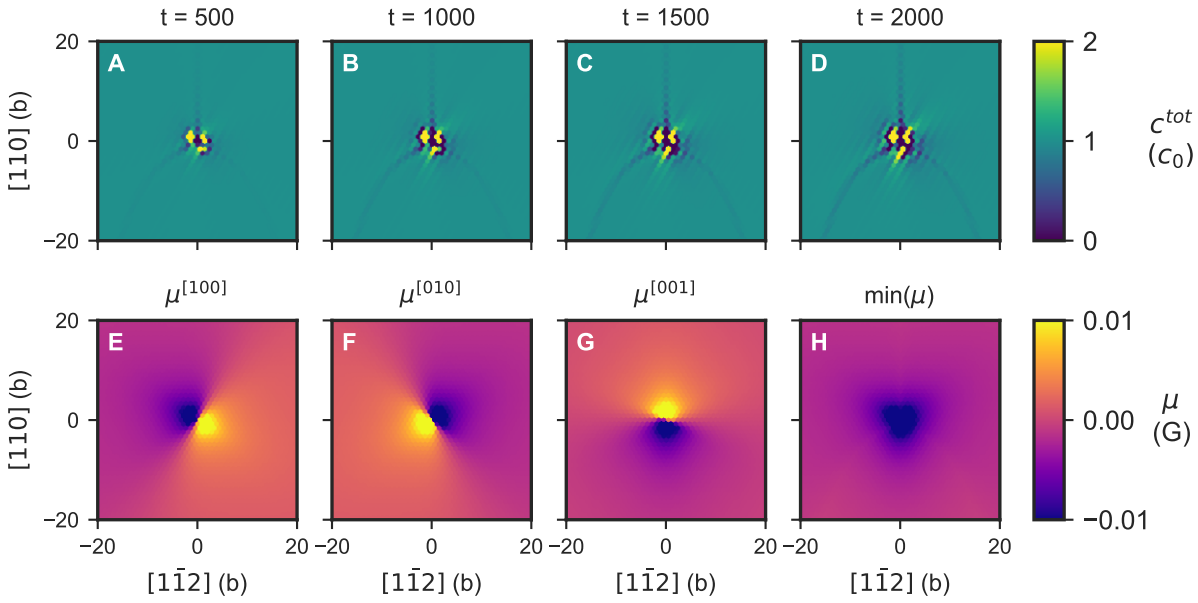

Figure 6.5: (A-D) The evolution of total oxygen concentration around a screw dislocation where c_0 is the bulk oxygen concentration. (E-G) The chemical potential of oxygen interstitials in different interstitial site orientations due to a screw dislocation stress field. (H) The minimum chemical potential of the three site orientations.

required to glide at least $1b$, which is indicated by the open symbols in Figure 6.9. This is in contrast to dislocation glide in interstitial-free Nb, which has a single critical stress, σ_b.

For edge dislocations, both the σ_i and σ_b increase with interstitial concentration. The dislocation core, in its initial position, decreases in width with increasing interstitial concentration, thus increasing σ_i. Because of the dislocation stress field, the region directly in front of the edge dislocation is depleted of interstitials as interstitial atoms flow to the tensile region below the slip plane. The dislocation is able to glide easily through this region for $3b$ before becoming pinned again where the interstitial concentration is non-zero. The stress required to overcome the barrier to glide into the interstitial region is then σ_b. When c_0 equals 0.05, the stress required to break into this region is so high that dislocations form elsewhere in the cell where the stress is sufficiently high. In reality,

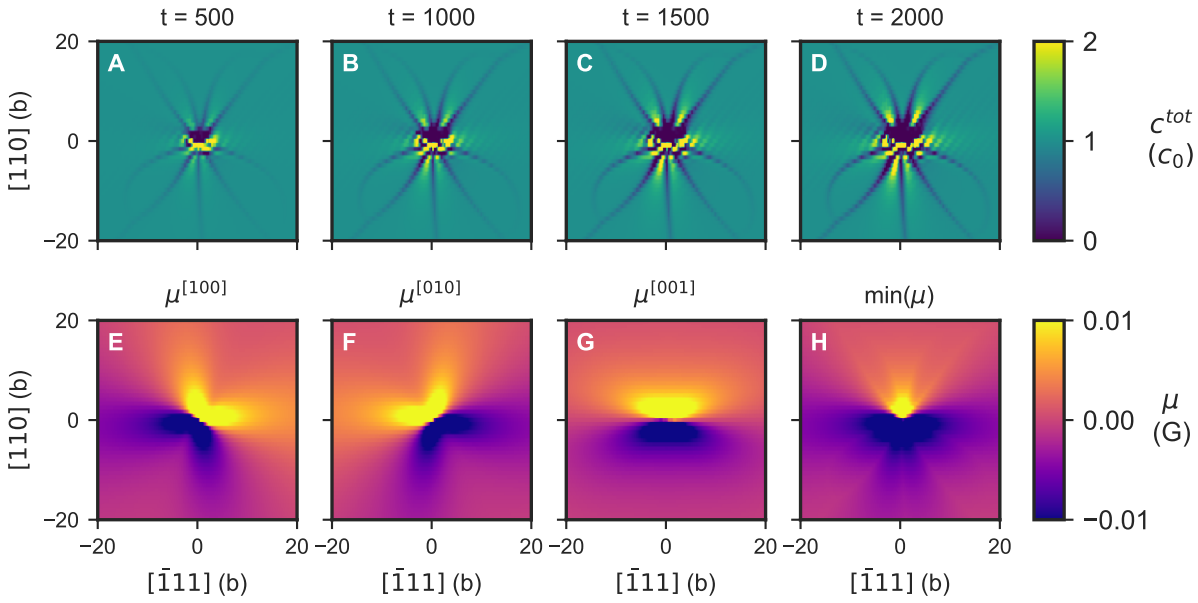

Figure 6.6: (A-D) The evolution of total oxygen concentration around an edge dislocation where c_0 is the bulk oxygen concentration. (E-G) The chemical potential of oxygen interstitials in different interstitial site orientations due to the edge dislocation stress field. (H) The minimum chemical potential of the three site orientations.

thermal assistance may be needed to overcome this high barrier, and thus this value is excluded from Figure 6.9. If, instead of 2000 timesteps, the interstitial field is relaxed for 500, 1000, or 1500 timesteps before the critical stress calculations, the linear trend of σ_b with average interstitial concentration continues to $c_0 = 0.05$. After fewer timesteps, the concentration at the dislocation cores is less extreme, and thus glide is still possible at $c_0 = 0.05$.

The critical stresses for screw dislocations follow a markedly different trend, as σ_i decreases with increasing concentration due to the change in core structure. Figure 6.10 shows the core structure for a screw dislocation with c_0 equal to 0.04 both before and after interstitial diffusion. After diffusion, the dislocation core is less spread onto the cross slip planes, as indicated by the lower magnitude of ϕ^2 and ϕ^3 on these planes. This is most noticeable on the (101) plane, which corresponds to ϕ^3. Because the spread,

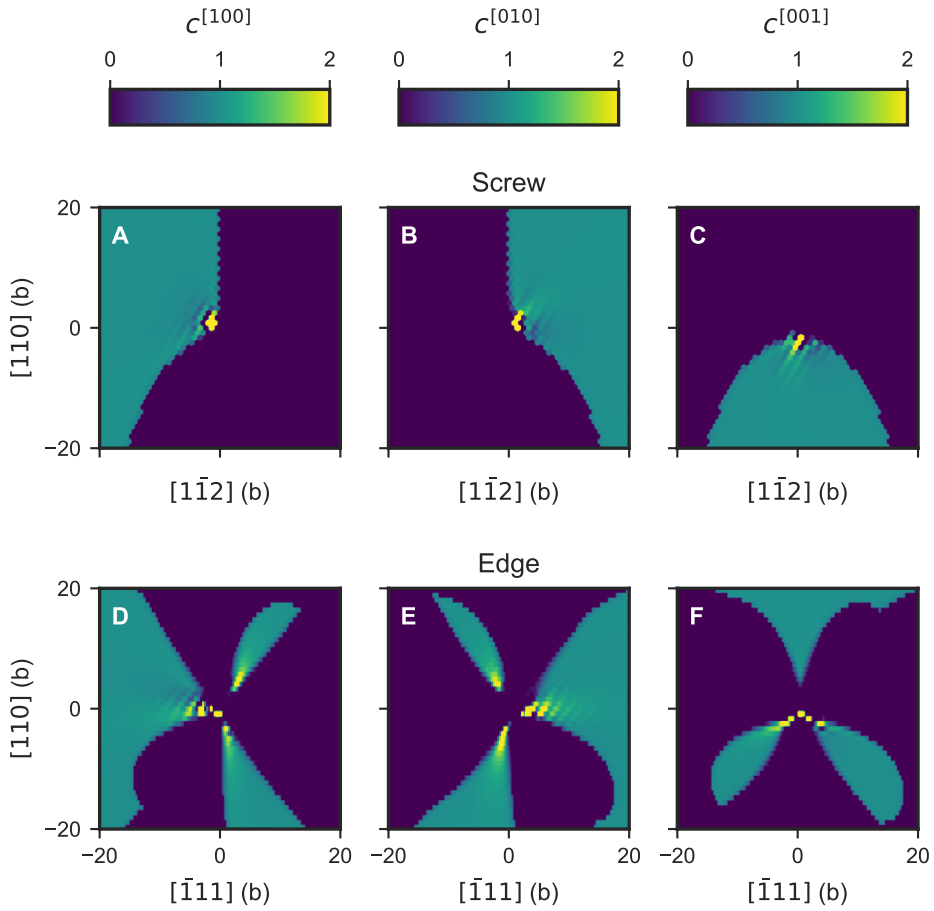

Figure 6.7: The concentration of each interstitial site orientation at time $t = 2000$ for a screw (A-C) and an edge (D-F) dislocation.

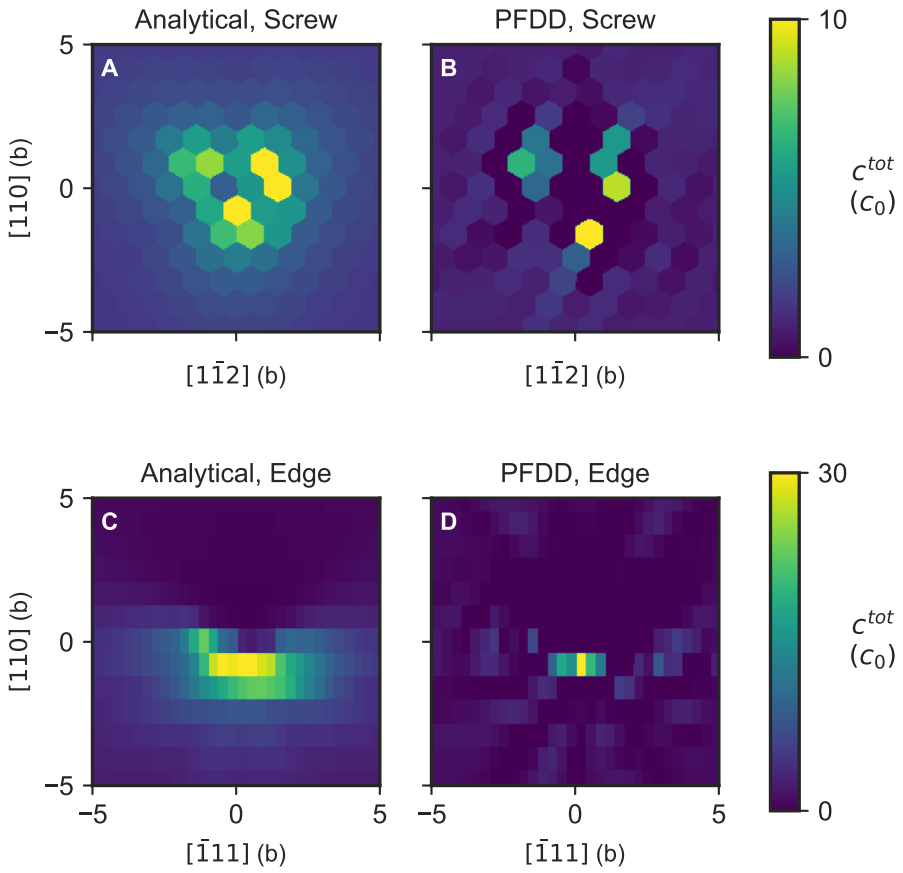

Figure 6.8: The interstitial distribution around screw and edge dislocations calculated both analytically and with PFDD.

non-planar screw core is more difficult to glide than compact cores, this has the effect of decreasing the glide stress.

After gliding $1b$, the dislocation encounters a region of high interstitial concentration and becomes pinned again. The breakaway stress σ_b is then the stress required to slip past this region. While σ_b increases with interstitial concentration like the edge dislocation, the magnitude of stress levels off around $c_0 = 0.02$. Closer inspection of the dislocation glide path reveals that, at these concentrations, the dislocation cross slips to an adjacent (110) plane to avoid a locally high concentration of interstitial atoms (Figure 6.9). This new glide plane is depleted of interstitials, and therefore the stress required for this process is less dependent on average concentration, and thus σ_b levels off towards a constant value.

When the maximum resolved shear stress plane is not the (110) habit plane, the screw dislocation is able to cross slip to a more favorable glide plane. The above simulations are repeated for the screw dislocation with the maximum resolved shear stress (MRSS) on the $(01\bar{1})$ or (101) plane. The critical resolved shear stress for dislocation glide is shown in Figure 6.11(A). The path of the dislocation gliding on the $(01\bar{1})$ plane is shown in Figure 6.11(C) by the sum of the three order parameters. Like the simulations above on the (110) plane, the dislocation will glide $1b$ on the (110) plane before becoming pinned. The dislocation will then have to overcome a high interstitial concentration on the $(01\bar{1})$ plane. At interstitial concentrations less than or equal to 0.03, the critical stress required for cross slip onto the $(01\bar{1})$ plane decreases with concentration, which is attributed to the decreased screw core spreading. At higher interstitial concentrations, the critical stress begins to increase sharply due to the significant increase in USFE with higher interstitial concentrations, and therefore higher stress required to break into these high concentration regions.

When the MRSS is on the (101) plane, the critical stress increases sharply even from at low interstitial concentrations. Cross slip is observed onto the (101) plane for $c_0 = 0.01$

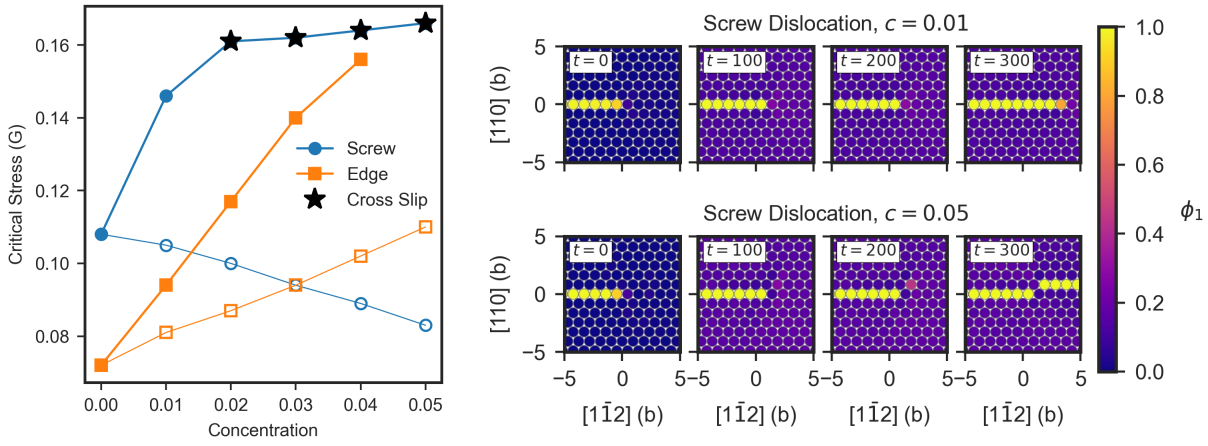

Figure 6.9: (Left) The stress required to initiate dislocation glide for screw and edge dislocations as a function of interstitial concentration. The open symbols correspond to the stress to glide at least one Burgers vector (σ_i), and the closed symbols correspond to the breakaway stress (σ_b) to glide completely across the slip plane. (Top Right) Image of screw dislocation glide at a lower interstitial concentration, which glides within the (110) habit plane. (Bottom Left) Image of screw dislocation glide at a higher interstitial concentration, which cross slip onto an adjacent (110) plane.

(Figure 6.11(D)), but above this concentration, the applied stress required is so high that dislocation nucleation is again observed in high-strain regions. Like the edge dislocation, this case most likely requires thermal activation to glide.

6.4 Discussion

The PFDD-interstitial formulation has several advantages over prior PFDD models and other methods of modeling dislocation-interstitial interactions. First, this model is the first phase-field model to include the tetragonal distortion created by interstitials in BCC materials. This significantly changes the interaction of interstitials with dislocations' stress fields, particularly screw dislocations, whose shear stress fields do not interact with hydrostatic strains. Including the tetragonal distortion necessitates tracking the concentration of multiple interstitial site types and coupling their total concentrations.

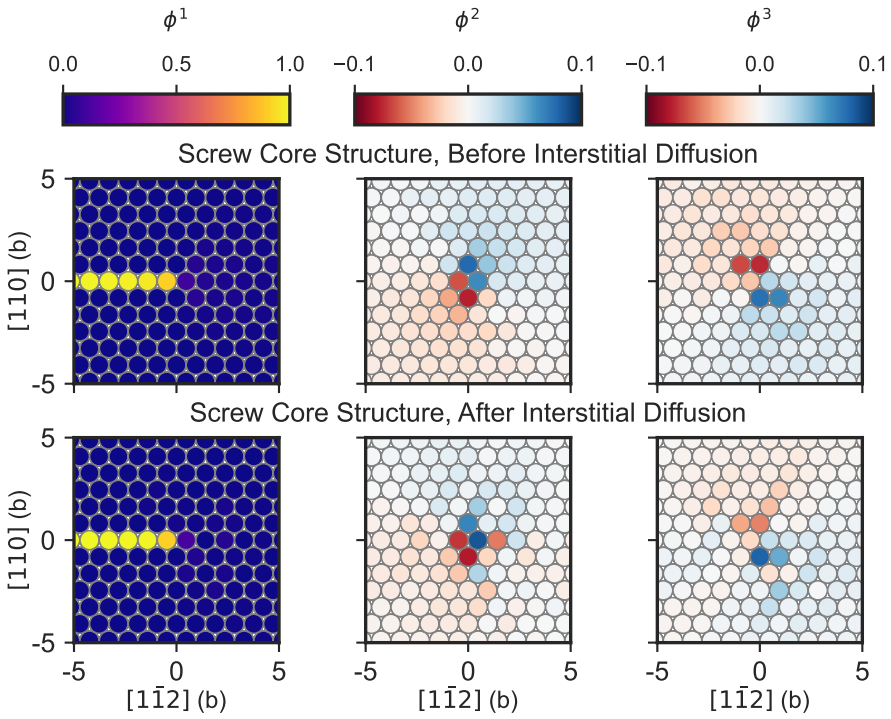

Figure 6.10: Screw dislocation core structure before (top) and after (bottom) interstitial diffusion for average concentration $c = 0.04$.

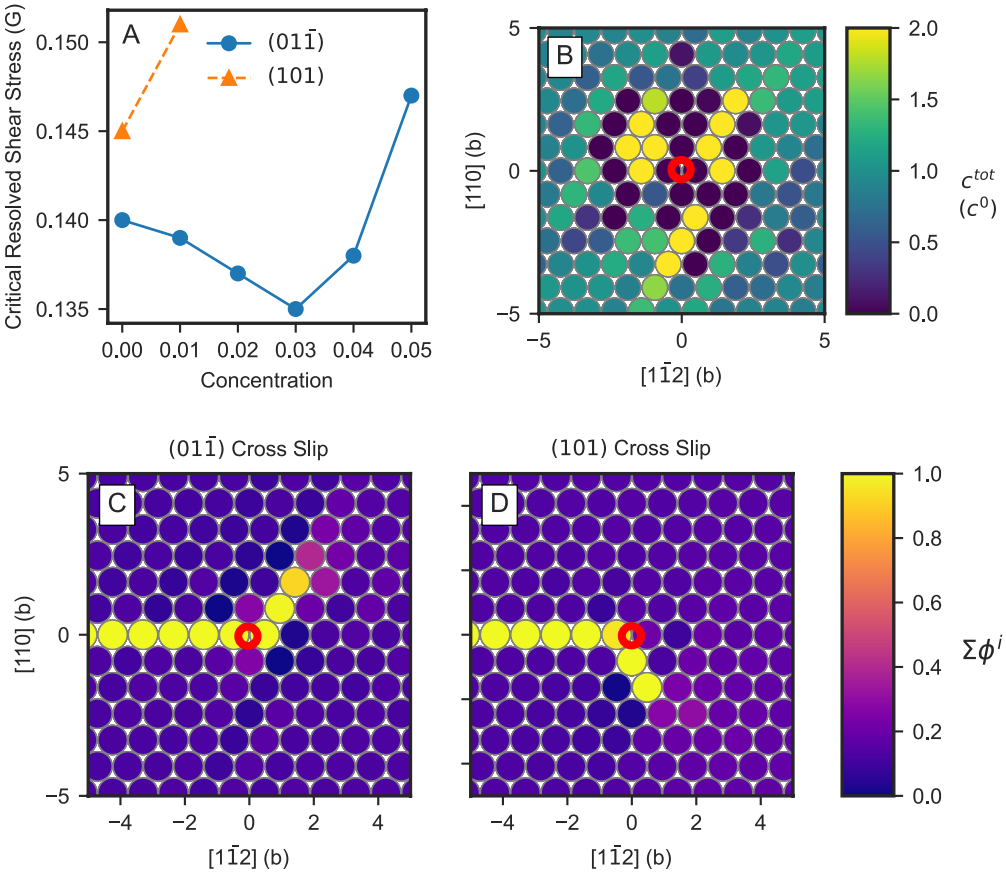

Figure 6.11: (A) The critical resolved shear stress required to initiate cross slip onto each of the two cross slip planes. (B) The total concentration of interstitials around the screw dislocation core. (C) and (D) The dislocation path during cross slip onto the (01$\bar{1}$) or (101) plane, respectively. The red circle indicates the initial position of the screw dislocation in (B), (C), and (D).

The model assumes interstitial diffusion from one site orientation to another at the same PFDD grid point was instantaneous, whereas diffusion between grid points is controlled by the interstitial mobility m_{int}, an assumption made in other models [221, 239]. By including a diffusive time scale, intermediate, pre-equilibrium interstitial concentration states can be captured. Finally, the combination of a modified Green's function and a blurring function significantly decrease the presence of Gibb's oscillations, an artifact of the Fourier transform.

The dislocation core calculations show that the core structures are influenced primarily by the short-range interactions, which is expected and has been shown in both phase-field and atomistic models [58, 59, 219]. Long-range interactions, on the other hand, control the diffusion of interstitials within the dislocation stress field and the formation of a Cottrell and Snoek atmosphere. The shape of the interstitial concentration fields around screw and edge dislocations qualitatively match analytical predictions, verifying the phase-field formulation [238–240]. The major difference between these calculations and prior analytic calculations is that the analytic calculations include an entropic term in the generalized chemical potential [238, 239], whereas the PFDD calculations are performed without temperature. This causes the PFDD-interstitial model to predict locally depleted interstitial regions at the border between two regions with different interstitial site types. At these borders, there is a cusp in the local chemical potential, and the atoms are driven towards local minima in the absence of thermal fluctuations.

As expected, the solute atmospheres increase the critical stress for a dislocation. While the breakaway stress σ_b increases linearly with interstitial concentration for edge dislocations, σ_b for screw dislocations levels off above a critical interstitial concentration. At higher concentrations, the dislocation will cross slip to a more favorable glide plane. This suggests that there is a limit to interstitial strengthening by increasing the glide stress alone; other mechanisms, like cross slip, can be activated and must be considered.

In addition to σ_b, the dislocations are able to glide a short distance, between 1 and $3b$, at a lower stress before becoming pinned. This initial glide stress σ_i is controlled by different factors for screw and edge dislocations. For screw dislocations, the dislocation cores become more planar, and σ_i decreases with interstitial concentration. Conversely, for edge dislocations, the narrower dislocation core causes σ_i to increase with interstitial concentration. While dislocation simulations in BCC metals frequently study screw dislocations only, these results suggest that screw and edge dislocations interact with interstitials in distinct ways and should both be considered.

This PFDD-interstitial model has the necessary components to simulate the various complicated dislocation-interstitial interactions that can take place, both in the short- and long-range. By controlling the ratio of the mobility coefficients m_{int} and m_{disl}, future simulations can include the dynamic nature of interstitial diffusion and dislocation glide to capture the Portevin-Le Chatelier effect. Because the model includes screw dislocation cross slip, the formation of kinks on alternating glide planes can allow for cross-kink formation, thought to be another important dislocation strengthening mechanism. Finally, including temperature in the model in the future would allow for a physical timescale to be obtained, and for thermally activated mechanisms, like kink-pair nucleation, to be simulated.

6.5 Conclusion

The PFDD model was extended to include the diffusion of interstitial solute atoms. The model tracks the local concentration of interstitial atoms through coupled phase-field variables, and both short- and long-range interactions are accounted for. The new formulation is verified for a model system by calculating Nb dislocation core structures in the presence of O interstitials, and then predicting the formation of interstitial at-

mospheres around static dislocation cores. These calculations show that the interstitials influence dislocation core structures through short-range interactions, whereas dislocations influence interstitial diffusion through long-range interactions. The critical stress required for dislocations to break away from a solute atmosphere increases linearly with concentration for edge dislocations, while screw dislocations are able to cross slip onto a more favorable glide plane above a critical concentration. In future work, the model can be used to study more complex interactions between dislocations and interstitial atoms, including the Portevin-Le Chatelier effect and cross kink formation.

Chapter 7

Effect of Interstitial Atoms on Dynamic Dislocation Glide

7.1 Introduction

Pure refractory metals readily absorb interstitials elements such as O, C, and H from the atmosphere, typically with deleterious effects on their mechanical properties [4]. These interstitials generally cause an increase in strength at the expense of ductility [43–45]. However, the mechanisms by which these elements affect dislocation behavior are not completely understood and are likely to be different for different interstitial atom types. In BCC crystals, larger interstitials like O and C occupy the octahedral sites in the lattice, creating a tetragonal distortion with three distinct orientations depending on the specific octahedral site. The interstitials may adopt the lowest energy orientation for a given stress state, forming a Snoek atmosphere [53].

H interstitials, which also have a negative impact on mechanical properties, are believed to affect dislocation glide through different mechanisms than larger interstitials like O or C. Instead of pinning dislocations, Hmay promote dislocation glide, causing

embrittlement through hydrogen-enhanced local plasticity (HELP) [66–68, 241]. Macroscopically, the increased dislocation mobility causes highly planar, localized slip, leading to failure [67]. Unlike O or C, H atoms are small and can diffuse quickly through the lattice, making it possible for interstitial atoms to keep up with gliding dislocations. The H interstitial atmosphere reduces the dislocation's effective stress field in a process known as hydrogen shielding, lowering interactions with obstacles and other dislocations and thereby increasing mobility [67, 242]. However, there is still controversy over whether hydrogen shielding is the cause of hydrogen-enhanced local plasticity (HELP), with some computational models attributing thee increased mobility to short-range core effects instead of long-range elastic effects [68–70, 243]. By comparison, C and O, being larger atoms, generally cannot diffuse fast enough to keep up with gliding dislocations. This can cause a serrated flow behavior in which dislocations repeatedly break free from and then are pinned by a trailing interstitial atmosphere, which is known as the Portevin-Le Chatelier effect [55, 71].

Because direct experimental observation of dislocation interactions with interstitials is extremely difficult, simulation tools can be used to understand dislocation mechanisms at the nanoscale. Due to the atomistic nature of interstitial-dislocation interactions, much of the modeling of interstitial effects is done with DFT or MD. DFT simulations are critical for determining the properties of isolated interstitial atoms [51] or, in some cases, dislocation core structures [57, 58, 61], but the length scales are generally too short to simulate the interactions between interstitials and dislocations. MD simulations can access longer length scales, but interstitial diffusion is rare on MD time scales. For this reason, most MD simulations examine a dislocation gliding through a random field of essentially stationary interstitial atoms, find that both screw and edge dislocations can become pinned when encountering a large interstitial atom like C or O [59, 64, 244]. Screw dislocations, which are especially important in BCC crystals, experience

more difficult glide due to pinning of migrating kinks and the formation of cross-kinks [59, 64]. However, none of these simulation are able to capture the effects of interstitial atmospheres trailing gliding dislocations, which is necessary to study mechanisms like hydrogen shielding and the Portevin-Le Chatelier effect.

There is significant interest in using mesoscale models, which can access longer time and length scales, to study interstitial-dislocation interactions. Elastic shielding effects have been included in discrete dislocation dynamics, showing the hydrogen shielding increased dislocation slip planarity and reduced dislocation pileup spacing in BCC metals [242]. Recently, a kinetic Monte Carlo model was used to study interstitial-dislocation interactions in W-O [71]. The model allowed for both interstitial diffusion and kink-pair nucleation and migration, and the simulations reveal the Portevin-Le Chatelier effect to occur only under certain temperature and strain rate combinations.

There remain open questions about the role of interstitials in dislocation glide in BCC crystals, and it is not fully understood how different types of interstitials, especially H compared to larger atoms like O or C, affect dislocations. Here, PFDD is used to study dislocation behavior in two model refractory-interstitial systems: Nb with O interstitials and W with H interstitials. The mesoscale time scales allow for simultaneous interstitial diffusion and dislocation glide, which is inaccessible for most atomistic simulation methods and has been minimally studied. The simulation parameters for Nb-O and W-H are obtained from both experiments and *ab initio* calculations.

PFDD is used to simulate perfectly straight, infinite edge and screw dislocations with dilute solute concentrations. The PFDD simulations reveal the different interstitial atmospheres that form around both edge and screw dislocations in the two systems due to differences in the interstitial site occupation of O and H. The critical stress required to glide is calculated as a function of interstitial concentration, showing that while O increases the breakaway stress for both screw and edge dislocations in Nb, H has minimal

impact on the critical stresses in W. Then, dislocation glide is simulated simultaneously with interstitial diffusion, varying the ratio between interstitial and dislocation mobility. In both systems, screw dislocation glide is enhanced by the presence of interstitials, while edge dislocation glide is enhanced in W-H and inhibited in Nb-O. The mechanisms responsible for these differences are examined and discussed. These simulations reveal how interstitial effects on dislocation glide varies depending on the interstitial type, site occupation, stress state, and mobility of the interstitials relative to dislocations.

7.2 Methods

The extended PFDD-interstitial formulation is described in Section 6.2. Several parameters are required to simulate a given solute-solvent system, including the elastic constants, lattice parameters, $\lambda_{ij}^{int,\beta}$, and the USFE as a function of concentration. For the two systems simulated here, Nb-O and W-H, the elastic constants and lattice parameters are taken from experimental measurements of pure Nb and W, respectively. The elastic constants are C_{11} = 245 GPa, C_{12} = 132 GPa, and C_{44} = 28.4 GPa for Nb and C_{11} = 523 GPa, C_{12} = 203 GPa, and C_{44} = 160 GPa for W, and the lattice constants are 3.301 Å and 3.165 Å respectively [168]. Full elastic anisotropy is employed, and all stresses in the simulations are normalized by the Voigt-averaged shear modulus G of the solvent element, 39.64 GPa for Nb and 160 GPa for W.

The interstitial distortion term $\lambda_{ij}^{int,\beta}$ can be obtained via experimental measurements or simulations [50, 56, 220]. The tensor for Nb-O was previously calculated in Chapter 6 using DFT calculations, and the value closely aligned with prior experimental measurements, and is given by

$$\lambda^{int,Nb-O} = \begin{pmatrix} 0.485 & 0 & 0 \\ 0 & -0.0645 & 0 \\ 0 & 0 & -0.0645 \end{pmatrix} \tag{7.1}$$

As expected for an octahedral site in BCC, this tensor has tetragonal symmetry, so there are three distinct orientations of the site that can have different chemical potentials. In all PFDD simulations of Nb-O, the three interstitial site types are included and interstitials will occupy the one with the lowest chemical potential.

H interstitials occupy the tetrahedral sites in W, creating a purely hydrostatic strain. Hou et al. calculated the excess volume of H in W for the tetrahedral site with DFT [245], which can be converted to a distortion tensor of

$$\lambda^{int,W-H} = \begin{pmatrix} 0.0677 & 0 & 0 \\ 0 & 0.0677 & 0 \\ 0 & 0 & 0.0677 \end{pmatrix} \tag{7.2}$$

In all PFDD simulations of W-H, only one interstitial site type is included as all tetrahedral sites are equivalent.

DFT is used to determine the USFE for each system as well as its dependence on local interstitial concentration following Eq. (6.22), which requires the interstitial-SF interaction energies. These were previously calculated for the Nb-O system (Section 6.3). To obtain the same parameters for the W-H system, DFT calculations were performed using VASP [230]. The projected augmented wave method is used with a plane-wave basis with cutoff energy of 600 eV. The Methfessel–Paxton smearing method is used with a smearing width of 0.2 eV. The ionic positions are relaxed with the conjugate gradient scheme until the energy change is less than 10^{-4} eV. The simulation cell has $\boldsymbol{x} = a[\bar{1}1\bar{2}]$, $\boldsymbol{y} = 6a[110]$, and $\boldsymbol{z} = \frac{a}{2}[\bar{1}11]$ where the equilibrium lattice parameter a for

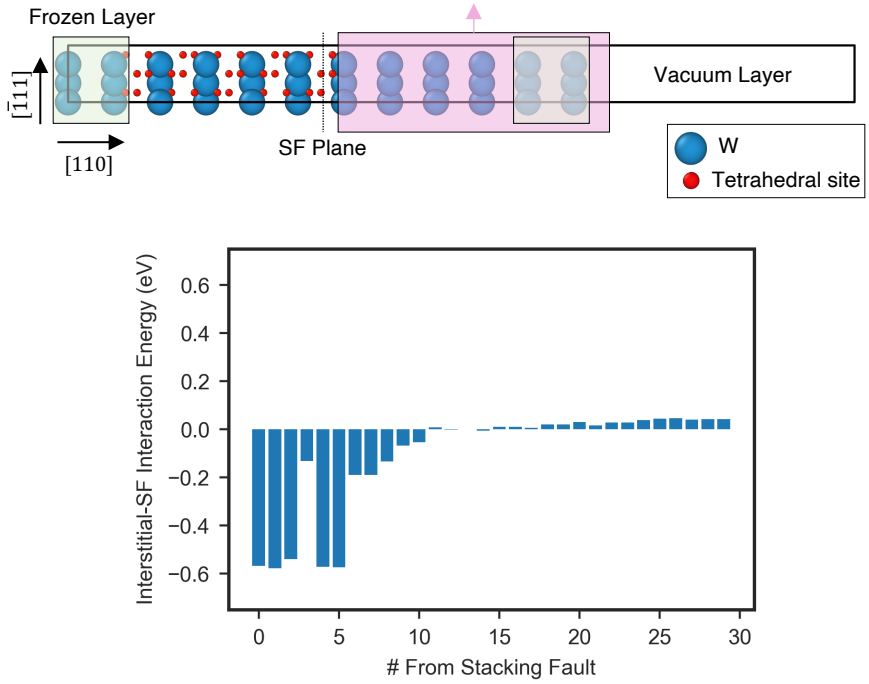

Figure 7.1: (Above) The simulation setup for DFT calculations of the stacking fault-interstitial interaction energies in W-H. There are 30 tetrahedral sites, numbered from 0 to 29 in increasing distance from the stacking fault. (Below) The calculated interaction energy for each site.

W equals 3.138Å [83]. A vacuum layer of 12 Å is added to the $\boldsymbol{y}$-dimension. The k-point mesh is 15 x 1 x 15. E_{bulk} is simply the energy of this structure after relaxation. E_{SF} is obtained by shifting the rightmost six (110) layers by $\frac{a}{4}[\bar{1}11]$. Then, the two outermost (110) layers on either side of the simulation cell are frozen, and the positions of all other atoms are relaxed in the $\boldsymbol{y}$ direction only.

Accounting for symmetry across the SF plane, 30 unique tetrahedral sites are identified within this structure (Fig. 7.1). To calculate E^i_{int-SF} for each of these sites, a H interstitial is placed in the site, and all atomic positions excluding the frozen layers are relaxed. The energy of the relaxed system is denoted $E^{int,i}_{bulk}$. Then, the rightmost 6 layers are translated, and the cell is relaxed again in the $\boldsymbol{y}$ direction only, giving $E^{int,i}_{SF}$.

The calculated interaction energies are plotted in Fig. 7.1. Only the ten interstitial sites nearest the SF have significant interactions with the SF. Using only these ten values within Eq. (6.22), the USFE for W varies with H concentration as

$$\gamma_{usf}(\boldsymbol{c}) = 1772 - 1330c[\mathrm{mJ/m^2}] \tag{7.3}$$

By contrast, the USFE for Nb increases with O concentration as

$$\gamma_{usf}(\boldsymbol{c}) = 677 + 1100c^{[100]} + 1100c^{[010]} + 74c^{[001]}[\mathrm{mJ/m^2}] \tag{7.4}$$

where $c^{[100]}$, $c^{[010]}$, and $c^{[001]}$ correspond to the concentration of octahedral sites with the specified orientation.

PFDD simulations are performed for both pure edge and pure screw dislocation dipoles. In all simulations, three order parameters are used, ϕ^1, ϕ^2, and ϕ^3, which all correspond to slip in the $[\bar{1}11]$ direction, and the slip planes are (110), $(01\bar{1})$, and (101), respectively. A non-orthogonal simulation cell is used with primitive vectors $\boldsymbol{e}_1 = [11\bar{1}]$, $\boldsymbol{e}_2 = [\bar{1}11]$, and $\boldsymbol{e}_3 = [1\bar{1}1]$. The grid spacing is $1b$ such that the grid points align with the atomic lattice. For screw dislocation simulations, a cell with size $128b$ x $8b$ x $128b$ is used, and a screw dislocation dipole is inserted by setting $\phi^1 = 1$ between two dislocations $64b$ apart with line direction $[\bar{1}11]$. For edge dislocation simulations, a cell with size $128b$ x $128b$ x $384b$ is used, and ϕ^1 is set to 1 between two dislocations with line direction $[1\bar{1}2]$, also $64b$ apart. When stress is applied to the system, it is always pure shear with the maximum resolved shear stress on the (110) plane. When stress is increased, it is incremented in steps of $0.001G$. In Eq. (1.8) and Eq. (6.20), the quantities $m_{disl}\Delta t$ and $m_{int}\Delta t/c^{tot}$ are both initially set to $0.25G^{-1}$. The dislocations are converged when the Euclidean norm of the change in order parameters between successive timesteps is less than 10^{-4}.

7.3 Results

7.3.1 Interstitial atmospheres

First, the interstitial atmospheres around screw and edge dislocations are calculated. Previously, it was shown that the shape of the relaxed interstitial fields do not depend on the initial average concentration c_0, so only one value is simulated here, $c_0 = 0.01$. The dislocation is allowed to relax until convergence is reached, and then the interstitials are allowed to diffuse for 500 timesteps. The concentration fields around the dislocation cores are shown in Fig. 7.2.

In the Nb-O system, interstitial atoms occupy octahedral sites, which have three distinct orientations of the tetrahedral distortion. As screw dislocations create only shear stresses, the interstitial atoms occupy three distinct lobes around the screw dislocation, where each lobe corresponds to a different octahedral site orientation. This matches analytical predictions [238–240]. At the intersections of these lobes, there is a local maximum cusp in the chemical potential. As interstitials flow towards lower chemical potential sites, there is a local depletion of interstitials at the intersections, which can be seen by the purple lines in Fig. 7.2A. The interaction of oxygen interstitials with edge dislocations is more complicated due to the presence of both hydrostatic and shear stresses around the dislocation, creating nine distinct regions with different preferred interstitial orientations. Generally, though, oxygen interstitials cluster below the edge dislocation in the tensile stress region, while the compressive region above the dislocation is depleted of interstitial atoms.

In the W-H system, on the other hand, all interstitial sites have equivalent distortions, which are exclusively hydrostatic. Because of this hydrostatic strain, the H atoms interact minimally with the screw dislocation's stress field. Only at the dislocation core itself does the concentration of H atoms differ from the average concentration c_0. In-

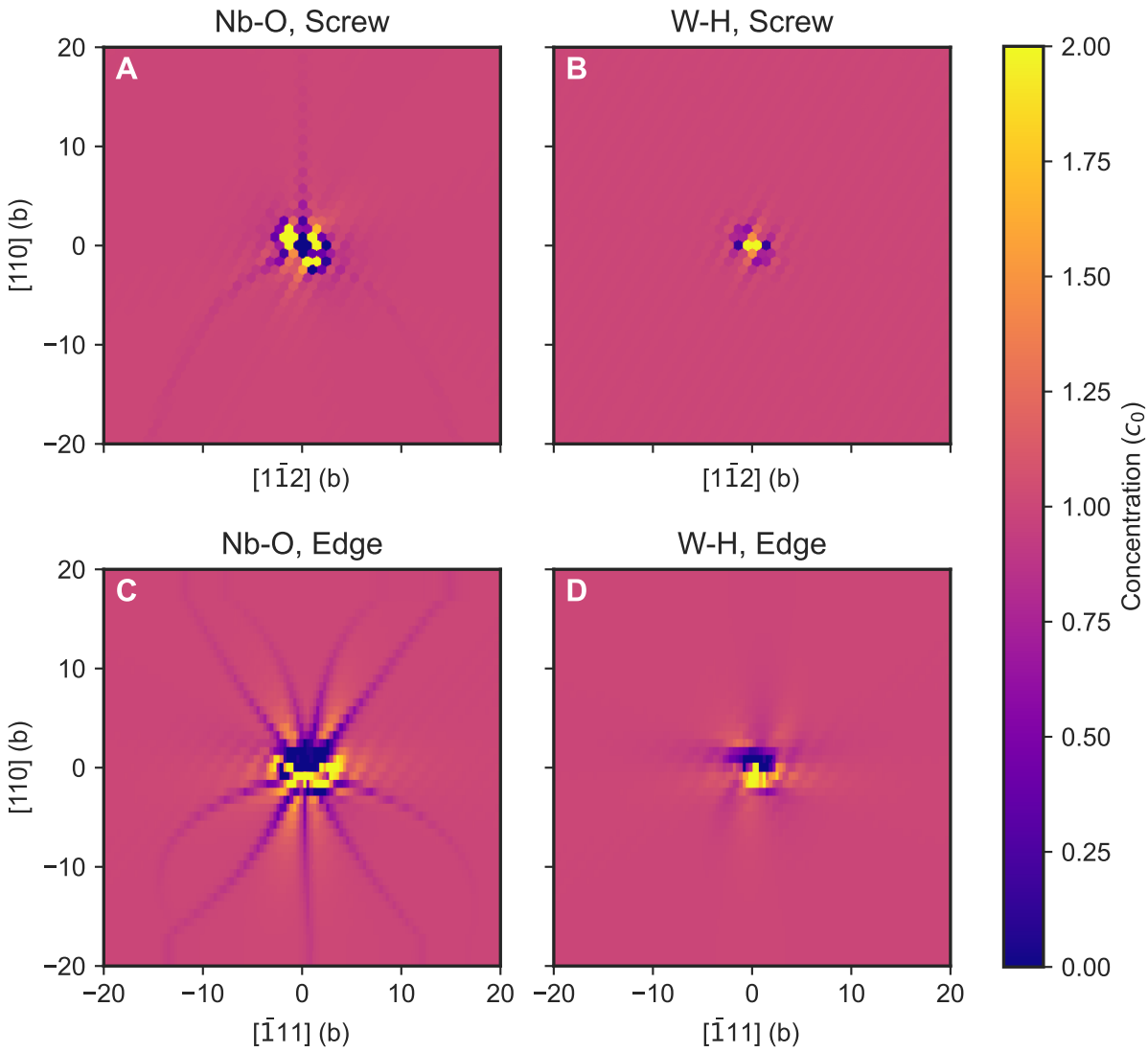

Figure 7.2: The interstitial concentration fields around screw and edge dislocations for Nb-O and W-H.

terstitial atoms flow towards the two grid points bordering the screw dislocation core, lowering the interstitial concentration of neighboring grid points. The atmosphere of H atoms around the edge dislocation is also more axisymmetric than in the Nb-O system. The compressive region is depleted of interstitials, while the tensile region has increased interstitial concentration. Because there is only one interstitial orientation, there are no cusps in the chemical potential landscape, so the locally depleted regions (identified as the purple lines in Figure 7.2A and C) are not present in the W-H system.

7.3.2 Dislocation glide

Critical glide stress

After allowing the interstitials to diffuse for 500 timesteps under zero stress, the critical stress to break away from the interstitial atmosphere was calculated for c_0 ranging from 0 to 0.01 (Fig. 7.3). Without interstitials (i.e., $c_0 = 0$), there is a single critical stress value. However, with interstitials, it is possible for the dislocation to glide a short distance before becoming pinned again by the interstitial atmosphere. Therefore, two critical stresses are identified: σ_i, the initial critical stress to glide more than $1b$, and σ_b, the breakaway stress to glide away from the interstitial atmosphere entirely. For the Nb-O system, the screw dislocation σ_i decreases with c_0 while σ_b increases. The decrease in σ_i can be attributed to a reduction in dislocation core spreading, and the increase in σ_b occurs when the dislocation encounters a locally high concentration of interstitials within its glide plane. The edge dislocation σ_i in Nb-O is insensitive to c_0 for the values tested here, while σ_b increases with c_0.

In the W-H system, both screw and edge dislocations are less sensitive to changes in c_0. The screw dislocation σ_b is constant regardless of c_0, and, similar to Nb-O, σ_i decreases slightly with c_0. Unlike Nb-O, edge dislocations in the W-H system do not

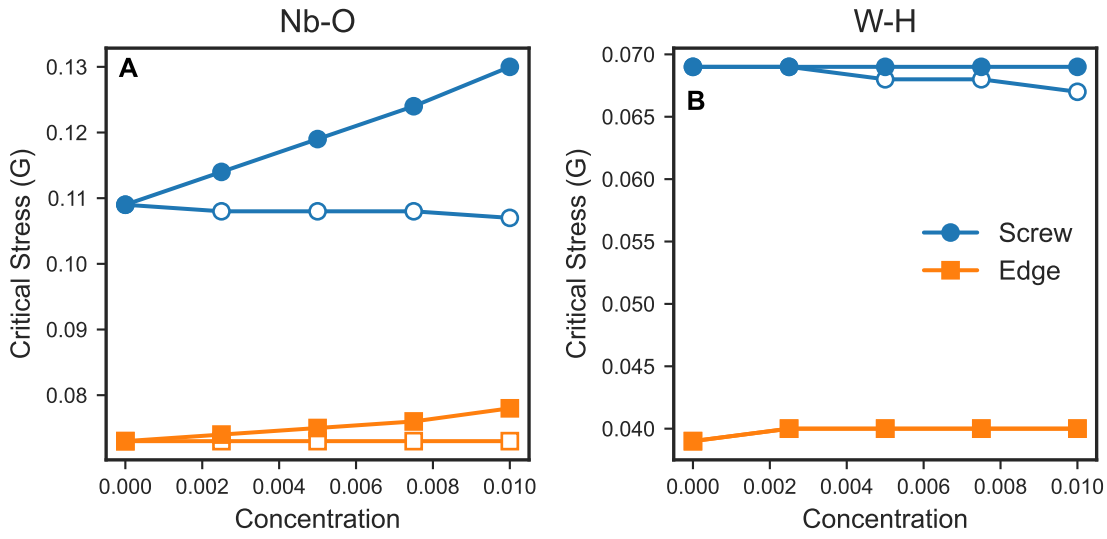

Figure 7.3: The critical stress required for glide of screw and edge dislocations in Nb-O and W-H. Open symbols correspond to the stress to glide at least one Burgers vector (σ_i), while closed symbols correspond to the breakaway stress (σ_b) to escape the interstitial atmosphere entirely.

exhibit different σ_i and σ_b. Because the concentration changes are limited to a small radius around the dislocation core, the initial stress required to initiate glide is adequate for breakaway from the interstitial atmosphere completely. The critical stresses increase slightly from $0.039G$ for the interstitial-free case to $0.040G$ with interstitials, although this is within the resolution of the critical stress calculations ($0.001G$). This is only a 3% increase for $c_0 = 0.01$ from the $c_0 = 0$ case, compared to an increase of 7% for the edge dislocation in Nb-O.

Interplay between screw dislocations and interstitial mobility

In all simulations thus far, either interstitial diffusion or dislocation evolution was simulated, but not both. Here, the interplay between dislocation glide and interstitial diffusion is investigated. First, define the mobility ratio R as $m_{int}b/m_{disl}$. In the following simulations, m_{disl} was held constant at 0.25 $(G\Delta t)^{-1}$ while m_{int} was varied to simulate

R = 0, 0.5, 1, and 2. The dislocation was allowed to relax under zero stress without interstitial diffusion until convergence, and then the applied stress σ_{app} was increased to a stress greater than the interstitial-free critical stress to observe simultaneous dislocation glide and interstitial diffusion. The interstitial distribution is initially homogeneous, and an average concentration $c_0 = 0.01$ was used in all cases.

The glide distances for screw dislocations are shown for a selection of applied stress values in Fig. 7.4. The lowest and highest applied stresses are shown along with an intermediate stress value. All of these stresses are above the critical stress, so "low" stress refers to stresses near the critical stress while "high" stresses are significantly higher than the critical stress. For both the Nb-O and W-H system, the glide behavior at the lowest stress value depends significantly on the value of R, with higher R increasing dislocation glide speed. At higher applied stresses, the dislocation glide behavior is insensitive to R in both systems.

From these simulations, the dislocation drag B can be calculated as $B = \sigma_{app} b/v$ where v is the dislocation velocity. As the dislocations glide, they accelerate slightly due to the influence of their periodic images, so only the first three glide steps (i.e., the first $3b$ of glide) are used to calculate v. The calculated B is shown in Fig. 7.5. In both Nb-O and W-H systems, B is sensitive to R at low applied stresses but not higher applied stresses. Below the stresses shown here, the dislocations are unable to glide at all. Therefore, there is a very narrow range of stresses for which R has an influence, approximately $0.111G$ - $0.113G$ for Nb-O and $0.068G$ - $0.071G$ for W-H.

To investigate why the mobility ratio R affects the dislocation drag at certain applied stresses, Fig. 7.6 and Fig. 7.7 show the evolution of the dislocation order parameter ϕ^1 and the total concentration. In the Nb-O system, the slip plane is depleted of interstitials directly in front of the dislocation, while there are increased interstitial concentrations in the out-of-plane direction (Fig. 7.6E). The interstitial atmosphere is different than the

zero-stress case (Fig. 7.2A) because, under the applied load, the interstitials adopt the [010]-oriented octahedral sites exclusively. The atmosphere decreases screw dislocation core spreading and makes screw dislocation glide easier, which is similar to the mechanism that causes the decrease in σ_i for screw dislocations in Nb-O.The reduced critical stress allows the dislocation to glide forward $1b$ more easily, where it then becomes pinned by a locally high interstitial concentration (Fig. 7.6F). However, unlike the critical stress calculations above, simulations with $R > 0$ allow the interstitials to rearrange around the new dislocation location (Fig. 7.6G). This rearrangement then allows the dislocation to glide another $1b$ forward. This process repeats as the dislocation glides completely across the slip plane in a cycle of $1b$ glide steps and interstitial rearrangement.

In the W-H system, H accumulates directly at the dislocation core itself. The increased concentration of interstitials slightly lowers the glide stress (Fig. 7.3), allowing the dislocation to glide more easily. The locally high concentration of interstitials glides along with the dislocation core. In both Nb-O and W-H, the constant rearrangement of interstitials around a gliding dislocation core leaves in its wake a slip plane that is locally depleted of interstitials.

Both Fig. 7.6 and Fig. 7.7 are shown for relatively low applied stress values, just above the screw dislocation critical stress. At high applied stresses, similar concentration fields are observed trailing the gliding dislocation core. However, there is a plateau in the calculated drag B around $1.5m_{disl}^{-1}$ for Nb-O and $1.1m_{disl}^{-1}$ for W-H (Fig. 7.5). Both of these drag values correspond to a dislocation velocity v in which the dislocations glides $1b$ approximately every 50 timesteps, indicating an upper limit to dislocation glide velocity. Even with the interstitial atmosphere created by $R > 0$, the dislocations are unable to increase the glide velocity beyond this, suggesting that there is a limit to the assistance interstitials can provide during glide.

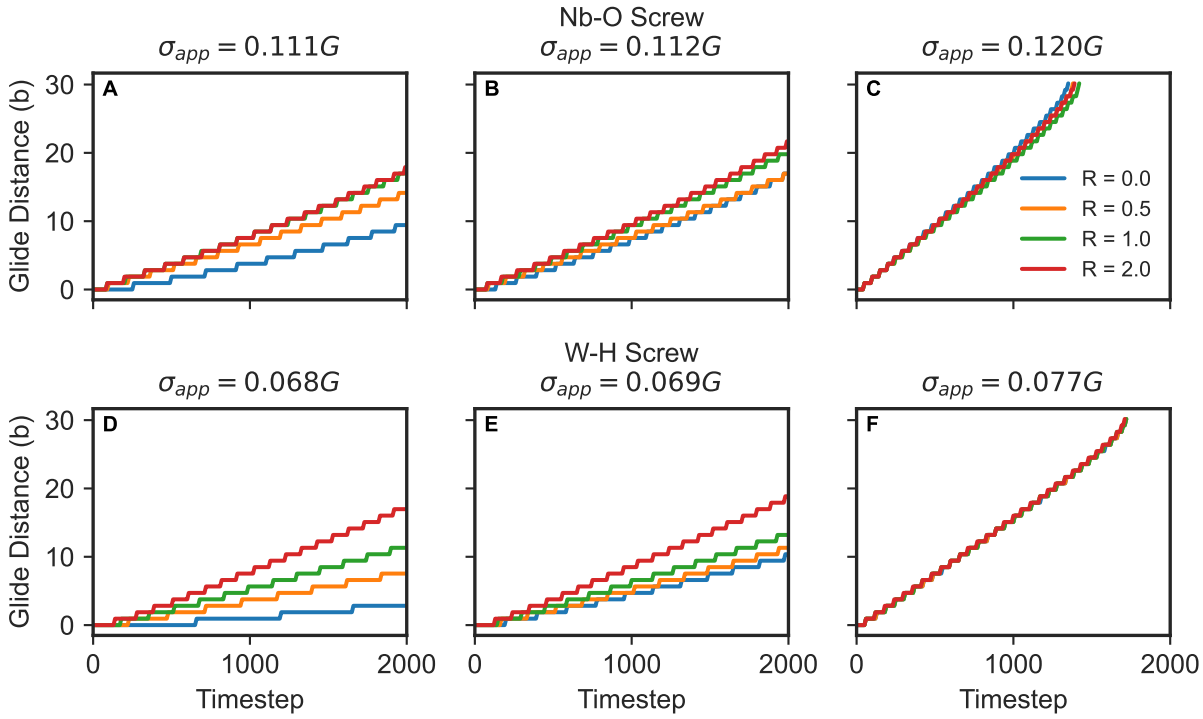

Figure 7.4: The distance a screw dislocation glides for three different applied stresses for different values of the interstial-dislocation mobility ratio R.

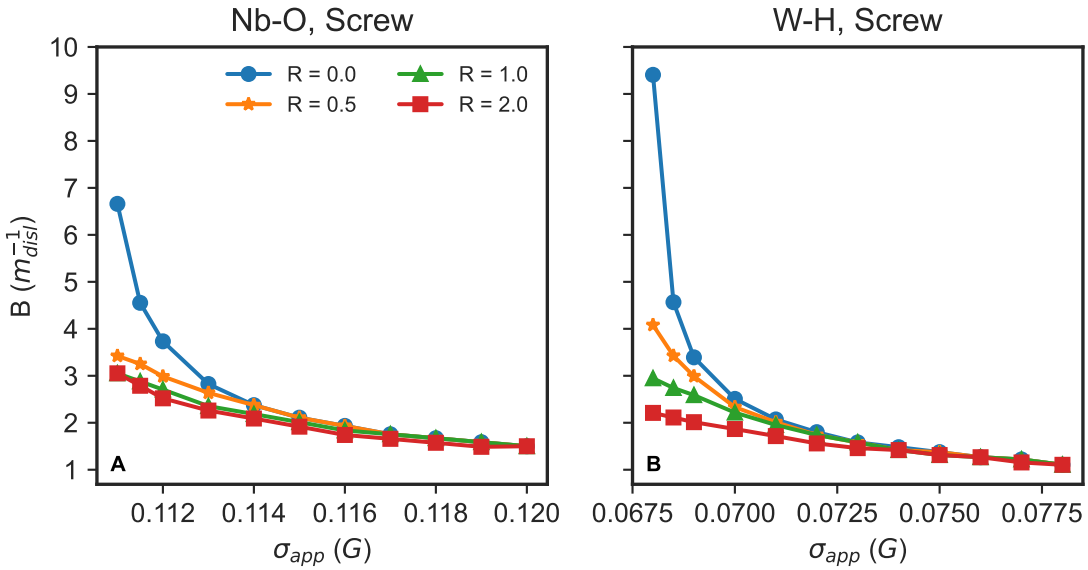

Figure 7.5: The calculated screw dislocation drag as a function of applied stress for different mobility ratios R.

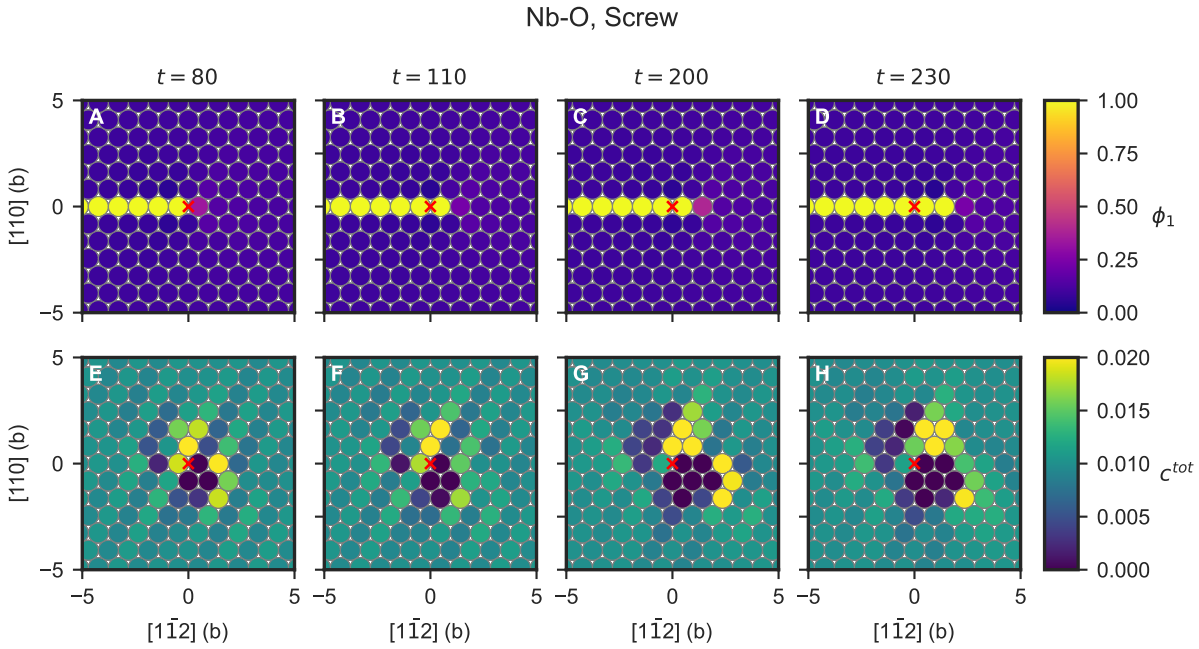

Figure 7.6: Screw dislocation glide process in Nb-O for $R = 2$ and a low applied stress $\sigma_{app} = 0.111G$. (A-D) show the dislocation order parameter while (E-H) show the interstitial concentration field at the same timesteps. For reference, the red X indicates the dislocation's initial position.

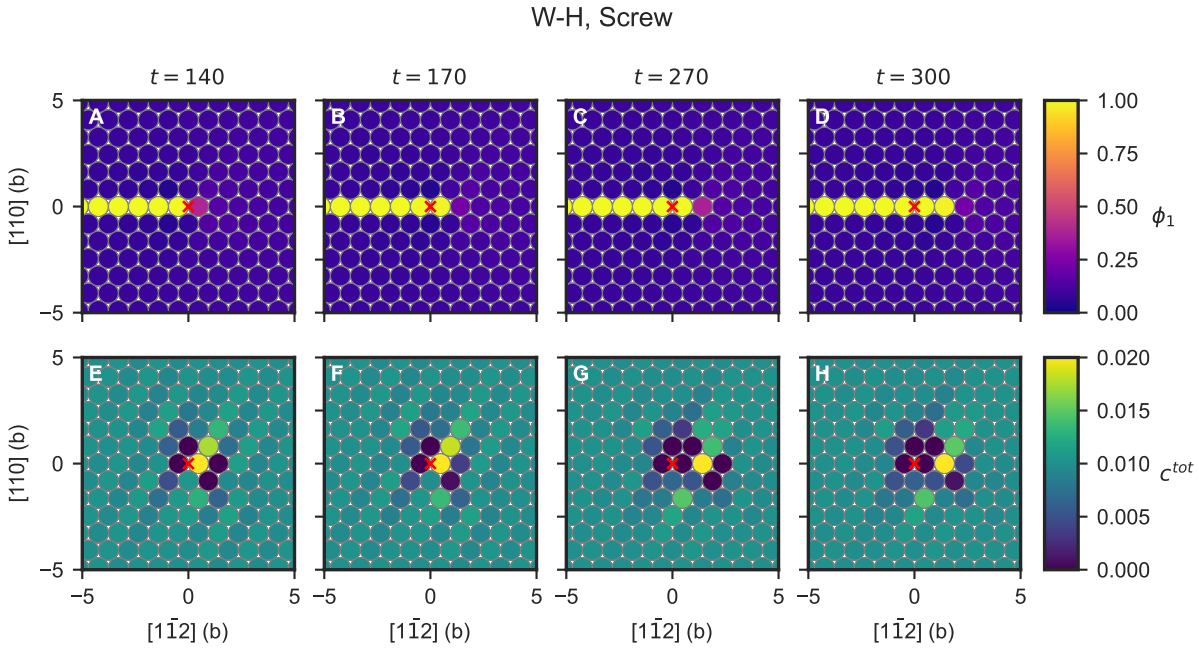

Figure 7.7: Screw dislocation glide process in W-H for $R = 2$ and a low applied stress $\sigma_{app} = 0.068G$. (A-D) show the dislocation order parameter while (E-H) show the interstitial concentration field at the same timesteps. For reference, the red X indicates the dislocation's initial position.

Interplay between edge dislocations and interstitial mobility

Analagous simulations were repeated for edge dislocations in both Nb-O and W-H. Figure 7.8 shows the glide distance over time for select applied stresses in both systems. At low stresses and $R >= 1$, the dislocation becomes pinned during glide. The interstitials are able to diffuse faster than the dislocation is gliding, increasing the concentration of interstitials near the dislocation cores and arresting dislocation glide. When R is lower or the applied stress is higher, the dislocations are able to glide completely across the slip plane without being trapped by the interstitials.

Because the dislocation velocities change over time, with some dislocations accelerating and others decelerating, the dislocation drag B calculated from either the beginning or end of the simulations do not represent the full dislocation behavior. Instead, the total distance traveled in the 2000 simulated timesteps is compared in Figure 7.9. In the Nb-O system, higher R values decrease the total distance traveled by the edge dislocation. When $R = 2$ and $\sigma_{app} < 0.085G$ or when $R = 1$ and $\sigma_{app} < 0.082G$, the edge dislocations decelerate or become pinned during the simulation. At all other stress and R combinations, there is a linear relationship between the distance traveled and σ_{app}. Unlike the screw dislocations, which converged to a similar velocity regardless of R at high σ_{app}, the edge dislocation glide distance is dependent on R for the full range of stress values simulated here.

In the W-H system, the dislocations with $R = 2$ become arrested at low σ_{app}, similar to those in the Nb-O system. However, for dislocations which glide freely, the ranking of distance with respect to R is reversed compared to Nb-O. Higher R values increase the dislocation glide distance, meaning that edge dislocation glide is enhanced by H in W. While the glide distances converge at higher stresses for $R = 0$, 0.5, and 1, the dislocation glide is still enhanced by $R = 2$ for the highest stress value simulated.

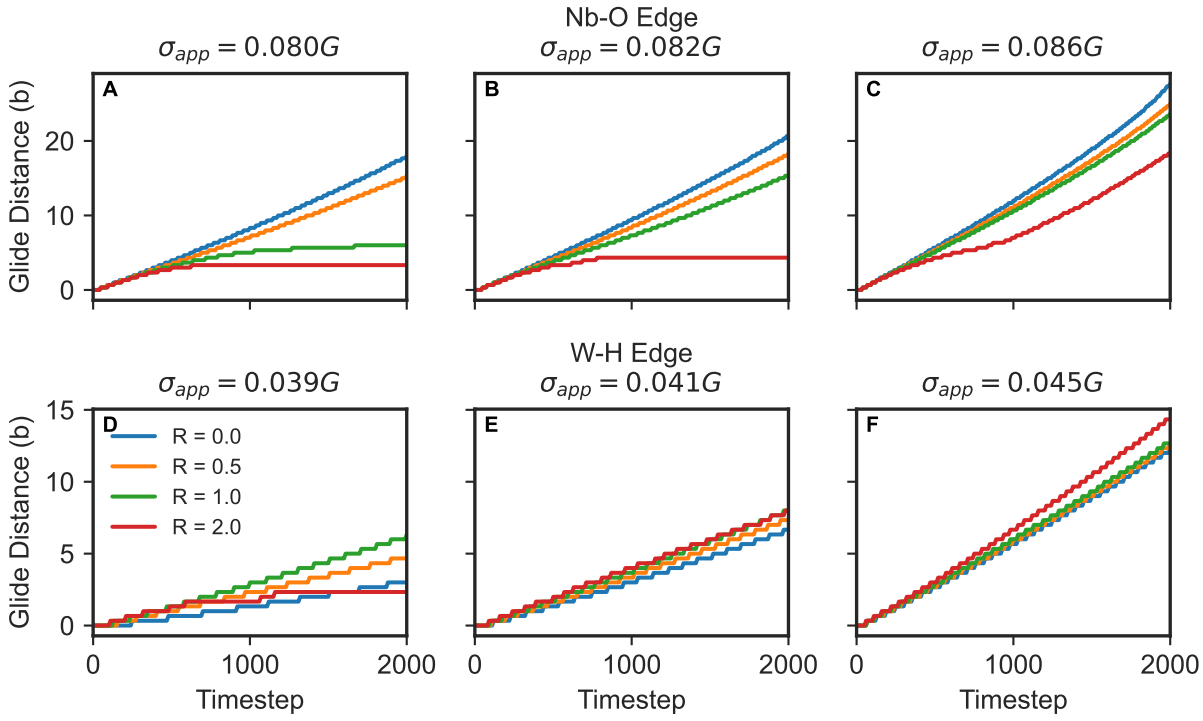

Figure 7.8: The distance an edge dislocation glides for three different applied stresses for different values of the interstitial-dislocation mobility ratio R.

Figure 7.10 shows the interstitial concentration and dislocation evolution for an intermediate stress value with $R = 1$ in Nb-O. Similar interstitial concentration fields are seen for other stresses and $R > 0$. Interstitials pile up below the glide plane in the tensile region, as well as within the glide plane itself. At low stresses and high R, the interstitials within the glide plane itself pile up to an extent that causes the dislocation to become pinned. In other cases, the interstitials only slow the dislocation glide.

In the W-H system, interstitials also accumulate within the slip plane in front of the edge dislocation Figure 7.11. Different values of R only change the magnitude of the interstitial atmosphere, not its shape (Fig. 7.12). As in the screw dislocation case, a locally high interstitial concentration follows the dislocation core as it glides, leaving a wake of locally interstitial-depleted material in both Nb-O and W-H.

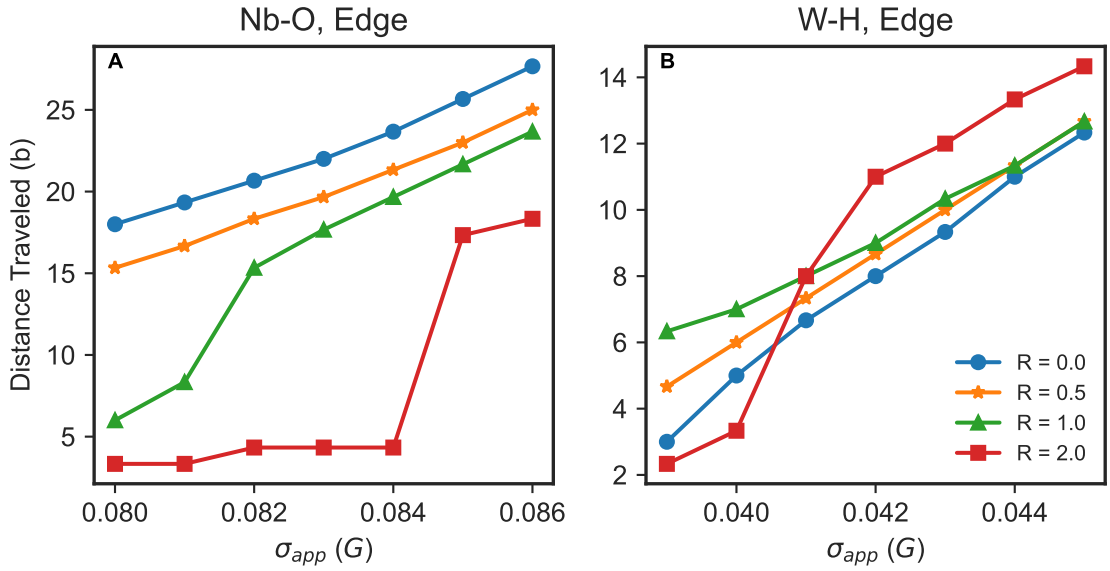

Figure 7.9: The total distance traveled by edge dislocations as a function of applied stress for different mobility ratios R.

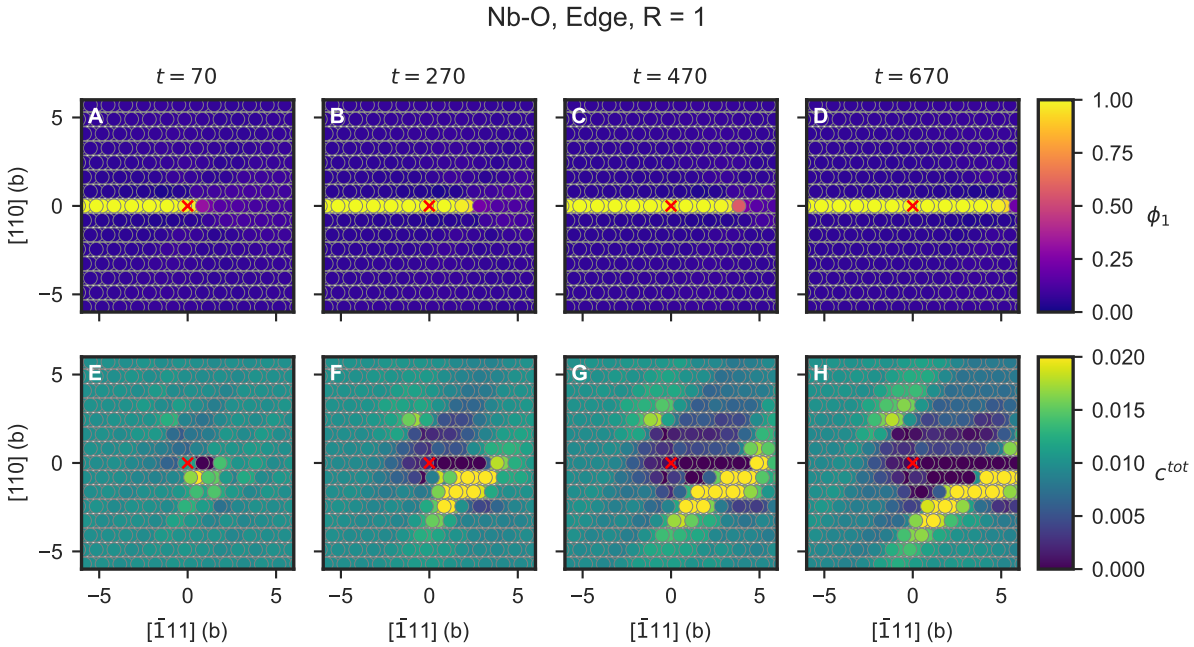

Figure 7.10: Edge dislocation glide process in Nb-O for $R = 1$ and an intermediate applied stress $\sigma_{app} = 0.082G$. (A-D) show the dislocation order parameter while (E-H) show the interstitial concentration field at the same timesteps. For reference, the red X indicates the dislocation's initial position.

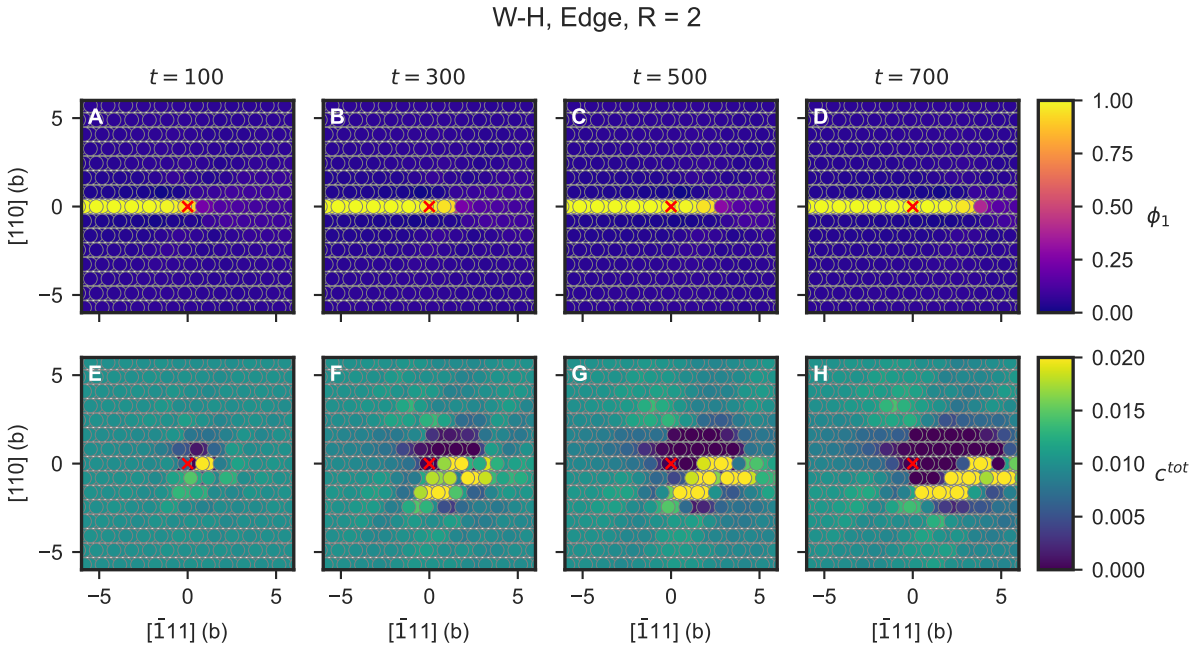

Figure 7.11: Edge dislocation glide process in W-H for $R = 2$ and an intermediate applied stress $\sigma_{app} = 0.043G$. (A-D) show the dislocation order parameter while (E-H) show the interstitial concentration field at the same timesteps. For reference, the red X indicates the dislocation's initial position.

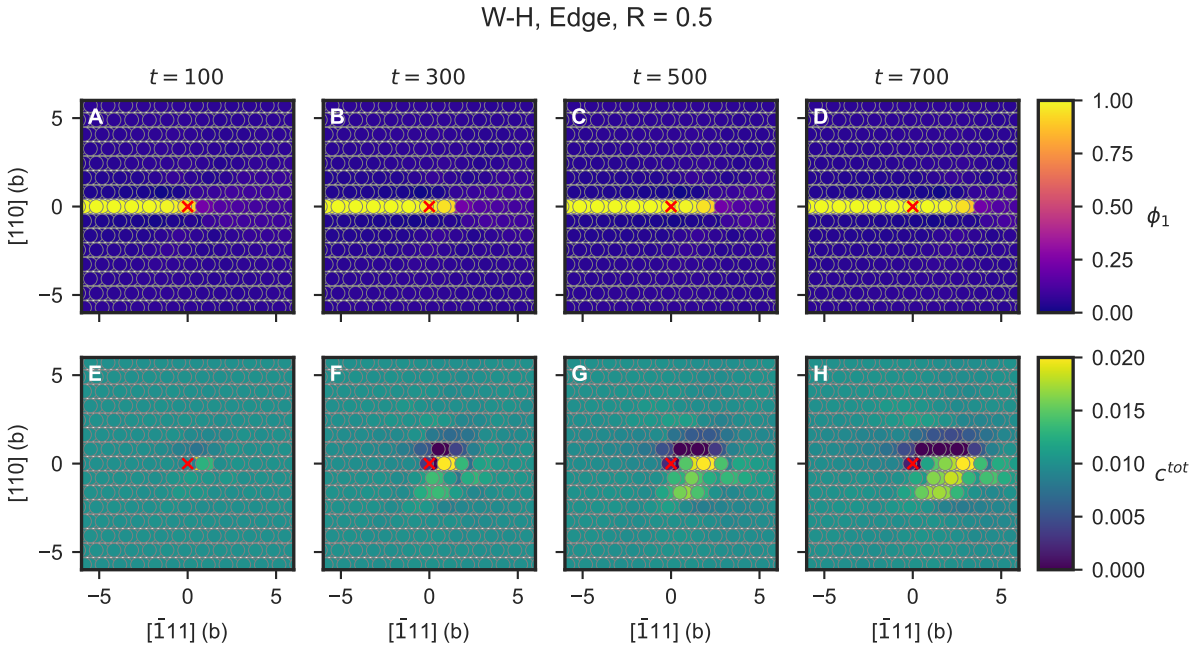

Figure 7.12: Edge dislocation glide process in W-H for $R = 0.5$ and an intermediate applied stress $\sigma_{app} = 0.043G$. (A-D) show the dislocation order parameter while (E-H) show the interstitial concentration field at the same timesteps. For reference, the red X indicates the dislocation's initial position.

7.4 Discussion

While O and H are both significant interstitial contaminants in refractory metals, these simulations show that they affect dislocations in different ways. Because H occupies tetrahedral sites and creates a purely hydrostatic strain, it is unable to interact with screw dislocation stress fields and has minimal impact on the critical stress of W. O interstitials, on the other hand, are able to interact with screw dislocations and increase the critical breakaway stress. Being a larger atom, O also interacts more strongly with edge dislocation stress fields, creating a more intense and wider-ranged interstitial concentration in Nb than H interstitials do in W.

The simulations show that screw dislocation glide is enhanced by the presence of interstitials in both the Nb-O and W-H systems but only within a narrow range of applied stress values. This is in contrast to atomistic simulation results which show decreased mobility of screw dislocations by interstitials [47, 71]. However, due to time scale constraints, atomistic simulations have only been performed in the low interstitial mobility regime, essentially $R = 0$ in the PFDD simulations. Those results are consistent with the increased critical stress of Nb-O screw dislocations when the interstitials are frozen (Fig. 7.3A), and it is likely that interstitials will affect glide differently depending on their mobility. Here, R is an artificial parameter that allows for any combination of interstitial-dislocation relative mobilities. In reality, H will have a much higher mobility than O, so it is possible that H will enhance screw glide while O is unable to diffuse quickly enough to have an effect.

Unlike screw dislocations, edge dislocations exhibit different behaviors in the two systems simulated here. In Nb-O, interstitials slow edge dislocation glide by increasing the critical stress required for glide. In W-H, interstitials increase the velocity of edge dislocations, and the effect is persistent over a wider range of stresses than for the screw

dislocations. While H had little effect on the critical stress of edge dislocations, it may be increasing the glide stress through a hydrogen-shielding type mechanism. Other simulation results have found that H increases dislocation mobility, but the conclusions are split on whether this is caused by long-range elastic shielding [242] or short-range core effects [243]. Future studies of dislocation pileup are necessary to fully understand why H increases edge dislocation glide.

It should be noted that temperature is not included in these simulations, which is especially significant for screw dislocation behavior. Screw dislocations in BCC crystals glide via thermally activated kink-pair nucleation and migration, which is not simulated here in the 0K PFDD simulations. The calculated 0K initial critical stresses for screw dislocations suggest that barrier for dislocation glide is lowered in the presence of interstitials for both systems. Kink-pairs may therefore be more likely to nucleate at high-concentration regions under thermal fluctuations. The resulting kinks are edge-oriented, and as seen in the pure edge glide simulations, interstitials slow down edge glide in Nb-O but accelerate edge glide in W-H. Therefore, screw dislocations may be accelerated in W-H by increased kink mobility but inhibited in Nb-O. Including temperature effects in future PFDD simulations will be necessary to untangle these mechanisms.

7.5 Conclusion

Phase-field dislocation dynamics was used to study the behavior of dislocations in the presence of interstitials in refractory metals. Two model systems were studied: H interstitials in W and O interstitials in Nb. These two interstitial types occupy different sites within the lattice, thereby interacting with dislocations in different ways. H interstitials interact minimally with screw dislocations due to their purely hydrostatic strains, while O interstitials interact with both screw and edge dislocations. The critical stress for dis-

locations to break away from their interstitial atmospheres increases with concentration in Nb-O for both screw and edge orientations. H, on the other hand, has minimal impact on the critical stresses for dislocations in W. When the interstitial atmosphere is able to follow a gliding dislocation, screw dislocation glide is enhanced in both systems, while edge dislocation glide is enhanced in W-H but inhibited in Nb-O.

Chapter 8

Summary and Outlook

8.1 Conclusions

In the work presented here, several separate extensions were made to PFDD to simulate specific systems of interest. The PFDD simulations of refractory MPEAs, including long dislocations, loops, and Frank-Read sources, reinforce the high variability and statistical nature of dislocations in these materials. This is one of the critical differences between MPEAs and pure metals or conventional alloys. Screw-oriented dislocations advance by forming a kink-pair in a low USFE regions, leading to a more extreme length-dependence in the critical stress of Frank-Read sources and a wide range in critical stresses to advance a screw dislocation. The critical stresses are highly dependent on the particular position of the dislocation within the lattice, so there will be a large distribution of weaker and stronger dislocations and sources within a crystal. SRO generally increases the mean critical stress due to the higher USFE values associated with SRO.

The PFDD simulations of pure Nb and W with O and H, respectively, reveal how different interstitial types affect screw and edge dislocations in distinct manners. The O interstitials interact more strongly with the stress fields of dislocations due to their larger

distortion with shear components, while H interstitials create smaller, purely hydrostatic distortions. The mobility of screw dislocations is enhanced by interstitials in both systems, as the interstitial atmosphere allows the screw dislocations to glide a short distance at a lower applied stress. Edge dislocations in the two materials exhibit opposite trends: O inhibits edge glide in Nb but H enhances edge glide in W.

8.2 Future Work

Temperature is an important aspect of dislocations in BCC materials and has not been considered here. Future work may incorporate thermal fluctuations into the PFDD model to simulate thermally activated behavior. The simulations presented here show that athermal kink-pairs form due to the underlying composition fluctuations, so understanding the presence of thermal and athermal kinks under different conditions would be necessary for understanding the mechanical properties of MPEAs at elevated temperatures. Future simulations may also include multiple dislocations and their interactions. As dislocations glide along their slip plane, the underlying USFE surface should change as the local composition shifts. This is especially important when SRO is included, as dislocation slip breaks the local SRO, potentially lowering the glide stress and increasing the mobility of subsequent dislocations.

The PFDD simulations here indicate that mobility of edge dislocations is enhanced by H in W, which may be indicative of hydrogen-enhanced local plasticity. Future work should examine dislocation pileup to probe for hydrogen shielding effects. Additionally, the inclusion of temperature would allow for the introduction of a real time scale, which would allow experimental or simulated values for dislocation mobility and interstitial diffusivity to be included in the PFDD simulations.

The work presented here both gives new insights into dislocation behavior in re-

fractory metals and advances the PFDD method itself. Future researchers can use the updated PFDD formulation and code to simulate their system of interest by obtaining the appropriate parameters. For MPEAs, a distribution of stacking fault energies is required, which can be calculated with atomistic simulations. Cross slip in BCC crystals is inherent to the three order parameter formulation and needs no additional parameters. Short-range order can be incorporated with the help of OTIS and requires the Warren-Cowley parameters for the system. Finally, interstitials can be included in PFDD by inputting the elastic dipole tensor and concentration-dependent USFE. The current formulation considers interstitials within a single element host lattice, but extensions could be made in the future to consider interstitials within an MPEA, which would be of great interest to the refractory MPEA community.

Bibliography

[1] D. B. Miracle and O. N. Senkov. "A critical review of high entropy alloys and related concepts". *Acta Materialia* 122 (2017), pp. 448–511. DOI: 10.1016/j.actamat.2016.08.081.

[2] R. A. Causey and T. J. Venhaus. "The use of tungsten in fusion reactors: a review of the hydrogen retention and migration properties". *Physica Scripta* 2001.T94 (2001), p. 9. DOI: 10.1238/physica.topical.094a00009.

[3] O. N. Senkov, G. Wilks, D. Miracle, C. Chuang, and P. Liaw. "Refractory high-entropy alloys". *Intermetallics* 18.9 (2010), pp. 1758–1765. DOI: 10.1016/j.intermet.2010.05.014.

[4] N. R. Philips, M. Carl, and N. J. Cunningham. "New Opportunities in Refractory Alloys". *Metallurgical and Materials Transactions A* 51.7 (2020), pp. 3299–3310. DOI: 10.1007/s11661-020-05803-3.

[5] M. Kaufmann and R. Neu. "Tungsten as first wall material in fusion devices". *Fusion Engineering and Design*. Proceedings of the 24th Symposium on Fusion Technology 82.5 (2007), pp. 521–527. DOI: 10.1016/j.fusengdes.2007.03.045.

[6] B. Cantor, I. T. H. Chang, P. Knight, and A. J. B. Vincent. "Microstructural development in equiatomic multicomponent alloys". *Materials Science and Engineering: A* 375-377 (2004), pp. 213–218. DOI: 10.1016/j.msea.2003.10.257.

[7] O. N. Senkov, J. M. Scott, S. V. Senkova, D. B. Miracle, and C. F. Woodward. "Microstructure and room temperature properties of a high-entropy TaNbHfZrTi alloy". *Journal of Alloys and Compounds* 509.20 (2012), pp. 6043–6048. DOI: 10.1016/j.jallcom.2011.02.171.

[8] A. Seeger. "LXV. On the theory of the low-temperature internal friction peak observed in metals". *Philosophical Magazine* 1.7 (1956), pp. 651–662. DOI: 10.1080/14786435608244000.

[9] C. Woodward and S. I. Rao. "Ab-initio simulation of isolated screw dislocations in bcc Mo and Ta". *Philosophical Magazine A* 81.5 (2001), pp. 1305–1316. DOI: 10.1080/01418610108214442.

[10] J.-P. Couzinié, L. Lilensten, Y. Champion, G. Dirras, L. Perrière, and I. Guillot. "On the room temperature deformation mechanisms of a TiZrHfNbTa refractory high-entropy alloy". *Materials Science and Engineering A* 645 (2015), pp. 255–263. DOI: 10.1016/j.msea.2015.08.024.

[11] L. Lilensten, J.-P. P. Couzinié, L. Perrière, A. Hocini, C. Keller, G. Dirras, and I. Guillot. "Study of a bcc multi-principal element alloy: Tensile and simple shear properties and underlying deformation mechanisms". *Acta Materialia* 142 (2018), pp. 131–141. DOI: 10.1016/j.actamat.2017.09.062.

[12] J.-P. Couzinié and G. Dirras. "Body-centered cubic high-entropy alloys: From processing to underlying deformation mechanisms". *Materials Characterization* 147 (2018), pp. 533–544. DOI: 10.1016/j.matchar.2018.07.015.

[13] F. Wang, G. H. Balbus, S. Xu, Y. Su, J. Shin, P. F. Rottmann, K. E. Knipling, J.-C. Stinville, L. H. Mills, O. N. Senkov, I. J. Beyerlein, T. M. Pollock, and D. S. Gianola. "Multiplicity of dislocation pathways in a refractory multiprincipal element alloy". *Science* 370.6512 (2020), pp. 95–101. DOI: 10.1126/science.aba3722.

[14] O. N. Senkov, S. Senkova, D. Miracle, and C. Woodward. "Mechanical properties of low-density, refractory multi-principal element alloys of the Cr-Nb-Ti-V-Zr system". *Materials Science and Engineering A* 565 (2013), pp. 51–62. DOI: 10.1016/j.msea.2012.12.018.

[15] F. G. Coury, M. Kaufman, and A. J. Clarke. "Solid-solution strengthening in refractory high entropy alloys". *Acta Materialia* 175 (2019), pp. 66–81. DOI: 10.1016/j.actamat.2019.06.006.

[16] Thomas H. Courtney. *Mechanical Behavior of Materials*. 2005.

[17] I. Toda-Caraballo and P. E. Rivera-Díaz-Del-Castillo. "Modelling solid solution hardening in high entropy alloys". *Acta Materialia* 85 (2015), pp. 14–23. DOI: 10.1016/j.actamat.2014.11.014.

[18] C.-C. Juan, K.-K. Tseng, W.-L. Hsu, M.-H. Tsai, C.-W. Tsai, C.-M. Lin, S.-K. Chen, S.-J. Lin, and J.-W. Yeh. "Solution strengthening of ductile refractory HfMoxNbTaTiZr high-entropy alloys". *Materials Letters* 175 (2016), pp. 284–287. DOI: 10.1016/j.matlet.2016.03.133.

[19] S. I. Rao, B. Akdim, E. Antillon, C. Woodward, T. A. Parthasarathy, and O. N. Senkov. "Modeling solution hardening in BCC refractory complex concentrated alloys: NbTiZr, Nb 1.5 TiZr 0.5 and Nb 0.5 TiZr 1.5". *Acta Materialia* 168 (2019), pp. 222–236. DOI: 10.1016/j.actamat.2019.02.013.

[20] S. Yin, Y. Zuo, A. Abu-Odeh, H. Zheng, X.-G. Li, J. Ding, S. P. Ong, M. Asta, and R. O. Ritchie. "Atomistic simulations of dislocation mobility in refractory high-entropy alloys and the effect of chemical short-range order". *Nature Communications* 12 (2021), p. 4873. DOI: 10.1038/s41467-021-25134-0.

[21] S. Rao, C. Varvenne, C. Woodward, T. Parthasarathy, D. Miracle, O. N. Senkov, and W. Curtin. "Atomistic simulations of dislocations in a model BCC multicomponent concentrated solid solution alloy". *Acta Materialia* 125 (2017), pp. 311–320. DOI: 10.1016/j.actamat.2016.12.011.

[22] S. Yin, J. Ding, M. Asta, and R. O. Ritchie. "Ab initio modeling of the energy landscape for screw dislocations in body-centered cubic high-entropy alloys". *npj Computational Materials* 6.1 (2020). DOI: 10.1038/s41524-020-00377-5.

[23] X. Wang, F. Maresca, and P. Cao. "The hierarchical energy landscape of screw dislocation motion in refractory high-entropy alloys". *Acta Materialia* 234 (2022), p. 118022. DOI: 10.1016/j.actamat.2022.118022.

[24] C. D. Statham, D. A. Koss, and J. W. Christian. "The thermally activated deformation of niobium-molybdenum and niobium-rhenium alloy single crystals". *Philosophical Magazine* 26.5 (1972), pp. 1089–1103. DOI: 10.1080/14786437208227366.

[25] G. Dirras, J. Gubicza, A. Heczel, L. Lilensten, J. P. Couzinié, L. Perrière, I. Guillot, and A. Hocini. "Microstructural investigation of plastically deformed Ti20Zr20Hf20Nb20Ta20 high entropy alloy by X-ray diffraction and transmission electron microscopy". *Materials Characterization* 108 (2015), pp. 1–7. DOI: 10.1016/j.matchar.2015.08.007.

[26] F. Mompiou, D. Tingaud, Y. Chang, B. Gault, and G. Dirras. "Conventional vs harmonic-structured β-Ti-25Nb-25Zr alloys: A comparative study of deformation mechanisms". *Acta Materialia* 161 (2018), pp. 420–430. DOI: 10.1016/j.actamat.2018.09.032.

[27] C. Lee, F. Maresca, R. Feng, Y. Chou, T. Ungar, M. Widom, K. An, J. D. Poplawsky, Y.-C. Chou, P. K. Liaw, and W. A. Curtin. "Strength can be controlled by edge dislocations in refractory high-entropy alloys". *Nature Communications* 12.1 (2021), p. 5474. DOI: 10.1038/s41467-021-25807-w.

[28] C. Baruffi, F. Maresca, and W. A. Curtin. "Screw vs. edge dislocation strengthening in body-centered-cubic high entropy alloys and implications for guided alloy design". *MRS Communications* (2022). DOI: 10.1557/s43579-022-00278-2.

[29] F. X. Zhang, S. Zhao, K. Jin, H. Xue, G. Velisa, H. Bei, R. Huang, J. Y. P. Ko, D. C. Pagan, J. C. Neuefeind, W. J. Weber, and Y. Zhang. "Local Structure and Short-Range Order in a NiCoCr Solid Solution Alloy". *Physical Review Letters* 118.20 (2017), p. 205501. DOI: 10.1103/physrevlett.118.205501.

[30] J. Ding, Q. Yu, M. Asta, and R. O. Ritchie. "Tunable stacking fault energies by tailoring local chemical order in CrCoNi medium-entropy alloys". *Proceedings of the National Academy of Sciences* 115.36 (2018), pp. 8919–8924. DOI: 10.1073/pnas.1808660115.

[31] X. Chen, Q. Wang, Z. Cheng, M. Zhu, H. Zhou, P. Jiang, L. Zhou, Q. Xue, F. Yuan, J. Zhu, X. Wu, and E. Ma. "Direct observation of chemical short-range order in a medium-entropy alloy". *Nature* 592.7856 (2021), pp. 712–716. DOI: 10.1038/s41586-021-03428-z.

[32] W. Guo, W. Dmowski, J.-Y. Noh, P. Rack, P. K. Liaw, and T. Egami. "Local Atomic Structure of a High-Entropy Alloy: An X-Ray and Neutron Scattering Study". *Metallurgical and Materials Transactions A* 44.5 (2013), pp. 1994–1997. DOI: 10.1007/s11661-012-1474-0.

[33] P. Singh, A. V. Smirnov, and D. D. Johnson. "Atomic short-range order and incipient long-range order in high-entropy alloys". *Physical Review B* 91.22 (2015), pp. 1–12. DOI: 10.1103/physrevb.91.224204.

[34] J. S. Wróbel, D. Nguyen-Manh, M. Y. Lavrentiev, M. Muzyk, and S. L. Dudarev. "Phase stability of ternary fcc and bcc Fe-Cr-Ni alloys". *Physical Review B* 91.2 (2015), p. 024108. DOI: 10.1103/physrevb.91.024108.

[35] A. Fernández-Caballero, J. S. Wróbel, P. M. Mummery, and D. Nguyen-Manh. "Short-Range Order in High Entropy Alloys: Theoretical Formulation and Application to Mo-Nb-Ta-V-W System". *Journal of Phase Equilibria and Diffusion* 38.4 (2017), pp. 391–403. DOI: 10.1007/s11669-017-0582-3.

[36] Y. Ma, Q. Wang, C. Li, L. J. Santodonato, M. Feygenson, C. Dong, and P. K. Liaw. "Chemical short-range orders and the induced structural transition in high-entropy alloys". *Scripta Materialia* 144 (2018), pp. 64–68. DOI: 10.1016/j.scriptamat.2017.09.049.

[37] S. Zhao. "Local Ordering Tendency in Body-Centered Cubic (BCC) Multi-Principal Element Alloys". *Journal of Phase Equilibria and Diffusion* 42.5 (2021), pp. 578–591. DOI: 10.1007/s11669-021-00878-w.

[38] X. G. Li, C. Chen, H. Zheng, Y. Zuo, and S. P. Ong. "Complex strengthening mechanisms in the NbMoTaW multi-principal element alloy". *npj Computational Materials* 6.1 (2020). DOI: 10.1038/s41524-020-0339-0.

[39] W.-R. Jian, Z. Xie, S. Xu, Y. Su, X. Yao, and I. J. Beyerlein. "Effects of lattice distortion and chemical short-range order on the mechanisms of deformation in medium entropy alloy CoCrNi". *Acta Materialia* 199 (2020), pp. 352–369. DOI: 10.1016/j.actamat.2020.08.044.

[40] Y. Zeng, X. Cai, and M. Koslowski. "Effects of the stacking fault energy fluctuations on the strengthening of alloys". *Acta Materialia* 164 (2019), pp. 1–11. DOI: 10.1016/j.actamat.2018.09.066.

[41] L. Zhang, Y. Xiang, J. Han, and D. J. Srolovitz. "The effect of randomness on the strength of high-entropy alloys". *Acta Materialia* 166 (2019), pp. 424–434. DOI: 10.1016/j.actamat.2018.12.032.

[42] M. Sudmanns and J. A. El-Awady. "The effect of local chemical ordering on dislocation activity in multi-principle element alloys: A three-dimensional discrete dislocation dynamics study". *Acta Materialia* 220 (2021), p. 117307. DOI: 10.1016/j.actamat.2021.117307.

[43] M. G. Ulitchny and R. Gibala. "The effects of interstitial solute additions on the mechanical properties of niobium and tantalum single crystals". *Journal of The Less-Common Metals* 33.1 (1973), pp. 105–116. DOI: 10.1016/0022-5088(73)90061-1.

[44] M. Sankar, R. G. Baligidad, and A. A. Gokhale. "Effect of oxygen on microstructure and mechanical properties of niobium". *Materials Science and Engineering A* 569 (2013), pp. 132–136. DOI: 10.1016/j.msea.2013.01.025.

[45] P. J. Yang, Q. J. Li, T. Tsuru, S. Ogata, J. W. Zhang, H. W. Sheng, Z. W. Shan, G. Sha, W. Z. Han, J. Li, and E. Ma. "Mechanism of hardening and damage initiation in oxygen embrittlement of body-centred-cubic niobium". *Acta Materialia* 168 (2019), pp. 331–342. DOI: 10.1016/j.actamat.2019.02.030.

[46] E. Miura, K. Yoshimi, and S. Hanada. "Oxygen–molybdenum interaction with dislocations in Nb-Mo single crystals at elevated temperatures". *Acta Materialia* 50 (2002), pp. 2905–2916. DOI: 10.1016/s1359-6454(02)00115-5.

[47] G. Hachet, D. Caillard, L. Ventelon, and E. Clouet. "Mobility of screw dislocation in BCC tungsten at high temperature in presence of carbon". *Acta Materialia* 222 (2022), p. 117440. DOI: 10.1016/j.actamat.2021.117440.

[48] A. H. Cottrell and B. A. Bilby. "Dislocation theory of yielding and strain ageing of iron". *Proceedings of the Physical Society. Section A* 62.1 (1949), pp. 49–62. DOI: 10.1088/0370-1298/62/1/308.

[49] J. D. Eshelby. "The Continuum Theory of Lattice Defects". *Solid State Physics - Advances in Research and Applications* 3.C (1956), pp. 79–144. DOI: 10.1016/s0081-1947(08)60132-0.

[50] D. J. Bacon, D. M. Barnett, and R. O. Scattergood. "Anisotropic continuum theory of lattice defects". *Progress in Materials Science* 23.C (1980), pp. 51–262. DOI: 10.1016/0079-6425(80)90007-9.

[51] E. Clouet, C. Varvenne, and T. Jourdan. "Elastic modeling of point-defects and their interaction". *Computational Materials Science* 147 (2018), pp. 49–63. DOI: 10.1016/j.commatsci.2018.01.053.

[52] A. Nowick and B. S. Berry. *Anelastic relaxation in crystalline solids*. Academic Press, New York, 1972.

[53] J. L. Snoek. "Effect of small quantities of carbon and nitrogen on the elastic and plastic properties of iron". *Physica* 8.7 (1941), pp. 711–733. DOI: 10.1016/s0031-8914(41)90517-7.

[54] G. Schoeck and A. Seeger. "The flow stress of iron and its dependence on impurities". *Acta Metallurgica* 7.7 (1959), pp. 469–477. DOI: 10.1016/0001-6160(59)90028-8.

[55] S. C. Park, L. P. Beckerman, and R. E. Reed-Hill. "On the Portevin-Le Chatelier Effect Due to Snoek Strain Aging in the Niobium Oxygen System". *Metallurgical Transactions A* 14.2 (1983), pp. 463–469. DOI: 10.1007/bf02644223.

[56] E. Clouet, S. Garruchet, H. Nguyen, M. Perez, and C. S. Becquart. "Dislocation interaction with C in α-Fe: A comparison between atomic simulations and elasticity theory". *Acta Materialia* 56.14 (2008), pp. 3450–3460. DOI: 10.1016/j.actamat.2008.03.024.

[57] L. Ventelon, B. Lüthi, E. Clouet, L. Proville, B. Legrand, D. Rodney, and F. Willaime. "Dislocation core reconstruction induced by carbon segregation in bcc iron". *Physical Review B* 91.22 (2015), pp. 1–5. DOI: 10.1103/physrevb.91.220102.

[58] B. Lüthi, L. Ventelon, D. Rodney, and F. Willaime. "Attractive interaction between interstitial solutes and screw dislocations in bcc iron from first principles". *Computational Materials Science* 148 (2018), pp. 21–26. DOI: 10.1016/j.commatsci.2018.02.016.

[59] Y. Zhao, L. Dezerald, and J. Marian. "Electronic structure calculations of oxygen atom transport energetics in the presence of screw dislocations in tungsten". *Metals* 9.2 (2019). DOI: 10.3390/met9020252.

[60] B. Lüthi, L. Ventelon, C. Elssser, D. Rodney, and F. Willaime. "First principles investigation of carbon-screw dislocation interactions in body-centered cubic metals". *Modelling and Simulation in Materials Science and Engineering* 25.8 (2017). DOI: 10.1088/1361-651x/aa88eb.

[61] P. P. Borges, E. Clouet, and L. Ventelon. "Ab initio investigation of the screw dislocation-hydrogen interaction in bcc tungsten and iron". *Acta Materialia* 234 (2022), p. 118048. DOI: 10.1016/j.actamat.2022.118048.

[62] P. Grigorev, T. D. Swinburne, and J. R. Kermode. "Hybrid quantum/classical study of hydrogen-decorated screw dislocations in tungsten: Ultrafast pipe diffusion, core reconstruction, and effects on glide mechanism". *Physical Review Materials* 4.2 (2020), p. 023601. DOI: 10.1103/physrevmaterials.4.023601.

[63] M. Itakura, H. Kaburaki, M. Yamaguchi, and T. Okita. "The effect of hydrogen atoms on the screw dislocation mobility in bcc iron: A first-principles study". *Acta Materialia* 61.18 (2013), pp. 6857–6867. DOI: 10.1016/j.actamat.2013.07.064.

[64] A. Allera, F. Ribeiro, M. Perez, and D. Rodney. "Carbon-induced strengthening of bcc iron at the atomic scale". *Physical Review Materials* 6.1 (2022), p. 013608. DOI: 10.1103/physrevmaterials.6.013608.

[65] S. I. Rao, C. Woodward, B. Akdim, and O. N. Senkov. "A model for interstitial solid solution strengthening of body centered cubic metals". *Materialia* 9.February (2020), p. 100611. DOI: 10.1016/j.mtla.2020.100611.

[66] C. D. Beachem. "A new model for hydrogen-assisted cracking (hydrogen "embrittlement")". *Metallurgical and Materials Transactions B* 3.2 (1972), pp. 441–455. DOI: 10.1007/bf02642048.

[67] I. M. Robertson, P. Sofronis, A. Nagao, M. L. Martin, S. Wang, D. W. Gross, and K. E. Nygren. "Hydrogen Embrittlement Understood". *Metallurgical and Materials Transactions A* 46.6 (2015), pp. 2323–2341. DOI: 10.1007/s11661-015-2836-1.

[68] O. Barrera, D. Bombac, Y. Chen, T. D. Daff, E. Galindo-Nava, P. Gong, D. Haley, R. Horton, I. Katzarov, J. R. Kermode, C. Liverani, M. Stopher, and F. Sweeney. "Understanding and mitigating hydrogen embrittlement of steels: a review of experimental, modelling and design progress from atomistic to continuum". *Journal of Materials Science* 53.9 (2018), pp. 6251–6290. DOI: 10.1007/s10853-017-1978-5.

[69] J. Song and W. A. Curtin. "Mechanisms of hydrogen-enhanced localized plasticity: An atomistic study using α-Fe as a model system". *Acta Materialia* 68 (2014), pp. 61–69. DOI: 10.1016/j.actamat.2014.01.008.

[70] Z. Zheng, S. Liang, M. Huang, L. Zhao, Y. Zhu, and Z. Li. "Studying the effects of hydrogen on dislocation mobility and multiplication in nickel by phase-field method". *Mechanics of Materials* 173 (2022), p. 104443. DOI: 10.1016/j.mechmat.2022.104443.

[71] Y. Zhao, L. Dezerald, M. Pozuelo, X. Zhou, and J. Marian. "Simulating the mechanisms of serrated flow in interstitial alloys with atomic resolution over diffusive timescales". *Nature Communications* 11.1 (2020), p. 1227. DOI: 10.1038/s41467-020-15085-3.

[72] Y. Cui, G. Po, and N. M. Ghoniem. "A coupled dislocation dynamics-continuum barrier field model with application to irradiated materials". *International Journal of Plasticity* 104 (2018), pp. 54–67. DOI: 10.1016/j.ijplas.2018.01.015.

[73] M. Rhee, H. M. Zbib, J. P. Hirth, H. Huang, and T. d. l. Rubia. "Models for long-/short-range interactions and cross slip in 3D dislocation simulation of BCC single crystals". *Modelling and Simulation in Materials Science and Engineering* 6.4 (1998), p. 467. DOI: 10.1088/0965-0393/6/4/012.

[74] J. W. Cahn and J. E. Hilliard. "Free Energy of a Nonuniform System. I. Interfacial Free Energy". *The Journal of Chemical Physics* 28.2 (1958), pp. 258–267. DOI: 10.1063/1.1744102.

[75] S. M. Allen and J. W. Cahn. "A microscopic theory for antiphase boundary motion and its application to antiphase domain coarsening". *Acta Metallurgica* 27.6 (1979), pp. 1085–1095. DOI: 10.1016/0001-6160(79)90196-2.

[76] G. Schoeck. "The generalized Peierls–Nabarro model". *Philosophical Magazine A* 69.6 (1994), pp. 1085–1095. DOI: 10.1080/01418619408242240.

[77] Y. U. Wang, Y. M. Jin, A. M. Cuitiño, and A. G. Khachaturyan. "Phase field microelasticity theory and modeling of multiple dislocation dynamics". *Applied Physics Letters* 78.16 (2001), pp. 2324–2326. DOI: 10.1063/1.1366370.

[78] M. Koslowski, A. M. Cuitiño, and M. Ortiz. "A phase-field theory of dislocation dynamics, strain hardening and hysteresis in ductile single crystals". *Journal of the Mechanics and Physics of Solids* 50.12 (2002), pp. 2597–2635. DOI: 10.1016/s0022-5096(02)00037-6.

[79] J. R. Mianroodi, A. Hunter, I. J. Beyerlein, and B. Svendsen. "Theoretical and computational comparison of models for dislocation dissociation and stacking fault/core formation in fcc crystals". *Journal of the Mechanics and Physics of Solids* 95 (2016), pp. 719–741. DOI: 10.1016/j.jmps.2016.04.029.

[80] S. Xu, J. R. Mianroodi, A. Hunter, B. Svendsen, and I. J. Beyerlein. "Comparative modeling of the disregistry and Peierls stress for dissociated edge and screw dislocations in Al". *International Journal of Plasticity* 129 (2020), p. 102689. DOI: 10.1016/j.ijplas.2020.102689.

[81] T. Mura. "General theory of eigenstrains". *Micromechanics of defects in solids*. Ed. by T. Mura. Mechanics of Elastic and Inelastic Solids. Dordrecht: Springer Netherlands, 1987, pp. 1–73. DOI: 10.1007/978-94-009-3489-4_1.

[82] I. J. Beyerlein and A. Hunter. "Understanding nanoscale dislocation mechanics using phase field dislocation dynamics". *Philosophical Transactions of the Royal Society of London, Series A* 374.2066 (2016), p. 20150166. DOI: 10.1098/rsta.2015.0166.

[83] S. Xu, Y. Su, L. T. W. Smith, and I. J. Beyerlein. "Frank-Read source operation in six body-centered cubic refractory metals". *Journal of the Mechanics and Physics of Solids* 141 (2020), p. 104017. DOI: 10.1016/j.jmps.2020.104017.

[84] X. Peng, N. Mathew, I. J. Beyerlein, K. Dayal, and A. Hunter. "A 3D phase field dislocation dynamics model for body-centered cubic crystals". *Computational Materials Science* 171.August 2019 (2020), p. 109217. DOI: 10.1016/j.commatsci.2019.109217.

[85] K. Kang, V. V. Bulatov, and W. Cai. "Singular orientations and faceted motion of dislocations in body-centered cubic crystals". *Proceedings of the National Academy of Sciences* 109.38 (2012), pp. 15174–15178. DOI: 10.1073/pnas.1206079109.

[86] D. Terentyev, G. Bonny, C. Domain, and R. C. Pasianot. "Interaction of a $\frac{1}{2}\langle 111\rangle$ screw dislocation with Cr precipitates in bcc Fe studied by molecular dynamics". *Physical Review B* 81.21 (2010), p. 214106. DOI: 10.1103/physrevb.81.214106.

[87] J. Qian, C. Y. Wu, J. L. Fan, and H. R. Gong. "Effect of alloying elements on stacking fault energy and ductility of tungsten". *Journal of Alloys and Compounds* 737 (2018), pp. 372–376. DOI: 10.1016/j.jallcom.2017.12.042.

[88] S. Xu, J. K. Startt, T. G. Payne, C. S. Deo, and D. L. McDowell. "Size-dependent plastic deformation of twinned nanopillars in body-centered cubic tungsten". *Journal of Applied Physics* 121.17 (2017), p. 175101. DOI: 10.1063/1.4982754.

[89] S. L. Frederiksen and K. W. Jacobsen. "Density functional theory studies of screw dislocation core structures in bcc metals". *Philosophical Magazine* 83.3 (2003), pp. 365–375. DOI: 10.1080/0141861021000034568.

[90] C. Yang and L. Qi. "Modified embedded-atom method potential of niobium for studies on mechanical properties". *Computional Materials Science* 161 (2019), pp. 351–363. DOI: 10.1016/j.commatsci.2019.01.047.

[91] R. F. Zhang, J. Wang, I. J. Beyerlein, and T. C. Germann. "Twinning in bcc metals under shock loading: a challenge to empirical potentials". *Philosophical Magazine Letters* 91.12 (2011), pp. 731–740. DOI: 10.1080/09500839.2011.615348.

[92] L. H. Yang, P. Söderlind, and J. A. Moriarty. "Accurate atomistic simulation of $(a/2)\langle 111\rangle$ screw dislocations and other defects in bcc tantalum". *Philosophical Magazine A* 81.5 (2001), pp. 1355–1385. DOI: 10.1080/01418610108214446.

[93] L. Romaner, C. Ambrosch-Draxl, and R. Pippan. "Effect of rhenium on the dislocation core structure in tungsten". *Physical Review Letters* 104.19 (2010), p. 195503. DOI: 10.1103/physrevlett.104.195503.

[94] X. Zhang, J. Tang, L. Deng, G. Zhong, X. Liu, Y. Li, H. Deng, and W. Hu. "The effects of interstitial impurities on the mechanical properties of vanadium alloys: A first-principles study". *Journal of Alloys and Compounds* 701 (2017), pp. 975–980. DOI: 10.1016/j.jallcom.2017.01.135.

[95] G. Bonny, D. Terentyev, A. Bakaev, P. Grigorev, and D. V. Neck. "Many-body central force potentials for tungsten". *Modelling and Simulation in Materials Science and Engineering* 22.5 (2014), p. 053001. DOI: 10.1088/0965-0393/22/5/053001.

[96] M.-C. Marinica, L. Ventelon, M. R. Gilbert, L. Proville, S. L. Dudarev, J. Marian, G. Bencteux, and F. Willaime. "Interatomic potentials for modelling radiation defects and dislocations in tungsten". *Journal of Physics: Condensed Matter* 25.39 (2013), p. 395502. DOI: 10.1088/0953-8984/25/39/395502.

[97] L. T. W. Smith, Y. Su, S. Xu, A. Hunter, and I. J. Beyerlein. "The effect of local chemical ordering on Frank-Read source activation in a refractory multi-principal element alloy". *International Journal of Plasticity* 134 (2020), p. 102850. DOI: 10.1016/j.ijplas.2020.102850.

[98] F. C. Frank and W. T. Read. "Multiplication processes for slow moving dislocations". *Physical Review* 79.4 (1950), pp. 722–723. DOI: 10.1103/physrev.79.722.

[99] T. Chen, R. Yuan, I. J. Beyerlein, and C. Zhou. "Predicting the size scaling in strength of nanolayered materials by a discrete slip crystal plasticity model". *International Journal of Plasticity* 124 (2020), pp. 247–260. DOI: 10.1016/j.ijplas.2019.08.016.

[100] Y. Zhu, H. Wang, X. Zhu, and Y. Xiang. "A continuum model for dislocation dynamics incorporating Frank-Read sources and Hall-Petch relation in two dimensions". *International Journal of Plasticity* 60 (2014), pp. 19–39. DOI: 10.1016/j.ijplas.2014.04.013.

[101] Y. Zhang and A. H. W. Ngan. "Dislocation-density dynamics for modeling the cores and Peierls stress of curved dislocations". *International Journal of Plasticity* 104 (2018), pp. 1–22. DOI: 10.1016/j.ijplas.2018.01.009.

[102] O. N. Senkov, S. I. Rao, T. M. Butler, and K. J. Chaput. "Ductile Nb alloys with reduced density and cost". *Journal of Alloys and Compounds* 808 (2019), p. 151685. DOI: 10.1016/j.jallcom.2019.151685.

[103] S. Xu, J. R. Mianroodi, A. Hunter, I. J. Beyerlein, and B. Svendsen. "Phase-field-based calculations of the disregistry fields of static extended dislocations in FCC metals". *Philosophical Magazine* 99.11 (2019), pp. 1400–1428. DOI: 10.1080/14786435.2019.1582850.

[104] Y. Su, S. Xu, and I. J. Beyerlein. "Ab initio-informed phase-field modeling of dislocation core structures in equal-molar CoNiRu multi-principal element alloys". *Modelling and Simulation in Materials Science and Engineering* 27.8 (2019). DOI: 10.1088/1361-651x/ab3b62.

[105] C. Albrecht, A. Hunter, A. Kumar, and I. J. Beyerlein. "A phase field model for dislocations in hexagonal close packed crystals". *Journal of the Mechanics and Physics of Solids* 137 (2020), p. 103823. DOI: 10.1016/j.jmps.2019.103823.

[106] S. Ismail-Beigi and T. A. Arias. "Ab initio study of screw dislocations in mo and Ta: A new picture of plasticity in bcc transition metals". *Physical Review Letters* 84.7 (2000), pp. 1499–1502. DOI: 10.1103/physrevlett.84.1499.

[107] A. Mapar, H. Ghassemi-Armaki, F. Pourboghrat, and K. S. Kumar. "A differential-exponential hardening law for non-Schmid crystal plasticity finite element modeling of ferrite single crystals". *International Journal of Plasticity* 91 (2017), pp. 268–299. DOI: 10.1016/j.ijplas.2016.11.009.

[108] P. El Ters and M. A. Shehadeh. "Modeling the temperature and high strain rate sensitivity in BCC iron: Atomistically informed multiscale dislocation dynamics simulations". *International Journal of Plasticity* 112 (2019), pp. 257–277. DOI: 10.1016/j.ijplas.2018.09.002.

[109] R. Gröger and V. Vitek. "Single crystal yield criterion for chromium based on atomistic studies of isolated 1/2[111] screw dislocations". *International Journal of Plasticity* (2020), p. 102733. DOI: 10.1016/j.ijplas.2020.102733.

[110] C. R. Weinberger, G. J. Tucker, and S. M. Foiles. "Peierls potential of screw dislocations in bcc transition metals: Predictions from density functional theory". *Physical Review B* 87.5 (2013), pp. 1–8. DOI: 10.1103/physrevb.87.054114.

[111] M. Itakura, H. Kaburaki, and M. Yamaguchi. "First-principles study on the mobility of screw dislocations in bcc iron". *Acta Materialia* 60.9 (2012), pp. 3698–3710. DOI: 10.1016/j.actamat.2012.03.033.

[112] L. Ventelon, F. Willaime, E. Clouet, and D. Rodney. "Ab initio investigation of the Peierls potential of screw dislocations in bcc Fe and W". *Acta Materialia* 61.11 (2013), pp. 3973–3985. DOI: 10.1016/j.actamat.2013.03.012.

[113] L. Dezerald, L. Ventelon, E. Clouet, C. Denoual, D. Rodney, and F. Willaime. "Ab initio modeling of the two-dimensional energy landscape of screw dislocations in bcc transition metals". *Physical Review B* 89.2 (2014), pp. 1–13. DOI: 10.1103/physrevb.89.024104.

[114] J. Chaussidon, M. Fivel, and D. Rodney. "The glide of screw dislocations in bcc Fe: Atomistic static and dynamic simulations". *Acta Materialia* 54.13 (2006), pp. 3407–3416. DOI: 10.1016/j.actamat.2006.03.044.

[115] L. M. Hale, J. A. Zimmerman, and C. R. Weinberger. "Simulations of bcc tantalum screw dislocations: Why classical inter-atomic potentials predict 112 slip". *Computional Materials Science* 90 (2014), pp. 106–115. DOI: 10.1016/j.commatsci.2014.03.064.

[116] Y. Su, S. Xu, and I. J. Beyerlein. "Density functional theory calculations of generalized stacking fault energy surfaces for eight face-centered cubic transition metals". *Journal of Applied Physics* 126.10 (2019), p. 105112. DOI: 10.1063/1.5115282.

[117] S. Xu, E. Hwang, W.-R. Jian, Y. Su, and I. J. Beyerlein. "Atomistic calculations of the generalized stacking fault energies in two refractory multi-principal element alloys". *Intermetallics* 124 (2020), p. 106844. DOI: 10.1016/j.intermet.2020.106844.

[118] S. Zhao, Y. Osetsky, M. Stocks, and Y. Zhang. "Local-environment dependence of stacking fault energies in concentrated solid-solution alloys". *npj Computional Materials* 5.13 (2019). DOI: 10.1038/s41524-019-0150-y.

[119] Y. Z. Hu and K. Tonder. "Simulation of 3-D random rough surface by 2-D digital filter and fourier analysis". *International Journal of Machine Tools and Manufacture* (1992). DOI: 10.1016/0890-6955(92)90064-n.

[120] S. I. Rao, E. Antillon, C. Woodward, B. Akdim, T. A. Parthasarathy, and O. N. Senkov. "Solution hardening in body-centered cubic quaternary alloys interpreted using Suzuki's kink-solute interaction model". *Scripta Materialia* 165 (2019), pp. 103–106. DOI: 10.1016/j.scriptamat.2019.02.012.

[121] S. Xu, Y. Su, and I. J. Beyerlein. "Modeling dislocations with arbitrary character angle in face-centered cubic transition metals using the phase-field dislocation dynamics method with full anisotropic elasticity". *Mechanics of Materials* 139 (2019), p. 103200. DOI: 10.1016/j.mechmat.2019.103200.

[122] Y. Su, M. Ardeljan, M. Knezevic, M. Jain, S. Pathak, and I. J. Beyerlein. "Elastic constants of pure body-centered cubic Mg in nanolaminates". *Computional Materials Science* 174 (2020), p. 109501. DOI: 10.1016/j.commatsci.2019.109501.

[123] Q.-J. Li, H. Sheng, and E. Ma. "Strengthening in multi-principal element alloys with local-chemical-order roughened dislocation pathways". *Nature communications* 10.1 (2019), pp. 1–11. DOI: 10.1038/s41467-019-11464-7.

[124] A. J. Foreman. "The bowing of a dislocation segment". *Philosophical Magazine* 15.137 (1967), pp. 1011–1021. DOI: 10.1080/14786436708221645.

[125] R. Yuan, I. J. Beyerlein, and C. Zhou. "Emergence of grain-size effects in nanocrystalline metals from statistical activation of discrete dislocation sources". *Acta Materialia* 90 (2015), pp. 169–181. DOI: 10.1016/j.actamat.2015.02.035.

[126] R. Yuan, I. J. Beyerlein, and C. Zhou. "Coupled crystal orientation-size effects on the strength of nano crystals". *Scientific Reports* 6 (2016), p. 26254. DOI: 10.1038/srep26254.

[127] L. T. W. Fey, S. Xu, Y. Su, A. Hunter, and I. J. Beyerlein. "Transitions in the morphology and critical stresses of gliding dislocations in multiprincipal element alloys". *Physical Review Materials* 6.1 (2022), p. 013605. DOI: 10.1103/physrevmaterials.6.013605.

[128] B. Chen, S. Li, H. Zong, X. Ding, J. Sun, and E. Ma. "Unusual activated processes controlling dislocation motion in body-centered-cubic high-entropy alloys". *Proceedings of the National Academy of Sciences* 117.28 (2020), pp. 16199–16206. DOI: 10.1073/pnas.1919136117.

[129] F. Maresca and W. A. Curtin. "Mechanistic origin of high strength in refractory BCC high entropy alloys up to 1900 K". *Acta Materialia* 182 (2020), pp. 235–249. DOI: 10.1016/j.actamat.2019.10.015.

[130] R. Pasianot and D. Farkas. "Atomistic modeling of dislocations in a random quinary high-entropy alloy". *Computional Materials Science* 173 (2020), p. 109366. DOI: 10.1016/j.commatsci.2019.109366.

[131] F. Maresca and W. A. Curtin. "Theory of screw dislocation strengthening in random BCC alloys from dilute to "High-Entropy" alloys". *Acta Materialia* 182 (2020), pp. 144–162. DOI: 10.1016/j.actamat.2019.10.007.

[132] S. Xu, Y. Su, W.-R. Jian, and I. J. Beyerlein. "Local slip resistances in equal-molar MoNbTi multi-principal element alloy". *Acta Materialia* 202 (2021), pp. 68–79. DOI: 10.1016/j.actamat.2020.10.042.

[133] X. Wang, S. Xu, W.-R. Jian, X.-G. Li, Y. Su, and I. J. Beyerlein. "Generalized stacking fault energies and Peierls stresses in refractory body-centered cubic metals from machine learning-based interatomic potentials". *Computional Materials Science* 192 (2021), p. 110364. DOI: 10.1016/j.commatsci.2021.110364.

[134] M. S. Duesbery. "The influence of core structure on dislocation mobility". *Philosophical Magazine* 19.159 (1969), pp. 501–526. DOI: 10.1080/14786436908216308.

[135] J. W. Christian. "Some surprising features of the plastic deformation of body-centered cubic metals and alloys". *Metallurgical Transactions A* 14.7 (1983), pp. 1237–1256. DOI: 10.1007/bf02664806.

[136] A. Garratt-Reed and G. Taylor. "Optical and electron microscopy of niobium crystals deformed below room temperature". *Philosophical Magazine A* 39.5 (1979), pp. 597–646. DOI: 10.1080/01418617908239294.

[137] D. Caillard. "A TEM in situ study of alloying effects in iron. II-Solid solution hardening caused by high concentrations of Si and Cr". *Acta Materialia* 61.8 (2013), pp. 2808–2827. DOI: 10.1016/j.actamat.2013.01.049.

[138] J. Marian, W. Cai, and V. V. Bulatov. "Dynamic transitions from smooth to rough to twinning in dislocation motion". *Nature Materials* 3.3 (2004), pp. 158–163. DOI: 10.1038/nmat1072.

[139] X. Zhou, S. He, and J. Marian. "Cross-kinks control screw dislocation strength in equiatomic bcc refractory alloys". *Acta Materialia* 211 (2021), p. 116875. DOI: 10.1016/j.actamat.2021.116875.

[140] D. Hull, J. F. Byron, and F. W. Noble. "Orientation Dependence of Yield in Body-Centered Cubic Metals". *Canadian Journal of Physics* 45.2 (1967), pp. 1091–1099. DOI: 10.1139/p67-080.

[141] A. Seeger and U. Holzwarth. "Slip planes and kink properties of screw dislocations in high-purity niobium". *Philosophical Magazine* 86.25-26 (2006), pp. 3861–3892. DOI: 10.1080/14786430500531769.

[142] M. Duesbery, V. Vitek, and D. Bowen. "The effect of shear stress on the screw dislocation core structure in body-centred cubic lattices". *Proceedings of the Royal Society A* 332 (1973), pp. 85–1111. DOI: 10.1007/bf01596326.

[143] B. Joos and M. Duesbery. "The Peierls stress of dislocations: an analytic formula". *Physical Review Letters* 78.2 (1997), p. 266. DOI: 10.1103/physrevlett.78.266.

[144] L. Dezerald, L. Proville, L. Ventelon, F. Willaime, and D. Rodney. "First-principle prediction of kink-pair activation enthalpy on screw dislocations in bcc transition metals: V, Nb, Ta, Mo, W, and Fe". *Physical Review B* 91 (2015), p. 094105. DOI: 10.1103/physrevb.91.094105.

[145] V. Vitek. "Structure of dislocation cores in metallic materials and its impact on their plastic behaviour". *Progress in Materials Science* 36 (1992), pp. 1–27. DOI: 10.1016/0079-6425(92)90003-p.

[146] L. T. W. Fey, A. Hunter, and I. J. Beyerlein. "Phase-Field Dislocation Modeling of Cross-Slip". *Journal of Materials Science* (2022). DOI: 10.1007/s10853-021-06716-1.

[147] M. S. Duesbery and V. Vitek. "Plastic anisotropy in bcc transition metals". *Acta Materialia* 46.5 (1998), pp. 1481–1492. DOI: 10.1016/s1359-6454(97)00367-4.

[148] G. I. Taylor and C. F. Elam. "The distortion of iron crystals". *Proceedings of the Royal Society of London. Series A, Containing Papers of a Mathematical and Physical Character* 112.761 (1926), pp. 337–361. DOI: 10.1098/rspa.1926.0116.

[149] C. R. Weinberger, B. L. Boyce, and C. C. Battaile. "Slip planes in bcc transition metals". *International Materials Reviews* 58.5 (2013), pp. 296–314. DOI: 10.1179/1743280412y.0000000015.

[150] P. Jackson. "Dislocation modelling of shear in fcc crystals". *Progress in Materials Science* 29.1-2 (1985), pp. 139–175. DOI: 10.1016/0079-6425(85)90009-x.

[151] Q. Yu, L. Qi, T. Tsuru, R. Traylor, D. Rugg, J. Morris, M. Asta, D. Chrzan, and A. M. Minor. "Origin of dramatic oxygen solute strengthening effect in titanium". *Science* 347.6222 (2015), pp. 635–639. DOI: 10.1126/science.1260485.

[152] E. Clouet, D. Caillard, N. Chaari, F. Onimus, and D. Rodney. "Dislocation locking versus easy glide in titanium and zirconium". *Nature Materials* 14.9 (2015), pp. 931–936. DOI: 10.1038/nmat4340.

[153] C. Woodward and S. Rao. "Ab-initio simulation of (a/2)¡ 110] screw dislocations in γ-TiAl". *Philosophical Magazine* 84.3-5 (2004), pp. 401–413. DOI: 10.1080/14786430310001611626.

[154] N. Chaari, E. Clouet, and D. Rodney. "First-Principles Study of Secondary Slip in Zirconium". *Physical Review Letters* 112 (7 2014), p. 075504. DOI: 10.1103/physrevlett.112.075504.

[155] L. Ma, S. Xiao, H. Deng, and W. Hu. "Molecular dynamics simulation of fatigue crack propagation in bcc iron under cyclic loading". *International Journal of Fatigue* 68 (2014), pp. 253–259. DOI: 10.1016/j.ijfatigue.2014.04.010.

[156] G. Sainath and B. Choudhary. "Molecular dynamics simulations on size dependent tensile deformation behaviour of [110] oriented body centred cubic iron nanowires". *Materials Science and Engineering: A* 640 (2015), pp. 98–105. DOI: 10.1016/j.msea.2015.05.084.

[157] T. Suzudo, T. Onitsuka, and K.-i. Fukumoto. "Analyzing the cross slip motion of screw dislocations at finite temperatures in body-centered-cubic metals: molecular statics and dynamics studies". *Modelling and Simulation in Materials Science and Engineering* 27.6 (2019), p. 064001. DOI: 10.1088/1361-651x/ab235e.

[158] D. Weygand, L. Friedman, E. Van der Giessen, and A. Needleman. "Aspects of boundary-value problem solutions with three-dimensional dislocation dynamics". *Modelling and Simulation in Materials Science and Engineering* 10.4 (2002), p. 437. DOI: 10.1088/0965-0393/10/4/306.

[159] A. Arsenlis, W. Cai, M. Tang, M. Rhee, T. Oppelstrup, G. Hommes, T. G. Pierce, and V. V. Bulatov. "Enabling strain hardening simulations with dislocation dynamics". *Modelling and Simulation in Materials Science and Engineering* 15.6 (2007), p. 553. DOI: 10.1088/0965-0393/15/6/001.

[160] Z. Wang, I. Beyerlein, and R. LeSar. "The importance of cross-slip in high-rate deformation". *Modelling and simulation in materials science and engineering* 15.6 (2007), p. 675. DOI: 10.1088/0965-0393/15/6/006.

[161] W. Cai, V. V. Bulatov, S. Yip, and A. S. Argon. "Kinetic Monte Carlo modeling of dislocation motion in BCC metals". *Materials Science and Engineering: A* 309 (2001), pp. 270–273. DOI: 10.1016/s0921-5093(00)01689-0.

[162] A. Stukowski, D. Cereceda, T. D. Swinburne, and J. Marian. "Thermally-activated non-Schmid glide of screw dislocations in W using atomistically-informed kinetic Monte Carlo simulations". *International Journal of Plasticity* 65 (2015), pp. 108–130. DOI: 10.1016/j.ijplas.2014.08.015.

[163] A. Ngan. "A generalized Peierls-Nabarro model for nonplanar screw dislocation cores". *Journal of the Mechanics and Physics of Solids* 45.6 (1997), pp. 903–921. DOI: 10.1016/s0022-5096(96)00125-1.

[164] G. Lu, V. V. Bulatov, and N. Kioussis*. "A nonplanar Peierls–Nabarro model and its application to dislocation cross-slip". *Philosophical Magazine* 83.31-34 (2003), pp. 3539–3548. DOI: 10.1080/14786430310001634630.

[165] S. Zheng, D. Zheng, Y. Ni, and L. He. "Improved phase field model of dislocation intersections". *npj Computational Materials* 4.1 (2018), pp. 1–8. DOI: 10.1038/s41524-018-0075-x.

[166] A. Ruffini, Y. Le Bouar, and A. Finel. "Three-dimensional phase-field model of dislocations for a heterogeneous face-centered cubic crystal". *Journal of the Mechanics and Physics of Solids* 105 (2017), pp. 95–115. DOI: 10.1016/j.jmps.2017.04.008.

[167] X. Peng, A. Hunter, I. J. Beyerlein, R. A. Lebensohn, K. Dayal, and E. Martinez. "Non-orthogonal computational grids for studying dislocation motion in phase field approaches". *Computational Materials Science* 200 (2021), p. 110834. DOI: 10.1016/j.commatsci.2021.110834.

[168] H. Warlimont and W. Martienssen. *Springer Handbook of Materials Data*. Springer, 2018.

[169] A. Ruff. "Measurement of stacking fault energy from dislocation interactions". *Metallurgical Transactions* 1.9 (1970), pp. 2391–2413. DOI: 10.1007/bf03038368.

[170] C. Woodward, D. Trinkle, L. Hector Jr, and D. Olmsted. "Prediction of dislocation cores in aluminum from density functional theory". *Physical Review Letters* 100.4 (2008), p. 045507. DOI: 10.1103/physrevlett.100.045507.

[171] M. Jahnátek, J. Hafner, and M. Krajčí. "Shear deformation, ideal strength, and stacking fault formation of fcc metals: A density-functional study of Al and Cu". *Physical Review B* 79.22 (2009), p. 224103. DOI: 10.1103/physrevb.79.224103.

[172] A. Hunter, R. Zhang, and I. Beyerlein. "The core structure of dislocations and their relationship to the material γ-surface". *Journal of Applied Physics* 115.13 (2014), p. 134314. DOI: 10.1063/1.4870462.

[173] V. Vitek. "Intrinsic stacking faults in body-centred cubic crystals". *Philosophical Magazine* 18.154 (1968), pp. 773–786. DOI: 10.1080/14786436808227500.

[174] H.-J. Kaufmann, A. Luft, and D. Schulze. "Deformation mechanism and dislocation structure of high-purity molybdenum single crystals at low temperatures". *Crystal Research and Technology* 19.3 (1984), pp. 357–372. DOI: 10.1002/crat.2170190312.

[175] R. Ji, T. Phan, H. Chen, and L. Xiong. "Quantifying the dynamics of dislocation kinks in iron and tungsten through atomistic simulations". *International Journal of Plasticity* 128 (2020), p. 102675. DOI: 10.1016/j.ijplas.2020.102675.

[176] J. R. Low and A. M. Turkalo. "Slip band structure and dislocation multiplication in silicon-iron crystals". *Acta Metallurgica* 10.3 (1962), pp. 215–227. DOI: 10.1016/0001-6160(62)90119-0.

[177] N. Urabe and J. Weertman. "Dislocation mobility in potassium and iron single crystals". *Materials Science and Engineering* 18.1 (1975), pp. 41–49. DOI: 10.1016/0025-5416(75)90071-3.

[178] F. Louchet, L. P. Kubin, and D. Vesely. "In situ deformation of b.c.c. crystals at low temperatures in a high-voltage electron microscope Dislocation mechanisms and strain-rate equation". *Philosophical Magazine A* 39.4 (1979), pp. 433–454. DOI: 10.1080/01418617908239283.

[179] M. Duesbery and G. Richardson. "The dislocation core in crystalline materials". *Critical Reviews in Solid State and Material Sciences* 17.1 (1991), pp. 1–46. DOI: 10.1080/10408439108244630.

[180] G. Po, Y. Cui, D. Rivera, D. Cereceda, T. D. Swinburne, J. Marian, and N. Ghoniem. "A phenomenological dislocation mobility law for bcc metals". *Acta Materialia* 119 (2016), pp. 123–135. DOI: 10.1016/j.actamat.2016.08.016.

[181] L. T. W. Fey and I. J. Beyerlein. "Random Generation of Lattice Structures with Short-Range Order". *Integrating Materials and Manufacturing Innovation* 11.3 (2022), pp. 382–390. DOI: 10.1007/s40192-022-00269-0.

[182] H. Zheng, L. T. W. Fey, X.-G. Li, Y.-J. Hu, L. Qi, C. Chen, S. Xu, I. J. Beyerlein, and S. P. Ong. "Multi-scale Investigation of Chemical Short-Range Order and Dislocation Glide in the MoNbTi and TaNbTi Refractory Multi-Principal Element Alloys". *npj Computational Materials* Under Review (2022). DOI: 10.48550/arxiv.2203.03767.

[183] J. Cowley. "An approximate theory of order in alloys". *Physical Review* 77.5 (1950), p. 669. DOI: 10.1103/physrev.77.669.

[184] J. Fisher. "On the strength of solid solution alloys". *Acta metallurgica* 2.1 (1954), pp. 9–10. DOI: 10.1016/0001-6160(54)90087-5.

[185] B. Schonfeld. "Local atomic arrangements in binary alloys". *Progress in materials science* 44.5 (1999), pp. 435–543. DOI: 10.1016/s0079-6425(99)00005-5.

[186] N. Clement, D. Caillard, and J. Martin. "Heterogeneous deformation of concentrated Ni-Cr FCC alloys: Macroscopic and microscopic behaviour". *Acta Metallurgica* 32.6 (1984), pp. 961–975. DOI: 10.1016/0001-6160(84)90034-8.

[187] S. Dubiel and J. Cieslak. "Short-range order in iron-rich Fe-Cr alloys as revealed by Mössbauer spectroscopy". *Physical Review B* 83.18 (2011), p. 180202. DOI: 10.1103/physrevb.83.180202.

[188] P. Erhart, A. Caro, M. S. de Caro, and B. Sadigh. "Short-range order and precipitation in Fe-rich Fe-Cr alloys: Atomistic off-lattice Monte Carlo simulations". *Physical Review B* 77.13 (2008), p. 134206. DOI: 10.1103/physrevb.77.134206.

[189] W.-R. Jian, L. Wang, W. Bi, S. Xu, and I. J. Beyerlein. "Role of local chemical fluctuations in the melting of medium entropy alloy CoCrNi". *Applied Physics Letters* 119.12 (2021), p. 121904. DOI: 10.1063/5.0064299.

[190] Z. Xie, W.-R. Jian, S. Xu, I. J. Beyerlein, X. Zhang, Z. Wang, and X. Yao. "Role of local chemical fluctuations in the shock dynamics of medium entropy alloy CoCrNi". *Acta Materialia* 221 (2021), p. 117380. DOI: 10.1016/j.actamat.2021.117380.

[191] S. D. Wang, X. J. Liu, Z. F. Lei, D. Y. Lin, F. G. Bian, C. M. Yang, M. Y. Jiao, Q. Du, H. Wang, Y. Wu, S. H. Jiang, and Z. P. Lu. "Chemical short-range ordering and its strengthening effect in refractory high-entropy alloys". *Physical Review B* 103 (10 2021), p. 104107. DOI: 10.1103/physrevb.103.104107.

[192] D. Liu, Q. Wang, J. Wang, X. Chen, P. Jiang, F. Yuan, Z. Cheng, E. Ma, and X. Wu. "Chemical short-range order in Fe50Mn30Co10Cr10 high-entropy alloy". *Materials Today Nano* 16 (2021), p. 100139. DOI: 10.1016/j.mtnano.2021.100139.

[193] J. Wang, P. Jiang, F. Yuan, and X. Wu. "Chemical medium-range order in a medium-entropy alloy". *Nature Communications* 13.1 (2022), pp. 1–6. DOI: 10.1038/s41467-022-28687-w.

[194] R. Zhang, S. Zhao, J. Ding, Y. Chong, T. Jia, C. Ophus, M. Asta, R. O. Ritchie, and A. M. Minor. "Short-Range Order and Its Impact on the CrCoNi Medium-Entropy Alloy". *Nature* 581.7808 (2020), pp. 283–287. DOI: 10.1038/s41586-020-2275-z.

[195] C. G. Schön. "On short-range order strengthening and its role in high-entropy alloys". *Scripta Materialia* 196 (2021), p. 113754. DOI: 10.1016/j.scriptamat.2021.113754.

[196] Y. Wu, F. Zhang, X. Yuan, H. Huang, X. Wen, Y. Wang, M. Zhang, H. Wu, X. Liu, H. Wang, et al. "Short-range ordering and its effects on mechanical properties of high-entropy alloys". *Journal of Materials Science & Technology* 62 (2021), pp. 214–220. DOI: 10.1016/j.jmst.2020.06.018.

[197] J. Cowley. "Short-and long-range order parameters in disordered solid solutions". *Physical Review* 120.5 (1960), p. 1648. DOI: 10.1103/physrev.120.1648.

[198] A. Tamm, A. Aabloo, M. Klintenberg, M. Stocks, and A. Caro. "Atomic-scale properties of Ni-based FCC ternary, and quaternary alloys". *Acta Materialia* 99 (2015), pp. 307–312. DOI: 10.1016/j.actamat.2015.08.015.

[199] M. Mizuno, K. Sugita, and H. Araki. "Prediction of short-range order in CrMnFeCoNi high-entropy alloy". *Results in Physics* 34 (2022), p. 105285. DOI: 10.1016/j.rinp.2022.105285.

[200] M. Widom, W. P. Huhn, S. Maiti, and W. Steurer. "Hybrid Monte Carlo/molecular dynamics simulation of a refractory metal high entropy alloy". *Metallurgical and Materials Transactions A* 45.1 (2014), pp. 196–200. DOI: 10.1007/s11661-013-2000-8.

[201] E. Antillon, C. Woodward, S. Rao, B. Akdim, and T. Parthasarathy. "Chemical short range order strengthening in a model FCC high entropy alloy". *Acta Materialia* 190 (2020), pp. 29–42. DOI: 10.1016/j.actamat.2020.02.041.

[202] X. Huang, L. Liu, X. Duan, W. Liao, J. Huang, H. Sun, and C. Yu. "Atomistic simulation of chemical short-range order in HfNbTaZr high entropy alloy based on a newly-developed interatomic potential". *Materials & Design* 202 (2021), p. 109560. DOI: 10.1016/j.matdes.2021.109560.

[203] Z. Shen, J.-P. Du, S. Shinzato, Y. Sato, P. Yu, and S. Ogata. "Kinetic Monte Carlo simulation framework for chemical short-range order formation kinetics in a multi-principal-element alloy". *Computational Materials Science* 198 (2021), p. 110670. DOI: 10.1016/j.commatsci.2021.110670.

[204] C. Chen, Z. Deng, R. Tran, H. Tang, I.-H. Chu, and S. P. Ong. "Accurate Force Field for Molybdenum by Machine Learning Large Materials Data". *Physical Review Materials* 1.4 (2017), p. 043603. DOI: 10.1103/physrevmaterials.1.043603.

[205] X.-G. Li, C. Hu, C. Chen, Z. Deng, J. Luo, and S. P. Ong. "Quantum-Accurate Spectral Neighbor Analysis Potential Models for Ni-Mo Binary Alloys and Fcc Metals". *Physical Review B* 98.9 (2018), p. 094104. DOI: 10.1103/physrevb.98.094104.

[206] Y. Zuo, C. Chen, X. Li, Z. Deng, Y. Chen, J. Behler, G. Csányi, A. V. Shapeev, A. P. Thompson, M. A. Wood, and S. P. Ong. "Performance and Cost Assessment of Machine Learning Interatomic Potentials". *The Journal of Physical Chemistry A* 124.4 (2020), pp. 731–745. DOI: 10.1021/acs.jpca.9b08723.

[207] J. Qi, S. Banerjee, Y. Zuo, C. Chen, Z. Zhu, M. Holekevi Chandrappa, X. Li, and S. Ong. "Bridging the Gap between Simulated and Experimental Ionic Conductivities in Lithium Superionic Conductors". *Materials Today Physics* 21 (2021), p. 100463. DOI: 10.1016/j.mtphys.2021.100463.

[208] S. Xu. "Recent progress in the phase-field dislocation dynamics method". *Computational Materials Science* 210 (2022), p. 111419. DOI: 10.1016/j.commatsci.2022.111419.

[209] P. C. Gehlen and J. B. Cohen. "Computer Simulation of the Structure Associated with Local Order in Alloys". *Physical Review* 139 (3A 1965), A844–A855. DOI: 10.1103/physrev.139.a844.

[210] S. Xu, W.-R. Jian, and I. J. Beyerlein. "Ideal simple shear strengths of two HfNbTaTi-based quinary refractory multi-principal element alloys". *APL Materials* 10.11 (2022), p. 111107. DOI: 10.1063/5.0116898.

[211] A. Stukowski. "Visualization and analysis of atomistic simulation data with OVITO-the Open Visualization Tool". *Modelling and Simulation in Materials Science and Engineering* 18.1 (2010). DOI: 10.1088/0965-0393/18/1/015012.

[212] T. Kostiuchenko, F. Körmann, J. Neugebauer, and A. Shapeev. "Impact of Lattice Relaxations on Phase Transitions in a High-Entropy Alloy Studied by Machine-Learning Potentials". *npj Computational Materials* 5.1 (2019), p. 55. DOI: 10.1038/s41524-019-0195-y.

[213] A. Ghafarollahi, F. Maresca, and W. Curtin. "Solute/screw dislocation interaction energy parameter for strengthening in bcc dilute to high entropy alloys". *Modelling and Simulation in Materials Science and Engineering* 27.8 (2019), p. 085011. DOI: 10.1088/1361-651x/ab4969.

[214] J. Zýka, J. Málek, J. Veselý, F. Lukáč, J. Čížek, J. Kuriplach, and O. Melikhova. "Microstructure and Room Temperature Mechanical Properties of Different 3 and 4 Element Medium Entropy Alloys from HfNbTaTiZr System". *Entropy* 21.2 (2019), p. 114. DOI: 10.3390/e21020114.

[215] O. Senkov, D. Miracle, and S. Rao. "Correlations to Improve Room Temperature Ductility of Refractory Complex Concentrated Alloys". *Materials Science and Engineering: A* 820 (2021), p. 141512. DOI: 10.1016/j.msea.2021.141512.

[216] L. T. W. Fey, C. Reynolds, A. Hunter, and I. J. Beyerlein. "Phase-field modeling of dislocation-interstitial interactions". *Journal of the Mechanics and Physics of Solids* (2023), Under Review.

[217] B. A. Bilby. "On the interactions of dislocations and solute atoms". *Proceedings of the Physical Society. Section A* 63.3 (1950), pp. 191–200. DOI: 10.1088/0370-1298/63/3/302.

[218] S. Y. Hu, Y. L. Li, Y. X. Zheng, and L. Q. Chen. "Effect of solutes on dislocation motion — a phase-field simulation". *International Journal of Plasticity* 20 (2004), pp. 403–425. DOI: 10.1016/s0749-6419(03)00094-9.

[219] Z. Zheng, J. Chen, Y. Zhu, L. Zhao, M. Huang, S. Liang, and Z. Li. "An atomistically-informed phase-field model for quantifying the effect of hydrogen on the evolution of dislocations in FCC metals". *International Journal of Plasticity* 138.January (2021), p. 102937. DOI: 10.1016/j.ijplas.2021.102937.

[220] R. C. Pasianot. "On the determination of defect dipoles from atomistic simulations using periodic boundary conditions". *Philosophical Magazine Letters* 96.12 (2016), pp. 447–453. DOI: 10.1080/09500839.2016.1250965.

[221] J. Svoboda, G. A. Zickler, and F. D. Fischer. "An innovative concept for interstitial diffusion in stressed crystals". *International Journal of Solids and Structures* 134 (2018), pp. 173–180. DOI: 10.1016/j.ijsolstr.2017.10.036.

[222] T. Fan, L. Wei, B. Tang, L. Peng, and W. Ding. "Effect of temperature-induced solute distribution on stacking fault energy in Mg–X(X = Li, Cu, Zn, Al, Y and Zr) solid solution: a first-principles study". *Philosophical Magazine* 94.14 (2014), pp. 1578–1587. DOI: 10.1080/14786435.2014.890756.

[223] G. Kresse and J. Hafner. "Ab initio molecular dynamics for liquid metals". *Physical Review B* 47.1 (1993), p. 558. DOI: 10.1103/physrevb.47.558.

[224] G. Kresse and J. Hafner. "Ab initio molecular-dynamics simulation of the liquid-metal–amorphous-semiconductor transition in germanium". *Physical Review B* 49.20 (1994), p. 14251. DOI: 10.1103/physrevb.49.14251.

[225] G. Kresse and J. Furthmüller. "Efficient iterative schemes for ab initio total-energy calculations using a plane-wave basis set". *Physical Review B* 54.16 (1996), p. 11169. DOI: 10.1103/physrevb.54.11169.

[226] G. Kresse and J. Furthmüller. "Efficiency of ab-initio total energy calculations for metals and semiconductors using a plane-wave basis set". *Computational Materials Science* 6.1 (1996), pp. 15–50. DOI: 10.1016/0927-0256(96)00008-0.

[227] P. E. Blöchl. "Projector augmented-wave method". *Physical Review B* 50.24 (1994), p. 17953. DOI: 10.1103/physrevb.50.17953.

[228] G. Kresse and D. Joubert. "From ultrasoft pseudopotentials to the projector augmented-wave method". *Physical Review B* 59.3 (1999), p. 1758. DOI: 10.1103/physrevb.59.1758.

[229] J. P. Perdew, K. Burke, and M. Ernzerhof. "Generalized gradient approximation made simple". *Physical Review Letters* 77.18 (1996), p. 3865. DOI: 10.1103/physrevlett.77.3865.

[230] G. Kresse and J. Furthmüller. "Efficient iterative schemes for ab initio total-energy calculations using a plane-wave basis set". *Physical Review B* 54 (16 1996), pp. 11169–11186. DOI: 10.1103/physrevb.54.11169.

[231] D. Gottlieb and C.-W. Shu. "On the Gibbs phenomenon and its resolution". *SIAM Review* 39.4 (1997), pp. 644–668. DOI: 10.1137/s0036144596301390.

[232] F. Willot. "Fourier-based schemes for computing the mechanical response of composites with accurate local fields". *Comptes Rendus Mécanique* 343.3 (2015), pp. 232–245. DOI: 10.1016/j.crme.2014.12.005.

[233] F. Willot, B. Abdallah, and Y.-P. Pellegrini. "Fourier-based schemes with modified Green operator for computing the electrical response of heterogeneous media with accurate local fields". *International Journal for Numerical Methods in Engineering* 98.7 (2014), pp. 518–533. DOI: 10.1002/nme.4641.

[234] F. M. Waltz and J. W. Miller. "Efficient algorithm for gaussian blur using finite-state machines". *Machine Vision Systems for Inspection and Metrology VII*. Vol. 3521. SPIE. 1998, pp. 334–341. DOI: 10.1117/12.326976.

[235] J. Buchholz. "Absence of the Snoek Effect for Hydrogen in Tantalum". *International Meeting on Hydrogen in Metals* 2 (1972), pp. 544–556. DOI: 10.1002/bbpc.19720760847.

[236] V. K. Tewary. "Lattice distortion due to gas interstitials in bcc metals". *Journal of Physics F: Metal Physics* 3.8 (1973), pp. 1515–1523. DOI: 10.1088/0305-4608/3/8/006.

[237] W. Cai, R. B. Sills, D. M. Barnett, and W. D. Nix. "Modeling a distribution of point defects as misfitting inclusions in stressed solids". *Journal of the Mechanics and Physics of Solids* 66.1 (2014), pp. 154–171. DOI: 10.1016/j.jmps.2014.01.015.

[238] Y. Hanlumyuang, P. Gordon, T. Neeraj, and D. Chrzan. "Interactions between carbon solutes and dislocations in bcc iron". *Acta Materialia* 58.16 (2010), pp. 5481–5490. DOI: 10.1016/j.actamat.2010.06.024.

[239] J. Svoboda, W. Ecker, V. Razumovskiy, G. Zickler, and F. Fischer. "Kinetics of interaction of impurity interstitials with dislocations revisited". *Progress in Materials Science* 101 (2019), pp. 172–206. DOI: 10.1016/j.pmatsci.2018.10.001.

[240] A. W. Cochardt and G. Schoek. "Interaction Between Dislocations and Interstitial Atoms in Body-Centered Cubic Metals". *Acta Metallurgica* 3 (1955), p. 5. DOI: 10.1016/0001-6160(55)90111-5.

[241] T. Tabata and H. Birnbaum. "Direct observations of the effect of hydrogen on the behavior of dislocations in iron". *Scripta Metallurgica* 17.7 (1983), pp. 947–950. DOI: 10.1016/0036-9748(83)90268-5.

[242] H. Yu, A. Cocks, and E. Tarleton. "Discrete dislocation plasticity HELPs understand hydrogen effects in bcc materials". *Journal of the Mechanics and Physics of Solids*. The N.A. Fleck 60th Anniversary Volume 123 (2019), pp. 41–60. DOI: 10.1016/j.jmps.2018.08.020.

[243] L.-C. Huang, D. Chen, D.-G. Xie, S. Li, T. Zhu, D. Raabe, E. Ma, J. Li, and Z.-W. Shan. "Quantitative tests revealing hydrogen enhanced dislocation motion in α-iron" (2021). DOI: 10.21203/rs.3.rs-1059604/v1.

[244] K. Tapasa, Y. N. Osetsky, and D. J. Bacon. "Computer simulation of interaction of an edge dislocation with a carbon interstitial in α-iron and effects on glide". *Acta Materialia* 55.1 (2007), pp. 93–104. DOI: 10.1016/j.actamat.2006.08.015.

[245] J. Hou, X.-S. Kong, C. S. Liu, and J. Song. "Hydrogen clustering in bcc metals: Atomic origin and strong stress anisotropy". *Acta Materialia* 201 (2020), pp. 23–35. DOI: 10.1016/j.actamat.2020.09.048.